Hydro-Climatic Causes of Widespread Floods in Central Europe: On Rain-on-Snow and Vb-Cyclone Events

Dissertation

zur Erlangung des Doktorgrades

der Naturwissenschaften

vorgelegt beim Fachbereich 11 Geowissenschaften / Geographie

der Johann Wolfgang Goethe-Universität

in Frankfurt am Main

von

Amelie Simone Hoff

aus Neustadt a.d. Aisch

Frankfurt 2021

(D30)

Vom Fachbereich 11 Geowissenschaften / Geographie der

Johann Wolfgang Goethe-Universität als Dissertation angenommen.

Dekan: Prof. Dr. Georg Rümpker

Gutachter: Prof. Dr. Bodo Ahrens
Prof. Dr. Stephan Pfahl

Datum der Disputation: 28.01.2022

GOETHE UNIVERSITY FRANKFURT

Abstract

Faculty 11 of Geosciences / Geography

Institute for Atmospheric and Environmental Sciences

Hydro-Climatic Causes of Widespread Floods in Central Europe: On Rain-on-Snow and Vb-Cyclone Events

by Amelie Simone Hoff

The presented work investigates the hydro-meteorological and hydro-climatological drivers of widespread floods in Central Europe during the past century. Due to the strong seasonality of the detected flood drivers, the thesis is divided into two parts: the first part focuses on widespread winter floods and the second one on extreme summer floods. For analysing past flood events, we profited from the dynamically downscaled centennial ERA-20C reanalysis (continuously from 1901—2010). The downscaling was performed over Europe with a coupled regional atmosphere-ocean model (COSMO-CLM+NEMO) to represent the water cycle more realistic. These high resolution atmospheric data allowed us to study the four-dimensional atmospheric state during selected floods during the early decades of the 20th century for the first time with such a high temporal and spatial resolution.

During the winter half-year, the observed floods were particularly widespread. High peak discharges were recorded simultaneously in the Rhine, Elbe, and Danube catchments. Most of these trans-basin floods were compound events caused by rainfall during extensive snowmelt (i.e., rain-on-snow events). Interestingly, the winter flood time series exhibited a remarkable high flood frequency during the 1940s and 1980s, while other decades were flood-poor. We detected a synchronization of the inter-annual flood frequency with the superposition of the North Atlantic Oscillation (NAO) and the Scandinavian pattern (SCA). The negative NAO phase is often associated with large snowfall and cyclone tracks over southern Europe, while the negative SCA pattern correlates with total precipitation in the affected river catchments.

During the summer half-year, most extreme floods in Central Europe were caused by so-called Vb-cyclones propagating from the Mediterranean Sea north-eastward to Central Europe. So far in the literature, only a few Vb-events, which occurred during the past two decades, have been analysed. We extended the previous case studies by several past Vb-cyclone floods since 1900. We investigated the processes that intensify Vb-cyclone precipitation with Lagrangian moisture-source diagnostics and the parametric transfer entropy measure TE-linear. Overall, an enhanced and dynamically driven moisture uptake over the Mediterranean Sea was found to be characteristic for Vb-events with heavy precipitation. This is supported by high information exchange from evaporation over the western basin of the Mediterranean Sea

towards heavy precipitation in the Odra catchment. The dominating moisture uptake regions during the investigated events were, however, the European continent and the North Sea. A possible cause could be the pre-moistening of non-saturated continental moisture sources upstream of the affected river catchments as indicated by significant information exchange from land surface evaporation and soil moisture content along the Vb-cyclone pathway. Besides, evaporation over the Mediterranean Sea might contribute to Vb-cyclone intensification in the early stages of their development through latent heat release. On the catchment scale, orographic rainfall and convective precipitation further enhance the flood triggering rainfall. As expected, the Vb-cyclones mainly trigger precipitation along west-east orientated mountain ranges such as the Alps or Ore mountains due to their meridional pathway. Remarkably, during summer, we detected a convective fraction of up to 90% during the afternoons of individual days and up to 23% on average (based on convective cell tracking and convection-permitting simulations of selected flood events since 1900).

The presented analyses deepened the knowledge on atmospheric and hydroclimatic drivers of widespread floods in Central Europe. This will serve as a basis for future studies on the predictability of floods induced by rain-on-snow and Vb-cyclone precipitation events in the context of a changing climate.

GOETHE UNIVERSITÄT FRANKFURT

Kurzfassung

Fachbereich 11 Geowissenschaften / Geographie

Institut für Atmosphäre und Umwelt

Hydro-klimatologische Rahmenbedingungen von großräumigen Hochwassern in Mitteleuropa: von Regen-auf-Schnee und Vb-Ereignissen

von Amelie Simone Hoff

Die vorgelegte Arbeit untersucht die hydrometeorologischen und hydroklimatologischen Rahmenbedingungen von großräumigen Hochwasser in Mitteleuropa während des vergangenen Jahrhunderts. Aufgrund der starken Saisonalität der hochwasserverursachenden Wetterlagen und klimatischen Rahmenbedingungen ist die vorgelegte Arbeit in zwei Teile untergliedert, welche das Sommer- und Winterhalbjahr getrennt betrachten. Bei der Analyse vergangener Hochwasserereignisse profitierten wir von der kontinuierlichen dynamischen Regionalisierung der ERA-20C-Reanalyse von 1901 bis 2010. Die Regionalisierung über Europa wurde dabei mit einem gekoppelten regionalen Atmosphäre-Ozean-Modell (COSMO-CLM+NEMO) durchgeführt, um den Wasserkreislauf realistischer darzustellen. Mit diesem Datensatz war es uns möglich extreme Hochwasser der frühen Jahrzehnte des 20. Jahrhunderts zum ersten Mal mit einer so hohen zeitlichen und räumlichen Auflösung zu untersuchen.

Während des Winterhalbjahres traten besonders großräumige Hochwasser auf, die zeitgleich für schwere Überschwemmungen in den Einzugsgebieten von Rhein, Elbe und Donau sorgten. Die meisten dieser flussgebietsübergreifenden Hochwasser wurden durch das Abschmelzen großräumiger Schneebedeckung (auch in niederen Lagen) und gleichzeitigem Regen verursacht, sogenannte „Regen-auf-Schnee“ Ereignisse (im Englischen „rain-on-snow events“). Diese deutschlandweiten Hochwasser traten im vergangenen Jahrhundert interessanterweise nicht gleichmäßig auf, sondern gehäuft in einzelnen Jahrzehnten, wie zum Beispiel in den 1940er und den 1980er Jahren. Es zeigte sich, dass die hochwasserreichen Phasen gut übereinstimmen mit negativen Phasen der Nordatlantischen Oszillation (NAO) und des skandinavischen Luftdruckmusters (SCA). Die negative NAO-Phase geht dabei häufig mit großen Schneefällen und Tiefdruckzugbahnen über Südeuropa einher, während negative SCA-Indizes mit dem Gesamtniederschlag in den betroffenen Flusseinzugsgebieten korrelieren.

Im Sommerhalbjahr wurden die meisten extremen Überschwemmungen in Mitteleuropa durch sogenannte Vb-Tiefdruckgebiete verursacht, die sich typischerweise vom Mittelmeer aus nordostwärts nach Mitteleuropa verlagern. In der Literatur wurden bisher nur Vb-Ereignisse untersucht, die in den letzten zwei Jahrzehnten auftraten. Die vorgelegte Arbeit erweitert die Datengrundlage um weitere Vb-Hochwasserereignisse seit 1900. Dabei wurden die Prozesse, die den Niederschlag

der Vb-Tiefdruckgebiete verstärken, mithilfe von Lagrangescher Feuchtediagnostik und dem parametrischen Transferentropiemaß TE-linear untersucht. Dabei zeigte sich, dass die dynamisch verstärkte Verdunstung über dem Mittelmeer charakteristisch für Vb-Ereignisse ist, die mit hohen Niederschlagsmengen in den betroffenen Flussregionen einhergehen. Dies wird durch hohe Transferentropiewerte von Verdunstung im Mittelmeerraum bekräftigt. Dennoch sind die Hauptfeuchtequellen für diesen Niederschlag der europäische Kontinent und die Nordsee. Eine mögliche Ursache könnte sein, dass die Verdunstung über dem Mittelmeer zur Intensivierung des Vb-Tiefdruckgebietes durch freiwerdende latente Wärme beiträgt, vor allem in den frühen Stadien der Tiefdruckentwicklung. Außerdem könnte der Transport von Feuchte aus dem Mittelmeerraum Niederschlag und damit auch eine Erhöhung der Bodenfeuchte entlang der Zugbahn des Vb-Tiefs begünstigen. Die erhöhte Bodenfeuchte könnte dann über erneute Verdunstung den Niederschlag luftstromabwärts in den betroffenen Flusseinzugsgebieten verstärken. Dies ist im Einklang mit einer erhöhten Transferentropie von Bodenfeuchte und Verdunstung entlang der typischen Vb-Zugbahn. Auf der Einzugsgebietsskala verstärken orographischer und konvektiver Niederschlag das Hochwasserpotential von Vb-Ereignissen. Dabei sorgen Vb-Tiefdruckgebiete aufgrund ihrer meridionalen Zugbahn vor allem für Stauniederschläge in den zonal orientierten Gebirgszügen wie den Alpen oder der Erzgebirgsregion. In den Sommermonaten detektierten wir mithilfe der Nachverfolgung von konvektiven Zellzugbahnen in konvektionserlaubenden Simulationen einen konvektiven Niederschlagsanteil von bis zu 90% in den Nachmittagsstunden. Konvektiver und orographischer Niederschlag tragen somit wesentlich zur Niederschlagsintensivierung während Vb-Ereignissen bei.

Die vorgelegte Arbeit erweiterte das Wissen über die meteorologischen und hydroklimatischen Einflussfaktoren großräumiger Hochwasser in Mitteleuropa und wird als Grundlage dienen für weitere Studien zur Abschätzung des zukünftigen Hochwasserrisikos, insbesondere in einem sich ändernden Klima.

Contents

List of Figures

List of Tables

Abbreviations

AO	**A**rctic **O**scillation
AP	**A**tmospheric **P**roxy
CC	**C**lausius-**C**lapeyron
CMIP	**C**oupled **M**odel **I**ntercomparison **P**roject
COSMO-CLM	**Co**nsortium for **S**mall-scale **Mo**delling in **Cl**imate **M**ode
CPS	**C**onvection **P**ermitting **S**imulation
DWD	**D**eutscher **W**etter**d**ienst
EA	**E**ast **A**tlantic pattern
ECMWF	**E**uropean **C**entre for **M**edium-Range **W**eather **F**orecasts
EOF	**E**mpirical Orthogonal **F**unction
ERA-20C	ECMWF twentieth century reanalysis
GRDC	**G**lobal **R**unoff **D**ata **C**entre
NAO	**N**orth **A**tlantic **O**scillation
NCEP-20CR	NOAA's atmospheric 20th Century Reanalysis
NEMO	**N**ucleus for **E**uropean **M**odeling of the **O**cean
SCA	**Sca**ndinavian Pattern
SST	**S**ea **S**urface **T**emperature
TE	**T**ransfer **E**ntropy
TRIP	**T**otal **R**unoff **I**ntegrating **P**athways
UTC	**C**oordinated **U**niversal **T**ime

Chapter 1

Introduction

1.1 Space-time dynamics of extreme floods

River floods are one of the largest natural hazards in Europe and have a high socio-economic impact due to the damages and fatalities they cause. In general, flood impacts increased due to urbanization and economic growth (e.g., BARREDO, 2009; ELMER et al., 2012). Regarding future flood risk, climate change becomes increasingly an important driver. By 2080, WINSEMIUS et al. (2016) estimate an increase of the current global flood losses (~1 trillion US$ in 2010) by a factor of up to 17 without flood protection measures due to socio-economic growth and climate change. Another recent study revealed that the current European flood-rich period is extraordinary compared with flood records during the past 500 years (BLÖSCHL et al., 2020). Therefore, the reliable prediction of flood risk is of high relevance for flood protection actions. Initially, flood hydrology focused only on pure flood frequency analysis (as criticised by KLEMEŠ, 1974). In recent decades, however, the paradigm shifted towards an improved process understanding that links observed flood frequency with catchment characteristics and hydro-meteorological drivers (e.g., NIED et al., 2014; BLÖSCHL et al., 2017, 2019a; TARASOVA et al., 2019). Although flood research has achieved significant progress in recent years, we need more knowledge of the processes causing floods from a coherent hydrological, socio-economic, and meteorological perspective. In particular, it remains unclear how extreme floods differ from ordinary floods and which processes trigger such extreme events.

Extreme floods are complex phenomena. This is reflected in the lack of a unified definition. Similar to the definition of extreme weather and climate events by STEPHENSON (2008), extreme floods can be characterised from different perspectives. Extreme floods are often defined as high-impact events causing devastating damage. Furthermore, they occur rarely and with high return periods (occurrence probability, temporal aspect). Extreme floods can either develop over several days or even weeks like winter floods or intensify on a short time scale like flash floods (time duration aspect). Flash floods often show very high peak discharges with a heavy tail behaviour (hydrograph perspective, event scale) but are limited to a small spatial scale. Extreme floods can also be characterised by large flooded areas, so-called

trans-basin floods (UHLEMANN et al., 2010), due to their high socio-economic impact. Thus, extreme floods show complex space-time dynamics. Besides, floods are multivariate phenomena and depend on the complex interplay of, for example, precipitation magnitude and antecedent catchment soil moisture (BERGHUIJS et al., 2019; MERZ et al., 2020) or tributary river flows (GUSE et al., 2020). Thus, extreme floods are often compound events and can be caused by an unusual combination of processes rather than only the extremity of one specific variable (KLEMEŠ, 1993; LEONARD et al., 2014).

In comparison to flood frequency statistics, MERZ and BLÖSCHL (2008a,b) propose the concept of a so-called „flood frequency hydrology" that goes beyond pure frequency statistics and extends the information used in time, space, and in terms of hydrological processes such as the aforementioned catchment soil moisture and river routing characteristics. The temporal information expansion uses runoff records of nearby stream gauges with a longer time series or historical flood information such as flood marks on walls (MERZ and BLÖSCHL, 2008a,b). The spatial information extension can be achieved by taking neighbouring river catchments into account (MERZ and BLÖSCHL, 2008a,b). The causal information expansion focuses on the flood causing circumstances, including the rainfall time series, the synoptic conditions, and the catchment characteristics like the landform (MERZ and BLÖSCHL, 2008a,b; TARASOVA et al., 2019).

Like the flood itself, also the causing processes evolve on various temporal and spatial scales. Figure 1.1 illustrates the different scales and perspectives for floods induced by so-called Vb-cyclones (pronounced as five-b). On a hydro-climatic perspective, Vb-cyclones occur in temporal clusters synchronized with the North Atlantic Oscillation (NAO) and Arctic Oscillation (AO) as discussed in HOFSTÄTTER and BLÖSCHL (2019). From the hydro-meteorological perspective, one specific Vb-cyclone induces the flood event. The corresponding spatial scale is called synoptic scale. On the catchment scale, the flood event is triggered by orographically induced rainfall and convective cells (hydro-meteorological perspective). The respective discharge maxima are then measured at different gauges (hydrograph perspective).

1.2 Why an atmospheric perspective?

Generally, the local catchment conditions (including the soil moisture conditions and land use) play an important role, especially for smaller peak discharges and more localized floods (BLÖSCHL et al., 2007; WASKO and NATHAN, 2019). The catchment soil moisture conditions and its interplay with precipitation are also relevant for usually dry catchments (MERZ et al., 2020). In contrast, widespread floods and events with high peak discharges of more than ten years return period are highly influenced by precipitation (WASKO and NATHAN, 2019). Thereby, especially these extreme and widespread floods have a high damage potential and are of great relevance for flood protection and actions.

Not only the local weather (and synoptic) conditions but also the hydro-climatic circumstances have an impact on the flood-causing precipitation. For example, the December to February NAO phase affects the inter-annual variability of winter and

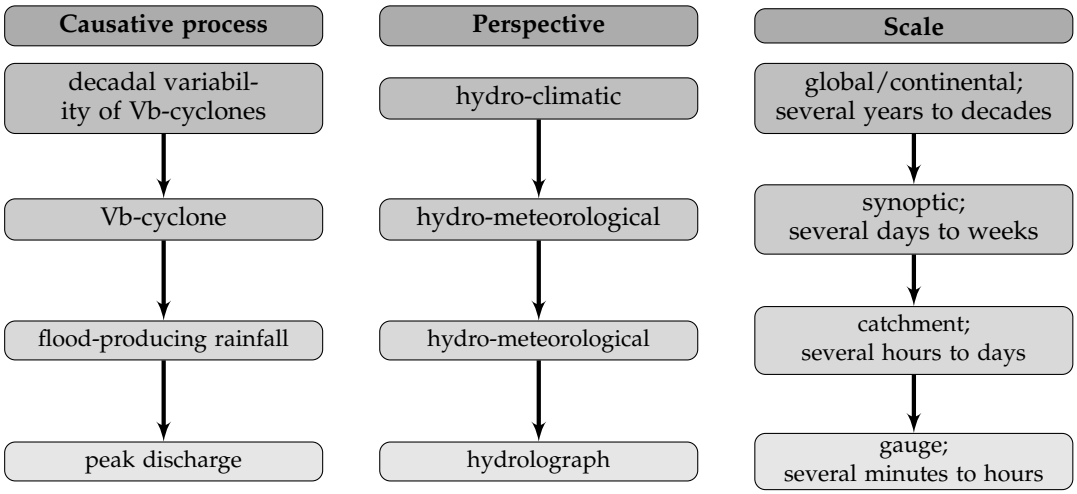

FIGURE 1.1: Different perspectives and scales of a river flood induced by a so-called Vb-cyclone, following the sketch of TARASOVA et al. (2019).

spring river flows on the Iberian Peninsula (TRIGO et al., 2004) and summertime extreme rainfall and flooding are more likely in parts of southern Europe during the negative phase of the Eastern Atlantic pattern (NOBRE et al., 2017). LUN et al. (2020) suggest an influence of the NAO on flood occurrence in Europe due to simultaneous turning points in the NAO index and the number of flood-poor and flood-rich stations around the 1970.

Besides the internal climate variability, climate change and its impact moved into the focus of research since the 1980s (BLÖSCHL et al., 2019b). The first three research questions of the twenty-three unsolved problems in hydrology stated by BLÖSCHL et al. (2019b) directly refer to climate change. A warming climate influences the probability of extreme floods by various processes. An increase of the atmospheric water capacity and thus more rainfall and flooding is expected with rising temperatures in a warming climate. DOTTORI et al. (2018) estimate an overall increase of global direct flood damage (in billion € per year) by up to 240% for a temperature increase of 1.5 °C. Moreover, increased snowmelt within the river catchments can enhance floods. In contrast, dry catchment soil conditions due to pre-ceding summer droughts can reduce the flood risk. Indeed, the dominating drivers of observed flood frequency changes in Europe are shifts in extreme precipitation, snowmelt, and antecedent catchment soil moisture (BERTOLA et al., 2021).

Due to such opposing processes, a warming climate can lead to regionally diverse changes in the seasonality and the severity of floods depending also on the investigated catchment size and return periods (MERZ et al., 2016; BERTOLA et al., 2020). In small catchments ($<$100 km^2) extreme floods tend to become more frequent, likely because of more intense convective rainfall events (BERTOLA et al., 2020). In larger catchments the trends are smaller or even negative, especially in northwestern France (BERTOLA et al., 2020). During 1960–2010, northwestern Europe was dominated by floods in autumn and winter (HALL and BLÖSCHL, 2018). Flooding increased in these regions due to increasing rainfall in these seasons (BLÖSCHL et al., 2019a). Thereby, the area of the North Sea shows a shift to later floods due to later winter storms. In comparison, floods in northeastern Europe are dominated by spring time floods (BLÖSCHL et al., 2017; HALL and BLÖSCHL, 2018) and show a

shift to earlier times (BLÖSCHL et al., 2017). In this region, flood discharged linked to higher temperatures in spring, and thus earlier snow melt with less overall snow cover (BLÖSCHL et al., 2019a). These changes in flood occurrence are in line with projected flood changes for the 21st century (KUNDZEWICZ et al., 2016; THOBER et al., 2018) and indicate that the recent flood changes are already due to a warming climate (BLÖSCHL et al., 2019a).

The observed spatial inhomogeneous flood trends strongly depend on the respective dominating flood type and corresponding atmospheric drivers like snow cover and rainfall amount. For estimating future flood risk, it is crucial to understand first the hydro-meteorological and climatic drivers of the past temporal flood variability (e.g., MERZ et al., 2014). The identified climate-flood links might then serve as sources of predictability of future flood occurrence. This is especially the case for widespread and extreme floods when the atmospheric drivers dominate in contrast to the local catchment state conditions.

1.3 About this thesis

Floods that affect several river basins simultaneously can cause immense socio-economic damages. Moreover, trans-basin floods are challenging for the coordination of flood protection measures beyond administrative boundaries (UHLEMANN et al., 2010; KRUG et al., 2020b). Widespread floods are also relevant for the insurance and re-insurance industry because many insurance cases occur in a large area (UHLEMANN et al., 2010). This spatial accumulation of losses has to be considered in the risk assessment (UHLEMANN et al., 2010). Besides, the temporal accumulation of flood losses, i.e. the occurrence of flood-rich years, is of particular interest (LUN et al., 2020). Thus, improved knowledge on the hydro-climatic drivers and predictability of such flood events is of high relevance.

This thesis investigates the atmospheric processes that cause widespread floods and their temporal accumulated occurrence (i.e., flood-rich years). The presented analyses focus on Central European floods. The advantage of doing so is a sufficiently high spatial and temporal data coverage for analysing widespread floods since the early decades of the 20th century. Note that the focus of this thesis lies on the atmospheric branch of the water cycle and excludes other flood driving processes, like the land use within the river catchment (e.g., TARASOVA et al., 2018; MERZ et al., 2020) and the flow accumulation of tributary rivers (GUSE et al., 2020).

Due to a strong seasonal dependency of the causative flood types (cf. NIED et al., 2014; TARASOVA et al., 2019), the analysis is divided into summer and winter flood events. In winter, snow cover increases the flood probability (MERZ et al., 2020). In Central Europe, but also other regions like Norway or the United States, several severe and widespread winter floods were caused by rainfall during snow melt, so-called rain-on-snow events (e.g., MCCABE et al., 2007; UHLEMANN et al., 2010; FREUDIGER et al., 2014; VORMOOR et al., 2016; LI et al., 2019). With increasing winter temperatures, both increasing and decrasing trends of rain-on-snow floods were observed, depending on the affected region. For example, the magnitude of rain-on-snow events increased in the upland basins of Germany, while the overall frequency

of these events decreased since 1950 (FREUDIGER et al., 2014). However, our analyses revealed that the temporal variability of rain-on-snow floods in Central Europe during the past century shows no homogenous trend but several periods of flood rich and flood poor years. Thus, for flood prediction in the context of a changing climate, it is of particular interest to firstly understand the potential hydro-climatic drivers of the past temporal flood variability besides the climate change signal.

In contrast, the widespread summer floods in Germany presented in this thesis show no particular inter-decadal variability but an increasing magnitude during the recent decades, with prominent examples during August 2002 or May/June 2013. Most of these floods were associated with so-called Vb-cyclones. The increasing flood severity is in line with an projected increase in precipitation intensity of Vb-cyclones under climate change conditions including a warmer Mediterranean Sea (KUNDZEWICZ et al., 2005; NISSEN et al., 2013; VOLOSCIUK et al., 2016; MITTERMEIER et al., 2019). Due to the Vb-cyclone pathway from the Gulf of Genoa to Central Europe, one might expect a large contribution of Mediterranean moisture to precipitation in Central Europe. Indeed, the studies of VOLOSCIUK et al. (2016) and MESSMER et al. (2017) detected a sensitivity of Central European precipitation to Mediterranean sea surface temperatures during Vb-cyclones events. However, recent studies on selected Vb-flood events since 2002 point towards diverse moisture source regions (e.g., SODEMANN et al., 2009; GANGOITI et al., 2011a; JAMES et al., 2004; GRAMS et al., 2014; KELEMEN et al., 2016). Interestingly, WINSCHALL et al. (2014) detected only minor contribution of the Mediterranean Sea to the flood-triggering precipitation in May 2010. Thus, based on these few flood events only, the role of the different moisture source regions - in particular the Mediterranean Sea - in precipitation intensification remains unclear. A distinct knowledge of moisture source regions, however, is crucial for interpreting projected changes in Vb-cyclone precipitation and frequency. This thesis fills this gap by analysing 16 historical flood events and the climatology of all Vb-cyclones from 1901 to 2010.

Vb-cyclones trigger especially heavy precipitation along the west-east orientated mountain ridges, such as the Alps and Ore mountains (GRAMS et al., 2014). In summer, convective processes play also an important role. For the August 2002 flood, RUDOLF and RAPP (2003) estimated a convective rainfall fraction of one third based on a subjective synopsis of observational data like radar observations. In the context of a warming climate, convective rainfall is of special interest. Studies on precipitation measurements observed an increase of saturation vapour pressure and thus convective precipitation of more than 7% per 1°C when air temperatures are above 12 °C (BERG et al., 2013). Several hypotheses have been stated for this so-called Super Clausius-Clapeyron effect. One assumption is that higher precipitation rates could be caused by an increased updraft within the convective cell inducing a large-scale moisture convergence and larger convective systems due to higher surface dew point temperatures (LENDERINK et al., 2017). So far, no quantitative analysis of the convective rainfall fraction was performed for past floods associated with Vb-events and the role of convective precipitation during this flood type remains unclear. Therefore, we tracked all convective cells during selected summer floods based on the Lagrangian approach of BRENDEL et al. (2014, and refined in BRISSON et al. 2018 and PURR et al. 2019) to gain more insights on the quantitative amount of convective rainfall.

The results discussed in this thesis are based on two published articles (KRUG et al., 2020b) and KRUG et al. (2021), and one manuscript in revision (KRUG et al., 2020a). Therefore, the results chapters are structured as independent units with an introduction, a brief data and method description, discussion of the results, and conclusions. The reader may either follow the storyline of the sequential chapters or directly read the respective results chapter of interest, even though this introduces some duplications in the method and data description sections.

The storyline of the thesis starts with a description of the data basis in chapter 2. A special focus lies on the coupled regional atmosphere-ocean model setup which was used within the DFG research unit FOR 2416 Space-Time Dynamics of Extreme Floods (SPATE) to dynamically downscale ERA-20C reanalysis for an improved water cycle and spatial representation of the orography. This high resolution ($\Delta x = 0.11^{\circ}$) atmospheric data set covers continuously the years from 1901 to 2010 and is a common data basis for all results chapters.

Chapter 3 describes the methods applied in this thesis. These include two midlatitude cyclone tracking approaches, the Lagrangian moisture source diagnostics, a convective cell tracking algorithm, and an information theoretical approach for advanced statistical analysis. In contrast to the brief methods description in the results chapters, the reader will find more detailed descriptions and illustrating figures for a deeper understanding.

Chapter 4 presents the most widespread and extreme flood events in Central Europe during the past century in the summer and winter season, respectively. Based on these flood events, chapter 5 focuses on the winter season and so-called rain-on-snow floods. The inter-annual variability of widespread and potential climatic drivers like specific cyclone pathways and atmospheric oscillations are discussed.

The chapters 6 to 8 investigate the atmospheric circumstances of heavy precipitation associated with so-called Vb-cyclones and widespread summer floods in the Elbe, Odra, and Danube river catchments. In chapter 6, the moisture uptake of the flood-causing precipitation is quantified for 16 selected events. Moreover, the source region characteristics, such as evaporation or sea surface temperatures, are analysed in the chapters 6 and 7. On the local catchment scale, orographically triggered precipitation and convective rainfall can increase the river discharges. We quantified the convective rainfall fraction for selected summer floods in chapter 8.

The thesis is framed by the conclusions in chapter 9. This chapter provides an overview of the key results of this thesis. The newly acquired knowledge on the intensification factors of widespread floods in Central Europe is highlighted and discussed in the context of recent scientific findings. Note that some paragraphs of the conclusions are taken from the abstracts of underlying studies (KRUG et al., 2020b,a, 2021). The thesis is completed by an outlook with suggestions for future analysis on intensification processes and the predictability of rain-on-snow and Vb-cyclone induced floods.

Chapter 2

Data basis

2.1 Hydrological data

2.1.1 River catchments in Central Europe (study area)

This thesis focuses on flood and heavy precipitation events in Central Europe. Figure 2.1 shows the affected macro-scale river basins, whereas the Danube river basin is the second largest one in Europe with about 801463 km^2 (ICPDR, 2020). The Danube river originates in Germany and flows southeastwards to the Black Sea. The macro-scale river catchments in northern Central Europe are the basins of the Rhine, Weser, Elbe and Odra river that route into the North Sea and Baltic Sea.

The climatic regime and the topography control the annual mean precipitation within the river catchments. The climate regime ranges from the maritime climate in the western subbasins and coastal areas to more continental climate in the eastern parts of the Elbe and Danube catchment, as well as the Odra catchment (e.g., MERZ et al., 2018; GUSE et al., 2020). That is often associated with winter floods in the Rhine and Weser catchment caused by prolonged precipitation, whereas the more continental catchments show a higher seasonal variability with flood events induced by snowmelt or heavy precipitation events (GUSE et al., 2020). Moreover, precipitation is triggered especially in the upland sections. For example, the middle Elbe mean annual precipitation is about 450 mm, while in the Ore mountains more than 1000 mm (IKSE, 2005; NIED et al., 2013). Besides the upland section, the Rhine and Danube river consists of an alpine section with elevations higher than 3000 m a.s.l. (FREUDIGER et al., 2014). The annual mean precipitation can exceed 1000 mm summed up over the sub-basins at the northern fringe of the Alps in the Danube catchment (KLING et al., 2012) pointing towards the role of orographic rainfall.

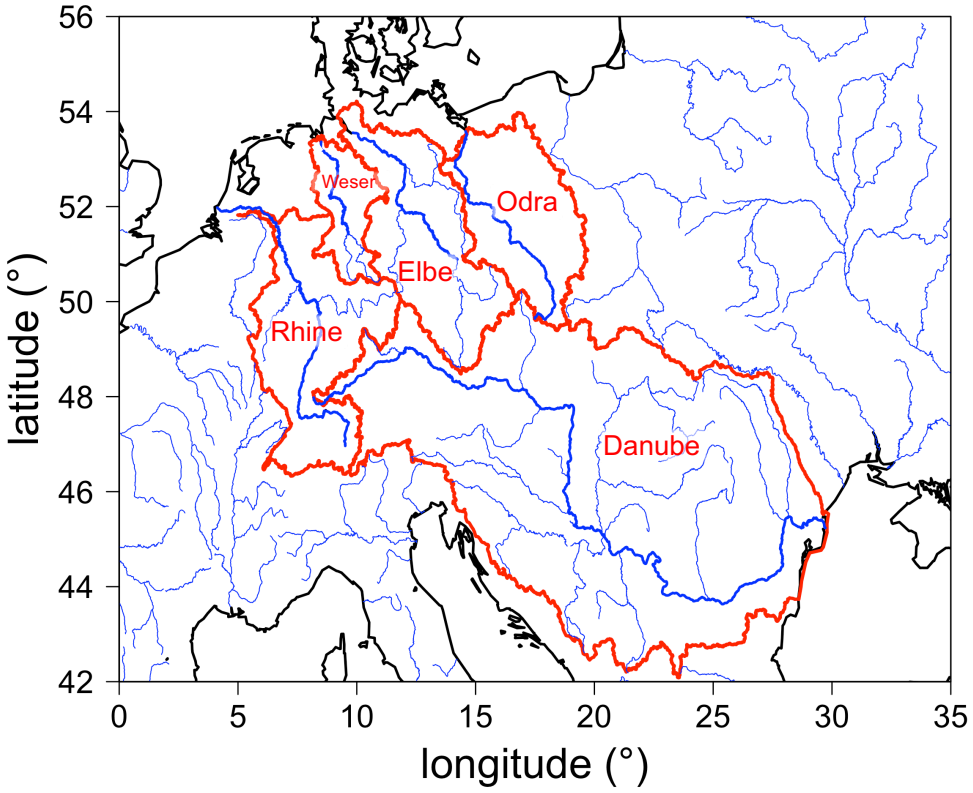

FIGURE 2.1: Rivers in Central Europe with the Rhine, Weser, Elbe, Odra, and Danube catchments based on shapefiles of the European Environment Agency (EEA) and the International Commission for Protection of Danube River (ICPDR).

2.1.2 GRDC river runoff Data

The Global Runoff Data Centre (GRDC) was founded in 1988 by the Bundesanstalt für Gewässerkunde (BfG) under the auspices of the World Meteorological Organization (WMO). The GRDC collects global discharge measurements to support international hydrological analyses and climate research. The data catalogue is continuously updated and covers more than 9000 river gauges with monthly or daily time series.

We required long time series for analysing potential hydro-climatic drivers of extreme floods in Central Europe. Therefore, GRDC gauges with the longest mean daily discharge records were selected. For the Central European region, in total eleven gauges with a catchment area of at least 10^4 km^2 were available since 1920 within the German administrative boundaries. These were the gauges Maxau, Würzburg, Cochem and Collogne for the Rhine catchment; Hannoversch Münden (Hann. Münden) and Intschede in the Weser catchment; Dresden, Calbe-Grizehne, Neu-Darchau in the Elbe catchment; and Ingolstadt and Hofkirchen in the Danube catchment. The selected gauges are within the German administrative boundaries and refer to a catchment area of at least 10^4 km^2. Overall, these measurements cover the years since 1920 with large data gaps during the Second World War, in particular in 1945.

2.2 Meteorological data

2.2.1 Station-based measurements in Germany

To gain deeper knowledge on the meteorological circumstances of selected flood events, we used the quality controlled station-based measurement data of the Climate Data Center, version v005 (2017). The data was provided by Deutscher Wetterdienst (DWD), the national weather service in Germany. The first station-based measurements have started in January 1781 with the station Hohenpeißenberg. The observations include on a daily scale, for example, the precipitation sum, the type of precipitation, the snow depth, the sun shine duration, and the mean air temperature.

Station-based observations over several decades and centuries suffer from inhomogeneities caused by changes of the measurement instrument, the sensor height, or the measurement time. Some aspects that were corrected by the quality control of DWD were, for example, the following (data set description for version v005, DWD). The total precipitation observed in the morning was consistently accounted for the previous day instead of the same day like it had been originally the case in records in eastern Germany before 1969 and in western Germany before 1971. Moreover, all measurements were converted to the same units for all stations. The quality of more recent observations was also reviewed based on the QualiMet software (SPENGLER, 2002) that reviews the completeness or spatial and temporal consistency of the observations (KASPAR et al., 2013).

Even though the station-based measurements provided by DWD were quality checked, some issues may remain. Therefore, we reviewed the time series of observation stations selected for the analysis in chapter 5 and checked manually whether inhomogeneities correlated with recorded changes in the measurement instrument or location to exclude suspicious time series from our analysis. We could not apply homogenisation methods because snow height and precipitation, the variables we focused on, are in general temporally highly variable. Moreover, we accounted in our analysis for the fact that 0 cm of snow height were recorded as missing values at some stations in western Germany until the late 1930s.

2.2.2 Four-dimensional atmospheric reference: the dynamically downscaled ERA-20C reanalysis

For analysing the atmospheric circumstances and potential hydro-climatic drivers of extreme flood events, it is crucial to have information about the consistent four dimensional atmospheric state with a high spatial and temporal resolution. Moreover, a long time series is required since extreme floods are by definition rare events. Atmospheric reanalyses serve as reference for the four dimensional atmospheric state. Sufficiently long reanalyses are the NOAA's atmospheric 20th Century Reanalysis (NCEP-20CR V2 COMPO et al., 2011) covering the years from 1871 to 2012 and the ECMWF twentieth century reanalysis (ERA-20C; POLI et al., 2016) covering the years from 1900 to 2010. Only surface observations like pressure measurements were assimilated for creating both reanalyses because satellite measurements have been available since the late 1970s. The spatial resolution of the NCEP-20CR V2 reanalysis

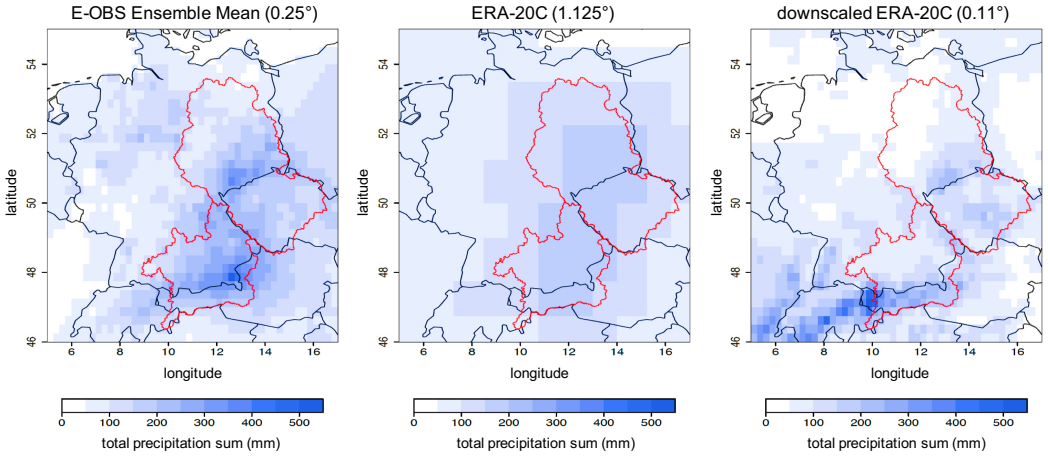

FIGURE 2.2: Total precipitation sums from 1st July to 20th July 1954 in E-OBS ensemble mean, ERA-20C reanalysis, and dynamically downscaled ERA-20C reanalysis. Figure adapted from Cristina Primo (Goethe-University Frankfurt, now at DWD).

is about 222 km (COMPO et al., 2011), while the ERA-20C reanalysis has a finer grid spacing with about 125 km (spectral truncation T159, POLI et al., 2016). Furthermore, snow climatologies in ERA-20C are better represented compared to NCEP-20CR V2 during the first half of the 20th century (WEGMANN et al., 2017). Therefore, ERA-20C reanalyses was selected as data basis in this thesis. However, the reanalysis data is too coarse-gridded for analysing the hydro-meteorological processes causing extreme flood events. A higher spatial and temporal resolution is needed to include local flood amplification factors (e.g., orographic rainfall) and to improve the representation of extreme events (ROCKEL, 2015, and references therein). Increasing computational resources during the past decades made it feasible to dynamically downscale global climate model output within a limited domain with so-called regional climate models. Such regional climate simulations improve the representation of atmospheric phenomena on a finer spatial and temporal scale (ROCKEL, 2015), despite of issues such as inconsistencies in the physics and dynamics of the global and regional climate model, unphysical treatment of the lateral boundary conditions, and temporal or spatial phase shifts compared to observations (HONG and KANAMITSU, 2014).

During the past decade, regional atmosphere models that are coupled with regional ocean models have been established (ROCKEL, 2015). Interactively coupled regional atmosphere and ocean models represent the Earth system in a physically more consistent way than atmospheric-only model setups which assimilate the ocean state as lower boundary conditions based on observations or reanalyses data. This is especially an issue when no or only pure observation data are available (ROCKEL, 2015). Therefore, we dynamically downscaled the centennial reanalyses with the coupled regional atmosphere-ocean model setup COSMO-CLM+NEMO. Previous studies showed that the coupling of the regional climate model COSMO-CLM with the ocean model NEMO further improves the simulation of local phenomena, such as snowbands in the Baltic Sea (PHAM et al., 2017), Mediterranean tropical-like cyclones (AKHTAR et al., 2014), Vb-cylone events (AKHTAR et al., 2019), soil moisture content (HO-HAGEMANN et al., 2015; KELEMEN et al., 2019), and local heat or cold waves (PRIMO et al., 2019).

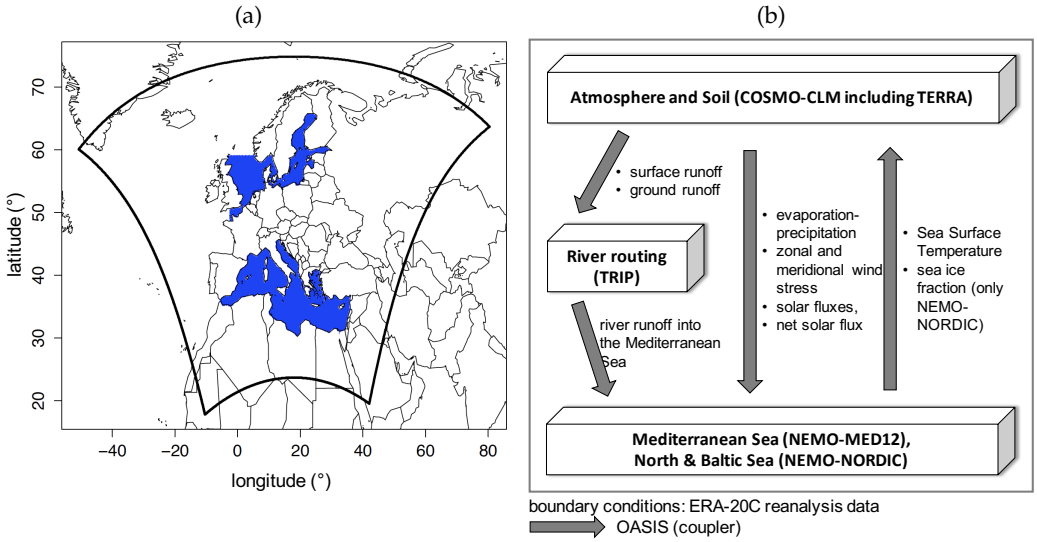

FIGURE 2.3: (a) shows the area of the coupled oceans in blue colour, as well as the domain of the RCM in black; (b) sketch of the model components.

Figure 2.2 illustrates the benefit of downscaling the ERA-20C reanalysis with COSMO-CLM+NEMO by the example of July 1954. During this month, extraordinary precipitation sums caused an extreme flood event in the Danube catchment. The coarsely resolved ERA-20C reanalysis captures only the west-east gradient of the total precipitation sums but not the observed locally high precipitation sums that exceed 400 mm along the northern fringe of the Alps and the Ore Mountains (E-OBS observation data; CORNES et al., 2018). The dynamically downscaled ERA-20C reanalysis captures this spatial distribution, even if the Alpine precipitation maximum is shifted towards the west compared to E-OBS. In north-western Germany, the E-OBS data show high precipitation (exceeding 150 mm). That is not captured by the ERA-20C reanalysis and the dynamically downscaled ERA-20C reanalysis. However, one has to keep in mind that the E-OBS ensemble mean relies on only a few station measurements in 1954, and uncertainties are higher in the early decades of the 20th century than in recent years. Overall, the simulated precipitation sums were improved by the dynamically downscaling with COSMO-CLM+NEMO to a horizontal resolution of about 0.11°. The ERA-20C reanalysis was continuously downscaled by Cristina Primo (IAU, Goethe-University Frankfurt, now at DWD) with this model setup for the period from 1901 to 2010. The following paragraphs describe the model components of this high-resolution and interactively coupled regional atmosphere-ocean setup.

COSMO-CLM

The Consortium for Small-scale Modelling in CLimate Mode (COSMO-CLM; ROCKEL et al., 2008) is a non-hydrostatic regional climate model based on the primitive thermo-hydrodynamical equations. We used COSMO v5.00 CLM 9 to dynamically downscale the ERA-20C reanalysis data to a horizontal resolution of 0.11° (Δx ∼12 km) and 40 vertical model levels up to the troposphere and lower stratosphere. Figure 2.3 (a) shows the downscaled region which includes the EURO-CORDEX and MED-CORDEX domain (GIORGI et al., 2009; SOMOT

et al., 2018). For time integration, a three-stage Runge-Kutta scheme after WICKER and SKAMAROCK (2002) was used with a time step of 90 s. The lateral boundary conditions were defined by the ERA20C-reanalysis data with a 1-way DAVIES (1976) relaxation scheme. The relaxation was performed for the horizontal wind fields u and v, the deviation pp from the reference pressure, and temperature T. In a long-term ERA40-driven regional climate simulation, JAEGER et al. (2008) found no significant benefit of spectral nudging for temperature and precipitation, which are variables of interest in the presented work. We applied no spectral nudging within the downscaling domain to avoid discontinuities in the internal regional climate model variability and account for the computational constraints of a coupled atmosphere-ocean model covering 110 years.

TERRA-ML coupled with TRIP

The default built-in land surface parametrization scheme of COSMO-CLM is the multilayer soil model TERRA-ML (GRASSELT, 2009; SCHRODIN, 2002; GRASSELT et al., 2008). We used the standard setup of TERRA-ML with nine vertical layers for simulating the hydrological and thermal processes. The soil layer midpoints are at 0.005 m, 0.025 m, 0.07 m, 0.16 m, 0.34 m, 0.7 m, 1.42 m, 2.86 m, 5.74 m, and 11.5 m. The tenth layer is the so-called climate-layer with prescribed water content and temperature (SCHRODIN, 2002).

In TERRA-ML, the vertical 1-D heat conduction equation (HCE-method; SCHRODIN, 2002), and the gravitational and capillary soil water flux (based on the continuity and the 1-D Darcy equation; GRASSELT, 2009) are solved for each grid cell independently. Output variables are, for example, the snow height, the surface temperature, the specific humidity at the ground, and the soil ice content.

The calculated runoff of the individual soil layers sums up to the total subsurface runoff of each grid cell. Lateral flows are neglected in TERRA-ML. Thus, it was coupled to the river routing model TRIP (Total Runoff Integrating Pathways; OKI and SUD, 1998), which simulates lateral water movement over land in river channels. OKI and SUD (1998) used digital elevation maps to automatically detect possible river channels and manually corrected the river flow networks based on published river routes.

NEMO

The atmospheric model COSMO-CLM was coupled every three simulation hours with regional implementations of the ocean general circulation model NEMO (Nucleus for European Modeling of the Ocean; MADEC and THE NEMO TEAM, 2016). NEMO uses the primitive equations with the 3-D velocity field, non-linear sea surface height, conservative temperature and the absolute salinity as prognostic variables. Figure 2.3 (a) shows the coupling regions over the Mediterranean Sea, the North Sea, and the Baltic Sea.

For the Mediterranean Sea NEMO-MED12 (e.g., BEUVIER et al., 2012; LEBEAUPIN BROSSIER et al., 2011; AKHTAR et al., 2018; DROBINSKI et al., 2018) based on NEMO v3.6 was used with a time step of 720 s. With a horizontal resolution of 1/12°

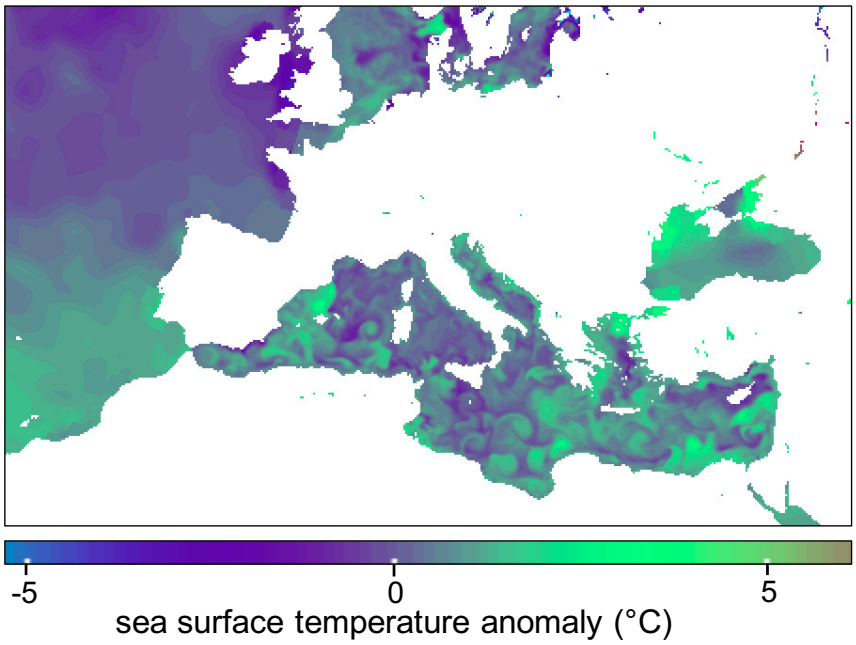

FIGURE 2.4: The colour shades show the daily sea surface temperature anomaly (°C) on the 1st January 2010 in the dynamically downscaled ERA-20C reanalysis (relative to the multi-year daily mean of 1st January during 1901–2010).

(∼5.5 km–8.0 km), it is eddy-resolving in the major part of the Mediterranean Sea (LEBEAUPIN BROSSIER et al., 2012). Figure 2.4 illustrates such small-scale flow structures in the Mediterranean Sea on the 1st January 2010. In contrast, the North Atlantic sea surface temperatures were calculated by the atmospheric model on a horizontal resolution of 0.11° and show therefore smoother gradients. In our NEMO-MED12 setup, 75 unevenly spaced vertical levels are employed. The layer thickness varies from 1 m layer thickness at the top up to 135 m at the ground level. The fresh water inflow of rivers routing into the Mediterranean Sea were considered by TRIP to close the water cycle.

We applied NEMO-NORDIC for the North Sea and Baltic Sea area (HORDOIR et al., 2013; DIETERICH et al., 2013; PHAM et al., 2014). NEMO-NORDIC is based on NEMO v3.31 and has a horizontal resolution of NEMO-NORDIC is about 3.7 km (two nautical minutes). Compared to NEMO-MED, NEMO-NORDIC also includes tidal forcing and the LIM3 sea ice model for simulating the sea ice cover (VANCOPPENOLLE et al., 2009). We used a time step of 180 s. Note that during some extreme winter storm events, the model setup was restarted with a higher NEMO-NORDIC time step of 120 s.

The coupler OASIS

The coupling of the atmosphere, ocean, and river runoff model components was performed with the OASIS3-MCT coupler (VANCOPPENOLLE et al., 2009; WILL et al., 2017). With OASIS all aforementioned model components are synchronized and the simulation timing was optimized. As the regional ocean and climate models have different grids, OASIS interpolates all coupled fields to the respective grid resolutions. OASIS passes information about evaporation, precipitation, u and v wind

stress, and (net) solar flux from the atmospheric model COSMO-CLM to NEMO like sketched in Figure 2.3 (b). COSMO-CLM receives the sea surface temperature and pressure calculated by NEMO. Furthermore, COSMO-CLM uses the sea ice mask of NEMO-NORDIC to calculate weighted average of the albedo in a grid cell based on the fraction of ice and open water (PHAM et al., 2014). Thus, partially sea ice covered grid boxes can be taken into account in COSMO-CLM.

Chapter 3

Methods and theoretic background

This chapter gives details on the applied methods in this thesis. Parts of the following sections are taken from the studies entitled *On the temporal variability of widespread rain-on-snow-floods* by A. Krug, C. Primo, S. Fischer, A. Schumann, and B. Ahrens, published in Meteorologische Zeitschrift (KRUG et al., 2020b), *Heavy Vb-cyclone precipitation: a transfer entropy application showcase* by A. Krug, P.K. Pothapakula, C. Primo, and B. Ahrens, published in Meteorologische Zeitschrift (KRUG et al., 2021), and *Moisture sources of heavy precipitation in Central Europe during Vb-cyclones* by A. Krug, F. Aemisegger, M. Sprenger, and B. Ahrens, submitted to Climate Dynamics (KRUG et al., 2020a, in revision).

3.1 Classification of trans-basin flood events

First of all, we need a relatively long time series of severe and widespread flood events for analysing the hydro-climatic drivers of such events in Central Europe. The classification of trans-basin floods is a particular challenge because it has to apply to several river catchments with different runoff regimes and statistical characteristics like fitted discharge distribution functions.

In general, a wide range of methods for flood event detection and classification exists (e.g., FISCHER and SCHUMANN, 2018). Some classifications use parameters related to the observed flood peaks like inundated areas or devastating effects (e.g., ASHLEY and ASHLEY, 2008; BARREDO, 2007) that are, however, depending on the land-use changes over time and are more difficult to quantify. So-called causative flood classifications distinguish the hydroclimatic, hydrometeorological, catchment state and hydrograph perspective (TARASOVA et al., 2019). With doing so, one can analyse flood-rich and flood-poor periods related to changes in flood generating mechanisms and climate drivers. However, such an approach is dependent on a high resolution and multivariate database and restricted to recent decades if large areas are studied. Other flood classification criteria depend on the peak discharge like the definition of floods based on return periods (e.g., PETROW et al., 2007) or peak over thresholds methods (e.g., MERZ et al., 2016; UHLEMANN et al., 2010). The

results derived with these approaches improve for longer time-series (e.g., FISCHER and SCHUMANN, 2018).

Regarding widespread floods, UHLEMANN et al. (2010) and GVOŽDÍKOVÁ and MÜLLER (2017) detected trans-basin floods with the peak over threshold approach and ranked all flood events according to their severity and spatial extent. However, with their method, a distribution function has to be approximated for each gauge. Moreover, not only a long time series but also high spatial coverage is needed. Therefore, they restricted their analysis to the years since 1952 when continuous measurements were available for a maximum number of gauges (UHLEMANN et al., 2010). To increase time series of trans-basin floods in UHLEMANN et al. (2010) and GVOŽDÍKOVÁ and MÜLLER (2017), we used the flood-classification described in FISCHER and SCHUMANN (2018) which is less dependent on the number of analysed gauges. With their approach, it was possible to extend the analysed time backwards by about three decades to the 1920s. Note that we could not include previous years and the year 1945 due to data availability.

The distribution-free ordinal classification of FISCHER and SCHUMANN (2018) is based on the so-called generalized Gauss or Camp-Meidell inequality (bound with the third moments; e.g., GÖB and LURZ, 2015):

$$\mathrm{P}\left(|\mathrm{X}| \geq k_p\right) \;\leq\; \left(\frac{3}{4}\right)^3 \frac{1}{k_p^3}\,\mathrm{E}|\mathrm{X}|^3, \tag{3.1}$$

where X is a random variable, in our case the discharge measurements. $\mathrm{E}|\mathrm{X}|^3$ is the corresponding third moment and represents the skewness of the tails, an important flood peak characteristic. The right hand side of equation (3.1) is equal to $(1-p)$, where p is the non-exceedence probability of the peak discharges. In this thesis, we classified the severity of small floods by a non-exceedence probability $p \geq 0.5$ (see Table 4.1 and Table 4.2, green), medium floods by $p \geq 0.8$ (yellow), large floods by $p \geq 0.933$ (magenta), and very large floods by $p \geq 0.966$ (red) like proposed by FISCHER and SCHUMANN (2018). Thus, the discharge thresholds k_p of the different flood classes are calculated for all catchments separately based on the selected non-exceedence probability p (FISCHER and SCHUMANN, 2018). This obviates the need to estimate suitable distribution functions which are highly dependent on the number of analysed gauges.

3.2 Extratropical cyclone tracking

Extratropical cyclones and their frontal systems strongly influence the daily weather in the mid-latitudes. They are a crucial driver of precipitation and link the Central European river catchments with remote moisture uptake regions, like the North Atlantic (HOFSTÄTTER et al., 2016). Therefore, we investigated the atmospheric circumstances of flood events also in the context of extratropical cyclones and their pathway.

Generally, each cyclone tracking algorithm consists of two analysis steps. Firstly, the detection of the cyclone track points (usually local pressure or relative vorticity minima), and secondly, the connection of track points at a time step with track points

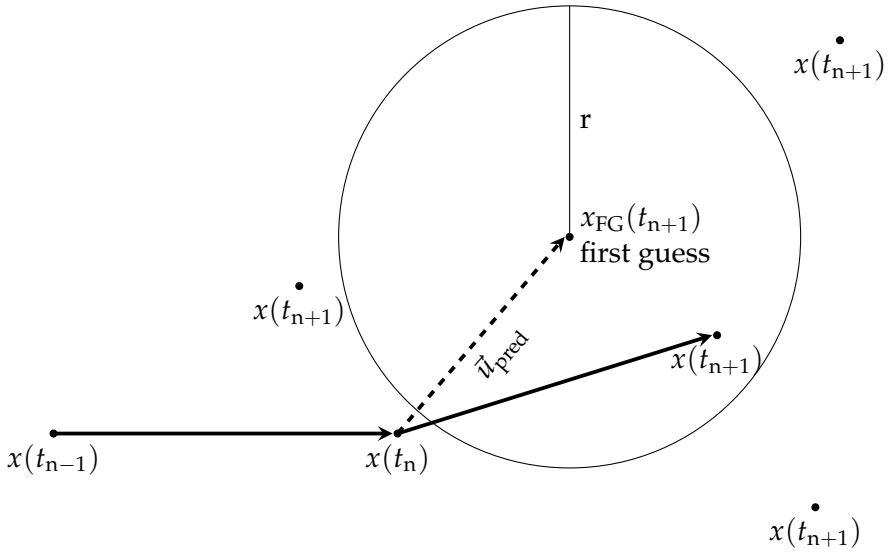

FIGURE 3.1: Schematic illustrating the cyclone tracking method following the approach of HOFSTÄTTER and CHIMANI (2012) with some simplifications.

at the following time step. Most tracking algorithms differ in the variable chosen for cyclone centre detection, the track point connection algorithm, or the choice of thresholds to exclude spurious low-pressure systems (NEU et al., 2013). The large variety of cyclone tracking algorithm reflects the complex structure of midlatitude cyclones. In contrast to tropical cyclones, they occur frequently and with large variations in the spatial and temporal extent, as well as the propagating velocity (NEU et al., 2013). Depending on the applied tracking algorithm, results differ mainly during the genesis and lysis phase of the cyclone, as well during a split or merge for the same database (RAIBLE et al., 2008; NEU et al., 2013).

The following sections describe the cyclone tracking algorithms applied in this thesis. Both approaches track the extratropical cyclones based on local pressure minima. The firstly presented algorithm uses in addition horizontal wind information and follows HOFSTÄTTER et al. (2016) with some simplifications.

First-guess approach following HOFSTÄTTER and CHIMANI (2012) and HOFSTÄTTER et al. (2016)

The cyclone trajectories at mean sea level pressure were tracked following the objective method of HOFSTÄTTER and CHIMANI (2012) and HOFSTÄTTER et al. (2016) which goes back to MURRAY and SIMMONDS (1991) and SIMMONDS et al. (1999). Firstly, a discrete cosine filter (DENIS et al., 2002) was applied to the mean sea level pressure field to avoid the detection of spurious local pressure minima, especially during weak gradient situations and at the edge of cyclones. The filter removed structures smaller than 400 km, and decreased smoothly up to 1000 km to pass all larger scales, like suggested by HOFSTÄTTER et al. (2016). Secondly, as sketched in

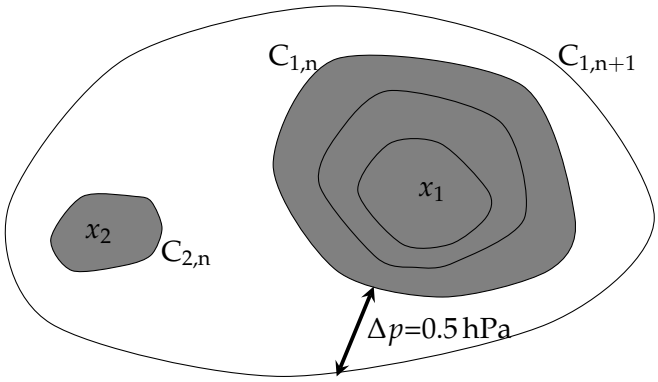

FIGURE 3.2: Schematic illustrating the cyclone area detection, adapted from WERNLI and SCHWIERZ (2006).

Figure 3.1, the following cyclone centre position ($x_{\mathrm{FG}}(t_{\mathrm{n+1}})$) was guessed with following equation (cf. equation 2, HOFSTÄTTER et al., 2016):

$$\vec{u}_{\mathrm{pred}} = w_1 \cdot \left[w_2 \cdot \vec{u}_{\mathrm{mslp}} + (1 - w_2) \cdot f_{red} \cdot \vec{u}_{700} \right], \tag{3.2}$$

with the horizontal wind vector at 700 hPa ($\vec{u}_{700}$) and mean sea level pressure ($\vec{u}_{\mathrm{mslp}}$). The factor w_1 was set to 0.60 like suggested in SIMMONDS et al. (1999). The factors $w_2 = 0.33$ and $f_{red} = 0.7$ are introduced to weight the upper level winds more and to account for increasing wind speeds with higher altitude (SIMMONDS et al., 1999; HOFSTÄTTER et al., 2016). Thirdly, the detected cyclone centre $x(t_{\mathrm{n+1}})$ nearest to this first guess within a search radius r of 200 km was estimated as the following track point.

In contrast to HOFSTÄTTER and CHIMANI (2012), HOFSTÄTTER et al. (2016), and HOFSTÄTTER et al. (2018), we tracked only closed depressions and the previous replacement vector was not used for estimating the propagation direction ($\mathbf{U}_{\mathrm{pst}}$ in equation 2, HOFSTÄTTER et al., 2016). Furthermore, HOFSTÄTTER et al. (2016) defined a score instead of using a search radius. The score of HOFSTÄTTER et al. (2016) considers not only the Euclidean distance but also the angle between the propagation vectors of the first guess and detected track point.

First-guess approach of WERNLI and SCHWIERZ (2006) and SPRENGER et al. (2017)

The method of WERNLI and SCHWIERZ (2006) and SPRENGER et al. (2017) is not only based one detected cyclone centres but takes also the spatial extension of cyclones into account. For each cyclone centre x_{k}, the outermost closed isobar $\mathrm{C_{k,n}}$ which encloses only x_{k} is defined as the corresponding cyclone field (Figure 3.2). The contour level interval was set to Δp=0.5 hPa starting with $p(x_{\mathrm{k}})$. For the cyclone tracking only the position of the cyclone centres are taken into account. The position of the following track point is detected by a first guess approach. Conversely to HOFSTÄTTER et al. (2016), only the previous displacement vector is used:

$$\vec{u}_{\mathrm{pred}} = 0.75 \cdot \left[\vec{x}_{\mathrm{Q}}(t_{\mathrm{n}}) - \vec{x}_{\mathrm{Q}}(t_{\mathrm{n-1}}) \right], \tag{3.3}$$

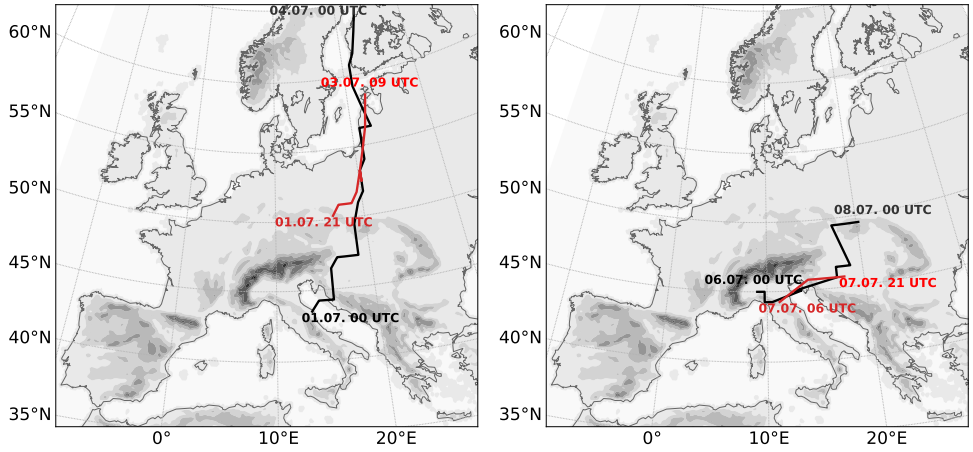

FIGURE 3.3: Selected cyclone tracks in July 1954 calculated with our tracking algorithm following HOFSTÄTTER et al. (2016) (black line) and the algorithm of WERNLI and SCHWIERZ (2006) (red line) based on ERA-20C reanalysis with a horizontal resolution of 0.75°.

with the cyclone track points $\vec{x}_Q$ at the current (t_n) and previous time step (t_{n-1}). The factor 0.75 accounts for the generally decreasing cyclone speed throughout the life cycle. The cyclone centre $x_Q(t_{n+1})$ nearest to the first guess within a search radius r smaller than 1000 km is assigned as new track point (see figure 3.1). Note, cyclone track points where topography exceeds 1500 m were excluded because of the extrapolation errors of the mean surface pressure values in these altitudes.

Comparison of both cyclone tracking approaches

Figure 3.3 shows two cyclones associated with the flood event in the Danube catchment in 1954. Both tracking approaches capture the cyclones. However, the tracking of WERNLI and SCHWIERZ (2006) and SPRENGER et al. (2017) detects a shorter cyclone track in this case. As already discussed in RAIBLE et al. (2008) and NEU et al. (2013), cyclone tracking results of different approaches differ mainly when the local pressure minima are weak or ambiguous, which is usually the case during the genesis or lysis phase.

The discrete cosine filter in the first tracking approach (black lines) can reduce the number of detected local minima by removing spurious lows. That may lead to a detection of longer tracks. Note, that the start point of both tracking algorithms differs in Figure 3.3, left panel, less than one day. Cyclone tracks lasting less than that time span were filtered out in the approach of WERNLI and SCHWIERZ (2006). Furthermore, the additional wind information in HOFSTÄTTER et al. (2016) helps when cyclones change their propagation direction following the upper level winds, like from the 07.07.1954 to the 08.07.1954 (Figure 3.3, right panel). Differences among the detected track points during the same time window were caused by the discrete cosine filter applied in the approach following HOFSTÄTTER et al. (2016) (black line). Note, both tracking algorithms do not explicitly take splitting and merging into account. We used the approach following HOFSTÄTTER and CHIMANI (2012) and HOFSTÄTTER et al. (2016) for selected cases. For analysing the years from 1901 to 2010, however, we applied the method of WERNLI and SCHWIERZ (2006) and SPRENGER et al. (2017) because it is computationally more efficient and has already

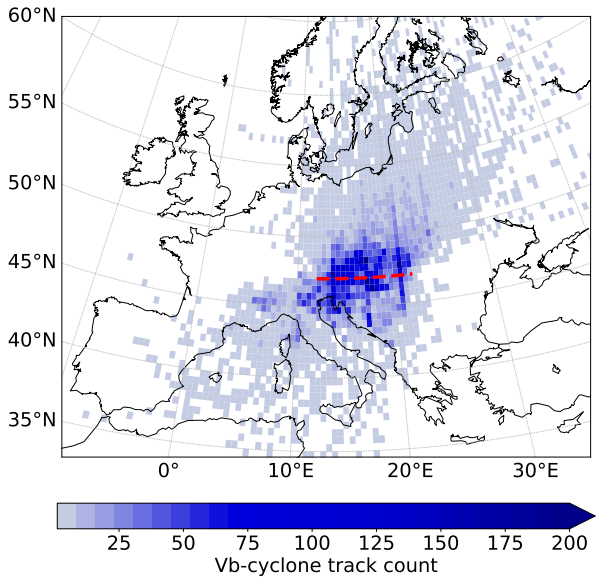

FIGURE 3.4: Vb-cyclone track count based on dynamically downscaled ERA-20C reanalysis data interpolated to a horizontal resolution of 0.5°.

been applied to a wide range of studies (e.g., RAIBLE et al., 2008; PAPRITZ et al., 2015; BÜELER and PFAHL, 2017; SPRENGER et al., 2017; STUCKI et al., 2020; THURNHERR et al., 2020b).

Vb-cyclone filtering

A special focus of this thesis lies on so-called Vb-cyclones propagating from the western Mediterranean Sea north-eastward over northern Italy along the eastern fringe of the Alps towards Central Europe. Some previous studies use relatively restrictive definitions and retrieved about 2-5 Vb-cyclones per year (HOFSTÄTTER and CHIMANI, 2012; MESSMER et al., 2015; NISSEN et al., 2013). However, these studies used different source and target region conditions, which complicates an intercomparison. Therefore, we used a simple and less restrictive classification and defined all cyclones crossing north-eastward the latitude 47°N between 12°E and 22°E as Vb-cyclones (cf. HOFSTÄTTER and BLÖSCHL, 2019). Based on this classification, about 10 Vb-cyclones occurred on average per year from 1901 to 2010 (dynamically downscaled ERA-20C, interpolated to 0.5° horizontal resolution). Figure 3.4 shows the corresponding cyclone frequency map.

3.3 Convective Cell Tracking

We tracked convective cells during selected flood events to estimate the convective rainfall fraction. The convective-cell tracking algorithm was firstly presented in BRENDEL et al. (2014) and further developed in BRISSON et al. (2018) and PURR et al. (2019). Such a Lagrangian approach has a relatively low sensitivity to spatial or temporal shifts in the model data in comparison with observations (BRISSON et al.,

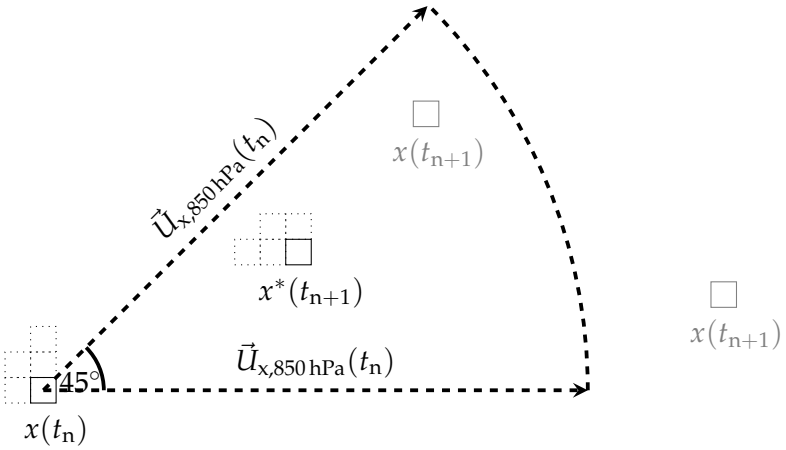

FIGURE 3.5: Schematic illustrating the convective cell tracking for one grid box $x(t_n)$ of a convective cell at the 850 hPa pressure level with the new location at $x^*(t_{n+1})$. The adjacent grid boxes of the grid boxes $x(t_n)$ and $x^*(t_{n+1})$ that belong to the same convective cell are sketched with dotted squares.

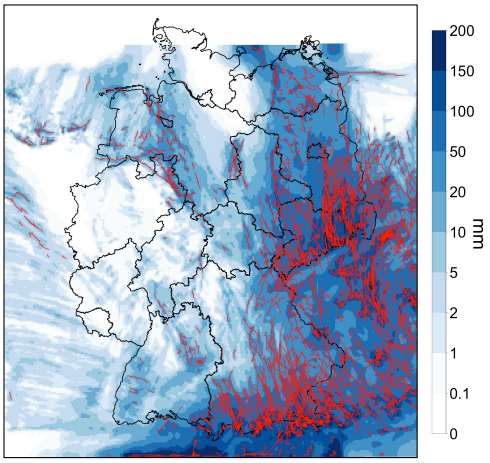

FIGURE 3.6: Total precipitation (blue shades) and detected convective cyclone trajectories (red) from 11.08.2000 to 13.08.2002 in CPS with COSMO-CLM driven by ERA-interim (PURR et al., 2019). Figure adapted from Christopher Purr (Goethe-University Frankfurt).

2018). Furthermore, it is possible to trace the evolution of convective-cell characteristics along the trajectories in contrast to Eulerian approaches (BRISSON et al., 2018).

In the following, we outline the latest version of the convective cell tracking procedure, as described in PURR et al. (2019, 2021). Firstly, for all time steps, we detected all adjacent grid cells with a precipitation intensity above 8.5 mm/h (within 5 min) as a potential convective cell. Secondly, for each convective-cell grid box $x(t_n)$, the potential location of the new cell grid box position $x^*(t_{n+1})$ at the following time step is detected within 45°-search cones at 850 hPa, 700 hPa, and 800 hPa, respectively. The wind vector at the respective pressure level defines the direction of each search cone, and the wind speed multiplied by a factor of two defines its length. A probability measure for each convective cell grid box $x(t_{n+1})$ within the search cone is calculated based on the Euclidean distance from the cone centre line, with the highest probability for the cell nearest to the cone centre line and the cone origin

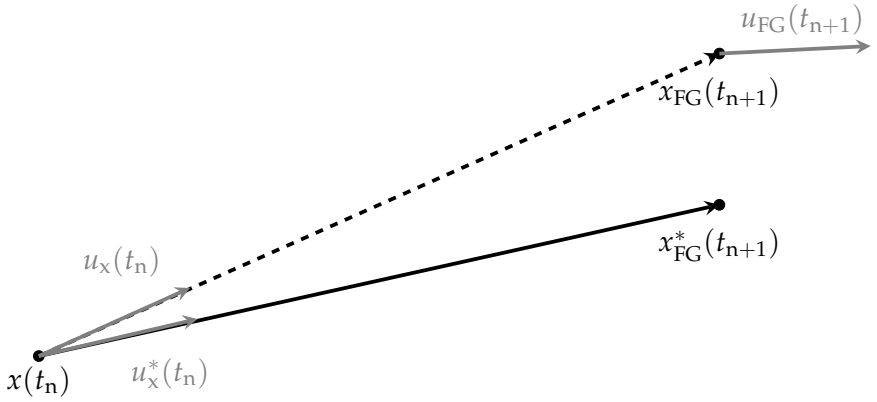

FIGURE 3.7: Schematic illustrating the iterative calculation of the position of the air parcel at t_{n+1} in LAGRANTO. Figure adapted with some changes from (SPRENGER and WERNLI, 2015).

at $x(t_n)$. We assign then the convective cell with the highest probability over all altitude levels and over all adjacent grid boxes as the new location of the convective cell, shown as $x^*(t_{n+1})$ in Figure 3.5. Note that this approach does not account for merging and splitting of convective cells. Overall, only feasible convective cells with a lifetime longer than 15 min and a size larger than four grid boxes are further analysed. For these cells, we trace the mean intensity, maximum intensity, cell area, cell speed, track length, and overall lifetime. Figure 3.6 shows as an example the derived convective cell trajectories during the Vb-cyclone event 2002 with a high occurrence frequency in south-east Germany and the Ore mountain region.

3.4 Evaporative moisture source diagnostics based on backward trajectories

We analysed the moisture source regions of selected precipitation events triggering floods to gain more insight into the processes that enhance flood producing rainfall and the particular role of the Mediterranean Sea. Our analysis was based on a Lagrangian approach that uses backward trajectory calculations. Such approach is computationally efficient and has been applied in many moisture source studies (e.g., STOHL and JAMES, 2004; SODEMANN et al., 2008b; SODEMANN and ZUBLER, 2010; SCHOLDER-AEMISEGGER, 2013; WINSCHALL, 2013). However, it includes uncertainties because the surface moisture uptake is derived from specific moisture changes along the trajectories (WINSCHALL et al., 2014). In comparison, an Eulerian approach, for example, moisture tagging with tracers, includes relevant processes like turbulent mixing but is computationally expensive (e.g., SODEMANN et al., 2008a; WINSCHALL et al., 2014). Furthermore, it has to be applied online to an atmospheric model simulation. Thus, in contrast to the Lagrangian approach, we could not employ Eulerian moisture tracing to our centennial reanalysis.

3.4.1 Backwards trajectories with LAGRANTO

The backward trajectories were calculated with the updated version of the Lagrangian analysis Tool LAGRANTO (version 2.0, WERNLI and DAVIES, 1997; SPRENGER and WERNLI, 2015). Lagrangian analyses numerically solve following air parcel trajectory equation (SPRENGER and WERNLI, 2015):

$$\frac{\mathrm{D}\vec{x}}{\mathrm{D}t} = \vec{u}(\vec{x}), \tag{3.4}$$

with the geographical position vector $\vec{x} = (\lambda, \Phi, z)$ and the corresponding 3-D wind vector $\vec{u}(\vec{x}) = (u, v, w)$. In particular, LAGRANTO uses an iterative Eulerian time step. Firstly, a first guess of the new air parcel position $x_{\mathrm{FG}}(t_{\mathrm{n}+1})$ is calculated based on current air parcel location $x(t_{\mathrm{n}})$ and the corresponding wind $u_{\mathrm{FG}}(t_{\mathrm{n}})$ (see Figure 3.7). The wind field is not constant over space and time. Therefore, the first guess is improved by further iterations. These consider also the wind velocity and direction at the previous first guess location for a more realistic displacement vector calculation. In detail, the displacement vector for the second iteration is calculated as follows:

$$u^*_{\mathrm{x}}(t_{\mathrm{n}}) = \frac{1}{2}\left[u_{\mathrm{x}}(t_{\mathrm{n}}) + u_{\mathrm{FG}}(t_{\mathrm{n}+1})\right]. \tag{3.5}$$

That means the improved estimation of the new air parcel position is determined by following equation:

$$x^*_{\mathrm{FG}}(t_{\mathrm{n}+1}) = x(t_{\mathrm{n}}) + u^*_{\mathrm{x}}(t_{\mathrm{n}}) \cdot \left[t_{\mathrm{n}+1} - t_{\mathrm{n}}\right]. \tag{3.6}$$

By default, three iterations step are applied in LAGRANTO with a time interval $[t_{\mathrm{n}+1} - t_{\mathrm{n}}]$ that is 1/12 of the temporal resolution of the input data. The spatial interpolation is performed in the horizontal with a bilinear interpolation and in the vertical with a linear one (WERNLI and DAVIES, 1997; SPRENGER and WERNLI, 2015). Along the trajectories various variables were traced for the moisture diagnostics, for example, specific humidity, temperature, planetary boundary height, total precipitation, surface evaporation, or heat fluxes.

Figure 3.8 shows the evolution of specific humidity along selected backward trajectories on the 28.10.1930 in our dynamically downscaled reanalysis (Δx=0.11°). During both time steps the specific humidity increases over the Mediterranean Sea. The cyclonic air flow from the Padan Plain over the Sea of Sicily north-eastwards along the eastern fringe of the Alps illustrates the importance of the Alpine mountain range on the air flow directions. Therefore, a high spatial resolution of the backtracking input data was crucial.

3.4.2 Moisture source diagnostics

In this study, a Lagrangian approach was used to identify the evaporative moisture sources of heavy precipitation events linked to extreme flood events (see chapter 5 and 6). The algorithm was based on the method of SODEMANN et al. (2008b), often referred to as WaterSip. The applied source code was written by Franziska Aemisegger (SCHOLDER-AEMISEGGER, 2013). The method is well established and

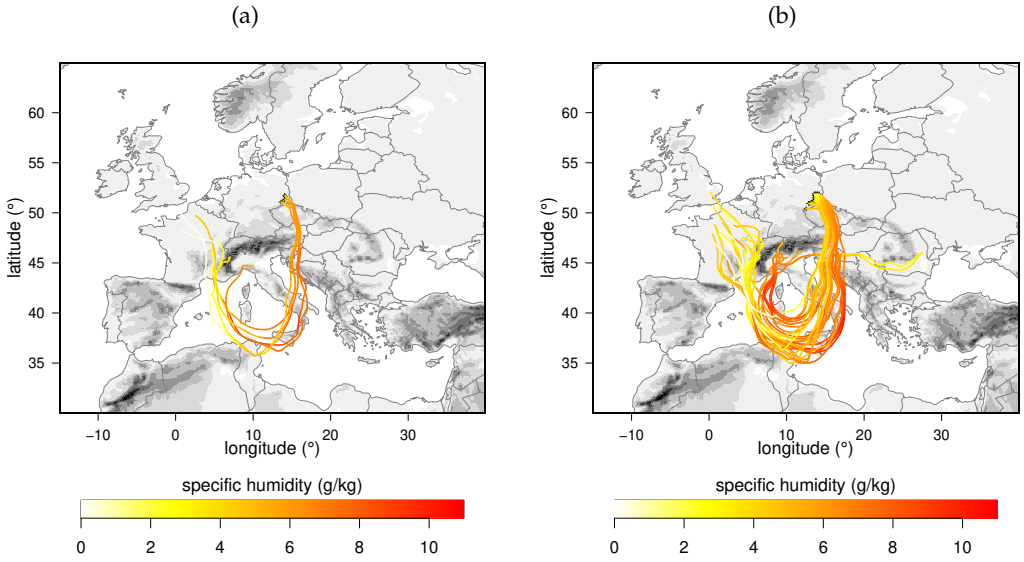

FIGURE 3.8: Specific humidity (g/kg) along selected four-day backward trajectories that start (a) on the 28.10.1930 (16 UTC) and (b) 28.10.1930 (17 UTC). Only the trajectories of air parcels exceeding 80% specific humidity at the start points are displayed. As data basis serves our dynamically downscaled reanalysis.

has already been applied to heavy precipitation and flood events (e.g., MARTIUS et al., 2013; WINSCHALL, 2013; GRAMS et al., 2014; WINSCHALL et al., 2014; PIAGET et al., 2015). Other applications were climatological analyses (e.g., SODEMANN et al., 2008b; SODEMANN and ZUBLER, 2010; WINSCHALL, 2013), or the application to interpret stable water isotope measurements (e.g., SODEMANN et al., 2008a; AEMISEGGER et al., 2014; STEEN-LARSEN et al., 2015; THURNHERR et al., 2020a).

We identified the evaporative moisture source regions based on changes of specific humidity $(\Delta q/\Delta t)$ along the air parcel trajectories. This approach assumes that freshwater fluxes between the surface and the atmosphere, i.e., surface evaporation E and precipitation P, are the governing subgrid-scale processes causing specific humidity changes (STOHL and JAMES, 2004; SODEMANN et al., 2008b):

$$\frac{\mathrm{D}q}{\mathrm{D}t} \approx \frac{\Delta q}{\Delta t} = E - P. \tag{3.7}$$

Note, other processes, like below-cloud or cloud evaporation, are not attributed. Thus, specific humidity changes due to these processes were also diagnosed as uptakes due to surface evaporation (e.g., SCHOLDER-AEMISEGGER, 2013). The individual moisture uptakes were weighted according to their contribution to the final humidity. After precipitation, i.e., $\Delta q < 0\,\mathrm{g\,kg^{-1}}$, the weight of previous uptakes is discounted. In detail, the following calculation steps were carried out:

1. All trajectory start points ($t = 0$) with specific humidity larger than 80% were selected to focus only on air parcels that are likely to produce precipitation in the region of interest (SODEMANN et al., 2008b; GRAMS et al., 2014). An exemplary trajectory is shown in Figure 3.9 with corresponding values in Table 3.1.

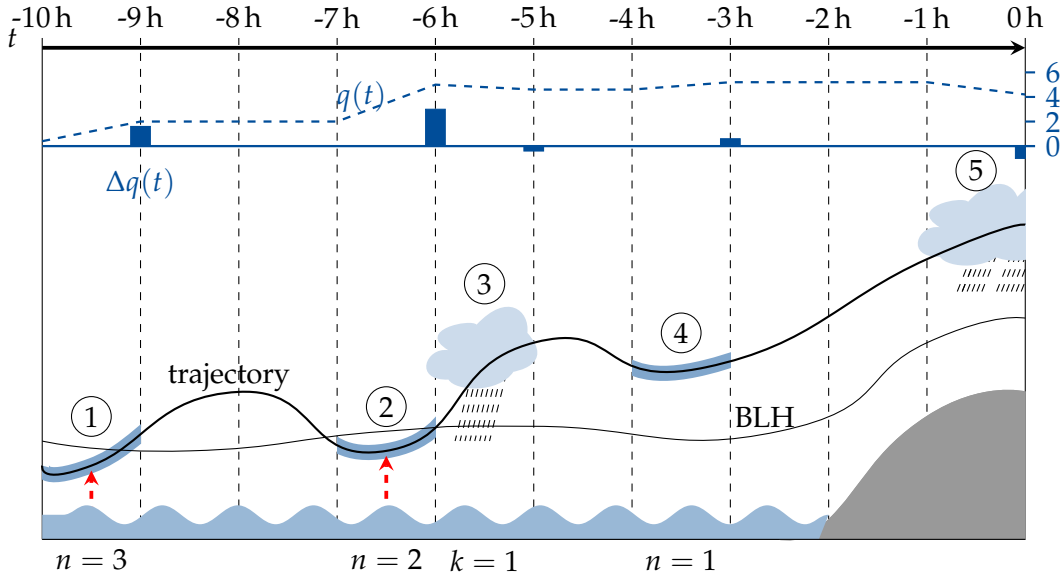

FIGURE 3.9: Modified sketch of the weighted moisture uptake calculations from SODEMANN et al. (2008b).

2. The changes of specific humidity q were traced along the backward trajectories (SODEMANN et al., 2008b):

$$\Delta q(t) = q(\vec{x}(t)) - q(\vec{x}(t - \Delta t)), \tag{3.8}$$

with a time step interval of $\Delta t = 1\,\mathrm{h}$ (blue bars in Figure 3.9). If an increase of more than 0.5 g/kg was detected, a moisture source was identified. This threshold was chosen to exclude spurious uptakes due to numerical noise (SODEMANN et al., 2008b).

3. Moisture uptakes close to the start time step of the backward trajectory (i.e., t=0) contribute more to the respective rainfall than previous moisture uptakes. For example, in Figure 3.9 the moisture uptake at ④ contributes more to the heavy precipitation event at ⑤ than the moisture uptakes at ② and ①. Therefore, all moisture uptakes were weighted and accumulated for all trajectories at each start time step. The weighted moisture uptake was calculated like proposed in SODEMANN et al. (2008b). Firstly, we calculated the fractional contribution f_n of the moisture uptake Δq_n that happened in advance of the analysed precipitation event (i.e., the backward-trajectory start at $t = 0$):

$$f_\mathrm{n} = \frac{\Delta q_\mathrm{n}(t_\mathrm{n})}{q_\mathrm{n}(t_\mathrm{n})}, \text{ with n} = 1, \tag{3.9}$$

and the moisture uptake amount $\Delta q_\mathrm{n}(t)$, as well as the corresponding specific humidity of the air parcel $q_\mathrm{n}(t)$ (see equation 3.8). For example, in Figure 3.9, $\Delta q_1 = 0.6\,\mathrm{g\,kg^{-1}}$ and $q_1 = 5.2\,\mathrm{g\,kg^{-1}}$, which leads to $f_1 = 0.12$.

4. The remaining moisture uptakes (i.e., $n > 1$, see Figure 3.9) have to be reduced by the moisture uptake contributions that occurred after these uptake events:

$$f_\mathrm{n} = \frac{\Delta q_\mathrm{n}(t_\mathrm{n})}{q_{\mathrm{n}-1}(t_{\mathrm{n}-1})}, \text{ with } t_{\mathrm{n}-1} > t_\mathrm{n}. \tag{3.10}$$

For example, the moisture uptake at ② (Figure 3.9) was calculated as follows: $f_2 = \Delta q_2 / q_1 = 3\,\mathrm{g\,kg^{-1}} / 5.2\,\mathrm{g\,kg^{-1}} = 0.58$.

5. In addition, precipitation (i.e., $\Delta q < 0$) occurring after a moisture uptake reduces the contribution of the previous moisture uptakes to the final precipitation event. Therefore, we reduced the moisture uptake f_n by considering these precipitation events (index k) with following equation:

$$f_\mathrm{n}^* = \frac{\Delta q_\mathrm{n}^*(t_\mathrm{n})}{q_{\mathrm{n}-1}(t_{\mathrm{n}-1})}, \text{ with } \Delta q_\mathrm{n}^*(t_\mathrm{n}) = \Delta q_\mathrm{n}(t_\mathrm{n}) + q_k \cdot f_\mathrm{n}. \tag{3.11}$$

The moisture uptake contribution without considering precipitation (f_n) was calculated after equation 3.10 and q_k is the specific humidity during the corresponding precipitation event. For example, the the moisture uptake at ② (Figure 3.9) was discounted to: $f_2^* = (\Delta q_2 + q_{k=1} \cdot f_2)/q_1 = (3\,\mathrm{g\,kg^{-1}} - 0.4\,\mathrm{g\,kg^{-1}} \cdot 0.58)/5.2\,\mathrm{g\,kg^{-1}} = 0.53$.

6. The above mentioned calculation steps 4. and 5. were repeated iteratively for all moisture uptakes and precipitation events after the respective moisture uptake, i.e., for $n-1$, $n-2$, $n-3$, and so forth.

7. In the example of Figure 3.9, in total 93% of the precipitation at ⑤ can be explained by moisture uptakes within the boundary layer, scaled with a factor of 1.5, and above. Note, the factor of 1.5 was applied to account for uncertainties in the boundary layer calculations. Many studies consider only the moisture uptake within the scaled boundary layer to ensure that the detected moisture increase originates from the surface and not from horizontal advection (SODEMANN et al., 2008b; GRAMS et al., 2014). However, SCHOLDER-AEMISEGGER (2013, section 3.1.4) detected above boundary layer uptakes that were still linked to surface evaporation via convection which is of high relevance during summer flood events. Therefore, we analysed the moisture uptake of air parcels, not only within the boundary, but also above. This is in accordance with WINSCHALL et al. (2014).

8. Selected meteorological variables were averaged over the whole moisture source region and weighted by the specific humidity contribution and saved as source condition data.

9. The weighted moisture uptakes were interpolated to a regular grid of 0.11° horizontal and summed up over the whole event (e.g., 4 days of 1 hourly backward trajectories). Finally, the total event moisture uptake was weighted by the total event precipitation at the trajectory start points.

3.5 Information theory approach: Transfer entropy

The Lagrangian moisture diagnostics, described in section 3.4.2, are computationally intensive. Thus, we could analyse only a few Vb-cyclone events with that approach, even though we detected more than one thousand Vb-cyclones from 1901

[1] The moisture uptake fraction was 0.80 without considering ②, ③, and ④, and about 0.32 considering only the moisture uptake at ②.

[2] The moisture uptake fraction was 0.58 without considering ③ and ④.

TABLE 3.1: Values of specific humidity q and final moisture uptake contribution f along the trajectory displayed in Figure 3.9.

t	**-10**	**-9**	**-8**	**-7**	**-6**	**-5**	**-4**	**-3**	**-2**	**-1**	**0**
q **(g kg^{-1})**	0.40	2.0	2.0	2.0	5.0	4.6	4.6	5.2	5.2	5.2	4.2
Δq **(g kg^{-1})**	–	1.6	–	–	3.0	−0.40	–	0.6	–	–	−1.0
f	–	0.28[1]	–	–	0.53[2]	–	–	0.12	–	–	–
		①			②	③		④			⑤

to 2010. Therefore, we applied a different approach to analyse a bulk of Vb-events and to compare them with the climatological mean state. In atmospheric sciences and climate studies often correlations are calculated for linear relationships and mutual information for nonlinear dependence between two variables. However, these methods are symmetric and contain no information about the direction of the component interaction, which is crucial for a better knowledge of the driving processes. Often, time-lagged correlations and regressions are used to detect the driving climate-system component. However, time-lagged correlations are sensitive to the auto-correlations and can lead to misleading quantifications of the interaction mechanisms and time lags (RUNGE et al., 2014).

Asymmetric information theory measures overcome these issues (POTHAPAKULA et al., 2019). They are based on the concept of Shannon entropy. The Shannon entropy $H(X)$ of a random variable X is defined as the amount of information needed to describe the random variable X (SHANNON, 1948):

$$H(X) = -\sum_{x} p(x) \cdot \log p(x), \tag{3.12}$$

with the probability mass function $p(x)$ of the random variable X. If a natural logarithm is applied, the unit of the entropy is called [nats]. Alternatively, the entropy can be expressed in [bits] if the logarithm base is 2. The random variable X is deterministic if the entropy $H(X)$ is equal to 0 nats (i.e., no uncertainty lies in the prediction of the outcome of X).

In some cases, the uncertainty in the prediction of X can be reduced with the knowledge of another random variable Y. The reduced amount of uncertainty is called mutual information I. The mutual information is derived from the corresponding Shannon Entropy H as follows (e.g., HLAVÁČOVÁ-SCHINDLER et al., 2007; BENNETT et al., 2019):

$$I(X;Y) = I(Y;X) = H(X) + H(Y) - H(X,Y), \tag{3.13}$$

where H(X,Y) represents the joint entropy, which is defined as

$$H(X,Y) = H(Y,X) = -\sum_{x}\sum_{y} p(x,y) \cdot \log p(x,y). \tag{3.14}$$

As already mentioned above, one disadvantage of the mutual information I is that it is a symmetric measure (like correlation). Thus, mutual information does not reveal the directional information transfer between X and Y. Moreover, if the systems X

and Y are driven by a common driver Z, the mutual information fails to unravel the dependence between the systems X and Y.

In case of a common driver Z, conditioning on the random variable Z gives a realistic dependence of X and Y. The corresponding information metric is known as conditional mutual information and defined as follows (HLAVÁČOVÁ-SCHINDLER et al., 2007; BENNETT et al., 2019):

$$I(Y;X|Z) = H(Y|Z) + H(X|Z) - H(Y,X|Z). \tag{3.15}$$

Based on this and by assuming a stationary Markov process, SCHREIBER (2000) introduced a measure known as transfer entropy (TE) which takes the dynamics of information transfer into account by conditioning the mutual information of X and Y to the past of Y. Thus, the TE is an asymmetric measure which quantifies not only the intensity but also the direction of information exchange from the source variable X to the target variable Y. The TE is often written in terms of conditioned mutual information (e.g., HLAVÁČOVÁ-SCHINDLER et al., 2007; BENNETT et al., 2019):

$$TE_{X\to Y} = I(Y;X^-|Y^-), \tag{3.16}$$

where X^- and Y^- denote the whole (possibly infinite) history of X and Y. As a compromise for computational complexity, equation (3.16) is usually reduced to following (SCHREIBER, 2000; BENNETT et al., 2019):

$$\begin{aligned} TE_{X\to Y} &= I(Y;X_{t-\tau}|Y_{t-\omega}) \\ TE_{X\to Y} &= \sum_x \sum_y p(y_t, y_{t-\omega}, x_{t-\tau}) \cdot \log \frac{p(y_t|y_{t-\omega}, x_{t-\tau})}{p(y_t|y_{t-\omega})}, \end{aligned} \tag{3.17}$$

with the time lag τ of the source variable X and the time lag ω of the target variable Y. The values of τ and ω in equation (3.17) are chosen depending on the system dynamics (e.g., VICENTE et al., 2011; BENNETT et al., 2019).

Chapter 4

Widespread floods during the past century

This chapter provides widespread flood events at gauges within the administrative boundaries of Germany since 1920. It serves as the fundament of this thesis that discusses the corresponding atmospheric processes triggering and intensifying these events. The flood classification described in section 3.1 was applied in cooperation with Ruhr-Universität Bochum (Andreas Schumann and Svenja Fischer) to half-yearly discharge maxima of selected GRDC gauges (section 2.1). We accounted for possible seasonal dependencies by calculating the maximum discharges of each summer (May – October) and winter half-year (November – April) instead of annual maxima. In the following, the events are presented for each half-year. Note that some parts of this chapter are taken from KRUG et al. (2020b).

4.1 Floods during the winter-half year

Table 4.1 shows the most severe trans-basin floods during the winter half-year. We detected half-yearly maximum GRDC discharges in all macro-scale catchments within seven days (see appendix, section B). That underlines the synchronicity of these winter flood events. Among all widespread floods since 1920, we selected for Table 4.1 the ones that fulfilled following conditions: at least three of the four macro-scale catchments (Danube, Elbe, Rhine, and Weser) were affected by a flood of class 2 (medium flood) and higher, or at least two macro-scale catchments were affected by a (very) large flood. Hence, we defined thresholds corresponding to a 15-year and 20-year flood, while UHLEMANN et al. (2010), who also studied trans-basin floods, used the threshold of a 10-year flood. Furthermore, we selected only the spatially most extensive floods (i.e., floods that affected the majority of all macro-scale catchments in Germany). On the contrary, UHLEMANN et al. (2010) applied a lower threshold of 10% inundated rivers, which usually results in floods that affect more than one catchment but are still localized to one region. Thus, in contrast to UHLEMANN et al. (2010), who detected 80 trans-basin floods in Germany during 1952–2002, we classified only twelve severe trans-basin floods because we

TABLE 4.1: Classification of the most intense trans-basin winter floods since 1920 based on half-yearly maximum GRDC discharges (provided by Andreas Schumann, Ruhr-Universität Bochum). The corresponding discharge values (m^3/s) are coloured according to the four flood classes defined by FISCHER and SCHUMANN (2018). The mean discharge (m^3/s) and catchment area (km^2) are added for each gauge.

river	gauge	mean discharge (m^3/s)	area (km^2)	01/1920	01/1926	03/1940	03/1942	02/1946	03/1947	01/1948	03/1981	03/1988	01/1995	01/2003	01/2011
Rhine	Maxau	1285	50196		3430	2250	2950	1910	2150	3040	3290	3930	3770	2740	2510
Main	Wuerzburg	116	14031	1450	916	817	1020	875	779	1320	800	1190	1190	1100	1310
Mosel	Cochem	314	27088	4020	3940	1340	1620	2380	1800	3730	1220	2290	3410	3140	2560
Rhine	Koeln	2099	144232	10700	10900	5980	8050	7080	5350	9890	6130	9550	10700	8840	7630
Weser	Hann.-Muenden	111	12442	1110	1300	795	927	1540	867	774	812	758	1010	903	818
Weser	Intschede	318	37720	1700	2290	1730	1860	3300	2220	1740	2370	1700	1910	2190	1320
Elbe	Dresden	329	53096	3190	1930	3110	1630	2190	2340	1780	2190	2010	1360	2000	2270
Saale	Calbe-Grizehne	112	23719			521	576	621	641	397	623	618	417	730	719
Elbe	Neu-Darchau	713	131950	3280	2260	3620	2210	2790	3500	2050	3550	3480	2170	3020	3590
Donau	Ingolstadt	313	20001		974	1590	1460	566	1070	1170	1000	1340	900	921	
Donau	Hofkirchen	641	47496	2820	2080	2770	2680	1540	2450	2360	1990	3010	2200	2100	2830

flood types: very small flood | small flood | medium flood | large flood | very large flood

focused on the most extreme cases in terms of spatial extent and peak discharge. Nonetheless, the intersection of both flood event lists is large. All the events we classified as a severe trans-basin flood during the period from 1952 to 2002 were within the first six highest-ranked events in UHLEMANN et al. (2010). The study of GVOŽDÍKOVÁ and MÜLLER (2017) covers the extended time-period from 1951 until 2013. The trans-basin floods based listed in Table 4.1 were among the 15 highest ranked events in their flood list.

Interestingly, we retrieve the same twelve flood events if we apply the same selection procedure to all trans-basin floods during the winter and summer half-year, as well. In other words, the most widespread and severe flood events occurred during the winter half-year, while the summer events have been more localized. That indicates that winter-related processes fostered spatially extended floods. Note, if we reduced our threshold of affected river basins to only two, we would also classify the Vb-floods in August 2002 and in July 2013 as trans-basin flood events in the Elbe and Danube river catchments (see Table 4.2). That agrees with UHLEMANN et al. (2010) and GVOŽDÍKOVÁ and MÜLLER (2017), who detected summer floods as intense but less widespread events.

Furthermore, the twelve trans-basin floods during winter show a temporal clustering. Interestingly, five of the twelve events occurred in the 1940s. In addition, trans-basin floods were more frequent in the 1980s (Table 4.1, UHLEMANN et al., 2010; GVOŽDÍKOVÁ and MÜLLER, 2017). Note that we found only two trans-basin floods during the 1980s in contrast to UHLEMANN et al. (2010) and GVOŽDÍKOVÁ and MÜLLER (2017) because we applied higher thresholds for the spatial extent and peak discharges. On the contrary, the 1930s and early 1960s were flood-poor periods.

4.2 Floods during the summer-half year

Table 4.1 shows the most severe trans-basin floods during the summer half-year. These summer floods were more regional events than the trans-basin winter floods. As in the winter half-year, we selected only the severest events with half-yearly peak discharges within one week in at least one sub-basin of the macro-scale river catchments. The only exception is the flood in the Rhine and Danube catchment

TABLE 4.2: Classification of the most widespread summer floods since 1920. Methods and color coding are the same as in Figure 4.1.

river	gauge	mean discharge (m^3/s)	area (km^2)	06/1926	06/1940	07/1954	06/1965	05/1970	05/1983	05/1999	08/2002	08/2005	06/2013
Rhine	Maxau	1285	50196	3400	2410	2160	3530	3960	4210	4060	2670	3110	4000
Main	Wuerzburg	116	14031	247	152	374	516	383	371	255	128	136	896
Mosel	Cochem	314	27088	1020	164	117	531	2740	3410	285	236	91.9	
Rhine	Koeln	2099	144232	4400	2620	2740	5060	7640	9800	4480	2850	3130	6130
Weser	Hann.-Muenden	111	12442	224	65	92.7	126	338	411	92.3	100	72.1	
Weser	Intschede	318	37720	349	207	353	417	930	738	299	521	188	
Elbe	Dresden	329	53096	2590	1050	2300	1820	943	347	233	4500	645	3910
Saale	Calbe-Grizehne	112	23719		97.9	440	396	429	190	99.8	290	71.6	1000
Elbe	Neu-Darchau	713	131950	2750	1090	2890	2240	2420	959	601	3410	775	4070
Donau	Ingolstadt	313	20001	1130	1800	1100	1810	883	645	2190	1560	1720	
Donau	Hofkirchen	641	47496	1900	2660	3290	2920	1720	976	3290	2860	2630	3360

flood types: very small flood | small flood | medium flood | large flood | very large flood

(14./15.05.1970) and the flood in the Elbe and Weser catchment (01.05.1970, see appendix, table B.2). Note that we also included the well-known event in June 2013 in our list, even though no corresponding half-yearly discharge maxima were recorded for some gauges.

The majority of the summer floods reached the highest discharges in the Danube and Elbe catchment. The only exceptions were the very large flood during May 1983 and the medium flood in May 1970 in the Rhine and Mosel river catchments. The 1983 flood was caused by high rainfall amount in these basins from the 15.04.1983 to 19.05.1983 (SCHRÖDER, 1990). In the headwaters of the Mosel even more than 200 mm were recorded during this period (SCHRÖDER, 1990). Moreover, the soil was already supersaturated due to a preceding flood in April (SCHRÖDER, 1990). Similarly, the flood in May 1970 was also caused by rainfall over several days and preceded by a winter flood in February in the Rhine basin.

4.3 Open research questions

Overall, the most widespread floods among all severe floods in Germany occurred during the winter half-year. During summer, the floods were more localised with particular high discharges in the Elbe and Danube catchment. These results are in line with HALL and BLÖSCHL (2018) analysing the seasonality of floods at individual gauges. They conclude predominantly winter floods in Central Europe except for the Alpine region and some parts of eastern Central Europe that are more affected by spring to summer floods.

The following research questions investigated in this thesis are based on the aforementioned flood event classification. The flow chart in Figure 4.1 illustrates the content of this thesis. The first research question which arises for the winter and summer floods is following:

1. What are the main hydro-meteorological flood drivers?

We address this research question for widespread winter floods in chapter 5. In summer, all widespread floods with particular high discharges in the Elbe and Danube catchment were associated with so-called Vb-cyclones (cf. STAHL and HOFSTÄTTER, 2018; KRUG et al., 2020a, and references therein).

A remarkable characteristic of the widespread winter floods was the temporal clustering in the 1940s and 1980s. It remains unknown whether climate drivers of the observed temporal flood clustering exist or whether it was caused by the random coincidence of flood-triggering meteorological circumstances. Therefore, the second research question addressed in chapter 5 is:

2. Do hydro-climatic drivers of the observed temporal clustering of widespread winter floods exist?

The second part of the presented work focuses on the summer half-year. In contrast to the widespread winter floods, no clusters of flood-rich and flood-poor years are obvious. Instead, the intensity of widespread summer floods seems to have increased in recent decades. On average, 4 to 10 cyclones follow the Vb-pathway per year, whereas, only a few Vb-cyclones caused extreme floods. Due to the Vb-cyclone pathway, one might expect a strong influence of the Mediterranean Sea on Vb-cyclone precipitation. However, despite recent research on Vb-cyclones associated with Vb-cyclone induced floods (e.g., GRAMS et al., 2014; MESSMER et al., 2017), the role of specific moisture source regions remains under debate. Thus, the chapters 6 and 7 discuss following research question:

3. What is the role of various moisture source regions, especially the Mediterranean Sea, in precipitation during Vb-cyclones?

Besides, Vb-cyclone precipitation is especially triggered in mountainous regions such as the Alps. In summer, convective processes during the afternoon can cause high rainfall intensities, especially if they coincide with stratiform precipitation linked to the Vb-cyclone. This increases the flood potential of Vb-cyclones and impacts the timing of the flood peak. Therefore, we study for selected past flood events following research question in chapter 8:

4. How important is convective rainfall during Vb-cyclone floods?

Finally, the key findings addressing these three research questions are summarized in the conclusions chapter.

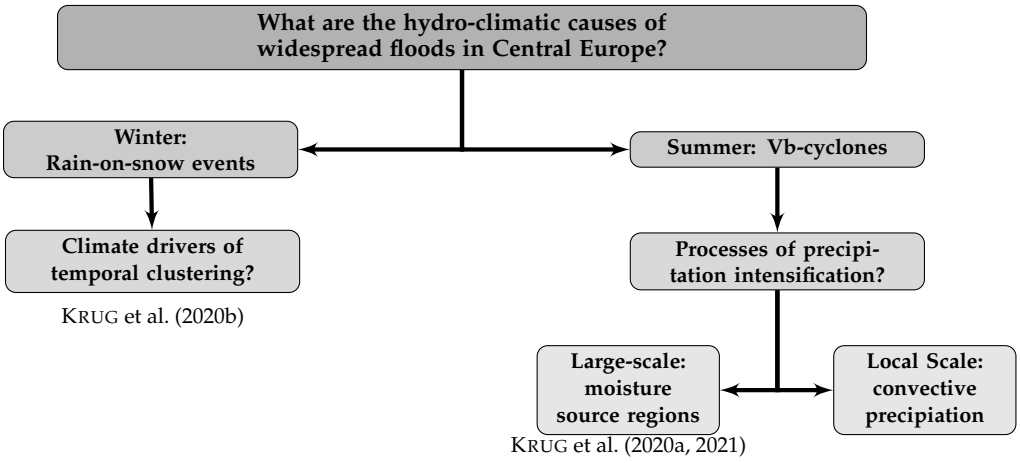

FIGURE 4.1: Flow chart illustrating the content of this thesis.

Chapter 5

Temporal variability of rain-on-snow floods

FIGURE 5.1: Flooding of the Aisch river (Bavaria) due to a rain-on-snow event in January 2021. The photography was taken by Tatjana Plachert at the street B470 (close by Reinhardshofen, Bavaria) on the 30.01.2021.

This chapter focuses on the first two research questions stated in the previous chapter. In detail, the main hydro-meteorological drivers of widespread winter floods during the past century are discussed. Based on this, the following sections investigate potential hydro-climatic causes of the observed temporal flood variability with flood-poor and flood-rich decades, such as the North Atlantic Oscillation. Please note that this chapter is mainly taken from the study entitled *On the temporal variability of widespread rain-on-snow-floods* by A. Krug, C. Primo, S. Fischer, A. Schumann, and B. Ahrens, published in Meteorologische Zeitschrift (KRUG et al., 2020b).

5.1 Trans-basin floods

River floods are a common natural hazard with a high social impact due to the large economic damages they cause. For example, the average annual losses due to floods in Europe from 2000 to 2018 were about 6.4 bn US$ (inflation-adjusted in 2018 values; MUNICH RE, 2019). Some events are of special relevance in flood risk assessment, like widespread and temporally accumulated events. Well-known examples of widespread floods, so-called trans-basin floods (UHLEMANN et al., 2010), in the Danube and Elbe catchments were the ones in August 2002 (e.g., ULBRICH et al., 2003a,b; BRÁZDIL et al., 2006) and May/June 2013 (e.g., BLÖSCHL et al., 2013; GRAMS et al., 2014; SCHRÖTER et al., 2015). The Rhine, Elbe, and Danube catchments were affected in March 1988 or the Rhine and Weser catchment in January 1995 (UHLEMANN et al., 2010; GVOŽDÍKOVÁ and MÜLLER, 2017). Traditionally, flood risk assessment and management focused on the catchment perspective (MERZ et al., 2014). During recent decades, the view has broadened and interdisciplinary processes have also been included (e.g., MERZ et al., 2014). One of these are atmosphere-catchment interactions, especially the link of climate variability and flood occurrence (MERZ et al., 2014). However, the current large-scale flood risk assessment still considerably lacks the modelling of multidisciplinary system processes (VOROGUSHYN et al., 2018).

The atmosphere-catchment interactions causing spatially extended floods vary depending on the region affected. For example, in Great Britain, catchment characteristics dominate the spatial dependence of floods and precipitation or flood events are spatially less extended with larger return periods (KEEF et al., 2009). However, in Switzerland, the orography and the flow direction of the wind fields play an important role (SCHMOCKER-FACKEL and NAEF, 2010b). Overall, widespread floods in Switzerland are mainly caused by large-scale rainfall events and snowmelt, especially in the Rhine river catchment (SCHMOCKER-FACKEL and NAEF, 2010a). Snowmelt is also relevant in Central Europe. For example, the spatially most extended floods in the Czech Republic occurred during snowmelt, even though they were less intense than rainfall floods during summer (RODDA, 2005). In Germany, the most widespread floods occur predominantly during winter while summer floods are more localized (UHLEMANN et al., 2010). This is in coincidence with the sensitivity study of GVOŽDÍKOVÁ and MÜLLER (2017) who adopted the cumulative indicator defined in UHLEMANN et al. (2010), which ranks trans-basin floods according to the spatial flood extent and the flood magnitude. If higher discharge thresholds are applied, summer floods are higher ranked compared to winter floods (GVOŽDÍKOVÁ and MÜLLER, 2017). Both, UHLEMANN et al. (2010) and GVOŽDÍKOVÁ and MÜLLER (2017), detect a nonuniform temporal distribution

of trans-basin floods in Central Europe. Interestingly, flooding was more frequent in the 1980s, followed by a flood-poor period during the 1990s. However, possible causes of such temporal clusters remain still unknown.

Such a potential driver of the interannual up to decadal flood variability is the climate variability and linked to that, atmospheric teleconnection patterns. For example, the North Atlantic Oscillation (NAO) is an atmospheric teleconnection pattern which is associated with heavy rainfall and flood damage anomalies over large areas in Europe (NOBRE et al., 2017). In winter, snow cover and its melting is also an important flood ingredient (e.g., UHLEMANN et al., 2010; GVOŽDÍKOVÁ and MÜLLER, 2017). During the positive phase of the NAO and Arctic Oscillation (AO) in winter and spring, PALL et al. (2019) detected a more frequent occurrence of rainfall during snowmelt in Norway due to increased rainfall, especially in the southwest region of Norway. This coincides with COHEN et al. (2015) who also detected a positive correlation of rainfall during snow cover and the NAO/AO in north-eastern Europe. Moreover, COHEN et al. (2015) conclude a negative correlation in Central Europe due to a snow-cover increase during the negative NAO phase. Further studies detected a significant correlation of the NAO and the snow-cover over Central Europe, especially during mid-winter (e.g., GUTZLER and ROSEN, 1992; CLARK et al., 1999; LATERNSER and SCHNEEBELI, 2003; BEDNORZ, 2008; HENDERSON and LEATHERS, 2010). In addition to the NAO, HENDERSON and LEATHERS (2010) found a significant correlation of the so-called Eastern Atlantic pattern (EA) and Scandinavian pattern (SCA) with the mean winter snow cover extent in Europe. Also PALL et al. (2019) detected a negative correlation of the SCA index and rain-on-snow events in the northern region of Norway during spring. Note, SCHMOCKER-FACKEL and NAEF (2010a) excluded a relation of floods in Switzerland and the NAO, analysing time series starting in 1500. This is in accordance with the fact, that the Alpine area is part of the transition zone of the northern and southern NAO dipole (LEHR et al., 2012).

Our study aims to shed more light on the potential atmospheric causes of the temporal trans-basin flood variability in Germany described by UHLEMANN et al. (2010) and GVOŽDÍKOVÁ and MÜLLER (2017). In particular, we want to answer the following research question:

1. What were the hydro-meteorological causes of widespread and severe floods in Germany during the 20th century?

Since we detected that most events were caused by rainfall during snowmelt, we focused on the temporal variability of this flood type in the following. It is crucial to restrict the analysis to one specific causative hydro-meteorological flood type (TARASOVA et al., 2019). Otherwise, the investigated interannual flood variability would be influenced by a superposition of various atmospheric drivers and the individual flood-causing processes could not be studied. Thus, our second research question is:

2. Can the coincidence of snowmelt and rainfall or atmospheric teleconnection patterns, like the NAO, EA, and SCA, explain the interannual up to decadal variability of widespread floods in Germany?

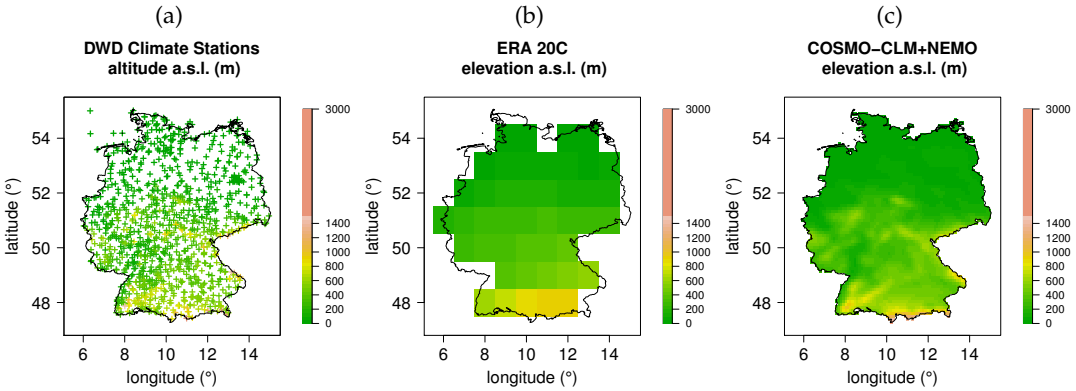

FIGURE 5.2: Location and altitude above sea level of DWD climate stations (a). Grid cell altitude of (b) ERA-20C reanalysis and (c) with COSMO-CLM+NEMO dynamically downscaled ERA20C-data. Reanalysis and simulation data were clipped with the vg2500 shapefile of the German Federal Agency for Cartography and Geodesy, Frankfurt am Main, 2011.

To answer these questions, we considered widespread floods since 1920 to extend the time series of previous studies and to cover more extreme events (see section 4.1). Section 5.3 describes the temporal evolution of hydro-meteorological variables during selected widespread floods and the synoptic-scale atmospheric conditions in terms of cyclone trajectories. Afterwards, we discuss the temporal variability of the coincidence of rainfall and snowmelt (section 5.4.1) and atmospheric teleconnection patterns (section 5.4.2) from 1900 to 2010. Finally, we summarize our key findings in section 5.5.

5.2 Data and methods

The atmospheric conditions of widespread floods in Germany were analysed based on three hydro-meteorological data sets. This section describes them and the applied methods.

5.2.1 Station-based meteorological measurements

To analyse the flood-causing atmospheric circumstances, we used the quality controlled station-based measurement data of the Climate Data Center, version v005 (2017). The data was provided by Deutscher Wetterdienst (DWD), the national weather service in Germany. More details on the data and applied quality control can be found in section 2.2.1.

Although, the first station-based measurements have started in January 1781, we focused on the time period from January 1900 to December 2010, to be consistent with the atmospheric model data (section 5.2.2). In total, 1094 climate stations were available. Figure 5.2a displays the corresponding station locations and altitudes in metres above mean sea level. However, the daily observations covered different sub-time periods with an increasing number of stations during the second half of the 20th century. Furthermore, the climate stations were not homogeneously distributed over the different altitude ranges. For example, from 1900 to 2010, 79 climate stations

were in total available from 600 m to 800 m, and 27 stations from 800 m to 1000 m altitude.

During the past century, the most widespread floods in Germany were caused by rain during snowmelt (see section 5.3; UHLEMANN et al., 2010; GVOŽDÍKOVÁ and MÜLLER, 2017). Therefore, we defined an atmospheric proxy for floods (AP) on a date k to investigate the temporal variability of snowmelt and simultaneous rainfall. However, neither snow density nor snow water equivalent was reported in station-based observations. Consequently, we used the change in the daily snow height measurements as a proxy for the amount of snowmelt. Based on this, the atmospheric proxy AP is defined as follows:

$$AP_k = \text{rank}\left(\sum_{d=k}^{k-M}(h_d - h_{d+1})\right) + \text{rank}\left(\sum_{d=k}^{k-N} p_d\right), \tag{5.1}$$

with the median rainfall p over Germany and the median snow height h over all stations measurements between, for example, 600 m and 800 m altitude. Note, the quantities of snow cover and thus snowmelt increase substantially with higher altitude levels. Therefore, we specified altitude ranges for snowmelt. Firstly, we calculated the $(M+1)$-day sum of the snowmelt in the selected altitude range for each time step. Secondly, we used a $(N+1)$-day period to calculate rainfall sums. Thirdly, we calculated the ranks for both time series separately and summed both rank values for each day (index d). However, no station-based measurements were available at 600 m – 800 m until the late 1930s. Thus, the station-based measurements were analysed for this altitudes during the time period 1 January 1940 until 31 December 2010.

5.2.2 Atmospheric model data and analysis based on ERA-20C reanalysis

This section introduces the atmospheric model data, as well as the cyclone trajectory detection and atmospheric teleconnection indices calculation.

Dynamically downscaling with COSMO-CLM+NEMO

The station-based observations were irregularly distributed in space, and only a few measurements were available during the first decades of the 20th century. On the contrary, reanalysis data overcomes these issues and provides us with a four-dimensional gridded state of the atmosphere. They are obtained with global numerical models, which also take assimilated observation data into account. The ECMWF twentieth century reanalysis (ERA-20C; POLI et al., 2016) covers the time period 1900 – 2010 with a horizontal resolution of about 125 km (spectral truncation T159). Only surface pressure and surface marine wind measurements were assimilated for creating the reanalysis. From 1900 to 2010, the number of assimilated surface pressure observations per month increased by a factor of 10^2 (POLI et al., 2016). This affects the accuracy of ERA-20C during the early decades. Nonetheless, WEGMANN et al. (2017) concluded an improved simulation of snow climatologies in ERA-20C compared to other reanalysis data during the first half of the 20th century.

Figure 5.2b shows the elevation of the individual grid-points. The orography is not well represented compared to the altitudes of the climate stations in Figure 5.2a. However, orography is essential for precipitation and other meteorological variables at the different altitude ranges. Therefore, the reanalysis data was dynamically downscaled to approximately 12 km horizontal resolution for the entire period from 1901 to 2010 (Figure 5.2c). The downscaling was performed over Europe with a high-resolution and interactively coupled atmosphere-ocean model setup. The atmospheric and land component of the simulation setup was the Consortium for Small-scale Modelling in Climate Mode (COSMO-CLM; ROCKEL et al., 2008). The atmospheric component COSMO-CLM was interactively coupled to regional implementations of the ocean general circulation model NEMO (Nucleus for European Modeling of the Ocean; MADEC and THE NEMO TEAM, 2016). We applied NEMO over the Mediterranean Sea (NEMO-MED12, e.g., LEBEAUPIN BROSSIER et al., 2011; BEUVIER et al., 2012; AKHTAR et al., 2018; DROBINSKI et al., 2018) and over the North- and Baltic Seas (NEMO-NORDIC, DIETERICH et al., 2013; HORDOIR et al., 2013; PHAM et al., 2014). With the river routing model TRIP (Total Runoff Integrating Pathways; OKI and SUD, 1998) the freshwater inflow of rivers routing into the Mediterranean Sea was considered in NEMO-MED12 to close the water cycle (for more details see section 2.2.2). PRIMO et al. (2019) and KELEMEN et al. (2019) present detailed performance studies on the dynamically downscaling of centennial reanalysis data with COSMO-CLM+NEMO.

Cyclone trajectories

To analyse the synoptic-scale atmospheric conditions during the flood events, we tracked all cyclones associated with our detected Germany-wide flood events in ERA-20C reanalysis data with a 3-hourly resolution. The cyclone trajectories at mean sea level pressure were tracked following the objective method of HOFSTÄTTER and CHIMANI (2012) and HOFSTÄTTER et al. (2016). Firstly, a discrete cosine filter (DENIS et al., 2002) was applied to the mean sea level pressure field to avoid the detection of spurious local pressure minima, especially during weak gradient situations and at the edge of cyclones. The filter removed structures smaller than 400 km, and decreased smoothly up to 1000 km to pass all larger scales, like suggested by HOFSTÄTTER et al. (2016). Secondly, the following cyclone track position was guessed with the help of the horizontal wind fields at the mean sea level pressure and 700 hPa. Thirdly, the detected cyclone centre nearest to this first guess was estimated as the following track point. In contrast to HOFSTÄTTER and CHIMANI (2012), HOFSTÄTTER et al. (2016), and HOFSTÄTTER et al. (2018), we tracked only closed depressions and no cyclone climatology was used for estimating the propagation direction (for more details see section 3.2). In the following, we focus only on cyclone trajectories which stayed at least 18 h in the region of interest in Central Europe: 0.5° E – 23.9° E and 44.3° N – 58.2° N.

Atmospheric teleconnection indices

To analyse potential climate drivers of flood-poor and flood-rich periods, we calculated the monthly mean indices of the North Atlantic Oscillation (NAO), the Eastern Atlantic (EA), and Scandinavian pattern (SCA) based on ERA-20C reanalysis data.

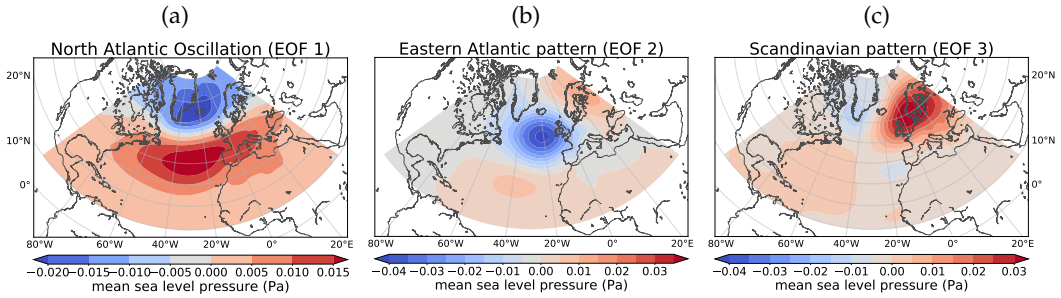

FIGURE 5.3: Spatial display of the first three empirical orthogonal functions of monthly mean sea level pressure anomalies in ERA-20C reanalysis.

They were defined as the first three leading eigenvectors of the principal component analysis of the monthly mean sea level pressure anomalies over the Atlantic sector (100° W, 40° E, 10° N, 80° N). The anomalies have been calculated based on the time period from 1900 to 2010. We accounted for grid-area imparity by multiplying the anomaly fields by $\sqrt{\cos\phi}$, where ϕ is the latitude (CHUNG and NIGAM, 1999; COMAS-BRU and MCDERMOTT, 2014). The resulting eigenvectors were standardised by the climatological mean and standard deviation of each month.

The first empirical orthogonal function (EOF) corresponds to the NAO and explained about 30% variance. The second EOF (EA) explained approximately 16%, and the third EOF (SCA) explained around 14%. The atmospheric oscillation indices derived by principal component analysis may have an opposite sign compared to other definitions in the literature (COMAS-BRU and MCDERMOTT, 2014). In our case, the positive NAO index showed positive anomalies over the Iberian Peninsula and negative anomalies over Iceland (Figure 5.3 a). The positive EA phase was defined by strong negative anomalies over the North Atlantic, west of Great Britain (Figure 5.3 b, opposite sign compared to COMAS-BRU and MCDERMOTT, 2014). The last mode, the SCA, showed a blocking high over the Scandinavian Islands (Figure 5.3 c).

Moisture uptake

The moisture uptake for precipitation associated with a widespread flood in March 1942 was identified with a Lagrangian approach (more details on the method can be found in section 3.4). Firstly, we calculated the seven-day backward trajectories with LAGRANTO (WERNLI and DAVIES, 1997; SPRENGER and WERNLI, 2015) for each hour during the selected period. Over $21{\cdot}10^3$ starting points were selected equidistantly every 20 km on 39 vertical levels from 250 m a.s.l. to 9750 m a.s.l. within 10°E, 16°E, 47°N 51.5°N (Figure 5.8, dashed rectangle). For calculating the moisture uptake, we focused on trajectories related to relative humidity exceeding 80% and thus precipitation (cf. GRAMS et al., 2014). Secondly, we detected the moisture source regions based on changes of specific humidity along the air parcel trajectories, by assuming that changes of specific moisture result from evaporation and precipitation (SODEMANN et al., 2008b; SCHOLDER-AEMISEGGER, 2013). The individual moisture uptakes were then weighted according to the method of SODEMANN et al. (2008b). We focused on moisture uptake of air parcels within the boundary layer. Finally,

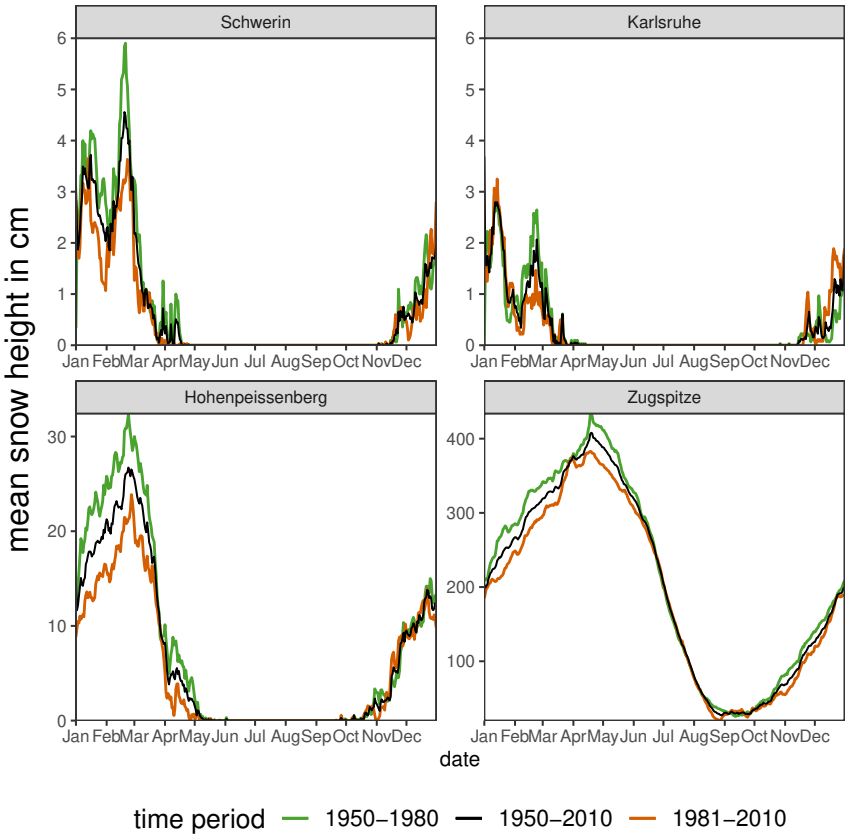

FIGURE 5.4: Seasonal cycle of observed snow cover in Schwerin, Karlsruhe, Hohenpeißenberg, and Zugspitze (meta-data see Table 5.1) during selected years. Note the different y-axis.

TABLE 5.1: Selected climate stations with meta-data. Information provided by DWD, the national weather service in Germany.

Station	station ID	measurement period	altitude (m)	latitude (°)	longitude (°)
Schwerin	04625	since 01.01.1890	59	53.64	11.39
Karlsruhe	02522	01.01.1876 – 31.10.2008	112	49.04	8.36
Hohenpeißenberg	02290	since 01.01.1876	977	47.80	11.01
Zugspitze	05792	since 01.08.1900	2964	47.42	10.98

the total event moisture uptake was weighted by the total event precipitation at the trajectory start points.

5.3 Synoptic-scale atmospheric conditions

In the following, we examine the hydro-meteorological conditions during the most intense trans-basin flood events listed in Table 4.1. Figure 5.4 shows the mean seasonal cycle of snow cover at selected climate stations (Table 5.1). For widespread rain-on-snow floods, snow cover not only at higher altitudes but also at lower levels are an important ingredient. The snow cover increases with the station altitude. In the Alps (i.e., Zugspitze), the largest snow melt occurs during summer. At lower altitude levels the snow cover decreases already in March and April. Thus, even though, the summer time snow melt in the Alps can increase the river discharges

of summer floods, Germany-wide rain-on-snow floods occur predominantly from January to March.

Figure 5.5, 5.6, and 5.7 illustrate the typical temporal evolution of selected hydrometeorological variables during trans-basin floods in March 1942, January/February 1995, and January 2003 based on (a) climate station data and (b) our dynamically downscaled reanalysis data. All widespread floods in Table 4.1 occurred during winter, thus the Figures 5.5, 5.6, and 5.7 include the snow cover at different altitude ranges. We excluded the altitudes above 1000 m. These usually have larger snow heights and would dominate the figure, even though they do not represent large areas in Germany. Since we focus only on floods affecting the majority of all macro-scale river catchments, we calculated spatial medians of all climate stations or simulation grid-points within the German administrative boundaries. The median is less affected by locally high values (e.g., of total precipitation) than the mean, and thus more representative for the entire domain and widespread events. Even though floods in Germany are also partly affected by upstream rainfall and snowmelt beyond the administrative boundaries, we only included German weather stations due to data availability. For consistency reasons, we also limited the analysis of our downscaled reanalysis data to the same domain, although a larger extend was available.

The trans-basin floods in 1942 and 1995 were caused by rainfall during snowmelt. Two up to three weeks prior to the first flood peak, the observations (Figure 5.5a, 5.6a) show a large snow cover at all altitude levels and a minimum temperature below the freezing point. With increasing temperatures and the melting of the snow, not only at lower altitudes but also in the mountainous regions, surface runoff was created. In addition, rainfall over several days caused then widespread flooding. For example, the rainfall from the 4 to the 7 March 1942 lead to a minor flood peak at Cologne (green line, Figure 5.5) on the 9 and 10 March. The half-yearly maximum discharge of 2680 m^3s^{-1} was reached on the 23 March 1942 after ongoing snowmelt and rainfall around the 19 March. In January 1995, the snow cover was smaller than in February 1942. On the contrary, the flood-triggering rainfall during the 18 January until 30 January 1995 was larger compared to 1942. The dynamically downscaled reanalysis data (Figure 5.5b, 5.6b) underestimated the snow cover. Some differences were caused by using all available model grid points within Germany (Figure 5.5b) compared to individual climate stations (Figure 5.5a). Nonetheless, the overall temporal evolution of the meteorological variables agree.

We analysed the remaining trans-basin floods in Table 4.1 similarly (not shown). These events were also caused by rainfall during spatially extended snowmelt, with the exception of the flood in January 2003. As illustrated in Figure 5.7, snowmelt played no role in the flood generation. By the end of the year 2002, the weather in Germany was dominated by a strong air mass boundary which caused heavy rainfall (FELL, 2003). Snowfall occurred in some areas of north-eastern Germany. The heavy rainfall during December 2002 and the beginning of 2003 was widespread. For example, on the 2 January, daily precipitation totals of 59.0 mm were measured at the climate stations in Teuschnitz (Bavaria), and 55.3 mm in Steinau-Seidenroth (Hessia). The Germany-wide median was about 15 mm. In some areas, like in Thuringia, more than twice of the climatological monthly mean precipitation was reported during December 2002 (SCHNEIDER et al., 2003). On the 4 January 2003, the median minimum temperature dropped and stayed around -10°C during the following days.

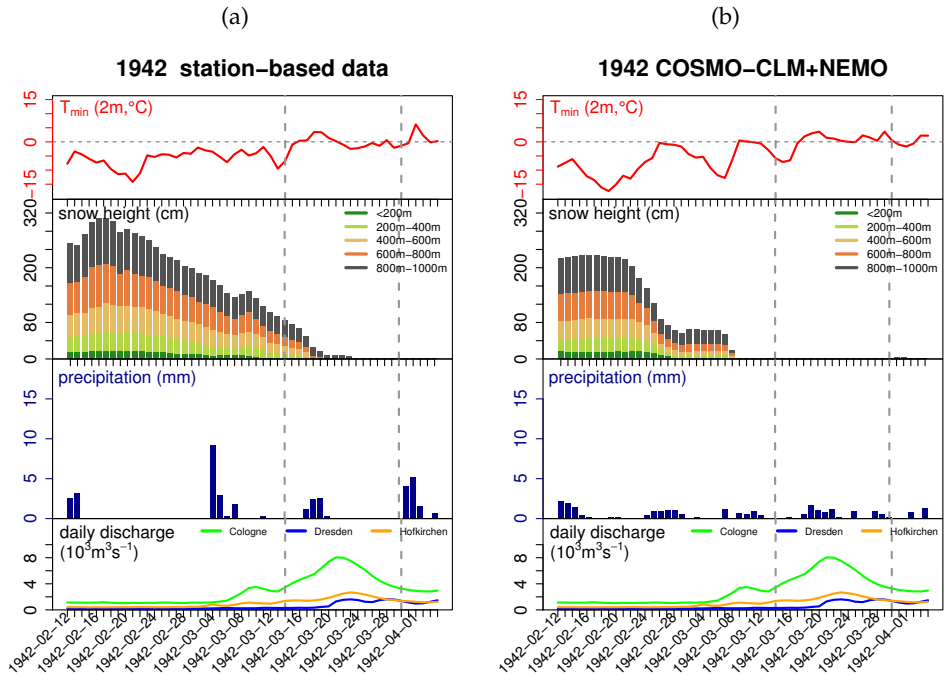

FIGURE 5.5: Temporal evolution of the trans-basin flood in March 1942 based on (a) station-based measurements and (b) with COSMO-CLM+NEMO dynamically downscaled ERA-20C reanalysis data. The first three panels show the median 2 m minimum temperature, the median snow-heights at different altitude ranges, and the median total precipitation respectively. The fourth panel in (a) and (b) shows the daily discharges at measurement sites in Cologne (Rhine), Dresden (Elbe), and Hofkirchen (Danube). The grey dashed lines mark the flood event.

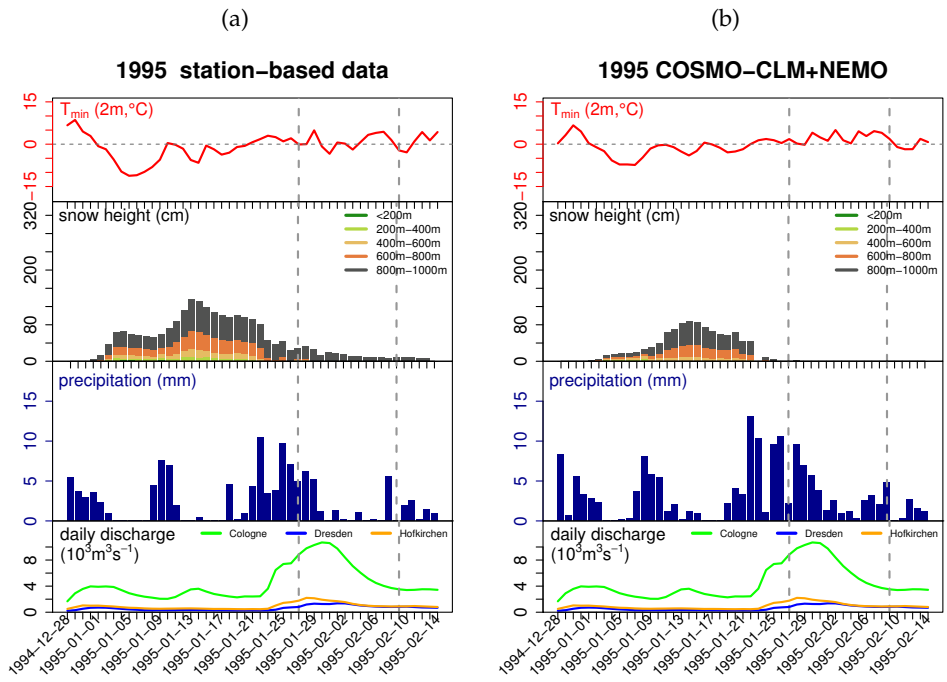

FIGURE 5.6: Same as Figure 5.5 but for the trans-basin flood during January and February 1995.

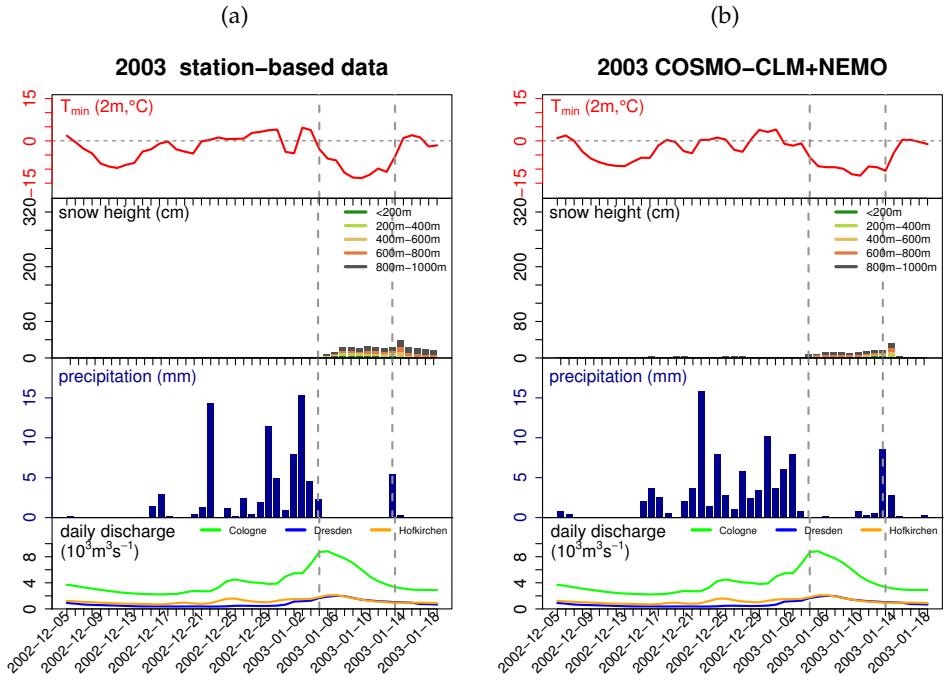

FIGURE 5.7: Same as Figure 5.5 but for the trans-basin flood in January 2003.

Thus, the precipitation fell as snow and the river discharges decreased. The timing of the rainfall, as well as the weather change to cold temperatures and snowfall were well represented in the dynamically downscaled reanalysis data.

Wintertime snowfall and rainfall in Central Europe is often associated with extratropical cyclones. Therefore, we tracked the cyclones during the trans-basin floods to get an overview of the synoptic-scale weather conditions. Figure 5.9 shows the cyclone trajectories at mean sea level pressure for the floods in 1942, 1995, and 2003. We focused on the time period 30 days prior to the first detected flood peak until the day of the last flood peak (gauges listed in Table 4.1) and selected all cyclone tracks which stayed at least 18 h in the region of interest (black rectangle).

During January 1995 and February 1942, several cyclones propagated from the North Atlantic over the North Sea and Baltic Sea. Therefore, Central Europe was influenced by moist and relatively warm maritime air masses. This cyclone pathway usually causes above than average precipitation in Germany, especially in the western regions (cf. "ATL" track type in HOFSTÄTTER et al., 2016). For example, the cyclone starting over Great Britain on the 18 March 1942 (Figure 5.9a, red track line) was associated with rainfall in Germany around the 20 March. The cyclone tracks starting over the North Atlantic on the 25 and 27 January 1995 caused rainfall during the end of January (Figure 5.9b).

Besides this northern cyclone path, several cyclones propagated over the Iberian Peninsula to the Adriatic Sea and then northwards during 1942. This southern cyclone path was associated with a blocking high pressure over north-eastern Europe around the 20 January 1942. During the 11.02.1942 and 12.02.1942, we detected a so-called Vb-cyclone propagating from the Sea of Sicily towards Central Europe along the eastern fringe of the Alps. While the centre of Europe was dominated by cold

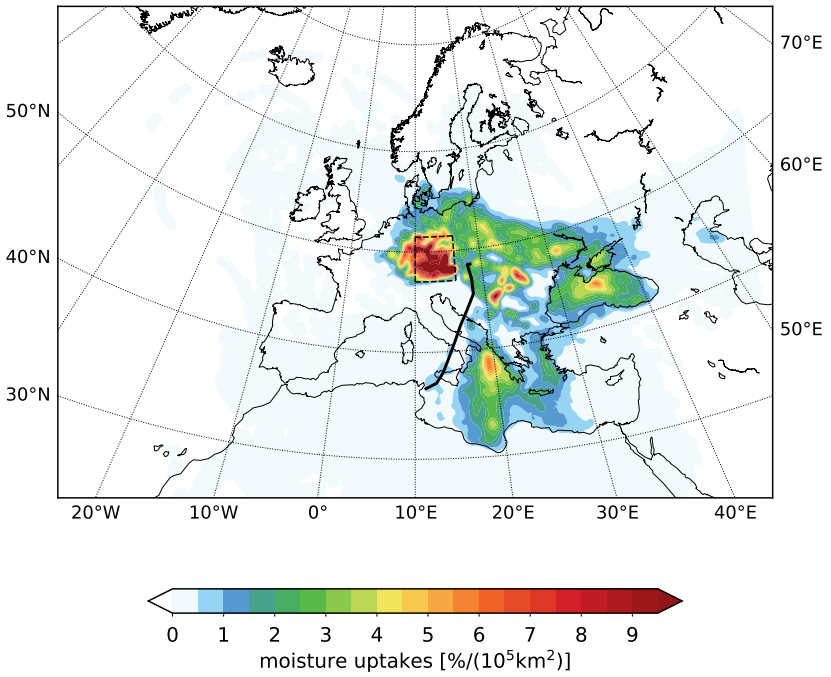

FIGURE 5.8: Moisture uptake within the boundary layer from 11.02.1942 00UTC to 12.02.1942 23UTC. The black line shows the corresponding Vb-cyclone track from 11.02.1942 00UTC to 12.02.1942 09UTC.

air, moist air masses from the Mediterranean were pushed northwards by the Vb-cyclone and caused heavy snowfall in Germany. Figure 5.8 shows the corresponding moisture uptake over the eastern basin of the Mediterranean Sea. Other moisture source regions were the European continent along the cyclone pathway and the Black Sea.

In December 2002 and January 2003, most cyclones propagated from the North Atlantic eastwards over the North Sea and southeastwards over Central Europe. Thus, Germany was dominated by moist and warm air-masses causing rainfall from the 16 December to the 4 January 2003. After the 4th of January, Central Europe was influenced by a short-wave upper-level trough and the temperature dropped. Along the trough, a cyclone propagated over France southwards to the Mediterranean Sea (orange, track end date 06 January). In parallel, a cyclone from Scandinavia moved southward to Germany (red track line, track end date 06 January). While Central Europe was influenced by polar air masses, both cyclones transported moist air to Central Europe (cf. appendix C, Figure C.2) and caused snowfall there.

5.4 The temporal flood variability during the 20th century

In the previous section, we described the atmospheric circumstances of trans-basin floods in Germany at an event and synoptic scale. On the contrary, this section focuses on the temporal flood clustering and investigates potential atmospheric and climate drivers for the period from 1900 to 2010. In the following, we analyse the most frequent trans-basin flood type in Germany, the rain-on-snow events. Firstly,

(a)

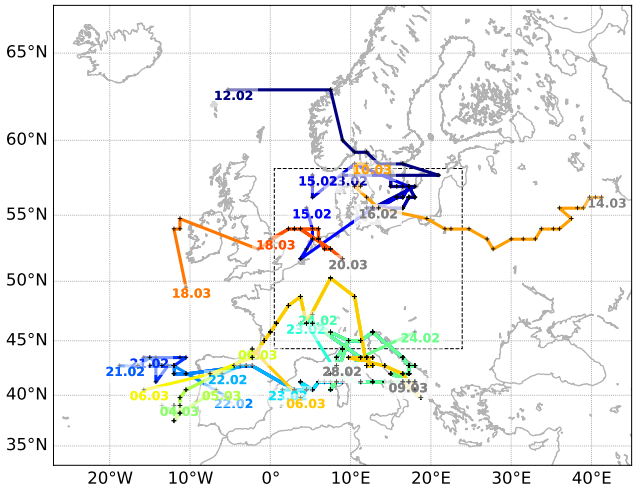

(b)

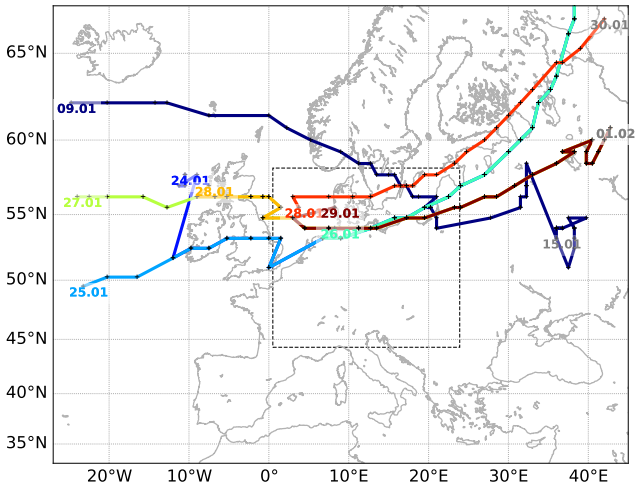

(c)

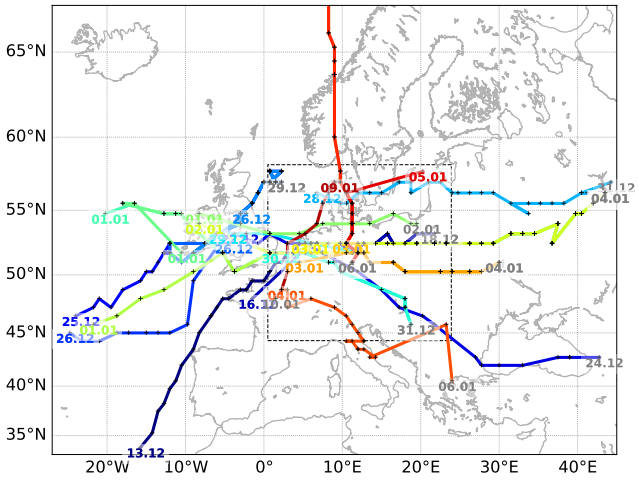

FIGURE 5.9: Cyclone tracks associated with (a) the March 1942, (b) January/February 1995, and (c) January 2003 floods. We focused on the time period 30 days prior to the first detected flood peak until the day of the last flood peak. Only cyclone tracks which stayed at least 18 h in the region of interest (black rectangle) were selected.

we examine the frequency of rainfall and snowmelt coincidence during the past century. Secondly, we analyse atmospheric teleconnection patterns, like the North Atlantic Oscillation (NAO), as a potential climate driver.

5.4.1 Coincidence of snowmelt and rainfall

We defined an atmospheric proxy for floods (AP) to analyse the temporal variability of snowmelt and simultaneous rainfall based on station measurements and our dynamically downscaled ERA-20C reanalysis data (see equation 5.2.1). As shown in section 5.3 (Figures 5.5 and 5.6), the snow height usually decreased about two weeks prior to the first flood peak. However, part of this snow height decrease was caused by an increase in snow density within the aging process of snow. Thus, we did not distinguish between fresh snow (low density) and old snow (higher density). Furthermore, snowmelt usually causes first increasing snow density and then surface runoff. Therefore, analysing snow heights instead of snow water equivalent introduced a bias. We partly compensated this bias by using a longer time period, i.e., $M = 14$ days, because then we also summed up over snow height decreases due to density increases. For rainfall, we used a 5-day period to calculate rainfall sums (i.e., $N = 4$), since the rainfall usually occurred several days in advance of the flood peaks (section 5.3).

Small changes of M (e.g., 13 or 15) and N (e.g., 3 or 5) did not alter the detected events significantly. Only the ranking changed slightly. If $M = 14$ was kept constant and $N >> 4$, e.g., $N = 14$, still widespread flood events were detected. In contrast to our selection, predominantly events with several consecutive heavy rainfall events were then determined. Examples of such events were the floods during January 1948, March 1988, or January/February 1995. If N was smaller than our selected 4 days, mainly events with heavy rainfall during only one or two days were detected. In cases of relatively small snow cover, rainfall during such a short period was not enough to cause extreme Germany-wide flooding, even if the rainfall occurred widespread. For example, if $N = 1$, also the rainfall on the 24th March 1986 was detected (among the 25 highest ranked dates) besides the trans-basin flood in March 1988 flood or the flood in the Rhine river in January 1982. If $N = 4 = \text{const.}$ and $M >> 14$, the detected snowmelt event and rainfall event may not be synchronized anymore. However, our focus lies on rain-on-snow events only. Conversely, if $M << 14$, also events with antedecent snow cover during just a few days were found. Such short-term snow cover has often smaller snow heights, and thus less water storage, and is further more localized. Thus, more regional and less extreme flood events were determined. For example, the flood in the Rhine river catchment during December 1967, or in the Elbe river catchment during January 1987 were among the 25 highest ranked dates with $N = 4$ and $M = 3$.

Figure 5.10 includes only the dates of the 50 largest AP values ($M = 14$, $N = 4$) to verify whether our atmospheric flood proxy is suitable for estimating extreme flood conditions. We used as reference the trans-basin floods in Table 4.1 and the most severe flood events published in UHLEMANN et al. (2010). Some events were detected with using snow heights at the altitude range 800 m – 1000 m but correspond to no flood event. One example was February 1966. During these days the snow was already gone below 800 m and snow mainly at higher altitudes melted. Therefore, the Germany-wide amount of melted snow water is smaller and more localized

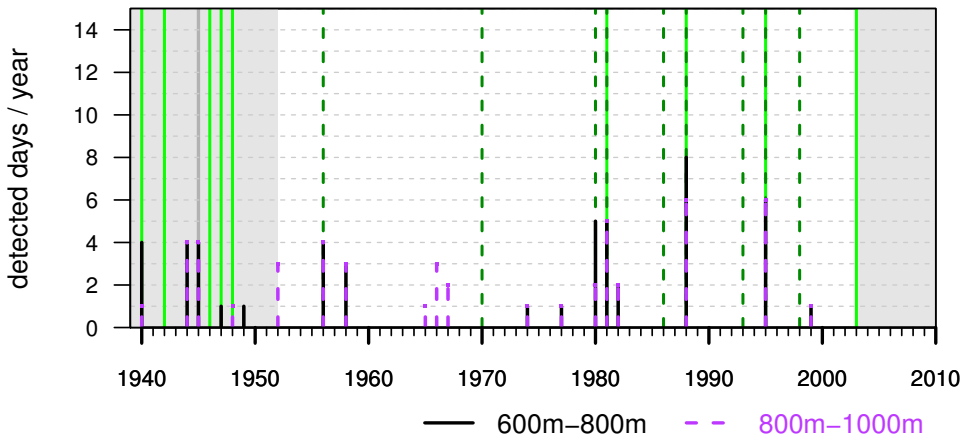

FIGURE 5.10: The lightgreen bars mark the flood events in Table 4.1, and darkgreen dashed lines show the ten highest ranked events in UHLEMANN et al. (2010). The black and magenta lines display the 50 days with highest rank of our atmospheric proxy based on snow heights at 600 m–1000 m. The time-periods not available for the hydrological flood detection of UHLEMANN et al. (2010) are grey-shaded.

to mountainous areas. Thus, no trans-basins floods were to be expected. Nonetheless, using snow heights from 600 m – 800 m or from 800 m to 1000 m gave similar results. Note, we did not expect to detect the flood events during 2003 and October-November 1998 (green dashed lines in Figure 5.10; UHLEMANN et al., 2010) with our atmospheric proxy. These events were caused by heavy rainfall only, and snowmelt was not involved in the flood-causing processes.

Since the Figure 5.10 has only a yearly resolution, it remains to be determined whether we detected Germany-wide flood events with our atmospheric proxy or other dates within the same year. Therefore, Table 5.2 lists the top 50 days detected by our atmospheric proxy *AP* considering snow-heights at 600 m – 800 m. All events, which correspond to flood events detected by our distribution-free classification or belong to the top 25 trans-basin flood events of UHLEMANN et al. (2010), are denoted by black letters. Overall, the detected dates of our atmospheric proxy match the flood events well, especially after the 1950s, when the number of climate stations increased significantly. The more consecutive days were detected with our atmospheric proxy, the intenser was the coincidence of snowmelt and rainfall and thus the potential of flooding. During 1988, the highest number of days was detected within the 50-highest ranked *AP* dates. These dates correspond to the trans-basin flood in March 1988. This is consistent with UHLEMANN et al. (2010) and GVOŽDÍKOVÁ and MÜLLER (2017). They also classified this event as the most widespread and intense winter flood during 1951–2013.

However, our atmospheric proxy also detected four flood events, which do not correspond to trans-basin floods (Table 5.2, grey letters). Although the snowmelt and rainfall during November 1944 caused flooding (e. g. at the Upper Rhine), the peak discharges were lower than the half-yearly maximum peaks. The events in February 1945 and March 1949 correspond to flooding based on half-yearly annual maxima, however, the peak discharges were too low to be classified as Germany-wide flood, especially in the Elbe river in 1945. Furthermore, 1945 was excluded in our trans-basin flood classification due to large gaps in the river-runoff data during this year.

TABLE 5.2: Dates of the detected 50 days with highest ranks of our atmospheric proxy. These events are shown in Figure 5.10 with black bars (snow heights at 600 m – 800 m, January 1940 – December 2010). Events which do not correspond to trans-basin flood events are written in grey colour.

19.03.1940 – 22.03.1940	03.03.1956–06.03.1956	05.01.1982–06.01.1982
24.11.1944–27.11.1944	08.02.1958–10.02.1958	15.03.1988–17.03.1988
12.02.1945–15.02.1945	29.12.1974	24.03.1988–29.03.1988
14.03.1947	03.02.1980–07.02.1980	25.01.1995–30.01.1995
17.03.1949	10.03.1981–14.03.1981	05.03.1999

The February 1958 event was associated with half-yearly maximum flood peaks, for example, in Cochem (Mosel) and Dresden (Elbe). Flooding in entire Germany occurred during the end of February and early March, but higher intensities (medium flood and larger) were reached only in the Rhine catchment. Note, UHLEMANN et al. (2010) listed this event as a trans-basin flood with rank 34.

In contrast to the station-based observations, the dynamically downscaled ERA-20C reanalysis data covered the complete 20th century, even though the ERA-20C reanalysis also relied on fewer observations in the early decades (POLI et al., 2016). Figure 5.11 shows the 120-highest ranked AP days in the observation data and corresponding dates in our dynamically downscaled ERA-20C reanalysis data (COSMO-CLM+NEMO). For calculating the atmospheric proxy, we focused only on snow heights at the altitude range from 600 m to 800 m. In contrast to Figure 5.10, we included also lower ranked floods of UHLEMANN et al. (2010) because Figure 5.11 displays a higher number of AP dates. The hydrological trans-basin flood classifications and the atmospheric proxy show an alternating succession of flood-rich periods, like the 1940s and 1980s, and flood-poor periods, for example, during the mid-1920s to the late-1930s. In Figure 5.10, which shows only the most severe dates, the clustering is less obvious during the 1980s.

Some events were only detected with the downscaled reanalysis data. For example, the events during December 1955, March 1979, February 2000, February 2005, December 2017, and January 2010. Of these events, only December 1955 and January 2010 were false alarms. The other events correspond to Germany-wide floods based on half-yearly discharges, however with weaker intensities as our selected thresholds (section 4.1, Table 4.1). Thus, our simulated snowmelt and rainfall were more intense compared to observations, but the temporal match was very good. The most intense event before 1920 was detected during February 1911 with eight consecutive AP dates and corresponded to flooding in the Rhine and Danube river (GRDC data). Unfortunately, we did not detect the well-known flooding in Central Europe during February 1909 due to underestimated snowcover during January 1909 in our downscaled reanalysis data. Overall, flood-poor and flood-rich decades alternated but no trend in flood frequency is obvious.

With a false alarm rate of, for example, 4 out of 15 (see Table 5.2), our atmospheric proxy based on snow height and rainfall measurements is indeed a suitable proxy for the coincidence of widespread snowmelt and rainfall (i.e., trans-basin flood-favouring atmospheric conditions). Even though we only focused on atmospheric parameters and did not include catchment conditions, trans-basin floods were detected. This may have the following reasons. Firstly, the larger the spatial extent of floods, the less pronounced is the influence of local catchment conditions. Secondly,

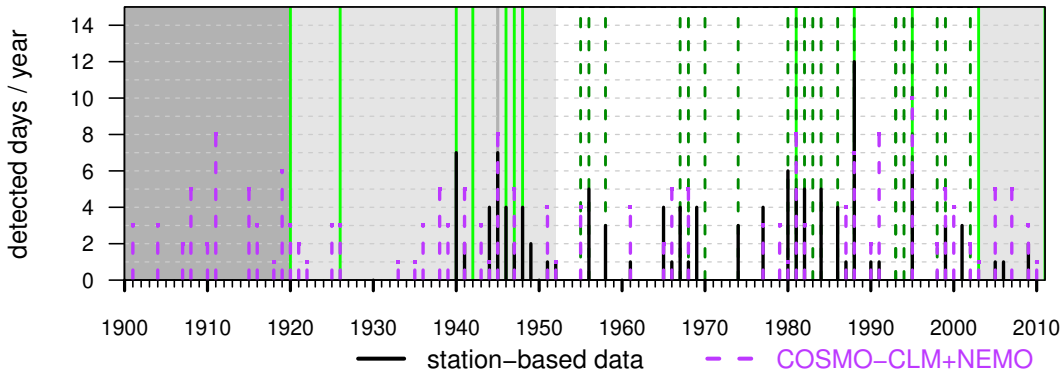

FIGURE 5.11: Lightgreen bars mark the flood events in Table 4.1. Darkgreen dashed lines mark the winter floods which are among the 25 most severe trans-basin floods in UHLEMANN et al. (2010). Black lines show the number of detected 120 days with highest rank of our atmospheric proxy, based on station measurements (snow height at 600 m-800 m). The magenta lines show the corresponding results based on our downscaled reanalysis. The time-periods which were excluded from the hydrological flood classification are grey-shaded.

the groundwater is usually refilled during mid- and late winter. But still, the saturation of the affected subcatchments influences the severity and spatial extent of floods. Therefore, information about soil moisture, for example, in terms of antedecent precipitation (FROIDEVAUX et al., 2015), might help to reduce the false alarm of our atmospheric proxy (Table 2, grey letters).

5.4.2 Atmospheric teleconnection patterns

The temporal flood variability covaried with the coincidence of widespread snowmelt and rainfall. The question remains whether this coincidence was by chance or modulated by an external driver like atmospheric teleconnection patterns. If climate drivers exist, they can be used as predictors for future decadal flood variability.

For analysing the long-term variability during the past century, the station-based measurements require a good temporal coverage. Hence, we selected climate stations which had more than 80% days with observations during each half of the past century. Most selected stations were located below 271 m altitude. Only five stations covered higher altitudes, ranging from 386 m to 2964 m above mean sea level. We did not combine snow measurements at low altitudes and mountainous or Alpine stations because the mean snow heights increase significantly with the altitude of the measurement station. Thus, in the following, we focused only on the station-based measurements at lower altitude levels, listed in Table 5.3, even though the snowmelt up to higher altitude levels was essential for the flooding (see section 5.3). We applied a threshold of 1 cm snow height to avoid artificially high correlation coefficients due to many zeros in our time series. Furthermore, 0 cm of snow height were recorded as missing values at two stations in western Germany (Karlsruhe and Kaiserslautern) until the late 1930s.

TABLE 5.3: Selected climate stations with meta-data. Information provided by DWD, the national weather service in Germany.

Station	station ID	measurement period	altitude (m)	latitude (°)	longitude (°)
Bremen	00691	since 01.01.1890	4	53.0450	8.7979
Wrixum/Foehr	05732	01.07.1887 – 30.06.2003	8	54.6928	8.5271
Schwerin	04625	since 01.01.1890	59	53.6425	11.3872
Cottbus	00880	since 01.01.1887	69	51.7760	14.3168
Magdeburg	03126	since 01.01.1881	76	52.1029	11.5827
Potsdam	03987	since 01.01.1893	81	52.3813	13.0622
Marnitz	03196	since 01.01.1902	81	53.3223	11.9319
Karlsruhe	02522	01.01.1876 – 31.10.2008	112	49.0382	8.3641
Jena	02444	since 01.01.1824	155	50.9251	11.5830
Kaiserslautern	02486	since 01.01.1901	271	49.4262	7.7557

Figure 5.12 displays the temporal variability of the median snow height, the median 2 m-minimum temperature anomaly, the NAO, the EA, and SCA index, during January, when we found highest correlations. In January, the Spearman's rank correlation coefficient ρ (SPEARMAN, 1904) was about -0.56 ($p < 0.01$) for monthly median snow heights and the monthly mean NAO index from 1901 to 2010. For monthly median temperature and NAO, the rank correlation coefficient ρ was about 0.61 ($p < 0.01$). The SCA index was correlated with temperature (-0.55, $p < 0.01$) and total precipitation (-0.69, $p < 0.01$) which agrees with COMAS-BRU and MCDERMOTT (2014), Figure 3. Other combinations were not significant.

Figure 5.13 shows the dependence of snow heights on the NAO index not only for the monthly medians (blue bars in Figure 5.12, black circles in Figure 5.13) but also the selected climate stations. The snow height measurements at different locations vary a lot, especially for small and negative NAO-Indices. The observed snow heights were small during both NAO phases, with the positive phase (Figure 5.13, purple histogram bars) prevailing. Snow heights smaller than 10 cm occurred predominantly during the positive phase when the westerly winds are usually intensified. This leads to mild winters in Northern and Central Europe (see e.g., HURRELL, 1995).

On the contrary, large snow heights occurred less often but primarily during the negative NAO phase (blue bars, Figure 5.13, histogram at the right margin). During the negative NAO phase, a positive pressure anomaly over Iceland and a negative anomaly over the Azores weakens the westerly flow which is associated with blocking highs over central and north-eastern Europe. Thus, temperature drops and the cyclone tracks are shifted to the south (see e.g., HURRELL, 1995). The large snow heights during the negative NAO phase (Figure 5.13) are in agreement with COHEN et al. (2015). In addition, BEDNORZ (2008) analysed the synoptic circumstances causing heavy snowfalls in the Polish–German lowlands. The average geopotential height fields of all days with a snowcover increase of more than 5 cm show a strong positive anomaly over Scandinavia and negative anomalies over the Azores. This spatial pattern is similar to the negative NAO phase. Furthermore, they distinguished three circulation patterns associated with this NAO-like atmospheric condition: a low-pressure system centred over the Baltic Sea, a cyclone centred over the Adriatic and the Ionic Sea, and a cyclone located between the previous two ones. The cyclone centre over the Mediterranean Sea corresponds to our southern cyclone path which was associated with snowfall, for example, at the beginning of January 2003 (Figure 5.9c, orange track line) with a NAO index value of -0.99 in December

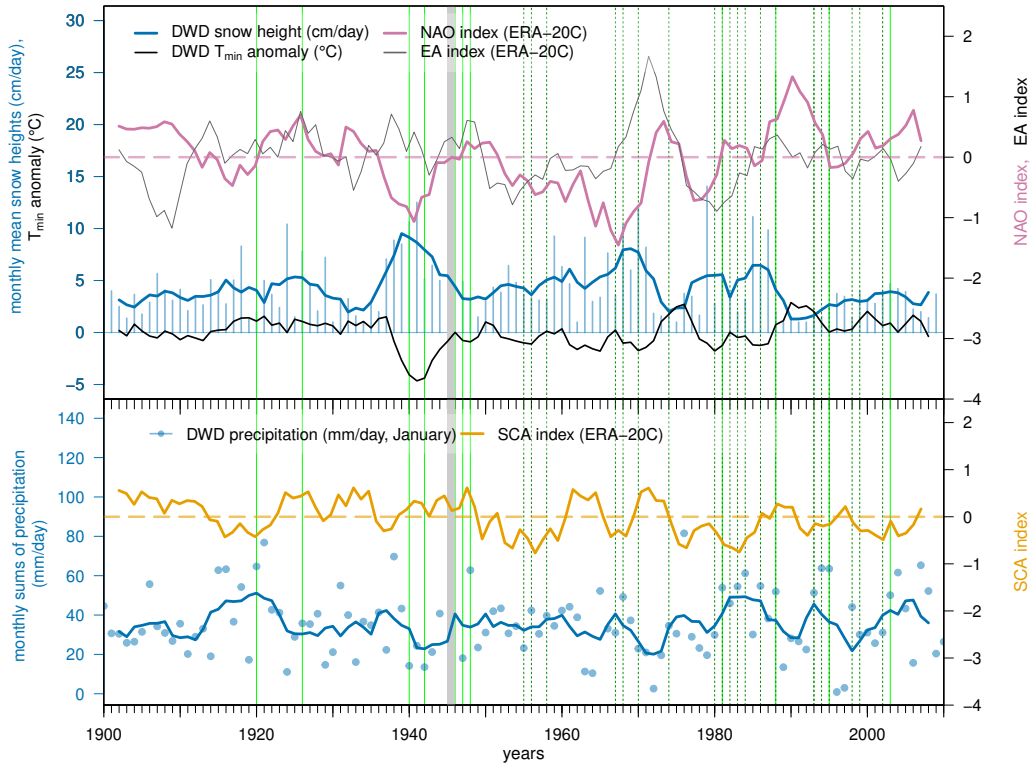

FIGURE 5.12: Monthly mean interannual variability of observed snow height and precipitation (median of selected stations) during January (blue bars and circles). The five-year moving averages of the observed snow height (blue), precipitation (blue), minimum temperature anomaly (black), NAO index (purple), EA index (grey), and SCA index (orange) are added with lines. The vertical grey bar shows the excluded period due to large data gaps (1 December 1944 – 31 December 1946). The trans-basin floods are marked with green bars like in Figure 5.11.

2002 and -0.07 in January 2003. Another example was the southward shifted cyclone path in 1942 during a negative NAO phase with an index value of -0.84. Overall, the NAO phase was less often negative than positive during the past century (Figure 5.14, upper histogram).

As expected, the median snow heights were large during the negative NAO phases around 1940 and from 1960 to the end of 1970 (Figure 5.12). However, the snow heights and temperature anomalies in the early 1960s were smaller and not associated with widespread flooding, even though the negative NAO phase was comparable to the NAO index in the 1940s. In general, the teleconnection patterns of the NAO are not stationary but affected by the East Atlantic pattern (EA) and the Scandinavian pattern (SCA) (MOORE et al., 2013; COMAS-BRU and MCDERMOTT, 2014). For southern UK, COMAS-BRU and MCDERMOTT (2014) detected drier conditions during positive NAO and EA, and wetter conditions during positive NAO and negative EA. However, the snow heights in Germany did not depend on specific EA or SCA phases and the contingency table of the EA and SCA phases reveals similar joint probabilities (Figure 5.13). Thus, a modulation of the NAO did not explain the lower snow cover in the early 1960s in spite of the pronounced negative NAO phase. Moreover, several trans-basin floods occurred in the 1980s, even though the NAO phase was weakly positive.

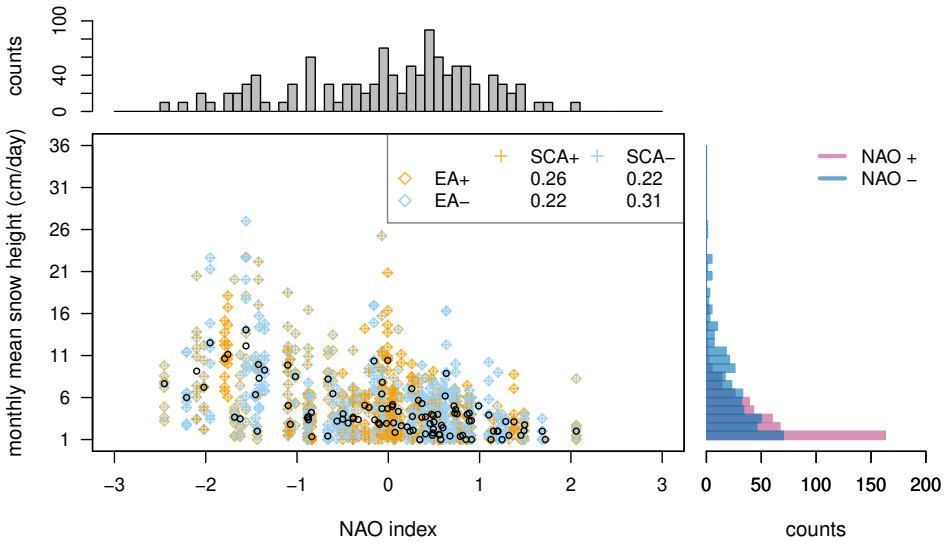

FIGURE 5.13: Scatter plot of the NAO index and January mean snow heights of the selected climate stations (Table 5.3). The plus signs and rhombi indicate EA and SCA phases respectively (see also the contingency table). The black circles show the median of all selected climate stations and correspond to the blue bars in Figure 5.12 (upper column). The marginal barplots show the histogram of the NAO index values (upper barplot) and the histogram of the January mean snow heights (barplot on the right side). The snow heights are divided into positive (purple) and negative NAO phase.

For detecting potential causes of the flood-poor period in the early 1960s or the flood clustering in the 1980s, also total precipitation has to be considered besides the snow cover. For example, the rainiest months often correspond to the month in which the trans-basin floods, listed in Table 4.1, occurred, like in March 1940 and 1988, February 1946, January 1948 and 1995 (lower panel of Figure 5.14). The SCA index was significantly inverse correlated with total precipitation (Figure 5.12). During the negative SCA phase, a low pressure system is located over Scandinavia which usually enhances the Atlantic cyclone track in Northern and Central Europe (BUEH and NAKAMURA, 2007). This northern cyclone path and associated precipitation triggered, for example, flooding in January/February 1995 during a SCA index of -1.15/-2.09 (see section 5.3). Therefore, Figure 5.14 shows a combined NAO+SCA index, i.e., 0.5·(NAO+SCA). We extended our analysis with the dynamically downscaled reanalysis data to the altitude range from 600 m to 800 m for snow heights, since especially snowmelt in mountainous areas was related to the trans-basin flood events.

The negative phase of the combined NAO+SCA index corresponds well to flood-rich periods, for example, during the early 1940s, late 1950s, late 1960s, and 1980s. On the contrary, the NAO+SCA phase was positive during the trans-basin floods in the late 1940s or in December 1974/January 1975. Nonetheless, the combined NAO+SCA index covaries better with the trans-basin flood variability than only NAO index, especially in 1920, the early 1960s (flood-poor period), and the 1980s. This corresponds to the fact that not only widespread snow cover (correlated with the NAO) is relevant for trans-basin floods but also the flood triggering total precipitation (correlated to the SCA).

Besides atmospheric teleconnection patterns, also increasing winter temperatures in recent decades (Figure 5.12, e.g., KREYLING and HENRY, 2011; FONTRODONA BACH

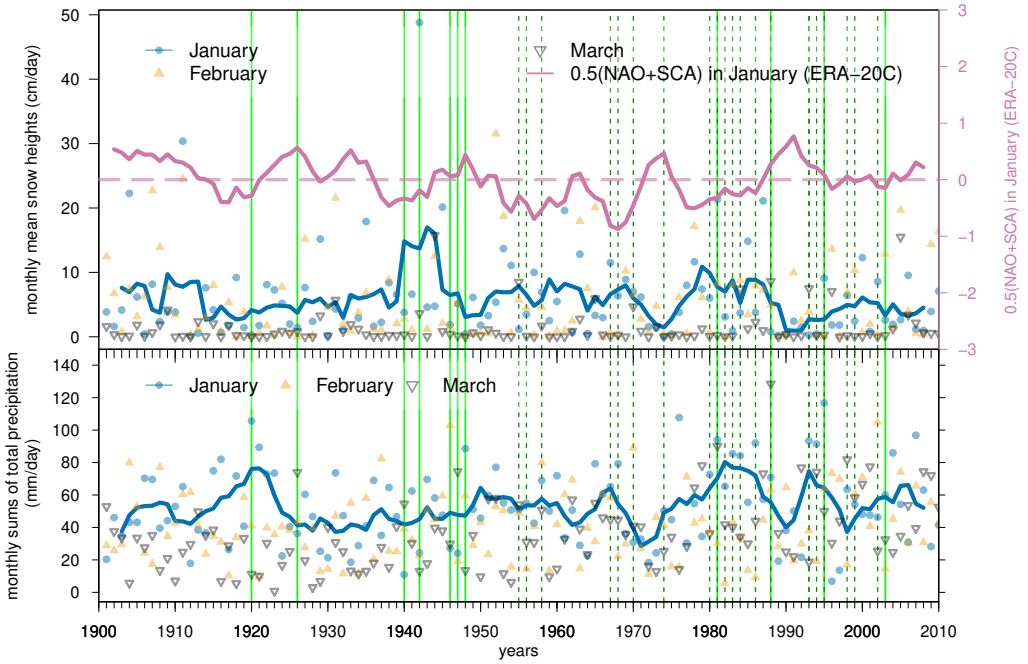

FIGURE 5.14: Monthly means of the median snow height (cm/day) at 600 m–800 m and monthly sums of median total precipitation (mm/day) in our downscaled reanalysis for January, February, and March, respectively. The combined NAO+SCA index in January is added in purple. All coloured lines display the respective five-year centred moving averages. The trans-basin floods are marked with green bars like in Figure 5.11 and Figure 5.12.

et al., 2018) affect the temporal variability of trans-basin floods in Germany. Since the 1940s, a decreasing tendency of widespread snow cover is obvious in station-based data (Figure 5.12, stations below 271 m altitude) and our simulation data (Figure 5.14, 600 m–800 m). Thus, the snow cover at lower and medium altitude ranges vanishes in recent decades earlier compared, for example, to the years from 1950 to 1980 (Figure 5.4). This is in line with earlier floods in north-eastern Europe since 1960 (BLÖSCHL et al., 2017) or observed decreasing trends in rain-on-snow events in lower elevation regions of the United States (MCCABE et al., 2007). Consequently, trans-basin winter floods may occur less often in future, especially in late spring. On the contrary, the coincidence of heavy rainfall and snowmelt may occur more often if the trend of increasing wintertime precipitation (Figure 5.14, March) and associated wet circulation patterns is ongoing (e.g., CASPARY, 1995; PETROW et al., 2009). Nonetheless, precipitation and snow cover had a large year-to-year variability during the 20th century and we detected no significant seasonal shift of the rainfall and snowmelt coincidence since the aforementioned processes have competing effects on widespread rain-on-snow floods. Thus, it remains unknown whether the increasing winter temperatures will cause fewer widespread winter floods in the future decades.

5.5 Conclusions

Motivated by previous studies of trans-basin floods in Central Europe (UHLEMANN et al., 2010; GVOŽDÍKOVÁ and MÜLLER, 2017; SCHRÖTER et al., 2015), we presented

the atmospheric conditions of such events and extended the previously analysed time period by about three decades. Therefore, we classified floods affecting the majority of all macro-scale catchments in Germany by a distribution-free ordinal classification (FISCHER and SCHUMANN, 2018) based on GRDC-data since 1920. Station-based observations (Climate Data Center, version v005 (2017), DWD) were used to investigate the atmospheric flood conditions. However, these measurements have large data gaps during the early decades of the past century. Hence, we extended our analysis to the period from 1901 to 2010 by dynamically downscaling ERA-20C reanalysis data. For this, we used the regional climate model COSMO-CLM (ROCKEL et al., 2008), which was interactively coupled with the regional ocean model NEMO (MADEC and THE NEMO TEAM, 2016). In the following, we answer the research questions of our study (see introduction in section 5.1):

1. The detected trans-basin floods (Table 4.1) were mainly driven by rainfall during widespread snowmelt (so-called rain-on-snow floods). The only exception was the event in January 2003 which was caused solely by spatially extended rainfall over several days (Figure 5.7). Heavy snowfall preceding the flood events was often associated with a cyclone pathway over the Iberian Peninsula/Mediterranean Sea northeastward. This cyclone pathway especially causes heavy snowfall over Central Europe if the continent is dominated by cold air masses and then moisture from the Mediterranean Sea is transported northward along the cyclone path. Other cyclones associated with the flood events followed a northern pathway starting over the North Atlantic. This cyclone type is usually associated with above average precipitation amounts, especially in western Germany (HOFSTÄTTER et al., 2016).

2. The observed temporal variability was largely explained by the coincidence of rainfall and snowmelt (at 600 m–800 m altitude), which we detected by calculating an atmospheric proxy for rain-on-snow floods (AP). The highest ranked dates of our atmospheric proxy agreed well with the widespread winter floods in Germany (UHLEMANN et al., 2010; GVOŽDÍKOVÁ and MÜLLER, 2017; FISCHER and SCHUMANN, 2018). Furthermore, the flood-rich (flood-poor) periods were partly explained by the negative (positive) phase of a combined North Atlantic Oscillation and Scandinavian pattern index (0.5(NAO+SCA), see Figure 5.14). During the negative NAO phase, the cyclone trajectories are usually shifted southwards with track points over the Mediterranean Sea which can cause heavy snowfall over Central Europe (e.g., February 1942 or January 2003; Spearman's rank correlation coefficient $\rho = -0.56$ ($p < 0.01$) for NAO index and median snow heights in January). Especially, the high snow cover during a negative NAO phase in the late 1930s, the 1940s, and late 1960s matched the higher frequency of trans-basin winter floods during that time. In addition, winter precipitation over Central Europe was inverse correlated with the SCA index ($\rho = -0.69$, $p < 0.01$ in January). During the negative SCA phase usually the Atlantic storm tracks are intensified (BUEH and NAKAMURA, 2007). On the contrary, some trans-basin floods occurred during a positive phase of the NAO and SCA index, for example, in January 1926 or January 1948.

Our results show that rainfall during snowmelt is an important driver of trans-basin floods in Germany. The temporal variability of such widespread floods corresponds to the coincidence of rain and snowmelt, as well as the negative NAO and SCA

phase. However, it remains still unknown, whether the ongoing trend of increasing winter temperature (e.g., DONAT et al., 2013; FONTRODONA BACH et al., 2018) will reduce the number of widespread rain-on-snow floods, and to what extent the coincidence of rainfall and snowmelt is driven by an external climate driver. This could be studied more closely with a stochastic model of a random rainfall and snowmelt time series. The influence of external forcing on the temporal flood clustering could be then investigated by adding a common term in the stochastic model simulating the climate drivers, like increasing winter time temperatures or atmospheric teleconnection patterns. Suitable candidates for this are the NAO and SCA. In addition, other teleconnection patterns which were not analysed in this paper may contribute to the interannual flood variability and should be included in future analysis, like the Atlantic Multi-decadal Oscillation (ZAMPIERI et al., 2013), the East Atlantic/Western Russia pattern (RUST et al., 2015), or the El Niño Southern Oscillation (NOBRE et al., 2017).

Chapter 6

Lagrangian moisture source diagnostics of precipitation during Vb-cyclones

FIGURE 6.1: Mulde river overflow with a flooded bridge (centre right side of the photo) in Döbeln, Saxony. The photography was taken by Sonja Strini on the 19.08.2002

Widespread floods with high peak discharges occurred not only during the winter but also during the summer half-year. Most events were associated with so-called Vb-cyclones. Due to their meridional pathway from the Mediterranean Sea towards Central Europe, one might expect that the Mediterranean Sea is the dominant moisture source region. This chapter sheds more light on the moisture uptake related to precipitation during Vb-events and the relevance of moisture source region characteristics (such as evaporation and SSTs over the Mediterranean Sea), and answers the third research question of this thesis (What is the role of various moisture source regions, especially the Mediterranean Sea, in precipitation during Vb-cyclones?, chapter 4). Please note that the following sections are taken from the manuscript *Moisture sources of heavy precipitation in Central Europe during Vb-cyclones* by A. Krug, F. Aemisegger, M. Sprenger, and B. Ahrens, submitted to Climate Dynamics (KRUG et al., 2020a, in revision).

6.1 Vb-cyclone induced floods

River floods are the most common and devastating natural hazard in Europe. Floods differ not only according to the spatial extent, temporal duration, and peak discharges, but also in terms of the hydroclimatic and hydrological causes (TARASOVA et al., 2019). In this study, we focus on precipitation occurring in weather situations associated with so-called Vb-cyclones that can trigger widespread floods in Central Europe, especially during the summer season (e.g., BLÖSCHL et al., 2013). These extratropical cyclones are defined by their pathway from the western Mediterranean Sea north-eastward over Northern Italy along the eastern fringe of the Alps to Central Europe (VAN BEBBER, 1891). Many devastating summer floods in the Central European macro-scale catchments of the Odra, Elbe, and Danube rivers were associated with that cyclone pathway.

Even though the classification of this special cyclone pathway goes back to VAN BEBBER (1891), Vb-cyclones have been the subject of many studies especially in the past two decades. Vb-cyclones occur rarely with about 4–10 events per year on average (HOFSTÄTTER and CHIMANI, 2012; MESSMER et al., 2015; HOFSTÄTTER and BLÖSCHL, 2019). Nonetheless, they are of high relevance for extreme precipitation events and floods in Central and Eastern Europe. MESSMER et al. (2015) concluded that 15% of the extreme precipitation (99th percentile) over Central Europe and the northern Alpine region are associated with Vb-cyclones. About 45% of the Vb-cyclones are linked with heavy precipitation (95th percentile) in the Czech Republic and Eastern Austria (HOFSTÄTTER et al., 2018), and about 40% of Vb-cyclones correlate with heavy precipitation (95th percentile) in the Elbe catchment, especially during April and May (NISSEN et al., 2013). In particular, Vb-cyclones with a distinct cutoff low in upper levels are linked to heavy precipitation (MESSMER et al., 2015; HOFSTÄTTER et al., 2018; MITTERMEIER et al., 2019).

Vb-cyclones occur throughout the year with a peak frequency in spring (HOFSTÄTTER and CHIMANI, 2012; MESSMER et al., 2015). HOFSTÄTTER et al. (2016) analysed the seasonal dependence of cyclone intensity for various pathways including the Vb-type. Measures for the cyclone intensity are the minimum core pressure or the maximum relative vorticity. The median intensity of Vb-cyclone shows no distinct seasonal cycle. Vb-cyclones are among the strongest cyclones in Europe throughout

the year, also with respect to cyclone precipitation (HOFSTÄTTER et al., 2016, 2018). During winter, some Vb-cyclones cause heavy snowstorms in Central Europe. An example is the Vb-cyclone in January 2010 (NISSEN et al., 2013).

Vb-cyclones are associated with extreme and widespread floods in Central Europe mainly during the summer half-year (e.g., BLÖSCHL et al., 2013; HOFSTÄTTER et al., 2016). Closer inspection reveals that the Vb-cyclone intensity is highly variable during the summer season in terms of the relative vorticity and often surpasses the intensity of Atlantic cyclones in winter that are related to winter storms in Europe. (HOFSTÄTTER et al., 2016). During winter, the main Vb-cyclogenetic processes are the dynamic coupling between the upper-level and the low-level orographic flow (e.g., in the Alpine region), as well as low-level baroclinicity (AEBISCHER and SCHÄR, 1998; TRIGO et al., 2002; HOFSTÄTTER et al., 2016). During summer, however, an essential additional ingredient for intense Vb-events are high equivalent potential temperatures and latent heat release in lower atmospheric levels over Northern Italy on the lee-side of the Alps (AEBISCHER and SCHÄR, 1998). This is supported by the sensitivity studies of VOLOSCIUK et al. (2016) and MESSMER et al. (2017) that showed an intensification of Vb-cyclone precipitation in Central Europe with increasing sea surface temperatures (SSTs) of the Mediterranean Sea. Furthermore, higher temperatures during summer increase the total water content (HOFSTÄTTER and CHIMANI, 2012) and thus moisture transport in the atmosphere, which in turn decreases the atmospheric stability and favours upward motion and precipitation (MESSMER et al., 2017). Due to the meridionally curved cyclone path, precipitation is then initiated especially along west-east oriented central European barriers like the Alps and Ore mountains (GRAMS et al., 2014). Note that MESSMER et al. (2017) found conversely a decrease of precipitation over the north-eastern flanks of the Alps for higher SSTs over the Mediterranean. This can be explained by an increase in precipitation along the eastern Adriatic coasts and thus decreased moisture flux north-eastward of the Alps.

However, not only the Mediterranean Sea is an evaporative moisture source during Vb-events. Besides the Mediterranean Sea, also the North Atlantic and Black Sea are relevant moisture sources during the August 2002 flood (JAMES et al., 2004; SODEMANN et al., 2009; GANGOITI et al., 2011a). In addition, moisture recycling over the European continent contributed to the heavy rainfall, especially towards the end of the event (JAMES et al., 2004; GANGOITI et al., 2011b, 2015). In August 2005 (WINSCHALL, 2013), May 2010 (WINSCHALL et al., 2014), and May/June 2013 (GRAMS et al., 2014; KELEMEN et al., 2016), moisture recycling over the European continent and the North Atlantic dominated, while the Mediterranean Sea only weakly contributed to the heavy rainfall. In contrast to the 2005, 2010 and 2013 floods, the Mediterranean was a substantial moisture source in the August 2002 flood, especially in the early stages, as shown by JAMES et al. (2004) and GANGOITI et al. (2011a). Moreover, the sensitivity study of MESSMER et al. (2017) points towards the particular role of the Mediterranean Sea in contrast to other moisture sources like the North Atlantic. Thus, the role of the Mediterranean seems to be variable across events. Overall, these Vb-events reveal quite diverse moisture source regions. One reason for this might be the choice of analysed events.

In the existing scientific literature, only the above mentioned floods triggered by Vb-cyclones in recent years (2002, 2005, 2010, and 2013) have been analysed quantitatively in terms of the evaporative moisture source regions. In this study, we extended

these case studies by investigating the moisture uptake during in total 16 Vb-events from 1901 to 2010 with focus on flood-producing precipitation in the Danube, Elbe, and Odra catchment regions. The moisture source diagnostics was based on a computationally demanding Lagrangian approach. Thus, it could not be applied to all Vb-cyclones from 1901 to 2010 that we detected in our dataset ($> 10^3$ events). For all Vb-cyclones, instead, we analysed the characteristics like evaporation, SST or soil moisture content in the moisture uptake regions identified with our 16 case studies. In doing so, we could investigate how source region characteristics differ for Vb-cyclones with high or low precipitation in the selected catchment regions. More specifically, in this study, we address the following research questions:

1. What are the evaporative moisture source regions of flood-causing precipitation during Vb-cyclones?
2. Which characteristics in the moisture source regions intensify the precipitation during Vb-cyclones?

As a data basis, we used the ERA-20C reanalysis data (POLI et al., 2016) that was dynamically downscaled over Europe with a high resolution and interactively coupled regional atmosphere-ocean model (COSMO-CLM+NEMO, AKHTAR et al., 2019; KELEMEN et al., 2019; PRIMO et al., 2019). We tracked the cyclone pathways according to WERNLI and SCHWIERZ (2006) and SPRENGER et al. (2017) to identify Vb-events. The evaporative moisture source regions were quantified based on a Lagrangian analysis with Lagranto (SPRENGER and WERNLI, 2015; WERNLI and DAVIES, 1997) and a moisture source diagnostic (SODEMANN et al., 2008b) for 16 selected Vb-events from 1901 to 2010 (section 6.3.2). The characteristics of identified moisture source regions were investigated for all detected Vb-events during 1901–2010 ranked with respect to their precipitation impact in the Danube, Elbe, and Odra river catchments (section 6.4). We discuss our findings and open research questions in section 6.5. Finally, we revisit the key findings of this chapter in section 6.6.

6.2 Data and methods

6.2.1 Dynamically downscaled ERA-20C reanalysis

The analysis was based on the ECMWF twentieth century reanalysis (ERA-20C; POLI et al., 2016) that assimilates surface pressure and marine surface wind measurements. The horizontal resolution is about 125 km (spectral triangular truncation T159; POLI et al., 2016). Vb-cyclones are strongly influenced by mountains (e.g., AEBISCHER and SCHÄR, 1998; TRIGO et al., 2002) and heavy rainfall is especially triggered along the east-west oriented mountain ranges (GRAMS et al., 2014). A higher spatial and temporal resolution is necessary to capture such local-scale processes involved in orographically induced precipitation. Therefore, the ERA-20C reanalysis was dynamically downscaled to a horizontal resolution of about 12 km ($\Delta x = 0.11^\circ$; KRUG et al., 2020b). Note that the highest mountain in the Alps (Ore Mountains) is the Mont Blanc (the Klínovec) with about 4800 m (1244 m) altitude. In our downscaled reanalysis the highest gridpoint in the Alps (Ore Mountains) was more realistically represented with 2960 m (792 m) compared to 1434 m (392 m) in ERA-20C

reanalysis (0.75° horizontal resolution; please note that the original resolution is a spectral truncation T159). The downscaled reanalysis covers an extended EURO-CORDEX domain (GIORGI et al., 2009) and continuously spans the years from 1901 to 2010. The temporal resolution of the output variables ranges from 1 h for variables such as total precipitation and surface temperature to 1 day for variables such as daily maximum 2 m temperature.

The dynamically downscaling was performed with the regional climate model COSMO-CLM (Consortium for Small-scale Modelling in Climate Mode; ROCKEL et al., 2008) which was interactively coupled with the regional ocean model NEMO (Nucleus for European Modeling of the Ocean; MADEC and THE NEMO TEAM, 2016) over the marginal seas (Mediterranean Sea, North Sea, and Baltic Sea) to better represent the components of the water cycle. The freshwater inflow of rivers routing into the Mediterranean Sea (except for the Nile) was implemented with the river routing model TRIP (Total Runoff Integrating Pathways; OKI and SUD, 1998) to close the regional water budget (so that, e.g., the Mediterranean salinity is consistent with precipitation over land; SEVAULT et al., 2014). The lateral boundary conditions were given by the ERA20C-reanalysis data with a 1-way DAVIES (1976) relaxation scheme. More details about the model setup and performance can be found in PRIMO et al. (2019) and in section 2.2.2.

6.2.2 Vb-Cyclone tracking

We applied the method defined by WERNLI and SCHWIERZ (2006) and refined in SPRENGER et al. (2017) to track all cyclones at mean sea level pressure with a 3-hourly resolution in the dynamically downscaled ERA-20C reanalysis (interpolated to 0.5°) from 1901 to 2010 within 25°W–45°E and 25°N–75°N. Cyclones were identified based on closed sea-level pressure isobars. The position of the deepest pressure within a closed isobar defined the cyclone centre. The cyclone centres at different time steps were connected to cyclone tracks. More specifically, the position of the following track point was detected by a first guess approach based on the previous displacement vector. The cyclone centre nearest to the first guess within a search radius smaller than 1000 km was then assigned as a new track point. Cyclone track points where topography exceeds 1500 m were excluded because of the extrapolation errors of the mean surface pressure values from these altitudes (WERNLI and SCHWIERZ, 2006). We excluded spurious cyclones with a life time shorter than 24 h. For simplicity, all cyclones crossing northward the 47°N latitude between 12°E and 22°E were classified as Vb-cyclones (cf. HOFSTÄTTER and BLÖSCHL, 2019, and section 3.2).

We extended the previous case studies of widespread floods associated with Vb-cyclones based on the detected Vb-cyclone events since 1901. For the first time, we analysed the moisture source regions of Vb-cyclone events during the early decades of the past century (e.g., in 1903 and 1954). By selecting events throughout the past century, we could investigate whether the detected contributions of the European continent and North Atlantic Ocean in previous studies depend on the few selected events in literature. We compared the detected Vb-cyclone tracks and simulated precipitation sums with historical flood events to select the events of interest in this study. As a reference, we used the Climatic Research Unit Timeseries (CRU TS v4.04, HARRIS et al., 2020) and E-OBS v 22.0e (CORNES et al., 2018) gridded observation

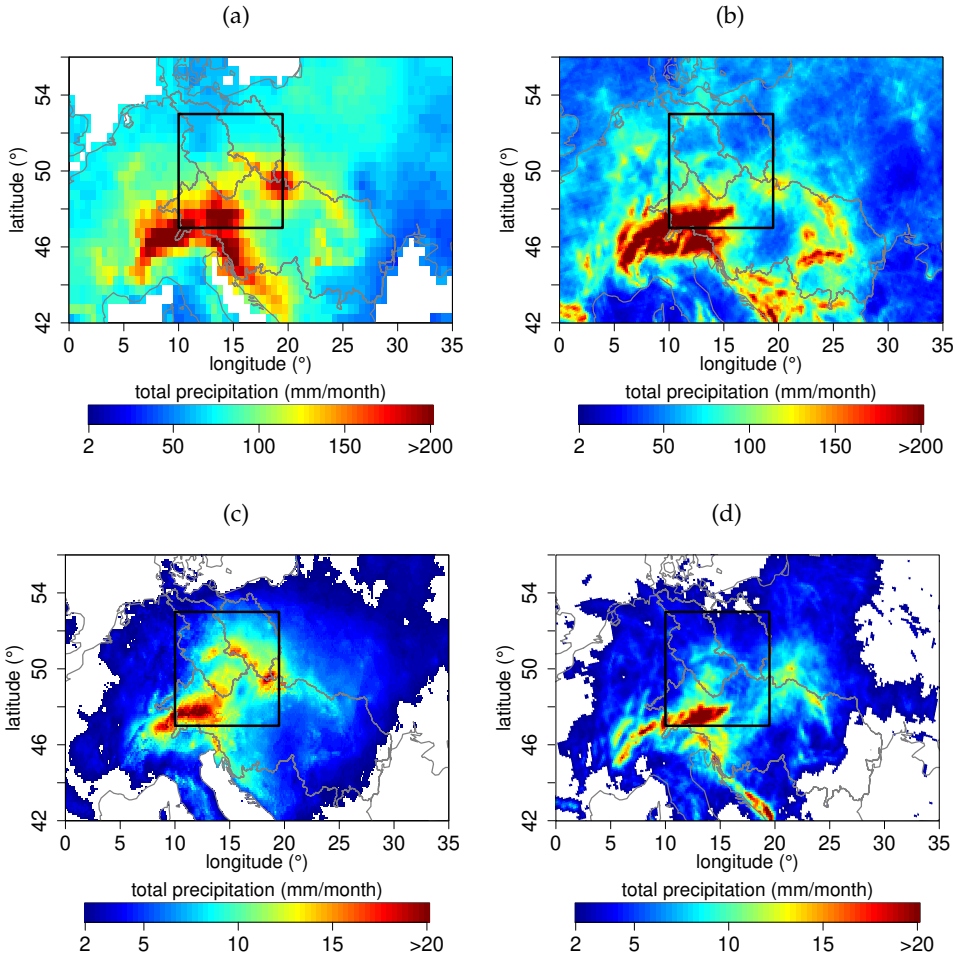

FIGURE 6.2: Monthly precipitation sums in (a) CRU-observational data and (b) the dynamically downscaled ERA-20C data averaged over July 1903, June 1926, October 1930, June 1936, and May 1949. The lower panels show the precipitation sums during the selected events No. 6 to 16 (start and end date in Table 6.1) in (c) E-OBS observational data and (d) the dynamically downscaled ERA-20C data.

data. We calculated monthly sums for the events prior to 1950 to fit the temporal resolution of CRU observation data (monthly precipitation sums due to data availability in the early decades of the past century). For defining the days for our moisture source diagnostics, we analysed the total precipitation sums in the domain of 10°E, 19.5°E, 47°N, and 53°N (including the catchment regions of interest, black rectangle in Figure 6.2) and selected the four consecutive days of most intense rainfall. All events occurred from May to August except for the flood in October 1930 (see Table 6.1, and references therein). The events in August 2002 and July 1954 were the most prominent ones in the past century besides the Central European flood in June 2013 (BLÖSCHL et al., 2013). The latter one was excluded from our analysis because the ERA-20C reanalysis only covers the years from 1900 to 2010. Other events, such as the flood in June 1936 or June 1979, were less intense but still affecting more than one river catchment. Please note that we did not include some events mentioned in

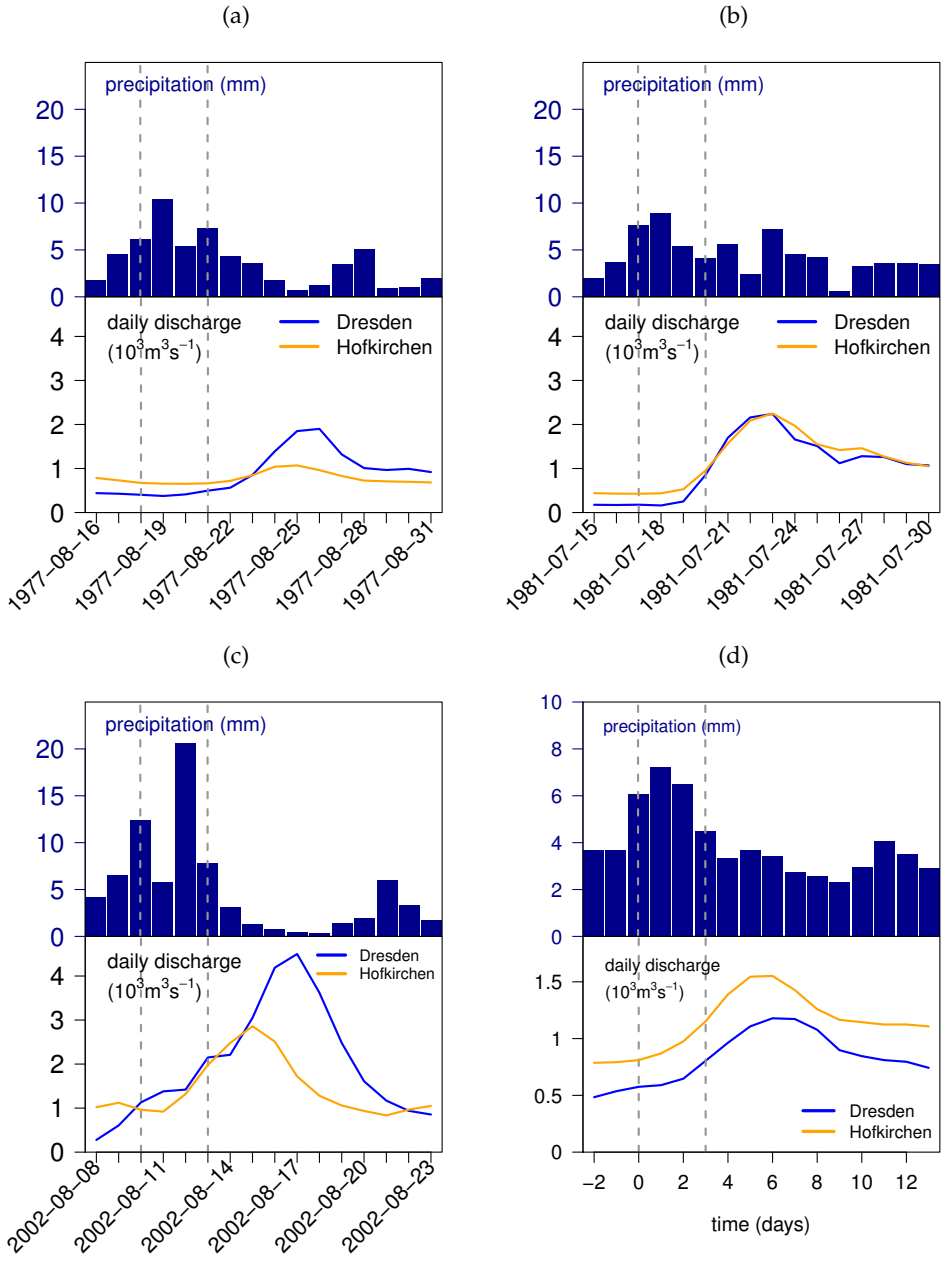

FIGURE 6.3: Temporal evolution of simulated mean daily precipitation sums in the region of 10° E, 19.5° E, 47° N, and 53° N (including all selected river catchments regions of interest, black rectangles in Figure 6.2) and daily GRDC river discharges measured at Dresden (Elbe) and Hofkirchen (Danube) (a) during the August 1977 event, (b) the July 1977 event, (c) the August 2002 event, and (d) averaged over all events listed in Table 6.1. We defined the start dates and end dates of our analyses (marked with dashed lines; see also Table 6.1) so that they cover the four days of the highest rainfall amounts in advance of the peak discharges.

STAHL and HOFSTÄTTER (2018) because the associated Vb-cyclone trajectories and precipitation sums were not captured well enough in the dynamically downscaled reanalyses (e.g., the May 1940 flood and the July 1985 event). We also excluded events that were limited to a relatively small region only (e.g., flood in northeastern Switzerland in June 1910 and the Vistula region in July 2001). The influence of the local catchment conditions is less pronounced for floods affecting more than one macro-scale river catchment, and the meteorological circumstances (such as heavy

TABLE 6.1: Floods in Central Europe associated with Vb-cyclones and the start and end date of the four-day heavy precipitation period analysed with the Lagrangian moisture diagnostics.

No.	start date	end date	selected references
1	11.07.1903	14.07.1903	KELLER (1903); FISCHER (1904); HELLMANN and VON ELSNER (1911)
2	23.06.1926	26.06.1926	SORG (1926); FABIAN and BARTELS (1928); FICKERT (1932)
3	26.10.1930	29.10.1930	FRIEDRICH (1930); WEICHMANN (1931); FICKERT (1932)
4	02.06.1936	05.06.1936	FISCHER (1938, p. 330), DREWS et al. (2003, Abb. 2-1)
5	20.05.1949	23.05.1949	KRESSER (1957, Tab. 1)
6	30.06.1954	03.07.1954	BLÖSCHL et al. (2013); BÖER et al. (1959)
7	21.07.1957	24.07.1957	BECKER and GRÜNEWALD (2003)
8	09.06.1965	12.06.1965	UHLEMANN et al. (2010); GVOŽDÍKOVÁ and MÜLLER (2017)
9	18.08.1977	21.08.1977	NAUMANN et al. (1978); BÖHM and WETZEL (2006)
10	16.06.1979	19.06.1979	UHLEMANN et al. (2010)
11	17.07.1981	20.07.1981	UHLEMANN et al. (2010); AKHTAR et al. (2019)
12	31.05.1986	03.06.1986	IONITA et al. (2015)
13	17.07.1997	20.07.1997	KUNDZEWICZ et al. (1999); HOFSTÄTTER and CHIMANI (2012)
14	10.08.2002	13.08.2002	SODEMANN et al. (2009); GANGOITI et al. (2011a,b, 2015)
15	20.08.2005	23.08.2005	WINSCHALL (2013, Chapter 3); AKHTAR et al. (2019)
16	15.05.2010	18.05.2010	WINSCHALL et al. (2014)

precipitation) dominate. In addition to the flood events mentioned in STAHL and HOFSTÄTTER (2018), past flood events associated with synchronous peak discharges in the Danube and Elbe catchment were selected, such as the event in July 1965 and July 1981 (see Figure 6.3).

6.2.3 Lagrangian moisture source diagnostics of selected cases

This study used a Lagrangian approach to identify the evaporative moisture source regions of 16 selected precipitation events associated with floods. We analysed four days of heavy precipitation for each event (Table 6.1). Figure 6.4 shows the corresponding mean total precipitation with a slight eastward shift throughout the events. During these four days, we calculated for every hour seven-day three-dimensional backward trajectories with LAGRANTO (WERNLI and DAVIES, 1997; SPRENGER and WERNLI, 2015) based on model level data with the height based hybrid vertical coordinate μ. We chose seven days because this is above the global mean atmospheric moisture residence time of about four to five days (LÄDERACH and SODEMANN, 2016). For periods shorter than five days, the moisture source region diagnostic would not give robust results. We did not use more than seven days backward trajectories because then the majority of backward trajectories left the domain of our downscaled reanalysis. Potentially relevant moisture sources from outside the regional domain were therefore neglected. In summer and autumn this share is most likely negligible, whereas in winter more long-range transport and influence from the North Atlantic outside the domain can be expected (AEMISEGGER et al., 2014). In total about $16{\cdot}10^3$ to $18{\cdot}10^3$ starting points were selected equidistantly every 15 km in the horizontal on 39 vertical levels from 250 m a.s.l. to 9750 m a.s.l. in the Danube, Elbe, and Odra catchment, respectively (Figure 6.4, orange rectangles). This high temporal and spatial resolution is crucial to capture relevant air streams, for example, around the Alps. We traced specific humidity and other meteorological

variables like wind, temperature, or the planetary boundary layer height along the trajectories for air parcels exceeding 80% relative humidity at their arrival point in the selected catchment regions. In this way, only trajectories related to high relative humidity and thus precipitation were considered (cf. GRAMS et al., 2014).

The evaporative moisture source regions were then identified by changes of specific humidity along the air parcel trajectories, assuming that changes of specific humidity result from evaporation and precipitation (SODEMANN et al., 2008b). The individual moisture uptakes were weighted according to the method of SODEMANN et al. (2008b), i.e., the contribution of each moisture uptake is reduced by following moisture uptakes and precipitation events along the air parcel trajectory. In accordance with AEMISEGGER et al. (2014) and WINSCHALL et al. (2014), we analysed the moisture uptake of air parcels irrespective of altitude, not only within the boundary layer but also above. Some uptakes above the boundary layer may actually be linked to surface evaporation via convection, which in fact might be of high relevance during summer. The explained fraction of moisture uptake was on average about 75% and limited by the domain of the dynamically downscaling. Finally, the total event moisture uptake was obtained by weighting the hourly moisture source contributions of each trajectory with its associated precipitation.

The moisture diagnostics were applied to the hourly trajectories during the respective four days listed in Table 6.1, that means in total 96 moisture uptake maps were calculated per flood event and river catchment. In terms of land sources, we differentiated between the Danube, Elbe, and Odra river catchment (orange rectangles in Figure 6.4) and the rest of the continent to analyse the temporal evolution of various moisture source contributions. Furthermore, we distinguished between the Mediterranean Sea (7°E, 22°E, 35°N, 46°N, grey polygon in Figure 6.5, sea grid points only), the North Sea and the Baltic Sea (50°N, 58.5°N, 30°E, 0°E, grey polygon in Figure 6.5, sea grid points), the North Atlantic (20°W, 0°W, 40°N, 60°N, grey polygon in Figure 6.5, sea grid points), the Black Sea, and other oceanic source regions. Please note, we did not select the whole Mediterranean Basin as region of interest but only the domain where the main moisture uptake in our case studies occurred. This corresponds also to the findings of KRUG et al. (2021) in which the selected Mediterranean region was found to play a key role for precipitation formation in the Odra (Poland) catchment area.

6.2.4 Climatological Analysis

Besides the above mentioned 16 case studies, we analysed for all 1107 Vb-cyclones during 1901–2010 the evaporation, SSTs, soil moisture content at 4 cm–10 cm, and wind speeds in the predefined moisture source regions. We calculated daily anomalies with respect to the analysis period (1901–2010) to remove the seasonal cycle and to account for possible systematic biases in the dynamically downscaled ERA-20C reanalysis. The spatial and temporal averages were calculated for each Vb-cyclone life time and pre-defined uptake region. For improved readability of the figures, we calculated the moving averages over 50 events and the local LOESS regression (Local Polynomial Regression Fitting; CLEVELAND et al., 1992) with corresponding prediction intervals based on the R software package stats v4.0.2 (R CORE TEAM, 2013). Moreover, we ranked all Vb-cyclones according to their total precipitation within the Danube, the Elbe, and Odra river catchment regions to gain more insights

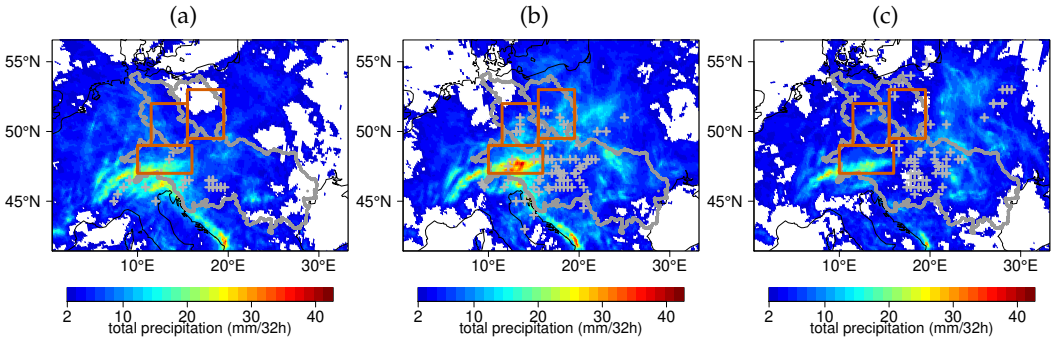

FIGURE 6.4: Mean total precipitation sum of the selected Vb-events (Table 6.1) in the dynamically downscaled reanalysis splitted into three event phases of 32 h each (from a to c). The grey crosses mark the corresponding Vb-cyclone centre positions. The orange rectangles show the backtracking start point regions within the Danube, Elbe, and Odra catchments (grey polygons).

in processes associated with Vb-cyclones causing heavy precipitation compared to Vb-events with only low or normal precipitation.

6.3 Case studies

6.3.1 Selected events from 1901 to 2010

Figure 6.2 shows the total precipitation sums of the selected events of interest (Table 6.1) in comparison to gridded CRU (HARRIS et al., 2020) and E-OBS (CORNES et al., 2018) observation data. Especially the Alps, Bohemian massif, and Carpathian mountains were affected by high rainfall sums (linked to atmospheric water vapour convergence; see appendix C, Figure C.3). The total precipitation events were captured by our dynamically downscaled ERA-20C reanalysis, even though the total precipitation sums over the Odra and Elbe catchment region were underestimated. As expected, Vb-cyclones often induce floods affecting more than one macro-scale river catchment. Figure 6.3 shows the synchronous occurrence of observed peak discharges in the Elbe and Danube river catchment and the preceding rainfall in our dynamically downscaled ERA-20C reanalysis for selected events and the average discharges and simulated precipitations sums for all selected events in our study (Table 6.1).

Among the selected events, highest peak discharges occurred in the Elbe and Danube river catchments on the 17.08.2002 with $4.50 \cdot 10^3$ $m^3 s^{-1}$ at the gauge Dresden (at Hofkirchen on the 15.08.2002 with $2.86 \cdot 10^3$ $m^3 s^{-1}$; Figure 6.3 c). Besides, high peak discharges were measured at Dresden on the 12.07.1954 with $2.30 \cdot 10^3$ $m^3 s^{-1}$ (at Hofkirchen on the 13.07.1954 with $3.29 \cdot 10^3$ $m^3 s^{-1}$), and at Dresden on the 23.07.1981 with $2.24 \cdot 10^3$ $m^3 s^{-1}$ (at Hofkirchen on the 23.07.1981 with $2.25 \cdot 10^3$ $m^3 s^{-1}$; Figure 6.3 b). Highest daily precipitation anomalies were simulated in our dynamically downscaled reanalysis for the August 2005 event (rank 17 in the selected Elbe region, rank 49 in the Danube region), the October 1930 event (rank 21 in the Elbe region), the July 1981 event (rank 35 in the Danube region), and the May 1986 event (rank 46 in the Odra catchment). During May 2010 precipitation anomalies of rank 80/93/99 were simulated in the Odra/Danube/Elbe catchment region of interest. In our simulation, also other Vb-events were associated with large

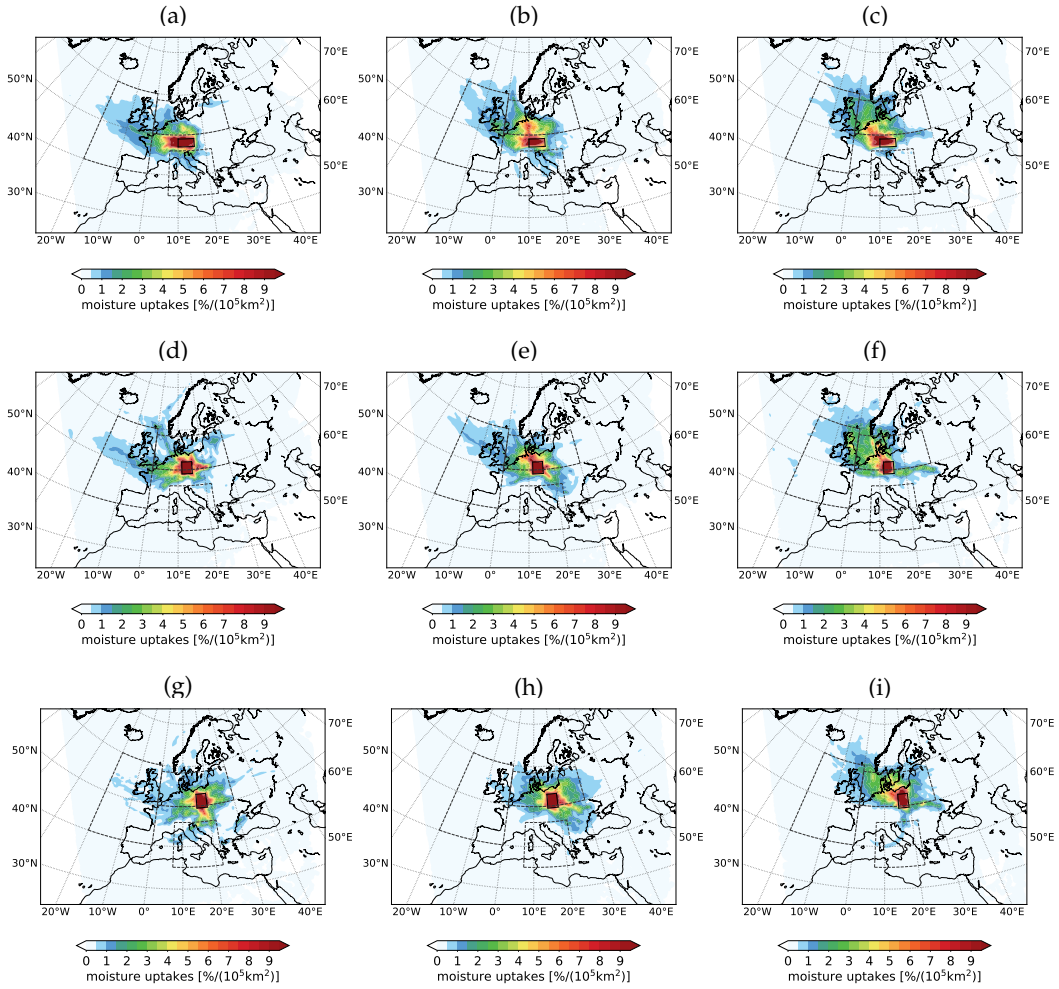

FIGURE 6.5: Moisture uptakes for precipitation in the Danube (panels a,b,c), Elbe (d,e,f), and Odra catchment (g,h,i) averaged over the events listed in Table 6.1. The columns show the time means of the first event phases (a,d,g), the middle (b,e,h), and the last event phases (c,f,i) with 32 h each. The integral over the entire moisture source region sums up to 100% of the explained moisture. The boxes show the domains of the moisture source regions in Figure 6.6.

precipitation anomalies but no widespread Vb-flood was reported, for example, during 08.08.2007–10.08.2007 (rank 100, Danube catchment). That event was associated with flooding in Switzerland, but no Vb-cyclone was mentioned in literature (BEZZOLA and RUF, 2009), even though we detected one Vb-cyclone with our less restrictive definition compared to HOFSTÄTTER et al. (2016). Nonetheless, a cutoff low was located over the Alpine region in August 2007 (BEZZOLA and RUF, 2009) – a synoptic situation that is often associated with Vb cyclones causing heavy precipitation (e.g., MESSMER et al., 2015; HOFSTÄTTER et al., 2018; MITTERMEIER et al., 2019). Potential causes for a discrepancy between observed flood events and simulated precipitation impact are a shift in the precipitation field or enhanced or decreased pre-saturation of the affected river catchments in the reanalysis data. Nonetheless, the dynamically downscaled reanalysis represents a physically consistent atmospheric data set.

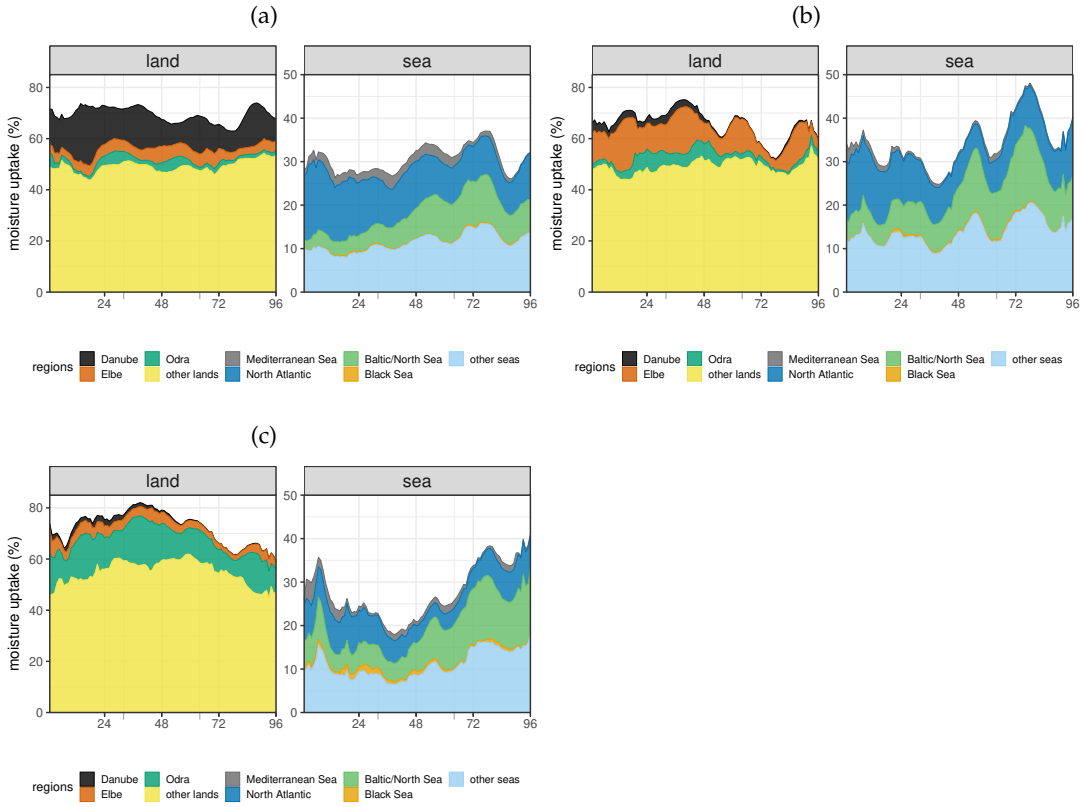

FIGURE 6.6: Relative percentage contribution of various moisture source regions to precipitation in the (a) Danube, (b) Elbe, and (c) Odra catchment averaged over all 16 events listed in Table 6.1. The x-axis corresponds to the four days of heavy precipitation selected for the moisture diagnostics. Note the different y-axis scales for land and sea source regions.

6.3.2 Evaporative moisture source regions of 16 selected cases

Figure 6.5 shows the average relative moisture uptake for the events listed in Table 6.1 with a focus on precipitation in (a,b,c) the Danube, (d,e,f) the Elbe, and (g,h,i) the Odra catchment. Throughout the three event phases, the moisture uptake was largest within the selected catchment region and surrounding continental surface. Overall, the moisture uptake over the European continent contributed to about 50%–80% of the precipitation falling in the selected river catchment area (Figure 6.6) and up to 90% during individual events (e.g., Figure 6.7c). Later in the Vb-event, when the cyclone centres recurve towards the Elbe and Odra catchment a larger share of moisture comes from regions north of the Alps, leading also to more precipitation north of the Alps (Figure 6.4b and c, Figure 6.5). At this stage, more moisture can be transported from the Baltic Sea and the North Sea south-eastwards to the river catchments. The contribution of the North Sea and Baltic Sea increased throughout the events, whereas the proportion of the North Atlantic and the land moisture uptake decreased accordingly (Figure 6.5 and 6.6, Elbe and Odra catchment).

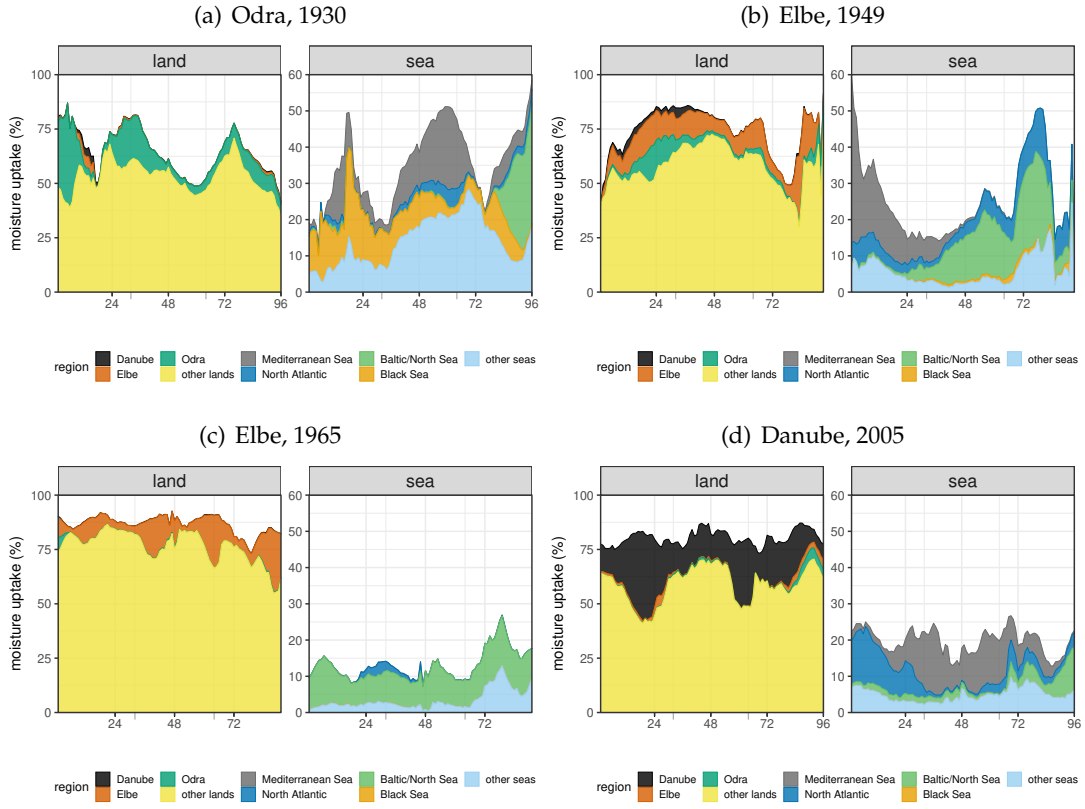

FIGURE 6.7: As in Figure 6.6, but for selected events and catchment regions.

The percental moisture uptake within the respective river catchment was only up to 20%, even though the intensity of these local uptakes were comparatively large considering the limited areal extent of the catchment (Supplement, Figure D.1). Interestingly, the eastern North Atlantic and the North Sea/Baltic Sea showed the highest moisture contribution among the marginal seas with up to 17% and 20% moisture uptake, respectively (Figure 6.5, 6.6). These moisture source regions correspond to summer mean moisture sources of the Alpine region (SODEMANN and ZUBLER, 2010, using 20-day backward trajectories). The North Atlantic Ocean contribution might be associated with another extratropical cyclone, because we quantified the moisture uptake of all precipitation within the river catchment areas, not only the one related to the Vb-cyclone. For the July 1997 event, AKHTAR et al. (2019) pointed to the fact that the flood-producing rainfall was not only linked to a Vb-cyclone but also another cyclone over the North Sea. The North Atlantic/North Sea contribution could also be linked to the northerly flow on the western side of the trough that is often involved in triggering cyclogenesis of the Vb-cyclones south of the Alps. The exact transport pathway of this northerly moisture, however, is still unclear. It might be moisture contributing to stratiform precipitation behind the cold front, or it could be moisture that was advected into the warm sector of the Vb-cyclone.

The Black Sea contributed to precipitation during the 1930 (Figure 6.7 a), 1949, and 2005 events, especially in the Odra catchment (Supplement, Figures D.2 – D.4). The mean moisture uptake over the Black Sea in general was highest for the Odra catchment but accounted only for up to 2% of the moisture uptake (Figure 6.6 c).

As mentioned in the introduction, due to the Vb-cyclone pathway a large contribution from the Mediterranean Sea might be expected. Here we find that the Mediterranean Sea, however, played overall only a minor role and affected more the Danube and Odra catchment than the Elbe region (Figure 6.5 and 6.6). Nonetheless, the Mediterranean Sea was a significant oceanic source during the 1930 flood, the 1949 flood (Figure 6.7b), and the 2005 flood for the selected river catchment regions, and during the 2002 event, the Mediterranean Sea contributed significantly to the Odra catchment. In contrast, we detected no moisture uptake over the Mediterranean Sea for precipitation in the Danube, Elbe, and Odra catchment during the 1965 (Figure 6.7c), the 1986, and the 2010 event. The temporal evolution of the moisture uptake in different regions reveals that, on average, the moisture uptake from the Mediterranean Sea contributed to the flood triggering heavy precipitation during the event start and decreased towards the end (Figure 6.6). That corresponds – together with an increasing influence of the North Sea and Baltic Sea during the events – to the Vb-cyclone pathway from the Mediterranean Sea to Central Europe. For some events, however, the event evolution was completely different. For example, the Mediterranean Sea was an important moisture source for precipitation in the Danube catchment only towards the end of the 1977 event. Another example is the August 2005 flood, during which the Mediterranean contribution was large in the middle of the event in the Danube catchment (Figure 6.7d). In the Elbe and Odra catchments, the Mediterranean Sea was a relevant moisture source during the last two days of that event (Supplement, Figures D.3, D.4).

In summary, the European continent is found to be by far the largest moisture source for the chosen 16 case studies of heavy precipitation events in the selected catchments. The major oceanic source regions were the North Atlantic and North Sea/Baltic Sea. Our results for Vb-cyclone events correspond to the climatological source regions. SODEMANN and ZUBLER (2010) analysed the moisture sources of precipitation in the European Alpine region during 1995-2002 and detected the North Atlantic Ocean, the Mediterranean Sea, the North Sea, the Baltic Sea, and the European land surface, with the European land surfaces dominating during the summer season.

The Mediterranean Sea played only a minor role as a source region, averaged over all selected Vb-cyclone events, but it is the region with a large variability in its contribution. More Vb-events have to be analysed to gain further insights into the role of the specific processes in the moisture source regions of precipitation during Vb-cyclones in the selected river catchments area. Therefore, a climatological perspective is adopted in the next section to investigate the moisture source conditions of Vb-cyclones that triggered heavy precipitation compared to Vb-events that were associated with low or normal precipitation.

6.4 Climatology of moisture source region characteristics during Vb-events from 1901 to 2010

In this section, we discuss the distinct characteristics of heavy precipitation producing Vb-events compared to normal Vb-events. Therefore, we ranked all Vb-cyclones according to their precipitation in the Danube, Elbe, and Odra river catchment regions (Figure 6.8). The ranked precipitation anomalies show a steep increase for

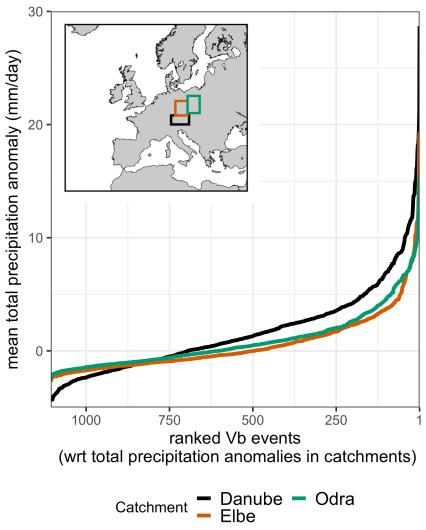

FIGURE 6.8: Ranked total precipitation anomalies in the Danube, Elbe, and Odra catchment during each Vb-cyclone from 1901 to 2010.

the highest ranked events in all river catchment regions (Figure 6.8, the daily climatology of 1901-2010 was removed for calculating the anomalies presented in this section). The Elbe, and Odra catchment have similar rainfall characteristics due to their close spatial location to each other. In contrast, the Danube catchment is usually affected earlier by the Vb-cyclone than the Elbe and Odra region due to the typical cyclone pathway around the eastern side of the Alps (Figure 6.4). Therefore, some moisture already rains out along the Alpine fringe before air masses propagate north-eastwards (Figure 6.2, 6.4), which reduces the direct moisture contribution of the Mediterranean Sea. Thus, the Danube catchment shows a higher variability with lower minimum values and overall higher precipitation anomalies for medium and high-ranked events in Figure 6.8.

In the following sections, we adopt this ranking of the Vb-cyclones for analysing the continental and oceanic moisture source conditions. We focus firstly on the moisture source conditions within the river catchments, such as soil moisture and the diurnal evaporation range, because the area-weighted uptakes were comparatively high (Section 6.4.1). Secondly, we discuss the properties of the oceanic moisture sources like ocean evaporation, the SST, and wind speed (Section 6.4.2).

6.4.1 River Catchments

High daily amplitudes of evapotranspiration together with positive soil-moisture anomalies can point towards an increased efficiency of convective precipitation processes (SCHÄR et al., 1999). Figure 6.9a shows the anomaly of the diurnal evaporation range $E_{max} - E_{min}$ during all Vb-events from 1901 to 2010 ranked according to the precipitation amount. Indeed, the anomalies of the diurnal evaporation range were larger for high precipitation Vb-cyclones, especially in the Danube catchment. That indicates that processes within the river catchment regions, such as the soil moisture-precipitation feedback and convective rainfall, might play a role, even though the moisture uptake was only up to 20% of the precipitation in the river

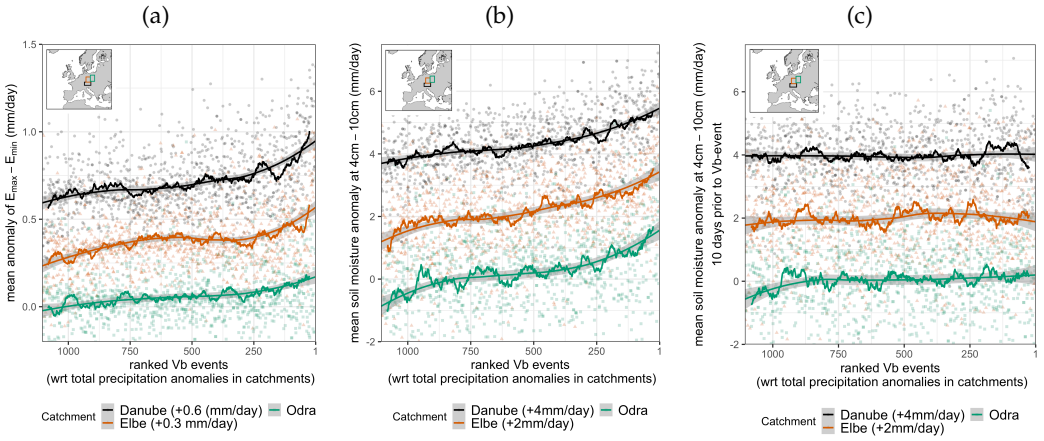

FIGURE 6.9: (a) Anomalies of diurnal evaporation range E_{max}-E_{min} and (b) soil moisture anomalies during the corresponding ranked Vb-events. (c) Soil moisture anomalies 10 days prior to the respective Vb-events. The lines show the moving average and the LOESS regression. Note, the data for Danube and Elbe catchment were shifted by constant values for improved readability.

catchments of interest in our case study. Similarly, these processes are probably relevant in other continental moisture source regions.

Figure 6.9b shows the daily soil moisture anomalies at 4 cm–10 cm soil depth averaged over the respective Vb-events. This soil depth reacts relatively fast to rainfall events. Results were similar for other soil layers except for deeper layers with more than 1 m depth (not shown). All river catchments show an increase of soil moisture anomalies from low to high precipitation Vb-cyclones. Rainfall during the respective Vb-events increases the soil moisture content, which is an important ingredient for local moisture uptake in the river catchment and over the rest of the continent.

On the contrary, the soil moisture conditions ten days preceding the event shows no positive anomaly for heavy precipitation events (Figure 6.9c). Only in the Odra catchment, low precipitation Vb-events correspond with drier antecedent soil conditions. Thus, mainly the event precipitation itself triggered the moisture uptake within the river catchments. Nonetheless, case studies like the one in HOHAGEMANN et al. (2015), analysing the July 1997 event, indicate some exceptions with precipitation linked to preceding soil moisture conditions.

6.4.2 Marginal Seas

In our 16 case studies (section 3), the eastern North Atlantic and the North Sea/Baltic Sea were the largest oceanic moisture source regions with a moisture uptake of up to 17% and 20% of the precipitation falling in the selected river catchments. Figure 6.10, middle and right panel, show the conditions of these moisture source regions during all ranked 1107 Vb-cyclones from 1901 to 2010 in terms of anomalies in oceanic evaporation, SST, and wind speed. Interestingly, the evaporation anomalies in the North Atlantic and the North Sea/Baltic Sea vary around zero and show no difference for Vb-cyclones with low precipitation compared to Vb-cyclones with heavy precipitation. That is also the case for SST and wind speed anomalies. For all river catchments, the wind speed anomalies over the North Sea/Baltic Sea and the North

Atlantic are negative or close to zero and induce therefore no evaporation enhancement.

Even though the Mediterranean Sea explained on average only up to 5% of the precipitation in the selected river catchments in our case studies (section 6.3.2), remarkable anomalies in evaporation, and wind speed show distinct differences between heavy precipitation and low to normal precipitation Vb-cyclones. The evaporation anomalies over the Mediterranean Sea were higher for Vb-cyclones with heavy precipitation in all river catchments (Figure 6.10, left panel). The overall increase is highest for the Danube catchment, likely because of the closest vicinity of this catchment to the Mediterranean Sea. Interestingly, these positive evaporation anomalies were associated with positive wind speed anomalies. The Spearman rank correlation coefficient R (SPEARMAN, 1904) for evaporation and wind speed anomalies over the selected Mediterranean region was about +0.7 ($p < 0.01$) for the 300 highest ranked precipitation events in all selected catchment regions (Figure 6.11). Positive wind speed anomalies and dynamic evaporative forcing are usually associated with negative SST anomalies. The mean Mediterranean SSTs and wind speed anomalies are weakly negatively correlated (R ranging from -0.25 to -0.3 for the 300 highest precipitation events, Figure 6.11). We discuss this in more detail in the following section and the result that, even though the Mediterranean Sea was only a minor moisture source region, an enhanced and dynamically driven moisture uptake was observed for heavy precipitation Vb-cyclones.

6.5 Discussion

Due to the Vb-cyclone pathway from the Mediterranean Sea north-eastwards to Central Europe, one might expect a high moisture contribution of the Mediterranean Sea to precipitation in Central Europe. Indeed, the studies of JAMES et al. (2004) and GANGOITI et al. (2011a) detect a substantial contribution of the Mediterranean Sea for the initial phase of the August 2002 flood. However, case studies on other floods such as the ones in May 2010 or May/June 2013 reveal only minor moisture uptakes over the Mediterranean Sea (GRAMS et al., 2014; WINSCHALL et al., 2014; KELEMEN et al., 2016). Our moisture source diagnostics of 16 Vb-cyclone events during 1901–2010 (Table 1) further supports this finding (Figure 6.6).

One might deduce that the Mediterranean Sea plays only a minor role for precipitation during Vb-cyclones in Central Europe. However, the study of MESSMER et al. (2017) shows increased precipitation with higher Mediterranean SSTs while an increase of North Atlantic SST has only marginal impact. Our climatological analysis reveals that heavy precipitation during Vb-cyclone events in the selected Danube, Elbe, and Odra catchment regions - were associated with positive evaporation anomalies over the Mediterranean Sea, whereas the North Atlantic and the North Sea/Baltic Sea evaporation anomalies showed no trend with the Vb-event ranks. Thus, during Vb-events, anomalously high evaporation over the Mediterranean Sea is linked with high precipitation in Central Europe, even though the moisture uptake contribution is relatively small. This is in accordance with CIRIC et al. (2018) concluding that the Mediterranean Sea contribution to precipitation in Central Europe is similar for extreme events compared to the climatological mean. The short-range transport of this moisture evaporated over the Mediterranean Sea

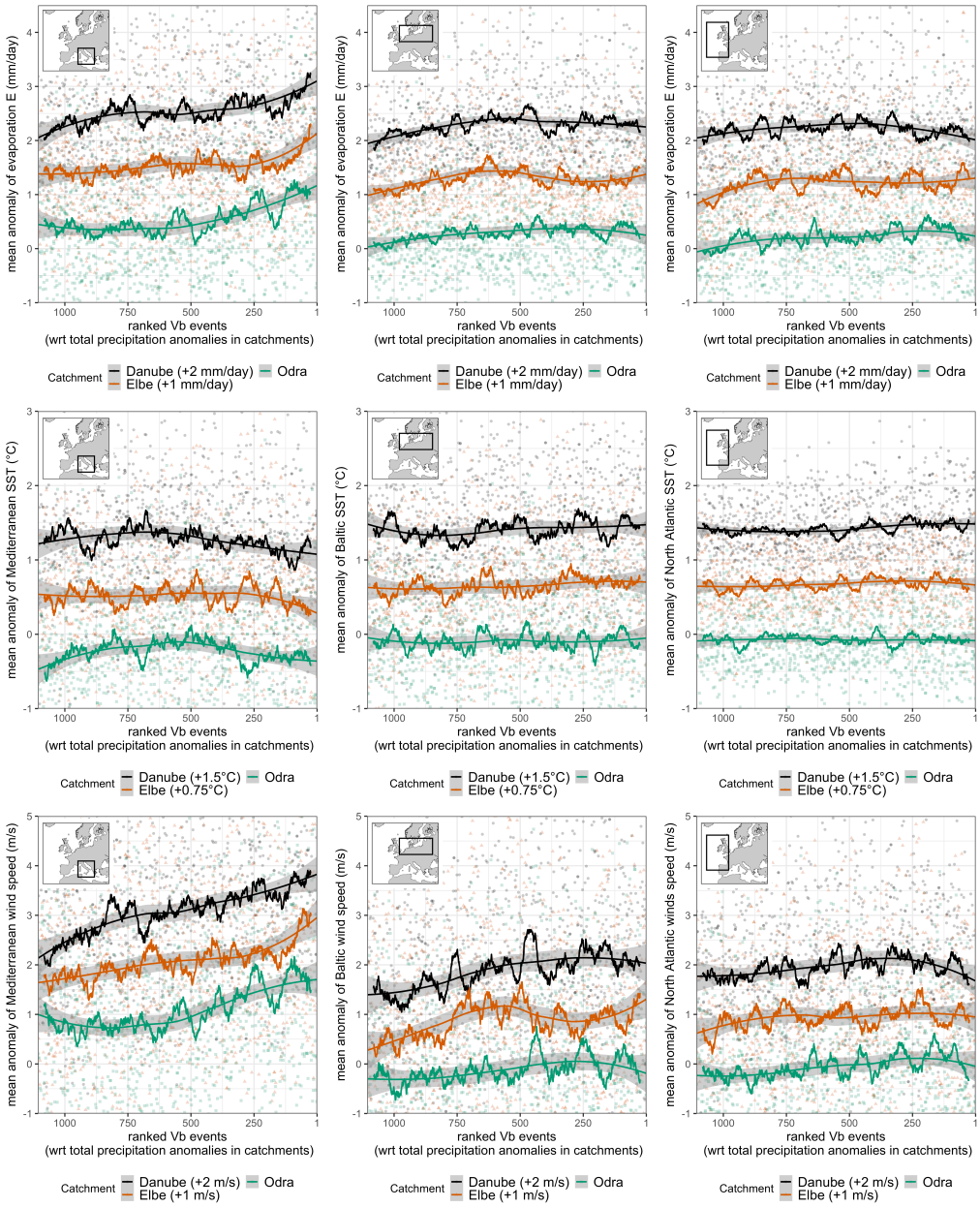

FIGURE 6.10: Anomalies of evaporation (upper row), sea surface temperatures (middle), and wind speed (lower row) in (left) the Mediterranean Sea, (middle) the North Sea and Baltic Sea, and (right) the North Atlantic during the corresponding ranked Vb-events. The lines show the moving average and the LOESS regression. Note, the data for Danube and Elbe catchment were shifted by a constant value for improved readability.

could contribute to Vb-cyclone intensification in the early stages of their development through latent heat release. The confluence of the moist Mediterranean air masses with other, relatively cold and dry air masses could intensify the frontal zones of the Vb-cyclone, especially during the presence of an upper-level trough over Central Europe (e.g., GRAMS et al., 2014). Moreover, the Mediterranean moisture might play a key role in pre-moistening continental moisture source regions that later on contribute to heavy precipitation downstream in the Danube, Elbe, and Odra catchments.

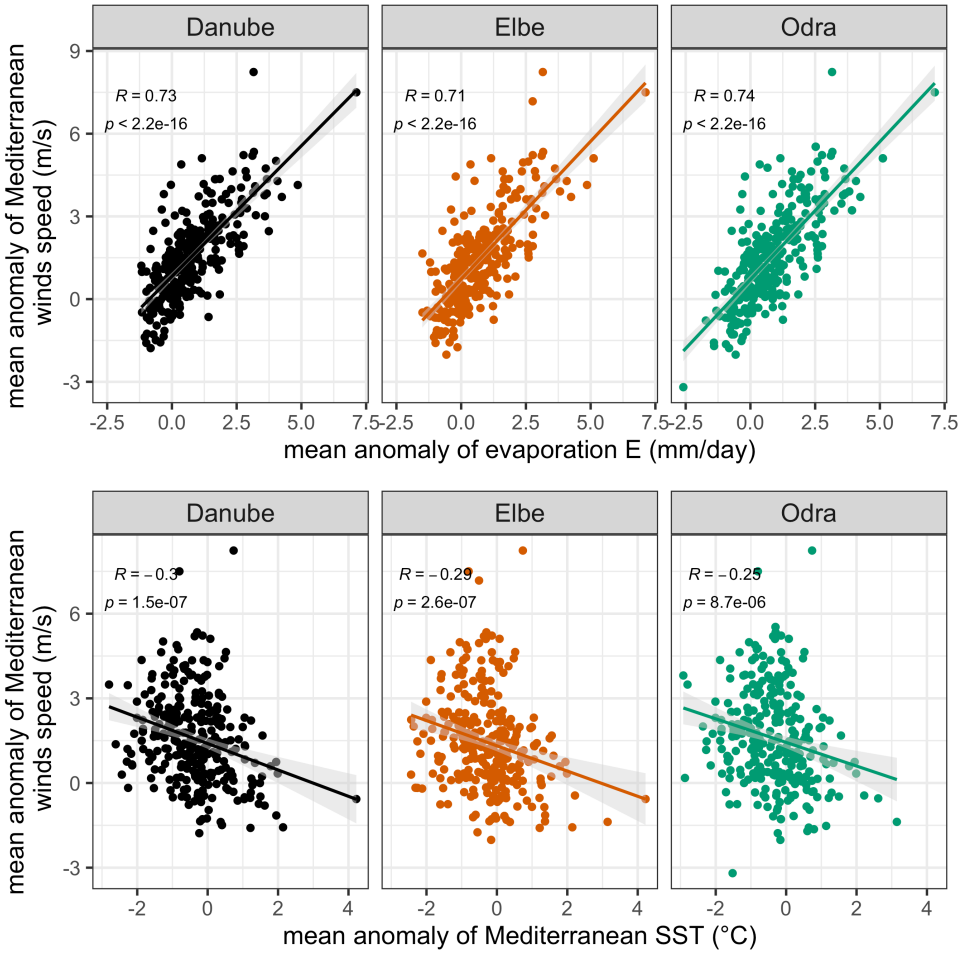

FIGURE 6.11: Scatter plots of Mediterranean evaporation, wind speed, and SST anaomalies for the 300 highest ranked precipitation events with the Spearman's rank correlation coefficient R (SPEARMAN, 1904).

Interestingly, we detected a dynamically driven evaporation enhancement during Vb-cyclones with heavy precipitation in our selected catchment regions. A similar behaviour was observed during strong evaporation events in the subpolar North Atlantic (AEMISEGGER, 2018). On the other hand, higher SSTs can be associated with higher evaporation, which might be the reason for the weakly negative correlation between SST and wind speed anomalies. High absolute SSTs during the initial phase of the Vb-cyclone may contribute to an increase of the precipitation during Vb-cyclones in the early stages of the cyclone development via enhanced upward moisture fluxes and a decreased atmospheric stability (cf. MESSMER et al., 2017).

The SST effect emphasizes the possible impact of the Mediterranean Sea on precipitation during Vb-cyclones in Central Europe, in particular in the context of rising SSTs in a warming climate (GIORGI, 2006). Moreover, these processes partly explain the seasonal distribution of extreme Vb-flood events occurring predominantly during summer, when absolute SSTs over the Mediterranean Sea are usually high (cf. MESSMER et al., 2017). Besides, we detected only a few Vb-events with high precipitation anomalies during the winter. Examples were the Vb-event during 25.12.1993 and 26.12.1993 (Danube, 54th highest precipitation anomaly) or during 21.11.1962 and 22.11.1962 (Odra, 5th highest precipitation anomaly) associated

with heavy snow fall in Central Europe (e.g., snow height increase from 0 cm on 21.11.1962 to 21 cm on 24.11.1962 in Berlin-Buch; Climate Data Center, version v005 (2017), DWD).

In our case studies, the diagnosed moisture sources depend strongly on the selected region of precipitation. For example, the moisture uptake over the Mediterranean Sea contributed in August 2005 to about 20% of the precipitation in the Danube catchment, but only to about 5% in the Elbe catchment (Figure 6.7d, D.3). Thus, the findings of our study may not be representative for other catchments and regions in Europe. Another shortcoming of our study is that we could not detect multiple precipitation and re-evaporation cycles with our Lagrangian moisture diagnostics. To gain more insights, one could perform backtracking and moisture source diagnostics for the preceding precipitation events, that built up the soil moisture contributing to the moisture uptake during the event of interest. However, this requires iterative moisture source diagnostics covering several months in advance of the event. In this study, some of the continental moisture uptakes might originate, for instance, from Mediterranean moist air masses that precipitated out upstream of our catchment regions earlier. Moreover, we focused exclusively on precipitation. For flood producing events, however, also the antecedent soil conditions and initial hydraulic load are important ingredients, as it was the case during June 2013 (SCHRÖTER et al., 2015).

6.6 Conclusions: the particular role of the Mediterranean Sea

Even though Vb-cyclones have a frequency of about four to ten events per year, only a few cause extreme flooding. These floods are among the most devastating ones in the Danube, Elbe, and Odra river catchments (e.g., the Elbe flood in August 2002). Our study aimed at shedding light on intensification processes of the precipitation inducing such extreme floods. Therefore, we quantified the moisture source regions of 16 historical floods linked to Vb-cyclones with a Lagrangian approach. Moreover, we analysed the moisture source characteristics during all 1107 Vb-cyclones in our dynamically downscaled ERA-20C data from 1901 to 2010. In the following, we answer the research questions of our study:

1. **What are the evaporative moisture source regions of flood-causing precipitation during Vb-cyclones?** For all 16 case studies, a mixture of different moisture source regions was observed. Overall, up to 80% of the precipitation originated from the continental surface, with the highest continental uptake within the respective river catchments (when taking the spatial extend into account) triggered mainly by the event precipitation itself (indicating important local precipitation recycling). Other main uptake regions were the North Sea/Baltic Sea and North Atlantic with up to 20% contribution. On average, the moisture contribution of the North Sea and the Baltic Sea increased, while the contribution of the North Atlantic and the continental surface decreased accordingly during the Vb-event evolution (likely linked to the cyclone centre recurving towards northern and eastern Central Europe). The Black Sea was a minor source region, affecting the Odra river catchment in a few cases. Also the Mediterranean Sea was only a minor source region on average. That supports previous case studies on selected flood events triggered by Vb-cyclones (e.g.,

SODEMANN et al., 2009; WINSCHALL et al., 2014; GRAMS et al., 2014; KELEMEN et al., 2016). Nonetheless, the relative importance of moisture source regions was highly variable for the individual events and river catchments. In particular, the share of Mediterranean moisture was highly variable from event to event. This highlights the complex dynamical interplay of different air masses leading to convergence of moisture during particularly severe Vb-floods.

2. **Which characteristics in the moisture source regions intensify the precipitation during Vb-cyclones**? Remarkably, the anomalies in evaporation, SSTs, and wind speed over the North Atlantic and North Sea/Baltic Sea showed no distinct trend with precipitation during Vb-cyclones in the Odra, Elbe, and Danube river catchment regions. Conversely, Vb-cyclones with high precipitation amounts were associated with positive evaporation anomalies over the Mediterranean Sea, even though the diagnosed moisture uptake in that region was relatively small in our case studies. Interestingly, these evaporation anomalies were dynamically driven and therefore linked with positive wind speed anomalies.

Overall, an enhanced and dynamically driven moisture uptake over the Mediterranean Sea was found to be characteristic for Vb-events with heavy precipitation, even though the dominating moisture uptake regions were the European continent and the North Atlantic and the North Sea/Baltic Sea. Possible underlying processes are beyond the focus of this study. In future studies, it would be interesting to analyse how short-range moisture transport from the Mediterranean Sea and resulting latent heat release could intensify Vb-cyclones during the early stages of the cyclone development. It could be beneficial to focus only on the moisture source regions of precipitation linked to the Vb-cyclone and not other systems to gain deeper insights into the role of the Mediterranean Sea. Such approach could be the consideration of a radius around the Vb-cyclone (e.g., MESSMER et al., 2020). Besides, further research is needed on the role of latent heat release later in the Vb-cyclone life cycle for prolonging atmospheric blockings (e.g., PFAHL et al., 2015; STEINFELD and PFAHL, 2019; STEINFELD et al., 2020) that may trigger the development of new Vb-cyclones (HOFSTÄTTER and BLÖSCHL, 2019). Moreover, it will be an issue of future research to quantify the role of convective precipitation for summer time intensification of precipitation during Vb-cyclones (e.g., GRAMS et al., 2014; MESSMER et al., 2015), also in the context of soil-precipitation feedback (SCHÄR et al., 1999; HO-HAGEMANN et al., 2015) which enhances the efficiency of convective precipitation within the river catchment.

The dynamically driven moisture uptake over the Mediterranean Sea highlights the importance of high-resolution regional climate simulations for improved wind fields in the Mediterranean Sea (HERRMANN et al., 2011; OBERMANN et al., 2018). Coupled regional atmosphere-ocean models can further improve the representation of air-sea interactions and thus cyclone characteristics, as demonstrated for selected Medicane events in AKHTAR et al. (2014).

Chapter 7

Information-theoretic diagnostic of Vb-cyclone precipitation intensification

FIGURE 7.1: Bridge in Döbeln (Saxony) damaged by the Vb-cyclone flood in August 2002. Photography taken by Sonja Strini on 23.08.2002 from an opposite perspective than in Figure 6.1.

This chapter illustrates the usefulness of the parametric transfer entropy measure TE-linear as a complementary approach to the Lagrangian moisture source diagnostics discussed in the previous chapter. Please note that the following sections are mainly excerpted from the study entitled *Heavy Vb-cyclone precipitation: a transfer entropy application showcase* by A. Krug, P.K. Pothapakula, C. Primo, and B. Ahrens, published in Meteorologische Zeitschrift (KRUG et al., 2021).

7.1 Application of information theory estimators

The Vb-cyclone pathway is associated with a high flood potential in Central Europe especially during summer (PETROW et al., 2007; NISSEN et al., 2013; NIED et al., 2014) and caused, for example, the July 1954 and August 2002 floods (BLÖSCHL et al., 2013). In previous studies, the origin of flood-triggering atmospheric moisture during Vb-cyclones has been investigated with Lagrangian moisture source diagnostics (e.g., GRAMS et al., 2014) or Eulerian moisture tagging (SODEMANN et al., 2009; WINSCHALL et al., 2014). In this study, we present a complementary and computationally less intensive approach using an information theory estimator.

Information theory estimators are based on the concept of Shannon entropy which was introduced by SHANNON (1948) in the context of data compression and transmission. After the study of SHANNON (1948), information theory methods have been applied to neurosciences (DIMITROV et al., 2011; LI et al., 2019, and references therein) and biology (DANCOFF and QUASTLER, 1953), and later on also to other fields like economics (e.g., MAASOUMI, 1993). In recent years, the role of information theory methods has grown also in earth system sciences in evaluating probabilistic forecasts (e.g., AHRENS and WALSER, 2008; WEIJS et al., 2010; KRAKAUER et al., 2013), in evaluating hydrological models (BENNETT et al., 2019), and in studying interactions in the global climate systems (e.g., DAS SHARMA et al., 2012; BHASKAR et al., 2017; GERKEN et al., 2019; POTHAPAKULA et al., 2019; YU et al., 2019; POTHAPAKULA et al., 2020).

Previous studies on information theory methods applied in climate sciences focused mainly on large spatial and temporal scales. For example, (BHASKAR et al., 2017) investigated the directional flow of information between various climate drivers and global mean temperature anomalies at monthly scales, and (POTHAPAKULA et al., 2019) examined (also with a monthly resolution) the information exchanged between the Pacific and the Indian Ocean. In this short contribution, however, we aim to motivate the application of information theory methods in studying the interactions also at regional climate scales and submonthly resolutions. Furthermore, we showcase the usefulness of information theory measures for studying extreme hydro-meteorological events. In particular, we demonstrate the usage of TE-linear for studying flood-causing Vb-cyclones in Central Europe. For this purpose, a transfer entropy (TE, SCHREIBER, 2000) measure is presented using the example of heavy Vb-cyclone precipitation in the Odra catchment region (Poland) in comparison to the climatological summer season (JJA) precipitation.

7.2 Data and Methods

7.2.1 Dynamically downscaled ERA-20C reanalysis

Even though Vb-cyclones occur about four to ten times per year, only a few cause flood-triggering rainfall (MESSMER et al., 2015) and hence a long time series with high spatial resolution is required to analyse the most intense Vb-cyclone precipitation events. Therefore, we studied daily evaporation and precipitation sums in the dynamically downscaled ECMWF twentieth century reanalysis (ERA-20C; POLI et al., 2016). We used a regional atmosphere-ocean model setup for downscaling the reanalysis continuously from 1901 to 2010 over an extended EURO-CORDEX domain (GIORGI et al., 2009) to a horizontal resolution of about 12 km ($\Delta x = 0.11°$; KRUG et al., 2020b). The regional climate model Consortium for Small-scale Modelling in Climate Mode (COSMO-CLM; ROCKEL et al., 2008) was interactively coupled with the regional ocean model NEMO (Nucleus for European Modeling of the Ocean; MADEC and THE NEMO TEAM, 2016) over the marginal seas (Mediterranean Sea, North Sea, and Baltic Sea) for an improved representation of the water cycle components. The model setup and its performance are discussed in PRIMO et al. (2019).

7.2.2 Selection of heavy Vb-cyclone precipitation events (Odra, Poland)

We tracked all cyclones with a 3-hourly resolution at mean sea level pressure in our dynamically downscaled ERA-20C reanalysis from 1901 to 2010 with the method of WERNLI and SCHWIERZ (2006) and refined in SPRENGER et al. (2017). The cyclone centres were defined by the position of the deepest pressure within a closed isobar. The cyclone centre locations were then connected to cyclone tracks by a first guess approach. Like proposed in HOFSTÄTTER and BLÖSCHL (2019), we classified all cyclones crossing the 47°N latitude northwards between 12°E and 22°E as Vb-cyclones (available at Zenodo, KRUG and AHRENS, 2020). In order to gain more insight in Vb-cyclone precipitation events, we compare these events with typical summer conditions since most of the heavy precipitation Vb-events occurred during the summer (HOFSTÄTTER and CHIMANI, 2012; MESSMER et al., 2015; KRUG et al., 2020a). Therefore, we analysed the information exchange from evaporation to precipitation during all summer months (JJA) from 1901 to 2010 and compared that with Vb-cyclone events. To focus on the most intense Vb-cyclone events, we selected only the 100 highest ranked Vb-cyclone precipitation events in the Odra catchment region (15.5°E, 19.5°E, 49.5°N, 53°N).

7.2.3 Transfer entropy measure TE-linear

The transfer entropy is usually defined as follows (SCHREIBER, 2000; BENNETT et al., 2019):

$$TE_{X \to Y} = I(Y; X_{t-\tau} | Y_{t-\omega}) \tag{7.1}$$

where I is the conditioned mutual information and τ defines the time lag of the source variable X; ω denotes the time lag of the target variable Y. Note that more details on the definition of transfer entropy can be found in section 3.5. In this study, we defined as target variable Y the daily precipitation amount averaged over the selected Odra catchment region and standardised with the multi-year (1901–2010) daily mean and standard deviation for the respective day of the year. Moreover, we defined as source variable X the standardised evaporation anomalies over land and oceanic grid boxes. During Vb-cyclone events, moisture uptake contributing to precipitation in the selected Odra/Poland region can occur already within the same day. This is, in particular, the case for continental source regions close to the selected river catchment and along the Vb-cyclone pathway, as well as the marginal seas for oceanic source regions. Thus, to keep the presented showcase brief and focused, we applied the TE-linear measure to daily data only with the time lags $\omega =$ 24 hours (i.e., one time step) and $\tau = 0$. In other words, we quantified the reduction in uncertainty about the present state of precipitation in the Odra catchment when knowing the state of evaporation during the same day and the precipitation in the Odra region of the day before (i.e., the persistence in precipitation). We refer to this in the following as a zero-day time lag between the source and target variables.

For calculating the TE, we applied a parametric estimation of TE, called TE-linear, which is based on a multivariate Gaussian assuming linear interactions (applicable as the standardised anomalies of precipitation averaged over the selected region of interest and evaporation at individual grid cells were approximately Gaussian distributed). Unlike non-parametric estimations of TE, the parametric estimation of TE (i.e., TE-linear) is relatively straightforward and robust, because it is less sensitive to the length of the time series and free of tuning parameters (POTHAPAKULA et al., 2019). We performed a significance test for the TE-linear measure with a significance level of 0.05 by considering 100 permuted surrogates of X and Y to test our hypothesis. In the following, we set the information exchange to zero in case it was not significant. For more details on the significance test, we refer to LIZIER (2014). Note that a TE of 0 nats refers to no information exchange, while any significant value above zero is considered as information exchanged in the following (cf. LIZIER, 2014; POTHAPAKULA et al., 2019, 2020). The applied source code is available at Zenodo (POTHAPAKULA et al., 2021).

7.3 Information exchange to heavy Vb-cyclone precipitation

Figure 7.2 shows the information exchange from local oceanic evaporation anomalies to precipitation in the Odra catchment during the whole summer season (JJA, left panel) and during the 100 highest ranked Vb-cyclone precipitation events (right panel). During the summer season, we detected high information exchange of more than $1.0 \cdot 10^{-2}$ nats (cf. range of values in POTHAPAKULA et al., 2019, 2020) from the evaporation over the North Sea, Bay of Biscay, and Gulf of Lion. During the heavy precipitation Vb-cyclones, the western basin of the Mediterranean Sea and the Adriatic Sea show the highest information exchange to the event precipitation. Besides, the information exchange is above $2.0 \cdot 10^{-2}$ nats for evaporation over the North Atlantic, east of Greenland, where sometimes strong large-scale ocean evaporation occurs (AEMISEGGER, 2018).

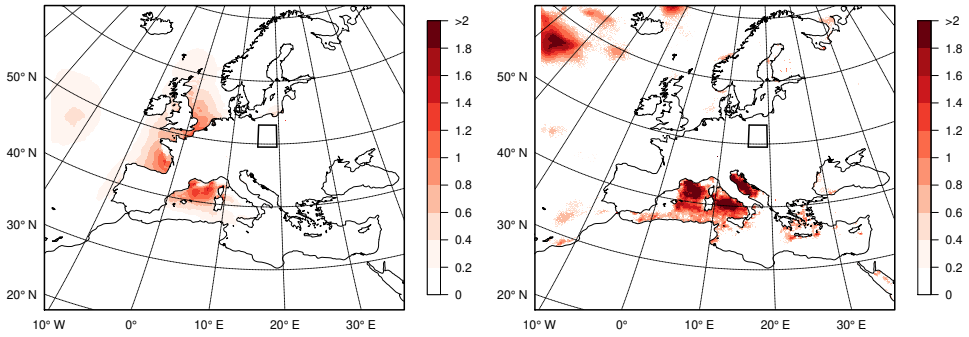

FIGURE 7.2: Significant information exchange (TE-linear, in 10^{-2} nats, bootstrapping with 0.05 significance level) from evaporation over the marginal seas (source) to total precipitation in the Odra catchment (target, black rectangle) during the summer season (JJA, left) and during the corresponding 100 highest ranked Vb-events (right) from 1901 to 2010.

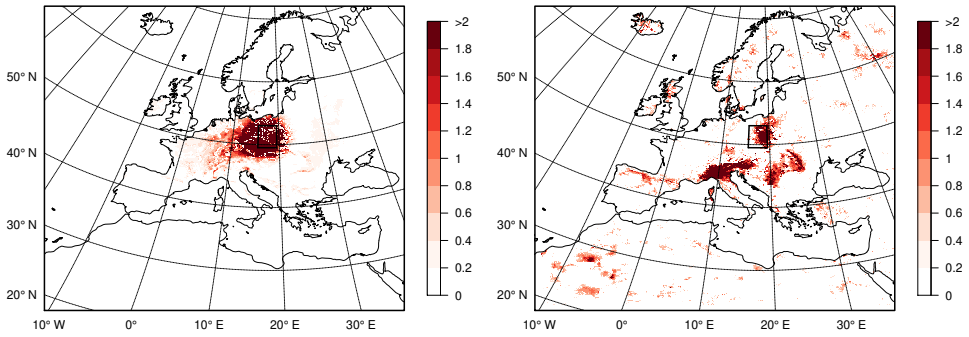

FIGURE 7.3: Same as Figure 7.2 but for evaporation anomalies over the land.

The information exchange of evaporation anomalies over land during the summer season is highest (TE-linear $> 2.0 \cdot 10^{-2}$ nats, Figure 7.3) within the selected region in the Odra catchment and surrounding surfaces, in particular, north of the Alps and westwards of the Odra catchment, which corresponds to westerlies. For the selected Vb-events, several regions with high information exchange were detected, especially the southern Alpine region, the Carpathian mountains, and the eastern part of the selected catchment region (Figure 7.3).

7.4 Discussion

The enhanced information exchange over the Mediterranean Sea during heavy precipitation Vb-cyclones is in line with previous studies that conclude a sensitivity of precipitation in Central Europe to Mediterranean Sea surface temperatures (VOLOSCIUK et al., 2016; MESSMER et al., 2017), even though the Mediterranean moisture contribution to Vb-cyclone precipitation was only minor compared to other oceanic source regions during several past Vb-flood events (e.g., WINSCHALL, 2013; WINSCHALL et al., 2014; GRAMS et al., 2014; KELEMEN et al., 2016; KRUG et al., 2020a). A possible reason for this might be an intensification of the Vb-cyclones during their early stages by the short-range transport of Mediterranean moisture and associated latent-heat release. Moreover, Mediterranean moisture may be relevant

for pre-moistening some continental moisture uptake regions. The latter hypothesis is supported by the enhanced information exchange of continental evaporation along the typical Vb-cyclone pathway from northern Italy along the eastern fringe of the Alps towards northern and eastern Central Europe. Note that the TE in that area is similar but more homogenous for soil moisture (appendix E, left panel of figure E.2). Thus, the TE approach applied to evaporation does not quantify the overall moisture uptake of precipitation like with Lagrangian diagnostics, but it detects the source regions associated with a precipitation intensification.

However, one has to be cautious with the interpretation of detected regions with high information exchange because information theory methods and other statistical approaches like correlation analyses give only indications of causative processes but no clear evidence. Moreover, detected information exchange which is distant to the Odra region does not necessarily imply a direct link of evaporation in these remote regions and precipitation in the Odra catchment via atmospheric moisture transport, especially if short time lags are used in equation (7.1). Examples of remote regions with high information exchange are the enhanced information exchange from the south-east of Greenland in Figure 7.2 (right panel) or from areas in eastern Europe and northern Africa in Figure 7.3 (right panel). These areas might be linked with contributing moisture uptake regions via common drivers, for example, an atmospheric blocking high.

Furthermore, the information theory approach reveals no information about the sign of the anomalies of interest. For example, the information exchange from the Mediterranean Sea surface temperatures (appendix E, figure E.1) shows a similar pattern like evaporation (7.2, right). One might deduce that high sea surface temperatures in the western basin enhance the moisture uptake there. However, KRUG et al. (2020a) showed that the opposite is the case: evaporation was intensified by high wind speeds and thus associated with lower SST anomalies for the highest precipitation impact Vb-cyclones, as selected in our study.

Our results with TE-linear are complementary to previous studies using Lagrangian moisture diagnostics or Eulerian moisture tagging. In contrast to these approaches, an advantage of the TE-linear method is that already a limited number of variables (i.e., total precipitation and evaporation) on a daily time scale provides the required information. For example, the TE-linear calculation without bootstrapping lasts for the 100 selected Vb-cyclone events and all source grid points less than one minute on a standard personal computer. For a moisture tagging analysis, however, tracer particles have to be implemented directly in the simulation. For Lagrangian analysis, temporally and spatially high-resolved 4D variables like atmospheric pressure, specific humidity, or wind fields are needed. The computational effort regarding only the input data is increased in comparison with TE-linear by a factor of the number of additionally used variables, times the number of vertical levels, times a factor of 8 if 3-hourly data is used instead of daily aggregations. Thus, TE-linear is significantly less computationally intensive with robust results.

7.5 Conclusions

The asymmetric information exchange measure TE-linear proofed as a useful tool for detecting the drivers of precipitation intensification in the Odra catchment. Our results show an enhanced information exchange to heavy Vb-cyclone precipitation from evaporation over the Mediterranean Sea and the European continent along the Vb-cyclone pathway. These findings are in accordance with previous studies which conclude a particular role of the Mediterranean Sea in precipitation intensification (VOLOSCIUK et al., 2016; MESSMER et al., 2017) and moisture uptake over the continental surfaces (e.g., WINSCHALL et al., 2014; KELEMEN et al., 2016). Future studies might use the TE-linear approach to investigate potential hydro-climatic drivers and teleconnections of other flood types, such as rain-on-snow floods (MERZ et al., 2020; KRUG et al., 2020b). In particular, large data amounts and long time series can be analysed robustly and computationally efficiently, for example, to filter out relevant variables, and regions. The associated processes can then be studied in further detail with other, more computationally intensive methods like Lagrangian backward trajectories.

Chapter 8

Convective rainfall during Vb-cyclone events

FIGURE 8.1: Flooded street „Borngasse“ in Döbeln (Saxony) due to the Vb-cyclone flood in August 2002. The photography was taken by Sonja Strini on the 19.08.2002.

Even though Vb-cyclones occur throughout the year, they are mainly associated with heavy precipitation and extreme floods in late spring and summer (PETROW et al., 2007; NISSEN et al., 2013; NIED et al., 2014). Recent events were the Elbe flood in August 2002 with a total precipitation sum of 312 mm within 24 h at Zinnwald-Georgenfeld (12.08.2002, 6 UTC - 13.08.2002, 0600 UTC; ULBRICH et al., 2003a; RUDOLF and RAPP, 2003) and the Elbe/Danube flood in June 2013 with a total precipitation sum of 405.1 mm within 96 h at Aschau-Stein (30.05.2013 6 UTC – 03.06.2013 6 UTC; STEIN and MALITZ, 2013). Both station-based observations correspond to a return period of more than 100 years (RUDOLF and RAPP, 2003; STEIN and MALITZ, 2013). Several factors favour Vb-cyclone precipitation with high rainfall amounts during the summer half-year. These are a higher water holding capacity (following the Clausius-Claperyon rate of about 7%°C^{-1} change of saturation vapour pressure at typical surface temperatures; MESSMER et al., 2015), higher Mediterranean SSTs and the associated moisture flux (VOLOSCIUK et al., 2016; MESSMER et al., 2017, see chapter 6), and convective processes that increase the efficiency of precipitation generation in summer (MESSMER et al., 2017). In the following chapter, the role of convective precipitation during selected Vb-cyclone events is investigated (i.e., the fourth research question stated in chapter 4).

8.1 Convective rainfall in regional climate simulations

Convective processes are of particular interest in the context of a warming climate. Studies on precipitation measurements observed a scaling of extreme precipitation larger than the Clausius-Clapeyron (CC) rate on a sub-daily timescale when air temperatures are about 15 °C to 23 °C in Europe (LENDERINK and VAN MEIJGAARD, 2008, 2010; PURR et al., 2019). A similar precipitation scaling was also observed in other climate zones, such as Hong Kong (sub-tropical climate, LENDERINK et al., 2011) or Australia (HARDWICK JONES et al., 2010, multiple climate zones including sub-tropical climate). For temperatures above 26 °C, the availability of atmospheric moisture becomes a limiting factor of extreme precipitation (HARDWICK JONES et al., 2010). In particular, convective rainfall temperature scaling corresponds to the so-called super Clausius-Clapeyron rate, while stratiform precipitation shows a scaling close to the CC rate (BERG et al., 2013). Thus, convective rainfall dominates extreme precipitation events with increasing temperature (BERG et al., 2013).

Several hypotheses have been proposed for the super-CC effect (TRENBERTH et al., 2003; LENDERINK and VAN MEIJGAARD, 2008). One concludes an increased updraft within the convective cell inducing a large-scale moisture convergence and larger convective systems due to higher surface dew point temperatures (LENDERINK et al., 2017). Besides, higher temperatures can change the dynamics of convective cells and lead to highly organized convective cell clusters with higher rainfall intensities (PENDERGRASS et al., 2016). In a warming climate, Vb-cyclone precipitation might show higher intensities if Vb-cyclone events are associated with convective rainfall for a substantial amount.

For the August 2002 flood, RUDOLF and RAPP (2003) estimated a convective rainfall fraction of one third and a doubling of precipitation due to orographic ascend based on a subjective synopsis of observational data. However, so far, no quantitative analysis was performed for past Vb-cyclone events. For analysing convective cells,

temporally (i.e., from minutes to about one hour) and spatially highly resolved data (at least on a kilometre scale) is crucial. Weather radar data could be considered as observation data basis. However, radar-based precipitation climatologies are only available for recent years and cover a short time period. For example the German radar-based climatology covers the years from 2001 to 2017 (WINTERRATH et al., 2018). An alternative data basis for analysing several extreme Vb-cyclone events are high-resolution regional climate simulations driven by atmospheric reanalysis data.

In coarser gridded regional climate simulations ($\Delta x > 5\,\text{km}$), deep convection is a subgrid process and therefore parameterised with convection parametrisation schemes. The review of PREIN et al. (2015) gives an overview of the challenges of such parameterisation schemes: For example, the representation of entrainment and detrainment of convective cells (DE ROOY et al., 2013; BECKER and HOHENEGGER, 2021), the soil-moisture precipitation feedback (HOHENEGGER et al., 2009; LEUTWYLER et al., 2021), the initialization of deep convection, and the precipitation efficiency (e.g., EMANUEL, 1991; GOCHIS et al., 2002; SAEED et al., 2017) remains schematic and causes high uncertainties in the climate sensitivity (KNIGHT et al., 2007; SHERWOOD et al., 2014; SCHNEIDER et al., 2017). Besides, the daily precipitation cycle is usually poorly represented (e.g., BROCKHAUS et al., 2008; KNIST et al., 2020) and the hourly precipitation maxima are underestimated (e.g., BAN et al., 2014). Despite of recent progress and improvements (e.g., DONNER et al., 2011; BECHTOLD et al., 2014), inconsistencies and errors due to inherent assumptions in convection schemes remain (e.g., JONES and RANDALL, 2011; HWONG et al., 2021).

The deep convection parametrisations can be turned off in regional climate simulations with high spatial resolutions at a kilometre scale ($\Delta x < 4\,\text{km}$, WEISMAN et al., 1997). The so-called convection-permitting simulations (CPS) partly overcome the above-mentioned issues of deep convection parametrisation schemes due to the improved representation of physical processes. CPS have a substantial added value in the simulation of precipitation, especially on sub-daily time scales (BRISSON et al., 2017). Coarser gridded regional climate models simulate the afternoon convective rainfall peak at mid-latitudes several hours before the observed maximum (BROCKHAUS et al., 2008; WALTHER et al., 2013). CPS improve the diurnal cycle of hourly precipitation (BAN et al., 2014; KENDON et al., 2012; CHAN et al., 2013; FOSSER et al., 2015; BRISSON et al., 2016a; PURR et al., 2019, 2021) and simulate the observed super-CC rate of extreme precipitation better than non-convection permitting simulations (BAN et al., 2014; PURR et al., 2021). On a daily scale, precipitation is improved mainly due to a better spatial representation of steep orography (PREIN et al., 2013; BRISSON et al., 2017). Furthermore, precipitation intensities for spatial scales below 50km are improved by CPS in comparison with regional climate simulations of around 12km grid size (PREIN et al., 2013; BRISSON et al., 2017). In addition, the diurnal variation of cloud cover is also improved (LANGHANS et al., 2013) due to the better representation of high range convection (BRISSON et al., 2016a). This also affects the shortwave and longwave net radiation (PREIN et al., 2013; FOSSER et al., 2015) and has a positive effect on the simulation of the diurnal cycle of surface temperature (BAN et al., 2014). Some issues remain, such as the representation of turbulence or the planetary boundary layer (PREIN et al., 2017) and shallow convection which has to be parametrized in CPS (BRISSON et al., 2017). CPS are usually applied over a limited area due to their high computational demands (SCHÄR et al., 2020).

TABLE 8.1: Past Vb-cyclones events associated with floods in Central Europe, the start and end date of the eleven-day analyses period, and corresponding total event precipitation $precip_{\text{tot}}$ and convective precipitation $precip_{\text{conv}}$ averaged over the central European domain (denoted with 0 in Figure 8.2).

No	start date	end date	References (e.g.,)	$precip_{\text{tot}}$ (mm/11days)	$precip_{\text{conv}}$ (mm/11days)
1	08.07.1903	18.07.1903	KELLER (1903)	32.0	10.2
2	23.10.1930	02.11.1930	FRIEDRICH (1930)	19.4	0.0
3	17.05.1949	27.05.1949	KRESSER (1957, Tab. 1)	54.2	12.0
4	28.06.1954	08.07.1954	BLÖSCHL et al. (2013)	51.5	7.0
5	15.08.1977	25.08.1977	NAUMANN et al. (1978)	47.1	7.7
6	15.07.1981	25.07.1981	AKHTAR et al. (2019)	62.0	7.7
7	07.08.2002	17.08.2002	SODEMANN et al. (2009)	55.4	10.0
8	17.08.2005	27.08.2005	WINSCHALL (2013)	41.4	11.6
9	12.05.2010	22.05.2010	WINSCHALL et al. (2014)	101.8	8.5

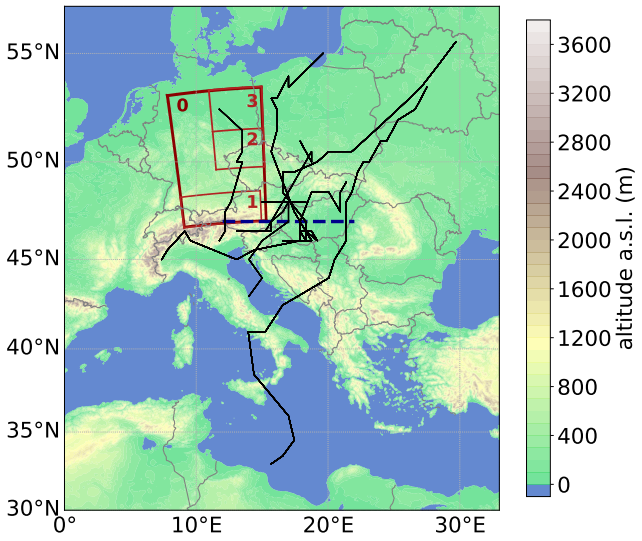

FIGURE 8.2: The black lines display the trajectories of the selected Vb-cyclones (crossing northeastward the latitude 47°N, blue dashed line). The model orography of the CPS is indicated with colour shades and red boxes show the regions of interest for the analyses of the convective rainfall fraction.

We performed CPS to investigate the role of convective rainfall during historic Vb-cyclone events associated with summer floods in the Danube, Elbe, or Odra catchment from 1901 to 2010. For this, we used the regional climate model COSMO-CLM ROCKEL et al. (2008) in a convection permitting setup that captures the convective shower characteristics well (BRISSON et al., 2018; PURR et al., 2019). We quantified the convective rainfall fraction by tracking all convective cells during the time period of interest with the approach of BRENDEL et al. (2014) which was further developed in BRISSON et al. (2018) and PURR et al. (2019).

8.2 Data and Methods

8.2.1 Event selection

We selected past Vb-cyclone events associated with floods in Central Europe based on Vb-cyclone tracks in the dynamically downscaled ERA-20C reanalyses (shown as black lines in Figure 8.2, KRUG and AHRENS, 2020) and literature review (Table 8.1 gives some references; see also chapter 6). Afterwards, we selected the days of interest with heavy precipitation in Central Europe. For all selected events, the investigated time period was eleven days and started about three days prior of the heavy precipitation (Table 8.1).

8.2.2 Convection permitting simulations

We took advantage of the cenntenial ECMWF twentieth century reanalysis (ERA-20C; POLI et al., 2016) for analysing historic Vb-cyclone events including floods during the early decades of the 20th century. Since the horizontal resolution of ERA-20C is relatively coarse gridded with about 125 km (spectral truncation T159), we performed our CPS with an intermediate nest, as suggested by BRISSON et al. (2016b).

In a first nest, we downscaled the centennial reanalysis over an extended EURO-CORDEX domain (GIORGI et al., 2009) to a horizontal resolution of about 12 km ($\Delta x = 0.11°$; KRUG et al., 2020b, 2021). The downscaling was performed with the regional coupled atmosphere-ocean model setup COSMO-CLM+NEMO (more details are given in section 2.2.2; PRIMO et al., 2019; KRUG et al., 2020b, 2021). In a second nest, we performed CPS over the MED-CORDEX domain (RUTI et al., 2016) with COSMO-CLM v5.0 ($\Delta x = 0.0275°$; ~3 km) laterally nudged towards the regional coupled atmosphere-ocean simulation with Davis relaxation scheme and hourly updates as recommended in AHRENS and LEPS (2021). The figures and tables in this section show the CPS after a relatively short spin-up time of two days as motivated by the study of STUCKI et al. (2020). The parametrisation of deep convection was turned off for the CPS and the shallow convection was parametrised after TIEDTKE (1989). Moreover, we applied a one-moment microphysics scheme including graupel, like recommended in BRISSON et al. (2016b) to improve the representation of deep convection (PURR et al., 2019, 2021).

Figure 8.3 shows the spatial distribution of the total event precipitation sums averaged over the selected events of interest since 1950 when E-OBS gridded observation data (v22.0e, ensemble mean; CORNES et al., 2018) was available for comparison. As expected precpitation was mainly triggered along the Alpine and Ore mountain regions. In our CPS data, precipitation over south-east Germany, the Bohemian Massif, and Ore mountains is underestimated, probably because the total precipitation is significantly overestimated over the Alps and a substantial amount of atmospheric moisture is already removed from the atmosphere upstream of the Ore mountain region. Nonetheless, a north-south and west-east gradient of precipitation is prominent in both data sets which is in accordance with the northward Vb-cyclone pathway over eastern Central Europe.

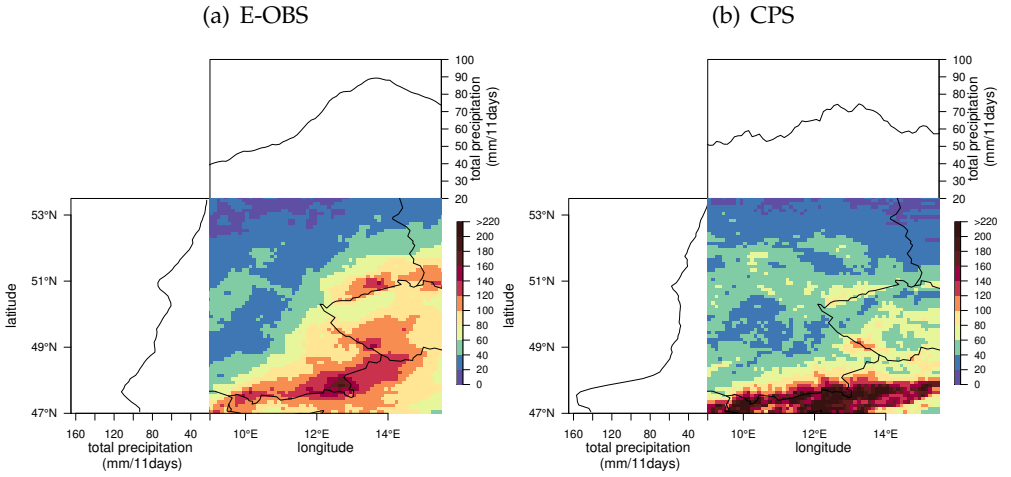

FIGURE 8.3: Spatial distribution of total event precipitation (1954, 1977, 1981, 2002, 2010 Vb-cyclone events, Table 8.1) in (a) E-OBS observation data and (b) the CPS simulations.

8.2.3 Convective cell tracking

We tracked convective cells based on 5 min total precipitation and wind fields in our CPS to quantify the convective rainfall fraction. The convective-cell tracking algorithm was first presented in BRENDEL et al. (2014) and refined in BRISSON et al. (2018) and PURR et al. (2019). Firstly, a convective cell is identified by all neighbouring grid cells with a precipitation intensity higher than 8.5 mm/h within 5 min. Secondly, the most likely location of the convective cell of interest is determined in the following time step by taking the low- to mid-tropospheric wind fields into account (cf. BRISSON et al., 2018). If a convective cell is detected in this area, it is associated with the convective cell of interest in the time-step before. The convective cell trajectories are detected by repeating these two iteration steps for all convective cells and time steps (BRENDEL et al., 2014; BRISSON et al., 2018; PURR et al., 2019, 2021). Such a Lagrangian approach has a relatively low sensitivity to spatial or temporal shifts in the model data as compared to observations (BRISSON et al., 2018). Furthermore, errors due to misplacement of convective cells in model simulations is reduced in contrast to Eulerian approaches (BRISSON et al., 2018).

Since precipitation during Vb-cyclones is mainly triggered along the west-east oriented mountain ranges (e.g., GRAMS et al., 2014), we analysed the convective rainfall fraction in four subregions (Figure 8.2): (0) the Central European domain, (1) the Alps and Alpine foothills region, (2) the Elbe/Ore mountain area, and in contrast to these, (3) parts of the middle Elbe region in the North German Plain.

8.3 Convective rainfall fraction during Vb-events

Table 8.1 lists the total precipitation sums and convective precipitation sums averaged over the central European domain (denoted with 0 in Figure 8.2). The highest rainfall amounts occurred during the 2010 (101.8 mm within eleven days), 1981, and 2002 Vb-cyclone events. We observed the lowest rainfall during the 1903 and 1930

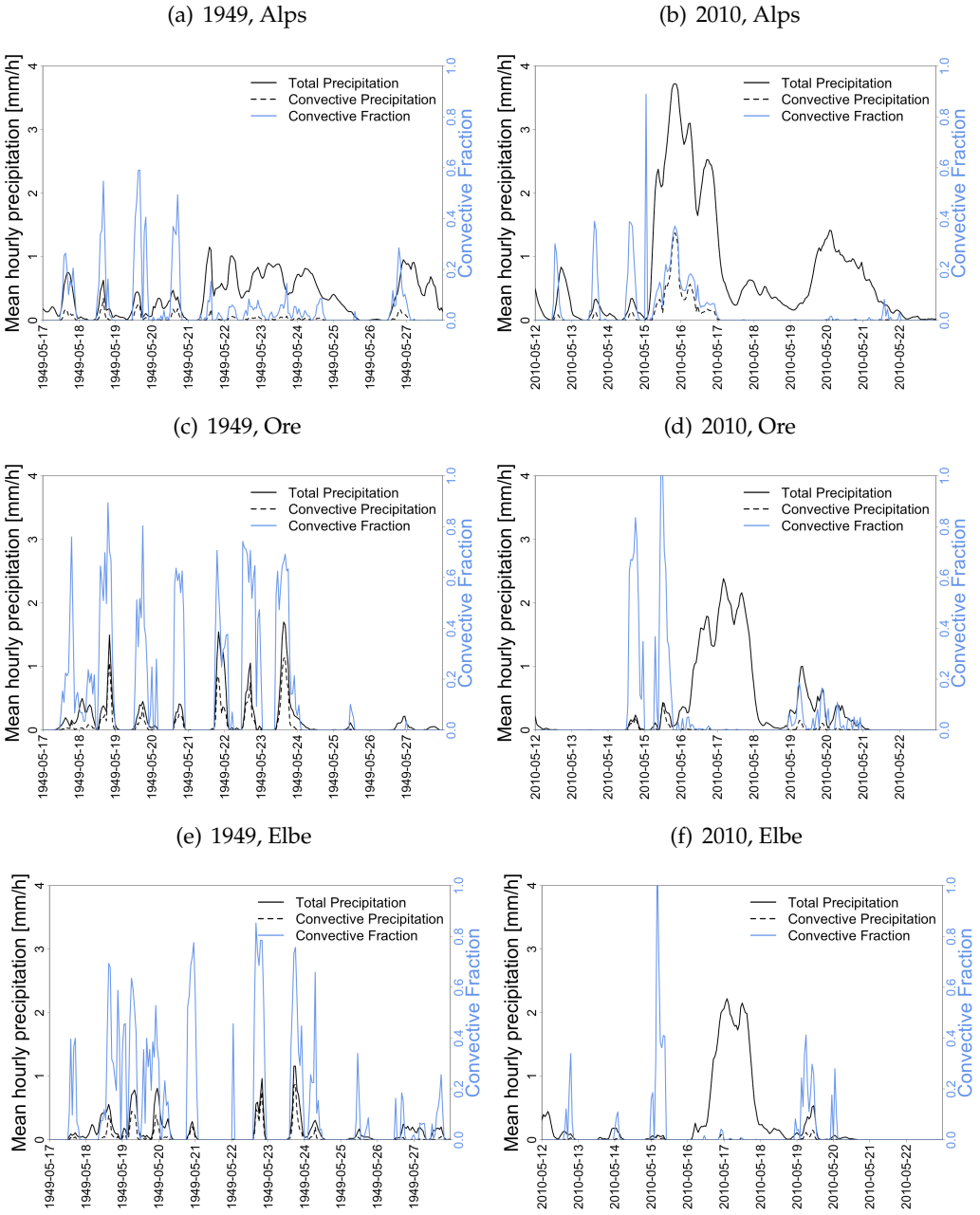

FIGURE 8.4: Total precipitation, convective precipitation, and convective rainfall fraction in the selected regions of interest (see Figure 8.2) during the Vb-cyclone floods in May 1949 and May 2010.

events, even though the convective rainfall sums were comparatively high during the 1903 Vb-cyclone compared to the 2002 event. As expected, we detected negligible convective rainfall during the 26.10.1930 and 31.10.1930 based on our classification of convective cells.

The convective rainfall fraction can substantially vary throughout the events. Figure 8.4 illustrates the temporal event evolutions for the May 2010 event with the highest total precipitation sum and the May 1949 event with the largest convective precipitation amount and the second largest convective rainfall fraction (after the August 2005 event). In all selected regions of interest, the hourly total precipitation sums

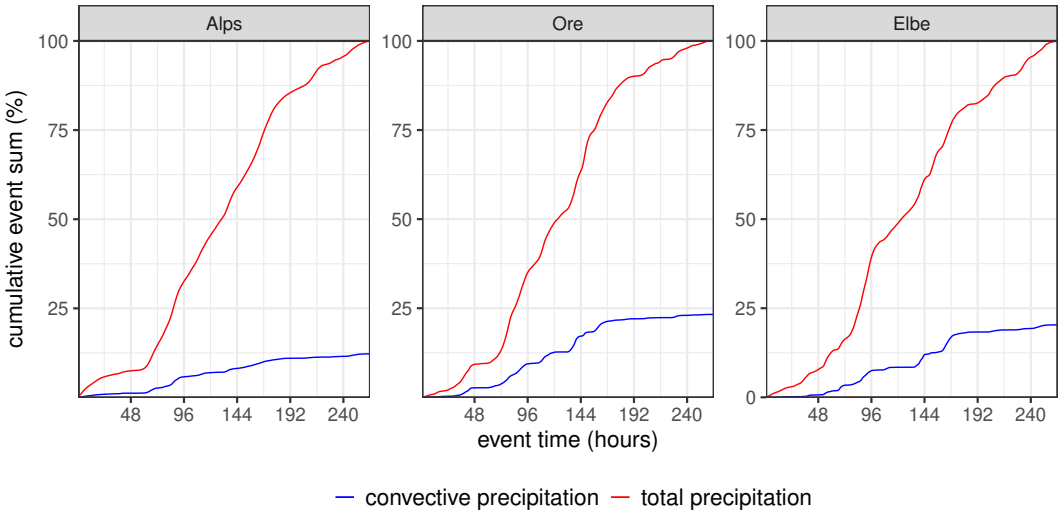

FIGURE 8.5: Cumulative sums of total precipitation and convective precipitation averaged over all Vb-cyclone events listed in Table 8.1 and regions of interest.

show a predominant daily cycle during the event in 1949 and during the first event days in 2010 which is mainly driven by convective rainfall processes in the afternoon. The corresponding convective rainfall fraction exceeds often 60% and reaches more than 90% on the 18.05.1949, 15.05.2010, and 19.08.2005 (Elbe region, not shown here). During the second half of the May 2010 event, stratiform precipitation dominates, especially in the Alpine region, and no daily cycle is evident. Note that the high stratiform rainfall amounts during the 15.05.2010 to 17.05.2010 started in the Alpine region and reached peak values later on in the Ore mountain and Elbe catchment region possibly related to the typical Vb-cyclone pathway.

On average, convective rainfall dominates during the first half of the investigated events in all selected regions of interest. The overall convective rainfall fraction was above 10% on average for the Alpine area, and more than 20% for the Elbe and Odra region (see Figure 8.5), which is in the order of magnitude of convective rainfall fractions in Germany shown in PURR et al. (2021). The similar convective rainfall fractions in mountainous and flatlands, such as the middle Elbe area, are in line with the LENGFELD et al. (2019) who detected hourly rainfall regardless of orography in German weather radar data (LENGFELD et al., 2019).

8.4 Discussion

We detected considerable convective rainfall fractions during the selected past Vb-cyclone events exceeding often 60%. As expected, the only exception was the Vb-cyclone event in October/November 1930 with no significant convective rainfall and only small total precipitation amounts. That is in line with RUDOLF and RAPP (2003) who concluded convective rainfall as an important ingredient for the Vb-cyclone flood event in August 2002 and MESSMER et al. (2017) mentioning convective processes relevant for Vb-cyclone precipitation during the summer season.

In the context of a warming climate, we expect an increase of the mean intensity per convective cell (PURR et al., 2021) linked to the super-CC scaling of extreme convective rainfall (BERG et al., 2013). Thus, as discussed in MESSMER et al. (2020), the convective processes, together with enhanced moisture fluxes over the Mediterranean Sea, might compensate the expected drying of the European continent (e.g., PAL et al., 2004) which is a relevant moisture source during Vb-cyclone events (e.g., KELEMEN et al., 2016; KRUG et al., 2020a). That is in line with the studies of MITTERMEIER et al. (2019) and NISSEN et al. (2013) detecting a significant increase of precipitation intensities during Vb-cyclones in a warming climate, while the Vb-cyclone frequency shifts with a decrease of events during summer and an increase during spring.

Not only the total amount of convective rainfall is relevant but also the timing of the maximum convective rainfall intensities. Convective rainfall has a predominant daily cycle with two peaks. The main peak during the afternoon is linked to the initiation of deep convection by solar radiation heating the ground surface and destabilizing the atmospheric boundary layer (PURR et al., 2021). Several hypothesis exist for the night-time peak which is more dominant in sub-tropical and tropical areas (YANG and SMITH, 2006; NICHOLLS, 2015; RUPPERT and HOHENEGGER, 2018). One assumption is that upper-level cooling due to the longwave emissions from deep convective cloud tops might enhance convection during night (RUPPERT and HOHENEGGER, 2018). MEREDITH et al. (2019) and PURR et al. (2021) deduce under future climate conditions (RCP8.5) an increasing frequency of convective cells during the night and early morning hours and a decrease during the afternoon. If the diurnal cycle of the convective precipitation coincides with the stratiform Vb-cyclone precipitation, especially high precipitation intensities are triggered. Thus, even though Vb-cyclones might be less frequent during summer in a warming climate, they may be associated with more extreme precipitation intensities in the afternoon and early morning hours and are highly relevant for future flood protection management.

The observed pronounced daily precipitation cycle driven by high convective rainfall amounts during the afternoons (Figure 8.4) can impact the timing of flood peaks and flood wave superposition of tributary rivers. This motivates the application of CPS for hydrological flood analyses, including also sensitivity studies for worst-case scenarios. However, the CPS data presented in this chapter did not capture the observed precipitation amounts in small mesoscale catchments, such as the Mulde catchment, well enough. With an overestimation of (stratiform) precipitation in the Alpine region, the amount of precipitation downstream of the Vb-cyclone pathway is reduced. Also the convective rainfall fraction in the Alpine region might be underestimated because of the simulated high stratiform precipitation amounts in that area (Figure 8.3; Figure 8.4a, b). Besides, the applied method could underestimate the number of convective cells over higher mountain ranges because orographically induced convection has a lower intensity at this early stage in the life cycle (PURR et al., 2019).

The observed misplacement bias of precipitation in our CPS (Figure 8.3) might be linked to the used ERA-20C reanalysis data that is based solely on surface observations due to data availability during the early decades of the 20th century (POLI et al., 2016). The same model setup using the European Centre for Medium-Range Weather Forecast Interim Reanalysis (ERA-Interim; DEE et al., 2011) produced more

a more realistic spatial precipitation distribution compared to radar data in the study of PURR et al. (2019) and PURR et al. (2021). The double-nesting in our CPS can favour space-time shifts of the simulated precipitation events. New atmospheric reanalyses data with a higher spatial resolution compared to ERA-20C allow running a CPS without an intermediate nest (AHRENS and LEPS, 2021). The study of RAFFA et al. (2021) shows that CPS with COSMO-CLM without two-step nests in ERA-5 reanalysis (HERSBACH et al., 2020) tend to perform better (especially in the case that no spectral nudging was applied) than the two-step nest approach while the computation costs are reduced.

8.5 Conclusions

We investigated the convective rainfall fraction during past Vb-cyclone events associated with floods in 1903, 1930, 1949, 1954, 1977, 1981, 2002, 2005, and 2010. Overall, we detected considerable convective fractions exceeding one third in the Alpine area and the Elbe catchment region, especially during the afternoons. Thus, deep convection and associated rainfall is an essential ingredient for flood intensification during summer, in particular in a warming climate (super Clausius-Clapeyron scaling; BERG et al., 2013). The pronounced daily cycle due to convective processing in the afternoon might affect the timing of floods and tributary river flow superposition. Extreme rainfall intensities and amounts can occur when the convective rainfall peak coincides with the stratiform precipitation associated with the Vb-cyclone. This points towards the role of convection-permitting simulations and high-resolution observation data like radar-based precipitation climatologies in analysing the atmospheric flood circumstances and worst-case scenarios.

Chapter 9

Concluding remarks

9.1 Key findings

Initially, hydrological flood analysis was focused on the local catchment scale and pure statistical analysis, for example, in terms of fitting mathematical models to runoff measurements while disregarding the physical processes (KLEMEŠ, 1974). During the past decades, the flood analysis has shifted towards larger spatial scales (e.g., LEHNER et al., 2006; UHLEMANN et al., 2010) and more process understanding such as the discussion of flood occurrence and characteristics in dependence of hydro-meteorological drivers (e.g., NIED et al., 2014; TARASOVA et al., 2019). Thus, hydrologists have increasingly become aware of the physical flood drivers beyond the local catchment scale (MCGREGOR, 2019). Thereby the atmosphere is a relevant flood driver because it acts as the main moisture supply of river catchments. The atmosphere influences floods on various temporal and spatial scales ranging from convective showers triggering local flash floods to internal climate variability, such as the North Atlantic oscillation adding predictability in long-range forecasts of winter rainfall in Great Britain (SVENSSON et al., 2015). Despite an increasing need for understanding the hydroclimatic flood drivers (HIRSCHBOECK, 1988) in the context of climate change and river flood forecast, there is still a knowledge gap on the causative processes of extreme flood events.

In particular, floods which affect several macro-scale river basins simultaneously can cause devastating damage. Future flood-risk assessment of trans-basin floods depends significantly on the knowledge about the causing atmospheric conditions and external climate drivers. Nonetheless, only a few studies have investigated widespread floods, their occurrence frequency, and their underlying hydro-meteorological processes. In this context, the presented thesis aims to further contribute to the knowledge of the hydro-climatic drivers of widespread floods in Central Europe since 1900. For doing so, we took advantage of a dynamically downscaled reanalysis over the whole past century which served as a physically consistent and four-dimensional atmospheric reference. The ERA-20C reanalysis was dynamically downscaled with the coupled regional atmosphere-ocean model COSMO-CLM+NEMO to a horizontal resolution of 0.11° (PRIMO et al., 2019; KRUG et al., 2020b). Based on this, we could study the atmospheric circumstances and

hydro-climatic flood drivers of extreme floods with a high spatial and temporal resolution. In particular, the extreme floods during the early decades of the 20th century could be studied in such a detail for the first time (e.g., the summer floods during 1903 and 1926). In the following, the key findings of the presented work are summarised.

What were the most widespread and severe floods in Central Europe during the 20th century?

The classification of trans-basin floods affecting several macro-scale river catchments is a special challenge because it has to be applicable to various catchments with different runoff characteristics. Therefore, the distribution-free ordinal classification of FISCHER and SCHUMANN (2018) was applied to GRDC data in cooperation with Ruhr-University Bochum (Andreas Schumann, Svenja Fischer). We selected only gauges within the German administrative boundaries to fulfil the requirement of a long timeseries (starting in 1920). The seasonality of flood drivers was addressed by analysing half-yearly maximum discharge time series. All of the most widespread floods with high discharges (corresponding to at least a 15-year flood) in the Rhine, Elbe, and Danube catchment occurred during the winter half-year. Interestingly, these trans-basin winter floods showed a temporal clustering with flood-rich years in the 1940s and 1980s, and flood-poor years in the 1930s or 1950s on the contrary. The trans-basin summer floods affected only the Elbe and Danube catchment with very large peak discharges and were associated with so-called Vb-cyclones propagating from the Mediterranean Sea north-eastward to Central Europe (with the exception of the Rhine flood in May 1983). We could not detect specific flood-rich decades of trans-basin summer floods since 1920, but observed particular high peak discharges during the past two decades.

Do possible hydro-climatic drivers of the observed temporal clustering of rain-on-snow events exist?

Most of the classified trans-basin floods were caused by the coincidence of rainfall and snowmelt. Note that during such compound events, often not the extremeness of the causing components (e.g., rainfall and snowmelt) but their unusual timing triggers extreme flood events (KLEMEŠ, 1993). Therefore, we investigated the interannual to decadal variability of such rain-on-snow events by building an atmospheric proxy based on snow cover and total precipitation. As expected, the temporal variability of our proxy largely corresponds to flood-rich and flood-poor periods. Based on this, we analysed potential climate drivers of such flood events. We found a negative correlation of the Scandinavian pattern (SCA) and total precipitation, as well as a negative correlation between the North Atlantic Oscillation (NAO) index and large snow cover. The latter is supported by the fact that snowfall in advance of the floods was often associated with a cyclone track over the Mediterranean Sea which often corresponds to the negative NAO phase. Overall, spatially extended floods in Germany occurred during the 20th century predominantly, when the superposition of NAO and SCA index was negative.

Which processes are associated with heavy precipitation during Vb-cyclone events?

Even though Vb-cyclones occur frequently with about four to ten events per year, only a few were associated with extreme floods during the past century. Therefore,

we analysed the processes intensifying Vb-cyclone precipitation with a special focus on well-known historic floods. In detail, we investigated from where the flood-producing rainfall originated (i.e., the moisture source regions) and how high the convective rainfall fractions were.

What is the role of various moisture source regions, especially the Mediterranean Sea, in precipitation during Vb-cyclones?

Past studies on recent extreme floods caused by Vb-cyclones point towards diverse moisture source regions (e.g., SODEMANN et al., 2009; GANGOITI et al., 2011b; GRAMS et al., 2014; KELEMEN et al., 2016). In particular, the role of the Mediterranean Sea seams to be contradictory (MESSMER et al., 2017). To extend the previous studies, we analysed the moisture sources of 16 past flood events since 1900 with Lagrangian diagnostics. Moreover, we analyse the source region characteristics (e.g., soil moisture, sea surface temperature) during 1107 Vb-events from 1901 to 2010 based on ERA-20C reanalysis dynamically downscaled with COSMO-CLM+NEMO. We observe moisture contributions by various source regions highlighting the complex dynamical interplay of different air masses leading to moisture convergence during Vb-cyclones. Overall, up to 80% of the precipitation originates from the European continent, indicating the importance of continental moisture recycling, especially within the respective river catchment. Other major moisture uptake regions are the North Sea, the Baltic Sea, the North Atlantic, and for some events the Black Sea. Remarkably, anomalies in these oceanic source regions show no connection to Vb-cyclone precipitation amounts. In contrast, the Vb-cyclones with the highest precipitation are associated with anomalously high evaporation in the Mediterranean Sea, even though the Mediterranean Sea is only a minor moisture source region on average. Interestingly, the evaporation anomalies do not associate with sea-surface temperature but with wind-speed anomalies indicating mainly dynamically driven evaporation. The particular role of the Mediterranean Sea hints towards possible importance of Mediterranean moisture for the early-stage intensification of Vb-cyclones and the pre-moistening of the continental uptake regions upstream of the target catchments. The latter hypothesis was supported by our application of the information theory measure TE-linear to the most intense Vb-cyclone precipitation events in the Odra catchment. We detected significant information exchange from evaporation over the European continent along the typical Vb-cyclone pathway. A noteworthy side outcome of this analysis was that information theoretic approaches like transfer entropy measures proved to be computationally very effective and complementary to more traditional methods such as Lagrangian and Eulerian diagnostics.

How important is convective rainfall during Vb-cyclone floods?

For the first time, we quantified the convective rainfall fraction for selected past flood events since 1901 with a Lagrangian convective cell tracking approach (BRENDEL et al., 2014; BRISSON et al., 2018; PURR et al., 2019, 2021). The ERA-20C reanalysis, dynamically downscaled to a horizontal resolution of about 2.8 km using COSMO-CLM, served as the data basis. As expected, the Vb-cyclones mainly triggered precipitation along west-east orientated mountain ranges such as the Alps due to their meridional pathway. Remarkably, we detected a convective fraction exceeding 60% in mountainous and flatland areas during the afternoons and up to 23% on average. The pronounced daily cycle of convective processing can affect the timing of floods

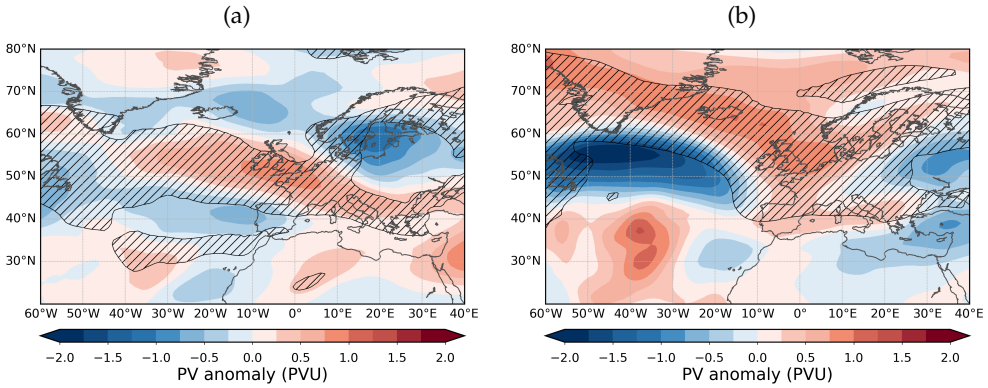

FIGURE 9.1: Potential Vorticity anomaly in ERA-20C (PV; vertically averaged from 500hPa-150hPa; anomalies with respect to monthly mean PV during 1979-2010) for (a) 01.06.1926–18.06.1926 and (b) 21.06.1954–04.07.1954. Black hatches display a standard deviation larger than 0.75 PVU following (GRAMS et al., 2014)).

and tributary river flow superposition. Extreme rainfall intensities and amounts can occur, especially when the stratiform Vb-cyclone precipitation coincides with the convective rainfall peak. Thus, convective rainfall is an essential ingredient for Vb-cyclone induced summer floods, in particular in the context of a warming climate (super Clausius-Clapeyron rate; e.g., BERG et al., 2013; PURR et al., 2021).

9.2 Outlook

The presented work improved the knowledge on atmospheric and hydro-climatic drivers of past widespread floods in Central Europe. However, further research is required to quantify the predictability of the event probability (i.e., predictability of 2nd kind, FRAEDRICH, 2007). The predictability of widespread flood events in Central Europe will be investigated during the second funding phase of the DFG research unit SPATE. The focus will remain on rain-on-snow events and floods induced by Vb-cyclones. The knowledge gained in this thesis will serve as a basis for quantifying the predictability of future flood-producing precipitation event probability, especially in a changing climate.

Regarding widespread winter floods, our analyses indicated an increased flood potential during years of negative NAO and SCA patterns. However, the opposite evolution of the underlying processes, such as increased winter rainfall but reduced spatial extent of snow cover and less ice jam in Central Europe (see chapter 5), impedes the quantification of future flood probability. Therefore, future studies will investigate with a stochastic model of rainfall and snowmelt, to what extent common external climate drivers (including also not yet analysed teleconnections and a warming climate trend) influenced the temporal rain-on-snow variability during the past (KIRSCHNER et al., 2021). The significance of observed and simulated years with high flood frequency could be quantified with a method derived from scan statistics by LUN et al. (2020). Based on these findings, the stochastic rain-on-snow model will be applied to the recently released CMIP6 climate projections (EYRING et al., 2016) that will help to gain further insights into how the flood event processes and the flood event probability could change in the future.

Regarding widespread summer floods, atmospheric blocking conditions might favour flood inducing Vb-cyclone events (HOFSTÄTTER and BLÖSCHL, 2019). That was beyond the scope of this thesis. The unusual meridional cyclone pathway during Vb-events is often associated with quasi-stationary atmospheric highs that block the common zonal cyclone path. Figure 9.1 displays atmospheric blockings associated with Vb-cyclone induced floods in June 1926 and July 1954. In both cases, we detected a blocking high over Scandinavia and south of it, which is in line with HOFSTÄTTER and BLÖSCHL (2019) concluding more frequent Vb-cyclones during Scandinavian blockings and LENGGENHAGER et al. (2019) detecting positive rainfall anomalies upstream of atmospheric blocks. Moreover, previous studies showed that latent heating associated with transient cyclones often prolongs atmospheric blocking situations (PFAHL and WERNLI, 2012; PFAHL et al., 2015; STEINFELD and PFAHL, 2019; STEINFELD et al., 2020). In our context, the latent heat release during the later stages of the Vb-cyclone lifecycle could prolong the atmospheric blocking, which might then induce successive Vb-cyclones (HOFSTÄTTER and BLÖSCHL, 2019). During the presented examples of the flood events in 1926 and 1954, also several succeeding Vb-cyclones were observed (see chapter 3, Figure 3.3; KRUG and AHRENS, 2020; STAHL and HOFSTÄTTER, 2018). The temporally clustered occurrence of Vb-cyclones has a high flood potential. However, further research is necessary on this positive feedback mechanism proposed by HOFSTÄTTER and BLÖSCHL (2019). Our new centennial reanalysis allows the analysis of the physical processes in a high temporal and spatial resolution, not only for recent Vb-events but also for many others during the whole past century. Based on such a long time series, it is possible to gain deeper insights into flood-favouring atmospheric blocking locations, their potential climatic drivers, and feedback processes that enhance the flood potential in Central Europe. Moreover, the representation of potential climate drivers of summer floods including atmospheric blocking events will be evaluated in the new CMIP6 projections (EYRING et al., 2016). The planned research will give more insight into how the flood event processes and the predictability of the event probability of Vb-cyclone induced and rain-on-snow floods will change in the future.

Appendix A

German Summary

Hintergrund

Während sich die Hochwasserforschung zunächst auf die statistische Analyse der hydrologischen Parameter wie Hochwasserstände fokussierte, verlagerte sich die Perspektive in den letzten Jahrzehnten auf eine ganzheitlichere Betrachtungsweise, welche die beobachtete Hochwasserhäufigkeit und -stärke mit meteorologischen und klimatologischen Ursachen verknüpft (z.B. NIED et al., 2014; TARASOVA et al., 2019). Die vorgelegte Arbeit ist eingebettet in diesen Paradigmenwechsel und befasst sich mit den hydrometeorologischen und hydroklimatischen Rahmenbedingungen schwerer großräumiger Hochwasser Mitteleuropas im vergangenen Jahrhundert. Zum einen sind großräumige Hochwasserereignisse, die mehrere Einzugsgebiete betreffen von großer sozio-ökonomischer Relevanz und eine besondere Herausforderung für Hochwasserschutz- und Katastrophenmanagement. Zum anderen treten bei überregionalen Hochwasser die lokalen Gegebenheiten im einzelnen Einzugsgebiet im Vergleich zu den hydrometeorologischen Bedingungen in den Hintergrund. Die Beschränkung auf die Einzugsgebiete in Mitteleuropa hatte dabei den Vorteil, dass eine ausreichend hohe räumliche und zeitliche Datenabdeckung zur Verfügung stand, um großflächige Hochwasser seit Beginn des 20. Jahrhunderts zu analysieren. Aufgrund einer starken saisonalen Abhängigkeit der meteorologischen Hochwasserursachen (vgl. NIED et al, 2014; TARASOVA et al., 2019) ist die Betrachtung in der vorgelegten Arbeit in Sommer- und Winterhochwasser aufgeteilt.

Gliederung der Arbeit, Datengrundlage und Methoden

Die in dieser Arbeit vorgestellten Untersuchungen und Schlussfolgerungen beruhen auf zwei veröffentlichten Zeitschriftenartikeln (KRUG et al., 2020b, 2021) und einem eingereichten Manuskript KRUG et al. (2020a). Die einzelnen Kapitel sind daher als eigenständige Einheiten gegliedert mit jeweils einer Einleitung, einer kurzen Daten-

und Methodenbeschreibung, einer Diskussion der Ergebnisse und den Schlussfolgerungen; auch wenn es dadurch zu Überschneidungen in den jeweiligen Abschnitten zur Datengrundlage und angewandten Methodik gibt. Somit kann der Leser entweder der Gliederung der vorgelegten Arbeit folgend die Kapitel nacheinander lesen oder nach Interesse direkt zu einem bestimmten Thema springen.

Die vorgelegte Arbeit ist dabei so aufgebaut, dass sie nach einer kurzen Themeneinführung zunächst in Kapitel 2 die Datengrundlage vorstellt. Ein besonderer Fokus liegt dabei auf der dynamischen Regionalisierung (Downscaling) der globalen ERA-20C Reanalysedaten. Die Regionalisierung über Europa wurde dabei mit einem gekoppelten regionalen Atmosphäre-Ozean-Modell durchgeführt, um den Wasserkreislauf realistischer darzustellen. Die Atmosphäre wurde mit dem regionalen Klimamodell COSMO-CLM modelliert. Dieses wurde interaktiv mit dem regionalen Ozeanmodell NEMO im Bereich der Randmeere (Mittelmeer, Nordsee und Ostsee) gekoppelt. Darüber hinaus wurde der Süßwasserzufluss von Flüssen, die in das Mittelmeer münden, mit dem Flussablaufmodell TRIP (Total Runoff Integrating Pathways; OKI and SUD, 1998) berücksichtigt. Die regionalisierte ERA-20C-Reanalyse ermöglichte es uns, den vierdimensionalen atmosphärischen Zustand während vergangener extremer Hochwasser in Mitteleuropa mit einer relativ hohen zeitlichen und räumlichen Auflösung (rund 12km) zu untersuchen. Die Analyse vergangener Hochwasser hat substantiell davon profitiert. So wurden einige Ereignisse der frühen Jahrzehnte des 20. Jahrhunderts zum erstmalig mit einer so hohen zeitlichen und räumlichen Auflösung untersucht.

In Kapitel 3 werden die theoretischen Grundlagen dieser Arbeit näher beleuchtet. Im Gegensatz zu den kurzen Methodenbeschreibungen in den einzelnen Kapiteln findet der Leser hier detailliertere Hintergrundinformationen. Zunächst wird die Klassifizierung der großräumigen Hochwasser in Mitteleuropa im vergangenen Jahrhundert nach der Methode von FISCHER and SCHUMANN (2018) vorgestellt. Um die synoptisch-skaligen Rahmenbedingungen während der damit bestimmten Hochwasser zu analysieren, wurden u.a. Tiefdruckzugbahnen bestimmt. Hierbei wurden zwei unterschiedliche Ansätze verwendet: zum einen die Methode von WERNLI and SCHWIERZ (2006) und SPRENGER et al. (2017), zum anderen die Methode von HOFSTÄTTER and CHIMANI (2012) und HOFSTÄTTER et al. (2016). In beiden Fällen werden zunächst die Zentren der Tiefdruckgebiete durch die Position des tiefsten Drucks innerhalb einer geschlossenen Isobare bestimmt. Dabei wird bei der Methode nach HOFSTÄTTER and CHIMANI (2012) und HOFSTÄTTER et al. (2016) das Bodendruckfeld vorher mit einem diskreten Kosinusfilter geglättet. Anschließend werden bei beiden Ansätzen die nachfolgenden Positionen der Tiefdruckzentren mithilfe eines sogenannten „First Guess“-Ansatzes verbunden.

Des Weiteren wurden in dieser Arbeit für ausgewählte Hochwasser im Zeitraum 1901 bis 2010 die Feuchtequellen des hochwasserverursachenden Regens quantifiziert. Dazu wurde ein Lagrangscher Ansatz angewendet. Dabei werden zunächst mithilfe von Lagranto (WERNLI and DAVIES, 1997; SPRENGER and WERNLI, 2015) die Rückwärtstrajektorien der im jeweiligen Einzugsgebiet niederschlagbringenden Luftmassenpakete berechnet, d.h. der Ursprung dieser Luftmassenpakete bestimmt (in einem Zeitfenster von sieben Tagen). Anhand der Änderung der spezifischen Feuchte entlang dieser Rückwärtstrajektorien, können Rückschlüsse gezogen werden, wo Feuchte über Oberflächenverdunstung aufgenommen wurde. Der verwendete Algorithmus von SCHOLDER-AEMISEGGER (2013) basiert auf der

Veröffentlichung von SODEMANN et al. (2008b) und wird häufig als WaterSip bezeichnet.

Ergänzend dazu wurden die Quellen starken Niederschlags während Sommerhochwasser auch mit einem informationstheoretischen Ansatz berechnet, der sogenannten Transfer-Entropie SCHREIBER (2000); BENNETT et al. (2019); POTHAPAKULA et al. (2019). Auf regionaler Skala kann konvektiver Niederschlag in den Sommermonaten eine Hochwassersituation verschärfen. Daher wurde erstmalig für ausgewählte historische Sommerhochwasser der Anteil des konvektiven Niederschlags quantifiziert. Dies geschah nach der Methode von BRENDEL et al. (2014), weiterentwickelt in BRISSON et al. (2018) und PURR et al. (2019), mithilfe einer Nachverfolgung der Zugbahn von konvektiven Zellen, d.h. ebenfalls mit einen Lagrangschen Ansatz.

In Kapitel 4 werden die großräumigsten Hochwasser in den Einzugsgebieten von Donau, Elbe, Rhein und Weser vorgestellt. Dabei sticht bei den Winterhochwasserereignissen vor allem die zeitliche Häufung in den 1940er Jahren und in den 1980er Jahren hervor. Die Hochwasser im Sommerhalbjahr sind insgesamt regionaler und betreffen vor allem die Donau und Elbregion. Dabei traten die extremsten Sommerhochwasser vor allem in den letzten Jahrzehnten auf, zum Beispiel im August 2002, August 2005, sowie Juni 2013.

Die nachfolgenden Kapitel untersuchen die hydrometeorologischen und hydroklimatischen Rahmendbedingungen dieser überregionalen Hochwasser. Dabei liegt in Kapitel 5 das Hauptaugenmerk auf der Frage, ob es hydroklimatische Treiber für die hochwasserreichen und hochwasserarmen Winter des vergangenen Jahrhunderts gibt oder die zeitliche Variabilität zufällig zustande gekommen ist. Die Kapitel 6, 7 und 8 widmen sich den Sommerhochwasser und gehen der Frage nach, welche Prozesse den Niederschlag in den Einzugsgebieten von Elbe, Oder und Donau intensivierte. Während sich die Kapitel 6 und 7 mit dem großräumigen Feuchtetransport zum jeweiligen Einzugsgebiet befassen, beschäftigt sich Kapitel 8 auf regionaler Skala mit der Bedeutung von orographisch ausgelöstem und konvektivem Niederschlag während ausgewählter historischer Sommerhochwasser.

Kapitel 9 fasst abschließend die Schlussfolgerungen der einzelnen Kapitel zusammen und gibt einen Ausblick auf zukünftige Arbeiten zum Thema.

Ergebnisse

Während des Winterhalbjahres traten besonders großräumige Hochwasser auf, die für schwere Überschwemmungen in den Einzugsgebieten von Rhein, Elbe und Donau sorgten. Die meisten dieser flussgebietsübergreifenden Hochwasser wurden durch das Abschmelzen großräumiger Schneebedeckung bis in niederen Lagen und gleichzeitigem Regen verursacht, sogenannte „Regen-auf-Schnee“ Ereignisse (im Englischen „rain-on-snow events“). Diese deutschlandweiten Hochwasser traten im vergangenen Jahrhundert interessanterweise nicht gleichmäßig auf, sondern gehäuft in einzelnen Jahrzehnten, wie zum Beispiel in den 1940er, den späten 1960er und den 1980er Jahren. Es zeigte sich, dass die hochwasserreichen Phasen gut mit negativen Indexwerten der Nordatlantischen Oszillation (NAO) und des

skandinavischen Luftdruckmusters (SCA) übereinstimmen. Die negative NAO-Phase geht dabei häufig mit großen Schneefällen und Tiefdruckzugbahnen über Südeuropa einher, während negative SCA-Indizes mit dem Gesamtniederschlag in den betroffenen Flusseinzugsgebieten korrelieren.

Im Sommerhalbjahr wurden die meisten extremen Hochwasser in Mitteleuropa durch sogenannte Vb-Tiefdruckgebiete verursacht, die sich typischerweise vom Mittelmeer aus nordostwärts nach Mitteleuropa verlagern. In der Literatur wurden bisher nur Vb-Ereignisse untersucht, die in den letzten zwei Jahrzehnten auftraten. Daher wurden in der vorgelegten Arbeit die vorangegangenen Studien erweitert durch die Analyse von weiteren Vb-Ereignissen seit 1900. Dabei wurden basierend auf einer Lagrangeschen Betrachtung die Feuchtequellregionen des hochwasserbringenden Niederschlags untersucht. Dies wurde komplementiert durch die Berechnung der Transferentropie von Verdunstung zu Niederschlag im ausgewählten Flusseinzugsgebiet mithilfe der sogenannten TE-linear Methode. Wir detektierten für die ausgewählten Sommerhochwasser verschiedene Feuchtequellregionen, die das komplexe dynamische Zusammenspiel verschiedener Luftmassen während des Durchzugs eines Vb-Tiefdruckgebietes hervorheben. Bis zu 80% des hochwasserverursachenden Niederschlags entstanden dabei aus Verdunstung über dem europäischen Kontinent, was die Bedeutung des kontinentalen Feuchterecyclings hinweist. Andere wichtige Feuchtequellregionen waren die Nordsee, die Ostsee, der Nordatlantik und für einige Ereignisse auch das Schwarze Meer.

Das Mittelmeer spielte im Durchschnitt nur eine untergeordnete Rolle als Feuchtequelle. Dennoch waren starke Vb-Niederschläge in den Einzugsgebieten der Donau, Elbe und Oder mit einer ungewöhnlich hohen Verdunstung im Mittelmeer verbunden. Dies spiegelt sich auch in einer hohen Transferentropie für Verdunstung im westlichen Mittelmeer wider. Interessanterweise wurde diese Verdunstung nicht durch überdurchschnittlich hohe Meeresoberflächentemperaturen im Mittelmeer verursacht, sondern sie wurde dynamisch durch hohe Bodenwindgeschwindigkeiten verstärkt. Daher spielt das Mittelmeer eine wichtige Rolle bei der Niederschlagsintensivierung, auch wenn der direkte Beitrag als Feuchtequellregion zum Niederschlag in den betroffenen Flussgebieten zum Teil nur gering war. Eine mögliche Ursache könnte sein, dass die Verdunstung über dem Mittelmeer zur Intensivierung des Vb-Tiefdruckgebietes durch freiwerdende latente Wärme beiträgt, vor allem in den frühen Stadien der Tiefdruckentwicklung. Außerdem könnte der Transport von Feuchte aus dem Mittelmeerraum Niederschlag und damit auch eine Erhöhung der Bodenfeuchte entlang der Zugbahn des Vb-Tiefs begünstigen. Die erhöhte Bodenfeuchte könnte dann über erneute Verdunstung den Niederschlag luftstromabwärts in den betroffenen Flusseinzugsgebieten verstärken. Diese Hypothese wird durch eine erhöhte Transferentropie von Bodenfeuchte und Verdunstung entlang der typischen Vb-Tiefdruckzugbahn unterstützt.

Im jeweiligen Einzugsgebiet verstärken orographischer und konvektiver Niederschlag das Hochwasserpotential von Vb-Ereignissen. Dabei sorgen Vb-Tiefdruckgebiete aufgrund ihrer meridionalen Zugbahn vor allem für Niederschläge in den zonal orientierten Gebirgszügen, wie zum Beispiel den Alpen oder der Erzgebirgsregion. In den Sommermonaten detektierten wir mithilfe der Nachverfolgung von konvektiven Zellzugbahnen einen Anteil des konvektiven Niederschlags von zum Teil über 60% in den Nachmittagsstunden. Wenn das Maximum des konvektiven Niederschlags mit dem stratiformen Niederschlag des

Vb-Tiefs zeitlich zusammenfällt, kann dies zu extremen Niederschlagsintensitäten führen. Somit spielen konvektive Niederschlagszellen in den Sommermonaten eine wichtige Rolle für die Hochwasserentstehung, insbesondere im Kontext der Klimaerwärmung (Super-Clausius–Clapeyron Beziehung; BERG et al., 2013; PURR et al., 2021).

Ausblick

Die vorgestellte Arbeit erweiterte das Wissen über die meteorologischen und hydroklimatischen Rahmenbedingungen vergangener großflächiger Hochwasser in Mitteleuropa. Weitere Forschung ist jedoch erforderlich, um die Vorhersagbarkeit der künftigen Hochwasserwahrscheinlichkeit zu quantifizieren. Dies wird Gegenstand der zweiten Förderphase der DFG-Forschergruppe SPATE sein. Der Fokus wird weiterhin auf Regen-auf-Schnee-Ereignissen und durch Vb-Tiefdruckgebiete induzierte Hochwasser liegen. Die in dieser Arbeit gewonnenen Erkenntnisse dienen dabei als Grundlage für die Quantifizierung der Vorhersagbarkeit zukünftiger Hochwasser verursachender Niederschlagsereignisse, insbesondere in einem sich ändernden Klima. Im folgenden wird kurz auf die geplanten Studien eingegangen.

Bei großflächigen Winterhochwasser (verursacht durch Regen auf Schneeschmelze) zeigte sich eine Häufung von Ereignissen in Jahren mit negativen NAO- und SCA-Indizes. Es blieb jedoch in der vorgelegten Arbeit Raum für Spekulationen, inwieweit zunehmende Wintertemperaturen die Häufigkeit und Intensität von großräumigen Winterhochwasser verändern wird. Grund dafür sind gegenläufige Entwicklungen der zugrunde liegenden Prozesse, wie z.B. vermehrter Winterregen auf der einen Seite, aber eine reduzierte räumliche Ausdehnung der Schneedecke in Mitteleuropa auf der anderen Seite (siehe Kapitel 5). Daher wird in weiteren Studien mit einem stochastischen Modell von Niederschlag und Schneeschmelze untersucht werden, inwieweit hydro-klimatologische Faktoren (einschließlich einer Zunahme der Mitteltemperatur) die zeitliche Regen-auf-Schnee-Variabilität in der Vergangenheit beeinflusst haben (KIRSCHNER et al., 2021). Dazu ist es wichtig zu überprüfen, ob gehäuft auftretende Ereignisse auch ein statistisch signifikantes Cluster darstellen. Ein geeignetes Werkzeug dafür ist die aus der Scan-Statistik abgeleitete Methode von LUN et al. (2020). Basierend auf diesen Erkenntnissen kann das stochastische Regen-auf-Schnee-Modell auf die kürzlich veröffentlichten CMIP6-Klimaprojektionen angewendet werden (EYRING et al., 2016), um die Vorhersagbarkeit von künftigen Winterhochwasser näher zu untersuchen.

In Bezug auf großräumige Sommerhochwasser, sollten künftige Studien näher die Bedeutung von sogenannten blockierenden Wetterlagen (d.h. quasi-stationären Hochdruckgebieten) untersuchen, welche die untypische meridionale Zugbahn von Vb-Tiefdruckgebieten begünstigen. Frühere Studien haben zudem gezeigt, dass freiwerdende latente Wärme im Bereich von Tiefdruckgebieten häufig blockierende Wetterlagen erhalten (PFAHL and WERNLI, 2012; PFAHL et al., 2015; STEINFELD and PFAHL, 2019; STEINFELD et al., 2020). In unserem Kontext könnte die durch ein Vb-Tief freigesetzte latente Wärme die vorherrschende blockierende Wetterlage verlängern, sodass weitere, aufeinanderfolgende Vb-Tiefdruckgebiete begünstigt werden könnten (HOFSTÄTTER and BLÖSCHL, 2019). Das zeitlich gehäufte Auftreten von Vb-Tiefdruckgebieten birgt dabei ein besonders hohes Hochwasserpotenzial.

Allerdings sind weitere Forschungen zu diesem, von HOFSTÄTTER and BLÖSCHL (2019) vorgestellten, positiven Rückkopplungsmechanismus notwendig. Die in der vorgelegten Arbeit verwendete 110 Jahre umfassende meteorologischen Reanalysedaten (siehe Kapitel 2), sowie die neuen CMIP6 Klimaprojektionen (EYRING et al., 2016) werden als Grundlage dienen, um weitere Einblicke in die Bedeutung von blockierenden Wetterlagen für Sommerhochwasser zu erhalten.

Appendix B

Widespread flood event dates

This chapter provides the dates when the half-yearly maximum discharges of widespread flood events were observed. Table B.1 shows the dates of widespread winter flood events. The corresponding peak discharge values are listed in chapter 4, table 4.1. Table B.2 shows the dates of trans-basin summer flood events (see chapter 4, table 4.2.).

TABLE B.1: Dates of the most intense trans-basin winter floods since 1920 based on half-yearly maximum GRDC discharges. The colour shading corresponds to the peak discharge values (cf. table 4.1).

river	gauge	mean discharge (m^3/s)	area (km^2)	01/1920	01/1926	03/1940	03/1942	02/1946	03/1947	01/1948	03/1981	03/1988	01/1995	01/2003	01/2011
Rhine	Maxau	1285	50196	NA	31/12/1925	20/03/1940	14/03/1942	08/02/1946	24/03/1947	31/12/1947	14/03/1981	26/03/1988	27/01/1995	05/01/2003	14/01/2011
Main	Wuerzburg	116	14031	16/01/1920	01/01/1926	22/03/1940	21/03/1942	11/02/1946	09/03/1947	31/12/1947	13/03/1981	29/03/1988	29/01/1995	06/01/2003	17/01/2011
Mosel	Cochem	314	27088	15/01/1920	01/01/1926	19/03/1940	20/03/1942	06/02/1946	08/03/1947	01/01/1948	11/03/1981	28/03/1988	27/01/1995	04/01/2003	09/01/2011
Rhine	Koeln	2099	144232	16/01/1920	01/01/1926	22/03/1940	21/03/1942	11/02/1946	15/03/1947	02/01/1948	16/03/1981	29/03/1988	30/01/1995	05/01/2003	10/01/2011
Weser	Hann.-Muenden	111	12442	13/01/1920	01/01/1926	20/03/1940	20/03/1942	10/02/1946	15/03/1947	15/01/1948	12/03/1981	29/03/1988	31/01/1995	05/01/2003	10/01/2011
Weser	Intschede	318	37720	18/01/1920	05/01/1926	25/03/1940	23/03/1942	12/02/1946	18/03/1947	18/01/1948	16/03/1981	31/03/1988	03/02/1995	07/01/2003	17/01/2011
Elbe	Dresden	329	53096	17/01/1920	02/01/1926	17/03/1940	28/03/1942	12/02/1946	21/03/1947	01/01/1948	15/03/1981	30/03/1988	01/02/1995	06/01/2003	17/01/2011
Saale	Calbe-Grizehne	112	23719	NA	NA	23/03/1940	22/03/1942	14/02/1946	17/03/1947	18/01/1948	17/03/1981	06/04/1988	03/02/1995	07/01/2003	18/01/2011
Elbe	Neu-Darchau	713	131950	25/01/1920	12/01/1926	31/03/1940	30/03/1942	20/02/1946	27/03/1947	15/01/1948	21/03/1981	05/04/1988	09/02/1995	13/01/2003	23/01/2011
Donau	Ingolstadt	313	20001	NA	31/12/1925	21/03/1940	21/03/1942	10/02/1946	13/03/1947	05/01/1948	14/03/1981	28/03/1988	27/01/1995	05/01/2003	NA
Donau	Hofkirchen	641	47496	17/01/1920	02/01/1926	23/03/1940	23/03/1942	12/02/1946	15/03/1947	06/01/1948	14/03/1981	28/03/1988	28/01/1995	06/01/2003	16/01/2011

flood types: very small flood | small flood | medium flood | large flood | very large flood

TABLE B.2: As in table B.1, but for widespread summer floods (cf. table 4.2).

river	gauge	mean discharge (m^3/s)	area (km^2)	06/1926	06/1940	07/1954	06/1965	05/1970	05/1983	05/1999	08/2002	08/2005	06/2013
Rhine	Maxau	1285	50196	23/06/1926	02/06/1940	12/07/1954	13/06/1965	14/05/1970	27/05/1983	16/05/1999	13/08/2002	24/08/2005	03/06/2013
Main	Wuerzburg	116	14031	07/07/1926	03/06/1940	14/07/1954	13/06/1965	15/05/1970	27/05/1983	23/05/1999	14/08/2002	24/08/2005	05/06/2013
Mosel	Cochem	314	27088	20/06/1926	26/05/1940	21/07/1954	12/06/1965	14/05/1970	29/05/1983	16/05/1999	29/08/2002	26/08/2005	NA
Rhine	Koeln	2099	144232	21/06/1926	04/06/1940	16/07/1954	13/06/1965	15/05/1970	30/05/1983	18/05/1999	15/08/2002	27/08/2005	05/06/2013
Weser	Hann.-Muenden	111	12442	06/07/1926	28/05/1940	20/07/1954	11/06/1965	01/05/1970	27/05/1983	29/05/1999	11/08/2002	21/08/2005	NA
Weser	Intschede	318	37720	16/06/1926	29/05/1940	21/07/1954	20/06/1965	01/05/1970	29/05/1983	16/05/1999	13/08/2002	17/08/2005	NA
Elbe	Dresden	329	53096	22/06/1926	02/06/1940	12/07/1954	13/06/1965	01/05/1970	26/05/1983	24/05/1999	17/08/2002	26/08/2005	06/06/2013
Saale	Calbe-Grizehne	112	23719	NA	02/06/1940	15/07/1954	14/06/1965	01/05/1970	28/05/1983	23/05/1999	16/08/2002	26/08/2005	07/06/2013
Elbe	Neu-Darchau	713	131950	30/06/1926	09/06/1940	21/07/1954	20/06/1965	01/05/1970	20/05/1983	17/05/1999	23/08/2002	31/08/2005	11/06/2013
Donau	Ingolstadt	313	20001	22/06/1926	02/06/1940	12/07/1954	13/06/1965	14/05/1970	28/05/1983	24/05/1999	14/08/2002	25/08/2005	NA
Donau	Hofkirchen	641	47496	23/06/1926	04/06/1940	13/07/1954	15/06/1965	15/05/1970	29/05/1983	26/05/1999	15/08/2002	26/08/2005	06/06/2013

flood types: very small flood | small flood | medium flood | large flood | very large flood

Appendix C

Vertically integrated moisture flux during selected flood events

This chapter discusses the vertically integrated moisture flux during selected winter and summer flood events in Central Europe. The following data basis and methods descriptions are partly taken from the report entitled *Water vapor transport and extreme precipitation events in the Mediterranean region* by A. Krug and B. Ahrens, DWD project 3043989/17-RAD (KRUG and AHRENS, 2018) and we refer to it for more details.

C.1 HOAPS-satellite and ERA-Interim reanalysis data

The Hamburg Ocean Atmosphere Parameters and Fluxes from Satellite Data (HOAPS-v3.3, ANDERSSON et al., 2010) have been updated by the time period from 2009 to the end of 2014 and are referred as HOAPS-4.0 satellite data. The data set includes monthly means of precipitation, evaporation, turbulent heat fluxes, wind, specific humidity, and the total column water content since 1987. These variables are retrieved by the Special Sensor Microwave/Imager (SSM/I) brightness temperature measurements over the ice-free ocean surface on a global range within $\pm 80^\circ$. The spatial resolution is $0.5^\circ \times 0.5^\circ$(ANDERSSON et al., 2010).

HOAPS-4.0 data is only available over large water surfaces with a distance of about 50 km to the coastline or sea ice. Therefore, ERA-Interim reanalysis data (DEE et al., 2011) have been used to fill the data gaps. ERA-Interim reanalysis data has an improved hydrological cycle relative to ERA-40 and uses assimilated cloud and rain satellite measurements (DEE et al., 2011). Therefore, it is useful for analyzing the atmospheric water fluxes (SEAGER and HENDERSON, 2013). The previous water vapor transport data was based on monthly ERA-Interim data with a horizontal resolution of 2.5°. For the new product, the temporal resolution of the input data was increased to 6-hourly data and the spatial resolution was changed to $0.75^\circ \times 0.75^\circ$. A grid point wise bias correction with respect to ERA-Interim was performed for the horizontal water vapor transport in the HOAPS-4.0 data over the ice-free sea to account for inhomogeneities between both data sets.

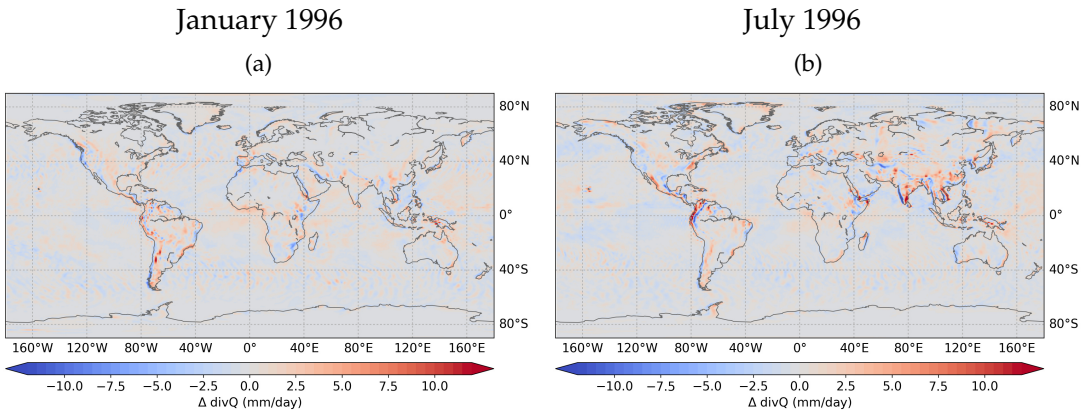

FIGURE C.1: Differences $\Delta \mathrm{div}Q$ of the horizontal water vapour transport in ERA-Interim reanalysis data calculated after equation C.2 and estimated by the equation C.5 as a reference in (a) January 1996 and (b) July 1996.

C.2 Vertical integration of the water vapour transport

In this theses, the water vapour transport during extreme floods was analysed from different perspectives. With the Lagrangian approach described in the previous section, the atmospheric moisture causing heavy precipitation in selected river catchment regions was backtracked to the moisture uptake regions. On the contrary, the Eulerian perspective with the monthly mean horizontal water vapour transport gives insights in regions of high water vapour convergence anomalies, in our case associated with flood-triggering heavy rainfall. Furthermore, it serves for comparison with the Lagrangian diagnostics.

The horizontal water vapour fluxes were based on HOAPS-satellite data over sea surfaces and ERA-Interim reanalysis data over land surfaces (section C.1) and calculated after the water balance equation, which summarizes the atmospheric processes in the water cycle (SOHN et al., 2004):

$$\frac{\partial(W + W_c)}{\partial t} + \mathrm{div}(\vec{Q} + \vec{Q}_c) = E - P, \tag{C.1}$$

with evapouration E, the change of the atmospheric water storage ($\partial(W + W_c)/\partial t$), the horizontal transport of water by the wind $\mathrm{div}(\vec{Q} + \vec{Q}_c)$, the precipitation P, the so-called „precipitable water“ W, and the liquid water path W_c. The horizontal water vapour flux vector is denoted as $\vec{Q}$. The water flux vector of the liquid and ice condensates is written as $\vec{Q}_c$. Both are defined as follows (e.g., WANG and YANG, 2008; CHIODO and HAIMBERGER, 2010) :

$$\vec{Q} = \frac{1}{g} \int_0^1 q \, \vec{V} \, \frac{\partial \eta}{\partial p} \mathrm{d}\eta, \tag{C.2}$$

$$\vec{Q}_c = \frac{1}{g} \int_0^1 q_l \, \vec{V} \, \frac{\partial \eta}{\partial p} \mathrm{d}\eta, \tag{C.3}$$

with gravity acceleration g, the specific humidity q, the liquid-water mixing ratio q_l, the horizontal wind vector $\vec{V}$, and the hybrid vertical coordinate η (ECMWF, 2015). Simmons and Burridge (1981) introduced η as a monotonic function of the pressure

p, the surface pressure p_s, and $p_0 = 1013.2\,\text{hPa}$:

$$\eta = \frac{p}{p_s} + \left(\frac{p}{p_s} - 1\right) \cdot \left(\frac{p}{p_s} - \frac{p}{p_0}\right). \tag{C.4}$$

The lowest level is defined as $\eta(p_s, p_s) = 1$, and the uppermost level as $\eta(0, p_s) = 0$. Such a hybrid coordinate follows the surface orography at the lower levels and converges to pressure levels in upper heights. It avoids biases in the diagnostics due to interpolating the model levels, on which all model equations are solved, to pressure levels. These are especially large in areas of steep orography and mountainous areas where the model output is extrapolated to pressure levels below the surface. The covariances were calculated based on the highest available temporal resolution like suggest by SEAGER and HENDERSON (2013). They observed an underestimated poleward moisture transport by midlatitude transient eddies when a coarser time resolution was used to calculate the humidity covariances. Afterwards, the monthly mean covariances were vertically integrated. Other bias are the small imbalances of the water balance (equation C.1) in the reanalysis data caused by the assimilation of moisture, wind and temperature from observations (TRENBERTH et al., 2011; SEAGER and HENDERSON, 2013). The largest biases in Figure C.1(a) and (b) appear in regions of high rainfall amounts with large spatial variation, for example, in Central America during the wet season, when uncertainties in precipitation fields of ERA-Interim are high. Please note, over oceans the residuals show „ripple“ structures like the surface geopotential. This could be caused by the fact that the ERA-Interim model is a spectral model.

Afterwards, the divergence of the horizontal water vapour transport $\text{div}\vec{Q}$ is calculated considering the Earth spheroid. Satellite data contains no information about the vertical profile of specific humidity and horizontal wind fields on a global scale. Therefore, the horizontal water vapour transport cannot be calculated directly after equation (C.2) with HOAPS satellite data. For the satellite data an indirect approach is used: The water flux of the cloud condensates are generally small compared to the water vapour flux (SOHN et al., 2004; SOHN and PARK, 2010). Thus the divergences of the cloud condensates $\text{div}\vec{Q}_c$ can be neglected. The change of the atmospheric water storage is small for long time periods, like seasonal or annual means, and the freshwater budget $(E - P)$ is mainly balanced by the water vapour transport (SOHN et al., 2004; SOHN and PARK, 2010). However, the storage term increases for shorter time periods. DOMINGUEZ et al. (2006) analyzed the impact of atmospheric moisture storage on precipitation recycling and concluded, that the moisture storage term has to be taken into account at a monthly or shorter time-scale. Thus, equation (C.1) simplifies to

$$\left\langle \text{div}\vec{Q} \right\rangle = \langle E - P \rangle - \left\langle \frac{\partial (W + W_c)}{\partial t} \right\rangle, \tag{C.5}$$

where the angle brackets denote the temporal mean values, such as monthly means. Hence, the divergence of the horizontal water vapour flux can be calculated indirectly with the freshwater budget $(E - P)$ and the change of the precipitable water in HOAPS satellite data over land.

C.3 Moisture flux during selected summer and winter flood events

The following figures present the vertically integrated moisture flux during selected floods in Central Europe (see chapter 4, table 4.1 and 4.2). We present only events since 1987 due to the availability of satellite data. Figure C.2 shows a high water vapour convergence anomaly over western Europe during March 1988 and January 1995 corresponding to extreme floods in the Rhine catchment (see also chapter 4 and 5). Moreover, the water vapour convergence was anomalously large in Central and Eastern Central Europe during March 1988, December 2010, and with weaker intensity also in January 2003. That corresponds to floods not only in the Rhine catchment but also in the Elbe catchment.

The eastward horizontal moisture flux (black arrows in figure C.2) transported water vapour zonally towards Central Europe in March 1988, January 1995, and January 2003. Thus, moisture originating from the North Atlantic and the North Sea/Baltic Sea contributed to the affected river catchments. In December 2010, the moisture flux over Central Europe was eastwards but relatively weak and with a meridional component over the Danube catchment region indicating some influence of the Mediterranean Sea in causing snowfall in Central Europe. This is in line with two Vb-cyclones during 18.12.2010–20.12.2010 and 25.12.2010–26.12.2010 (KRUG and AHRENS, 2020) which transported relatively warm and moist air masses from the Mediterranean Sea to Central Europe due to their typical cyclone pathway (cf. chapter 5, figure 5.8).

Figure C.3 shows the vertically integrated moisture flux during selected summer floods associated with Vb-cyclones (see also chapter 4 and 6-7). During the Vb-cyclone event in July 1997, the water vapour convergence was anomalously high over large areas in Central and Eastern Europe. The horizontal moisture flux was eastward from the North Atlantic/North Sea towards central and southern Europe. This moisture transport was likely associated with another cyclone propagating from Great Britain via the North Sea towards the Danube catchment region (AKHTAR et al., 2019). We detected also with our Lagrangian moisture source diagnostics a contribution of the North Atlantic and the North Sea/Baltic Sea for precipitation in the Danube, Elbe, and Odra catchment, while the contribution from the Mediterranean Sea was negligibly small during this Vb-cyclone flood event (see appendix, figures D.2–D.4). Besides, the moisture convergence during July 1997 was intensified over eastern Central Europe by westward continental moisture flux pointing towards continental moisture contribution to the flood-triggering precipitation.

In May 1999, August 2002, August 2005, May 2010, and June 2013, the horizontal moisture flux was small over the regions of high water vapour convergence. Therefore, assumptions of potential moisture source regions are not possible. For example, one might guess that the Mediterranean Sea contributed to precipitation in the Danube catchment region during May 2010 due to the northeastward moisture flux over the Adriatic Sea. However, our Lagrangian moisture source diagnostics detected no contribution of the Mediterranean Sea for this Vb-cyclone event. On the contrary, the Mediterranean Sea was a relevant oceanic moisture source during the May 2005 flood event which we cannot deduce from the monthly mean moisture

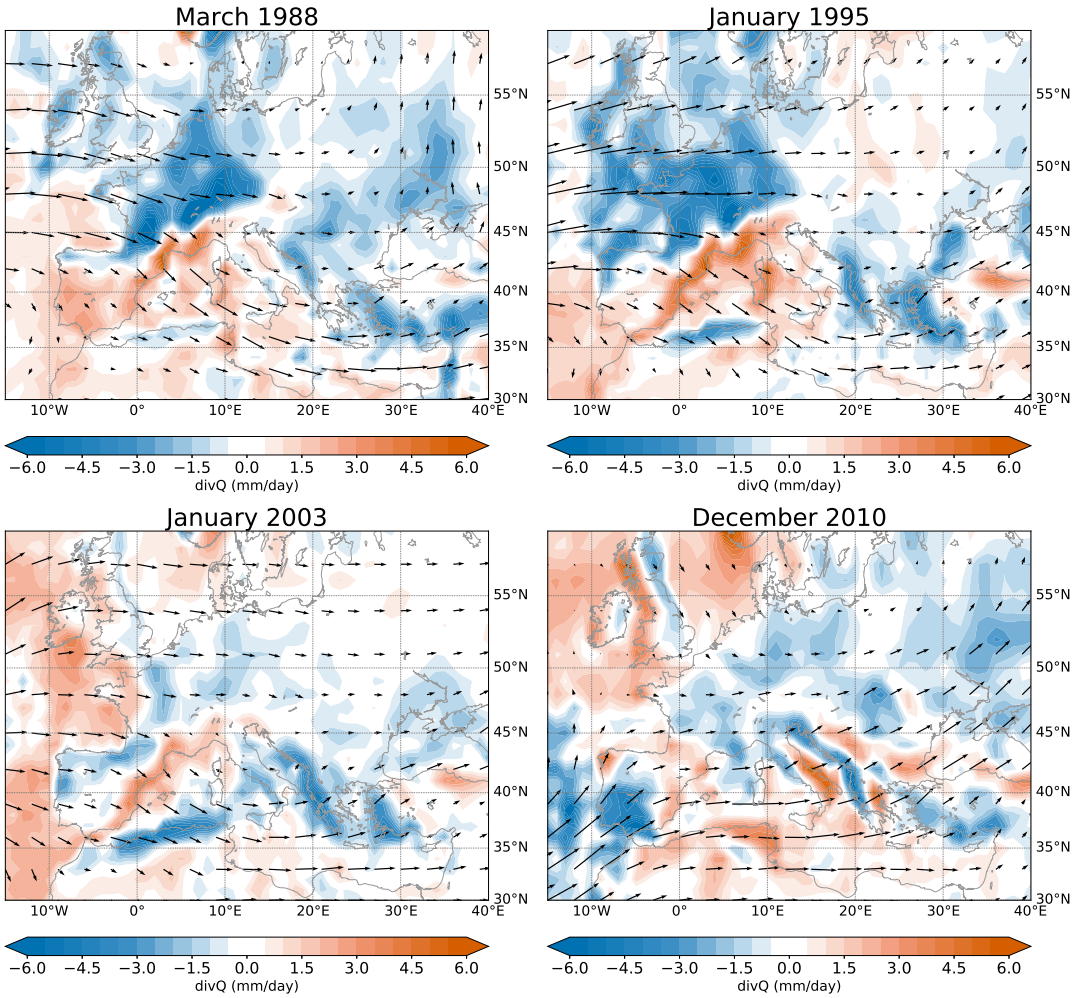

FIGURE C.2: Monthly mean horizontal moisture flux (black arrows) and anomalies of the divergence of the horizontal water vapour flux div$\vec{Q}$ with respect to 1987–2014 for selected winter flood events in Central Europe.

flux in the satellite and ERA-Interim reanalysis data. Note that during May 1999, a Vb-cyclone caused a flood in the Alpine region (STAHL and HOFSTÄTTER, 2018; STUCKI et al., 2012). We excluded this event from our Lagrangian moisture source diagnostics since the affected area did not include the Odra and Elbe river catchment (see high water vapour convergence in the Alpine region in figure C.3).

Due to the satellite data availability, we could only analyse monthly means of the horizontal water flux. Despite this coarse temporal resolution, the moisture flux data indicate the regions of high water vapour convergence related to positive precipitation anomalies and high water vapour fluxes can hint towards moisture source regions.

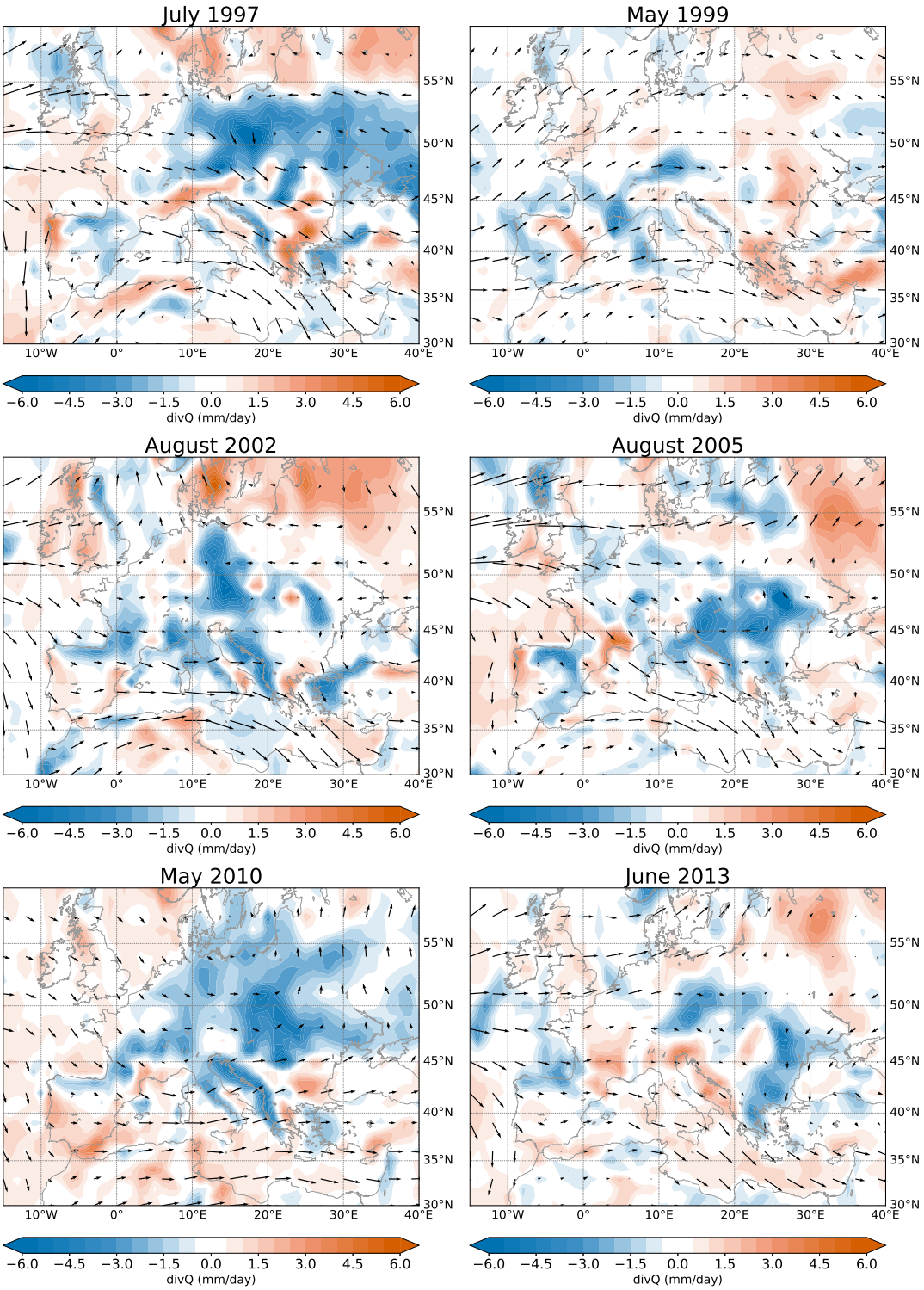

FIGURE C.3: As in figure C.2 but for selected summer flood events.

Appendix D

Moisture source diagnostics for selected Vb-cyclones

This chapter provides supplementary figures for chapter 6. Note that the figures are part of the study entitled *Moisture sources of heavy precipitation in Central Europe during Vb-cyclones* by A. Krug, F. Aemisegger, M. Sprenger, and B. Ahrens, submitted to Climate Dynamics (KRUG et al., 2020a, in revision).

D.1 Area-weighted mean moisture uptakes

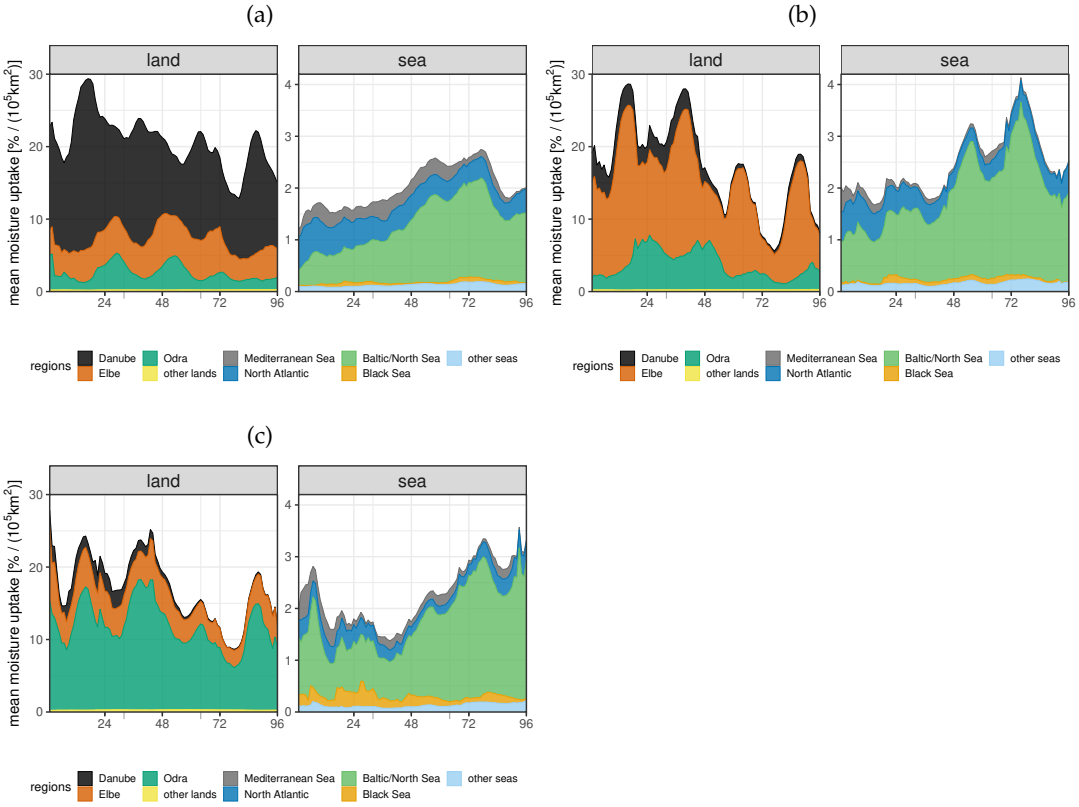

FIGURE D.1: Area-weighted mean moisture uptakes in various uptake regions for precipitation in the (a) Danube, (b) Elbe, and (c) Odra catchment averaged over all 16 events listed in Table 6.1. The x-axis corresponds to the four days of heavy precipitation selected for the moisture diagnostics. Note the different y-axis scales.

D.2 Temporal evolution of the individual events

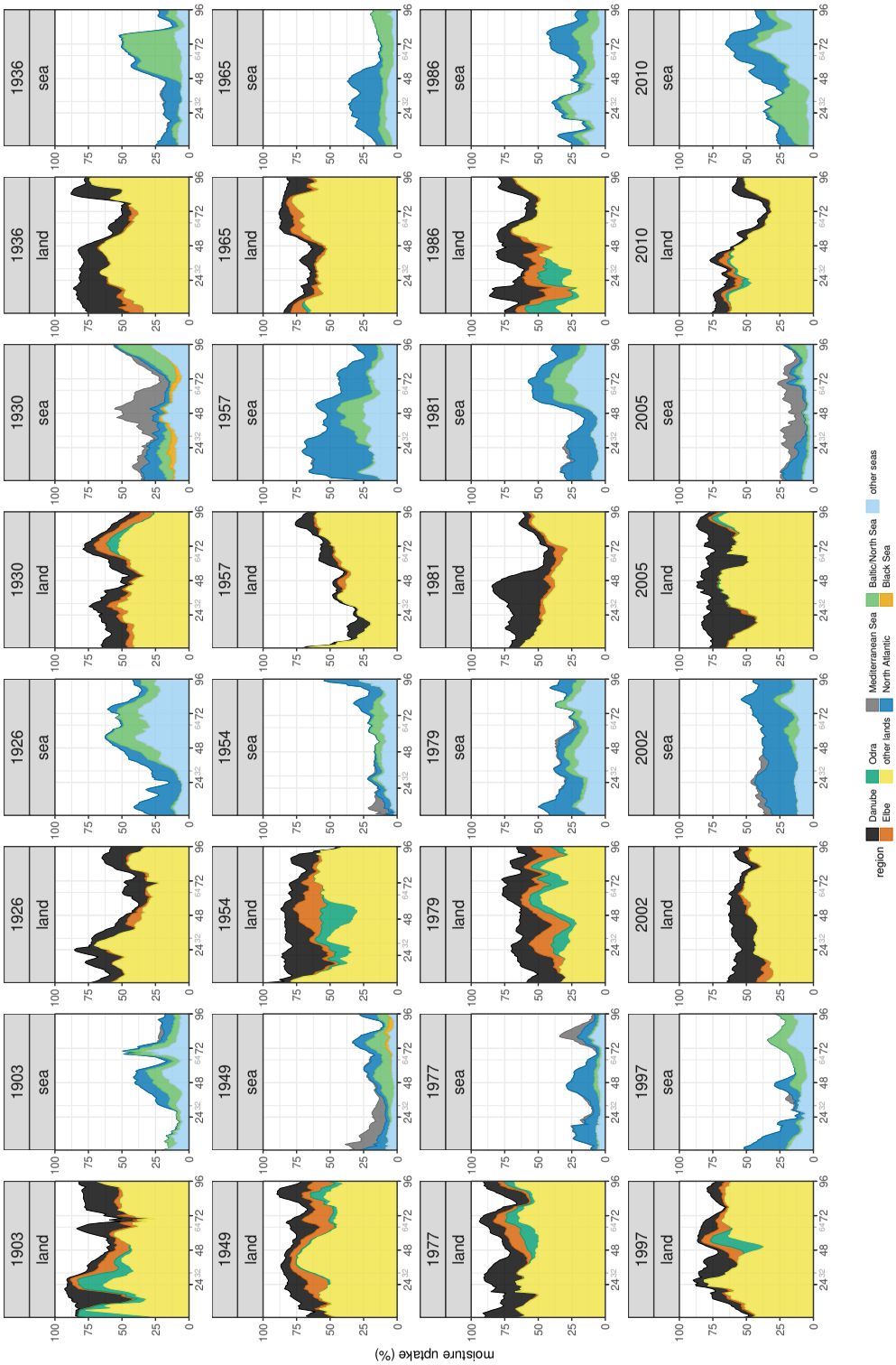

FIGURE D.2: Moisture contributions of various uptake regions to precipitation in the Danube catchment 6.1. The x-axis corresponds to the four days of heavy precipitation selected for the moisture diagnostics.

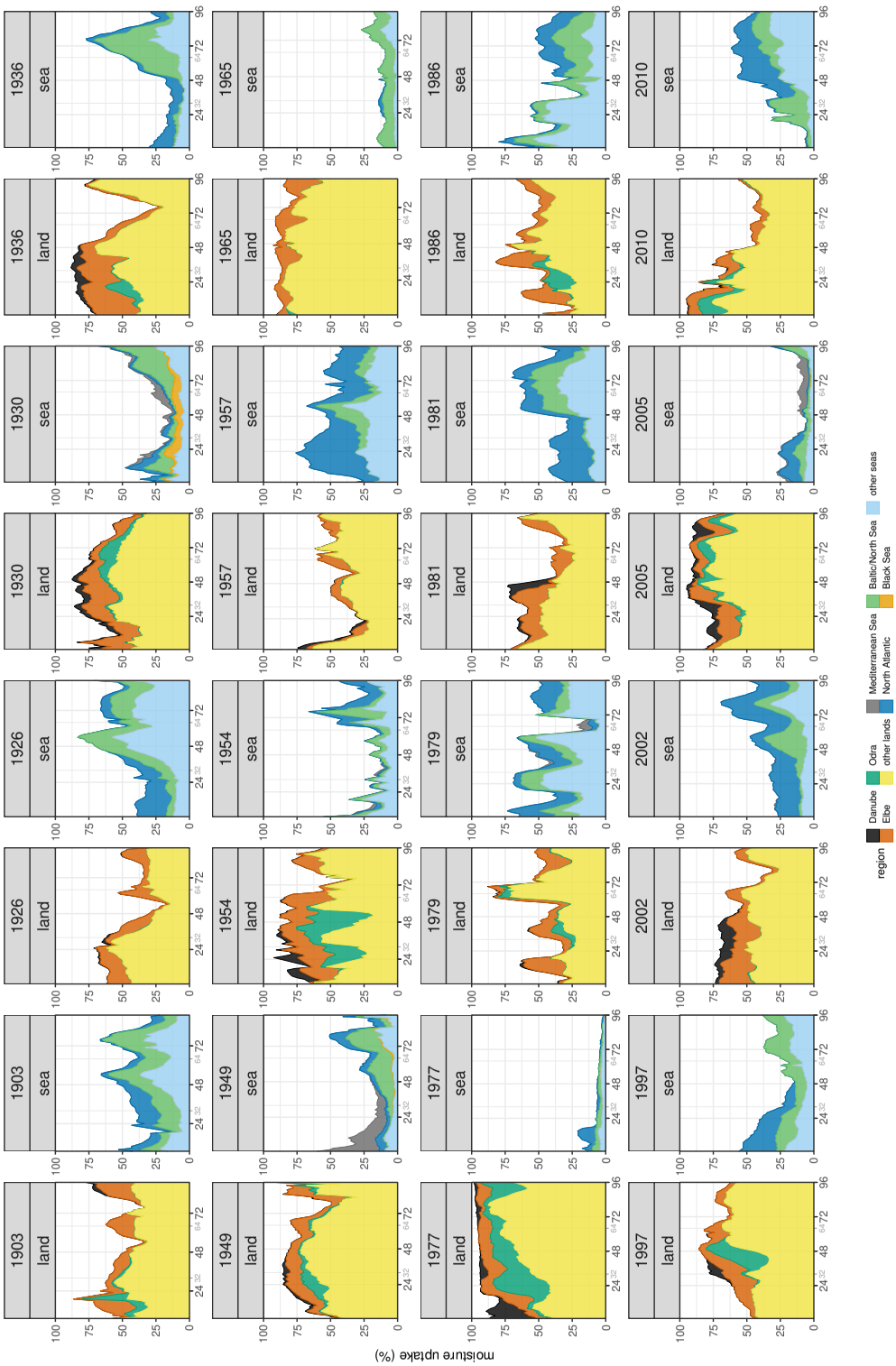

FIGURE D.3: The same as Figure D.2 but for the Elbe catchment region.

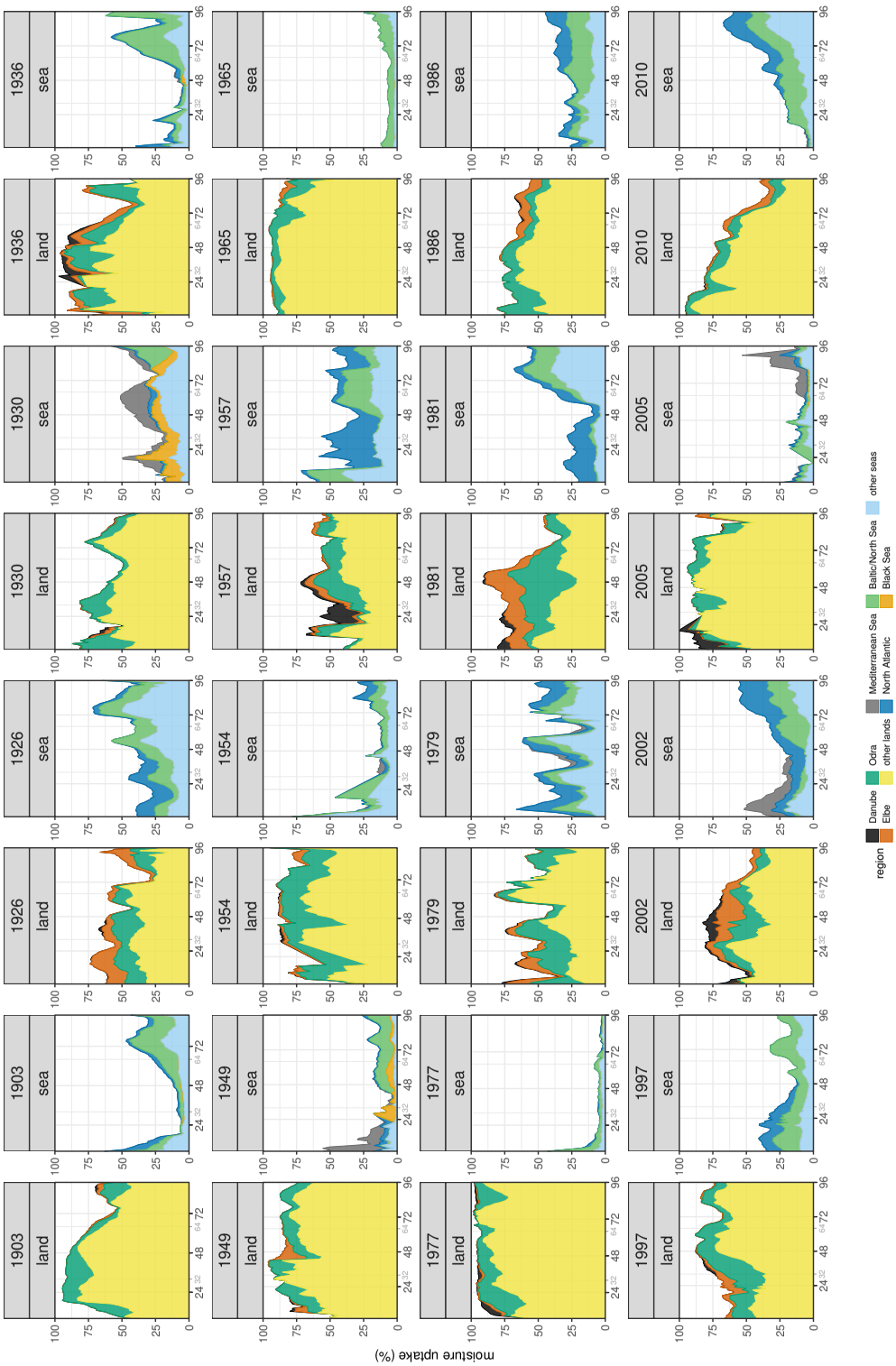

FIGURE D.4: The same as Figure D.2 but for the Odra catchment region.

Appendix E

Transfer Entropy from surface temperature and soil moisture to precipitation during selected Vb-cyclones

The figures in this appendix are supplementary for the chapter 7 and display the information exchange of selected variables in the dynamically downscaled ERA-20C reanalysis (see section 2.2.2) to precipitation in the Odra (Poland) catchment region.

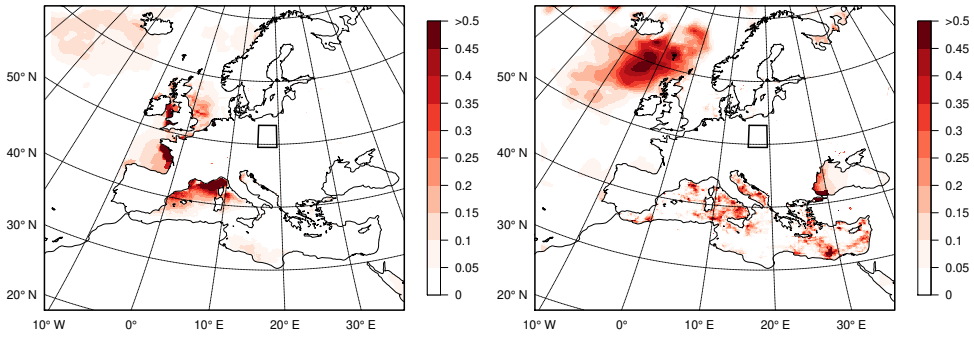

FIGURE E.1: Information exchange (TE-linear, in 10^{-2} nats) from surface temperature over the marginal seas (source) to total precipitation in the Odra catchment (target, black rectangle) during the summer season (JJA, left, 0.05 significance level) and during the corresponding 100 highest ranked Vb-events (right, including also insignificant values) from 1901 to 2010.

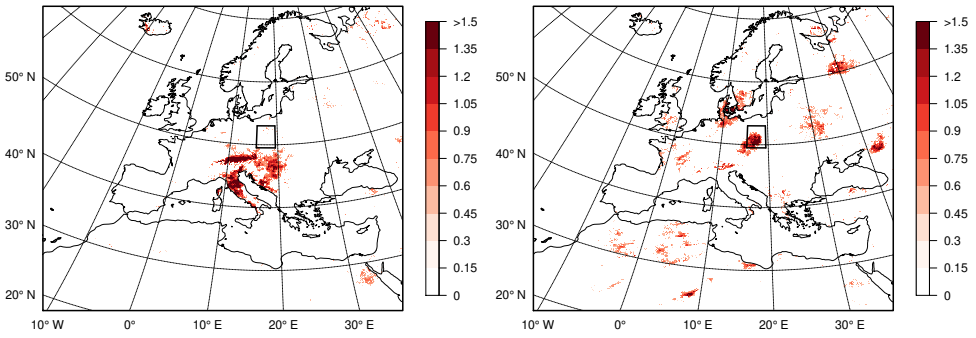

FIGURE E.2: Information exchange (TE-linear, in 10^{-2} nats) from soil moisture content at 4 cm–10 cm (source) to total precipitation in the Odra catchment (target, black rectangle) during the corresponding 100 highest ranked Vb-events from 1901 to 2010. The time lag τ (see equation 7.1) is 0 day in the left panel and 1 day in the left panel (both with 0.05 significance level).

Bibliography

AEBISCHER, U., C. SCHÄR, 1998: Low-Level Potential Vorticity and Cyclogenesis to the Lee of the Alps. – Journal of the Atmospheric Sciences **55**, 186–207, DOI: 10.1175/1520-0469(1998)055<0186:LLPVAC>2.0.CO;2.

AEMISEGGER, F., 2018: On the link between the North Atlantic storm track and precipitation deuterium excess in Reykjavik. – Atmospheric Science Letters **19**, e865, DOI: 10.1002/asl.865.

AEMISEGGER, F., S. PFAHL, H. SODEMANN, I. LEHNER, S.I. SENEVIRATNE, H. WERNLI, 2014: Deuterium excess as a proxy for continental moisture recycling and plant transpiration. – Atmospheric Chemistry and Physics **14**, 4029–4054, DOI: 10.5194/acp-14-4029-2014.

AHRENS, B., N. LEPS, 2021: Sensitivity of Convection Permitting Simulations to Lateral Boundary Conditions in Idealised Experiments. – Earth and Space Science Open Archive 33, DOI: 10.1002/essoar.10506295.1.

AHRENS, B., A. WALSER, 2008: Information-Based Skill Scores for Probabilistic Forecasts. – Mon Weather Rev **136**, 352–363, DOI: 10.1175/2007MWR1931.1.

AKHTAR, N., J. BRAUCH, A. DOBLER, K. BÉRANGER, B. AHRENS, 2014: Medicanes in an ocean–atmosphere coupled regional climate model. – Natural Hazards and Earth System Sciences **14**, 2189–2201, DOI: 10.5194/nhess-14-2189-2014.

AKHTAR, N., J. BRAUCH, B. AHRENS, 2018: Climate modeling over the Mediterranean Sea: impact of resolution and ocean coupling. – Climate Dynamics **51**, 933–948, DOI: 10.1007/s00382-017-3570-8.

AKHTAR, N., A. KRUG, J. BRAUCH, T. ARSOUZE, C. DIETERICH, B. AHRENS, 2019: European Marginal Seas in a regional atmosphere-ocean coupled model and their impact on Vb-cyclones and associated precipitation. – Climate Dynamics , DOI: 10.1007/s00382-019-04906-x.

ANDERSSON, A., K. FENNIG, C. KLEPP, S. BAKAN, H. GRASSL, J. SCHULZ, 2010: The Hamburg Ocean Atmosphere Parameters and Fluxes from Satellite Data – HOAPS-3. – Earth System Science Data **2**, 215–234, DOI: 10.5194/essd-2-215-2010.

ASHLEY, S.T., W.S. ASHLEY, 2008: The storm morphology of deadly flooding events in the United States. – International Journal of Climatology **28**, 493–503, DOI: 10.1002/joc.1554.

BAN, N., J. SCHMIDLI, C. SCHÄR, 2014: Evaluation of the convection-resolving regional climate modeling approach in decade-long simulations. – Journal of Geophysical Research: Atmospheres **119**, 7889–7907, DOI: 10.1002/2014JD021478.

BARREDO, J.I., 2007: Major flood disasters in Europe: 1950–2005. – Natural Hazards **42**, 125–148, DOI: 10.1007/s11069-006-9065-2.

BARREDO, J.I., 2009: Normalised flood losses in Europe: 1970-2006. – Natural Hazards and Earth System Sciences **9**, 97–104, DOI: 10.5194/nhess-9-97-2009.

BECHTOLD, P., N. SEMANE, P. LOPEZ, J.P. CHABOUREAU, A. BELJAARS, N. BORMANN, 2014: Representing Equilibrium and Nonequilibrium Convection in Large-Scale Models. – Journal of the Atmospheric Sciences **71**, 734–753, DOI: 10.1175/JAS-D-13-0163.1.

BECKER, A., U. GRÜNEWALD, 2003: Disaster Management: Flood Risk in Central Europe. – Science **300**, 1099–1099, DOI: 10.1126/science.1083624.

BECKER, T., C. HOHENEGGER, 2021: Entrainment and Its Dependency on Environmental Conditions and Convective Organization in Convection-Permitting Simulations. – Monthly Weather Review **149**, 537–550, DOI: 10.1175/MWR-D-20-0229.1.

BEDNORZ, E., 2008: Synoptic reasons for heavy snowfalls in the Polish–German lowlands. – Theoretical and Applied Climatology **92**, 133–140, DOI: 10.1007/s00704-007-0322-4.

BENNETT, A., B. NIJSSEN, G. OU, M. CLARK, G. NEARING, 2019: Quantifying Process Connectivity With Transfer Entropy in Hydrologic Models. – Water Resources Research 2018WR024555, DOI: 10.1029/2018WR024555.

BERG, P., C. MOSELEY, J.O. HAERTER, 2013: Strong increase in convective precipitation in response to higher temperatures. – Nature Geoscience **6**, 181–185, DOI: 10.1038/ngeo1731.

BERGHUIJS, W.R., S. HARRIGAN, P. MOLNAR, L.J. SLATER, J.W. KIRCHNER, 2019: The Relative Importance of Different Flood-Generating Mechanisms Across Europe. – Water Resources Research 2019WR024841, DOI: 10.1029/2019WR024841.

BERTOLA, M., A. VIGLIONE, D. LUN, J. HALL, G. BLÖSCHL, 2020: Flood trends in Europe: are changes in small and big floods different?. – Hydrology and Earth System Sciences **24**, 1805–1822, DOI: 10.5194/hess-24-1805-2020.

BERTOLA, M., A. VIGLIONE, S. VOROGUSHYN, D. LUN, B. MERZ, G. BLÖSCHL, 2021: Do small and large floods have the same drivers of change? A regional attribution analysis in Europe. – Hydrology and Earth System Sciences **25**, 1347–1364, DOI: 10.5194/hess-25-1347-2021.

BEUVIER, J., K. BÉRANGER, C. LEBEAUPIN BROSSIER, S. SOMOT, F. SEVAULT, Y. DRILLET, R. BOURDALLÉ-BADIE, N. FERRY, F. LYARD, 2012: Spreading of the Western Mediterranean Deep Water after winter 2005: Time scales and deep cyclone transport. – Journal of Geophysical Research: Oceans **117**, DOI: 10.1029/2011JC007679.

BEZZOLA, G.R., W. RUF, editors, 2009: Ereignisanalyse Hochwasser August 2007. Analyse der Meteo- und Abflussvorhersagen; vertiefte Analyse der Hochwasserregulierung der Jurarandgewässer. Umwelt-Wissen Nr. 0927. – Bundesamt für Umwelt, Bern.

BHASKAR, A., D.S. RAMESH, G. VICHARE, T. KOGANTI, S. GURUBARAN, 2017: Quantitative assessment of drivers of recent global temperature variability: an information theoretic approach. – Climate Dynamics **49**, 3877–3886, DOI: 10.1007/s00382-017-3549-5.

BLÖSCHL, G., S. ARDOIN-BARDIN, M. BONELL, M. DORNINGER, D. GOODRICH, D. GUTKNECHT, D. MATAMOROS, B. MERZ, P. SHAND, J. SZOLGAY, 2007: At what scales do climate variability and land cover change impact on flooding and low flows?. – Hydrological Processes **21**, 1241–1247, DOI: 10.1002/hyp.6669.

BLÖSCHL, G., T. NESTER, J. KOMMA, J. PARAJKA, R. PERDIGÃO, 2013: The June 2013 flood in the Upper Danube Basin, and comparisons with the 2002, 1954 and 1899 floods. – Hydrology and Earth System Sciences **17**, 5197–5212, DOI: 10.5194/hess-17-5197-2013.

BLÖSCHL, G., J. HALL, J. PARAJKA, R.A.P. PERDIGÃO, B. MERZ, B. ARHEIMER, G.T. ARONICA, A. BILIBASHI, O. BONACCI, M. BORGA, I. ČANJEVAC, A. CASTELLARIN, G.B. CHIRICO, P. CLAPS, K. FIALA, N. FROLOVA, L. GORBACHOVA, A. GÜL, J. HANNAFORD, S. HARRIGAN, M. KIREEVA, A. KISS, T.R. KJELDSEN, S. KOHNOVÁ, J.J. KOSKELA, O. LEDVINKA, N. MACDONALD, M. MAVROVA-GUIRGUINOVA, L. MEDIERO, R. MERZ, P. MOLNAR, A. MONTANARI, C. MURPHY, M. OSUCH, V. OVCHARUK, I. RADEVSKI, M. ROGGER, J.L. SALINAS, E. SAUQUET, M. ŠRAJ, J. SZOLGAY, A. VIGLIONE, E. VOLPI, D. WILSON, K. ZAIMI, N. ŽIVKOVIĆ, 2017: Changing climate shifts timing of European floods. – Science **357**, 588–590, DOI: 10.1126/science.aan2506.

BLÖSCHL, G., J. HALL, A. VIGLIONE, R.A.P. PERDIGÃO, J. PARAJKA, B. MERZ, D. LUN, B. ARHEIMER, G.T. ARONICA, A. BILIBASHI, M. BOHÁČ, O. BONACCI, M. BORGA, I. ČANJEVAC, A. CASTELLARIN, G.B. CHIRICO, P. CLAPS, N. FROLOVA, D. GANORA, L. GORBACHOVA, A. GÜL, J. HANNAFORD, S. HARRIGAN, M. KIREEVA, A. KISS, T.R. KJELDSEN, S. KOHNOVÁ, J.J. KOSKELA, O. LEDVINKA, N. MACDONALD, M. MAVROVA-GUIRGUINOVA, L. MEDIERO, R. MERZ, P. MOLNAR, A. MONTANARI, C. MURPHY, M. OSUCH, V. OVCHARUK, I. RADEVSKI, J.L. SALINAS, E. SAUQUET, M. ŠRAJ, J. SZOLGAY, E. VOLPI, D. WILSON, K. ZAIMI, N. ŽIVKOVIĆ, 2019a: Changing climate both increases and decreases European river floods. – Nature **573**, 108–111, DOI: 10.1038/s41586-019-1495-6.

BLÖSCHL, G., M.F. BIERKENS, A. CHAMBEL, C. CUDENNEC, G. DESTOUNI, A. FIORI, J.W. KIRCHNER, J.J. MCDONNELL, H.H. SAVENIJE, M. SIVAPALAN, C. STUMPP, E. TOTH, E. VOLPI, G. CARR, C. LUPTON, J. SALINAS, B. SZÉLES, A. VIGLIONE, H. AKSOY, S.T. ALLEN, A. AMIN, V. ANDRÉASSIAN, B. ARHEIMER, S.K. ARYAL, V. BAKER, E. BARDSLEY, M.H. BARENDRECHT, A. BARTOSOVA, O. BATELAAN, W.R. BERGHUIJS, K. BEVEN, T. BLUME, T. BOGAARD, P. BORGES DE AMORIM, M.E. BÖTTCHER, G. BOULET, K. BREINL, M. BRILLY, L. BROCCA, W. BUYTAERT, A. CASTELLARIN, A. CASTELLETTI, X. CHEN, Y. CHEN, Y. CHEN, P. CHIFFLARD, P. CLAPS, M.P. CLARK, A.L. COLLINS, B. CROKE, A. DATHE, P.C. DAVID, DE F.P.J. BARROS, DE G. ROOIJ, G. DI BALDASSARRE, J.M.

DRISCOLL, D. DUETHMANN, R. DWIVEDI, E. ERIS, W.H. FARMER, J. FEICCABRINO, G. FERGUSON, E. FERRARI, S. FERRARIS, B. FERSCH, D. FINGER, L. FOGLIA, K. FOWLER, B. GARTSMAN, S. GASCOIN, E. GAUME, A. GELFAN, J. GERIS, S. GHARARI, T. GLEESON, M. GLENDELL, A. GONZALEZ BEVACQUA, M.P. GONZÁLEZ-DUGO, S. GRIMALDI, A.B. GUPTA, B. GUSE, D. HAN, D. HANNAH, A. HARPOLD, S. HAUN, K. HEAL, K. HELFRICHT, M. HERNEGGER, M. HIPSEY, H. HLAVÁČIKOVÁ, C. HOHMANN, L. HOLKO, C. HOPKINSON, M. HRACHOWITZ, T.H. ILLANGASEKARE, A. INAM, C. INNOCENTE, E. ISTANBULLUOGLU, B. JARIHANI, Z. KALANTARI, A. KALVANS, S. KHANAL, S. KHATAMI, J. KIESEL, M. KIRKBY, W. KNOBEN, K. KOCHANEK, S. KOHNOVÁ, A. KOLECHKINA, S. KRAUSE, D. KREAMER, H. KREIBICH, H. KUNSTMANN, H. LANGE, M.L.R. LIBERATO, E. LINDQUIST, T. LINK, J. LIU, D.P. LOUCKS, C. LUCE, G. MAHÉ, O. MAKARIEVA, J. MALARD, S. MASHTAYEVA, S. MASKEY, J. MAS-PLA, M. MAVROVA-GUIRGUINOVA, M. MAZZOLENI, S. MERNILD, B.D. MISSTEAR, A. MONTANARI, H. MÜLLER-THOMY, A. NABIZADEH, F. NARDI, C. NEALE, N. NESTEROVA, B. NURTAEV, V.O. ODONGO, S. PANDA, S. PANDE, Z. PANG, G. PAPACHARALAMPOUS, C. PERRIN, L. PFISTER, R. PIMENTEL, M.J. POLO, D. POST, C. PRIETO SIERRA, M.H. RAMOS, M. RENNER, J.E. REYNOLDS, E. RIDOLFI, R. RIGON, M. RIVA, D.E. ROBERTSON, R. ROSSO, T. ROY, J.H. SÁ, G. SALVADORI, M. SANDELLS, B. SCHAEFLI, A. SCHUMANN, A. SCOLOBIG, J. SEIBERT, E. SERVAT, M. SHAFIEI, A. SHARMA, M. SIDIBE, R.C. SIDLE, T. SKAUGEN, H. SMITH, S.M. SPIESSL, L. STEIN, I. STEINSLAND, U. STRASSER, B. SU, J. SZOLGAY, D. TARBOTON, F. TAURO, G. THIREL, F. TIAN, R. TONG, K. TUSSUPOVA, H. TYRALIS, R. UIJLENHOET, VAN R. BEEK, VAN DER R.J. ENT, VAN DER M. PLOEG, A.F. VAN LOON, VAN I. MEERVELD, VAN R. NOOIJEN, VAN P.R. OEL, J.P. VIDAL, VON J. FREYBERG, S. VOROGUSHYN, P. WACHNIEW, A.J. WADE, P. WARD, I.K. WESTERBERG, C. WHITE, E.F. WOOD, R. WOODS, Z. XU, K.K. YILMAZ, Y. ZHANG, 2019b: Twenty-three unsolved problems in hydrology (UPH) – a community perspective. – Hydrological Sciences Journal **64**, 1141–1158, DOI: 10.1080/02626667.2019.1620507.

BLÖSCHL, G., A. KISS, A. VIGLIONE, M. BARRIENDOS, O. BÖHM, R. BRÁZDIL, D. COEUR, G. DEMARÉE, M.C. LLASAT, N. MACDONALD, D. RETSÖ, L. ROALD, P. SCHMOCKER-FACKEL, I. AMORIM, M. BĚLÍNOVÁ, G. BENITO, C. BERTOLIN, D. CAMUFFO, D. CORNEL, R. DOKTOR, L. ELLEDER, S. ENZI, J.C. GARCIA, R. GLASER, J. HALL, K. HASLINGER, M. HOFSTÄTTER, J. KOMMA, D. LIMANÓWKA, D. LUN, A. PANIN, J. PARAJKA, H. PETRIĆ, F.S. RODRIGO, C. ROHR, J. SCHÖNBEIN, L. SCHULTE, L.P. SILVA, W.H.J. TOONEN, P. VALENT, J. WASER, O. WETTER, 2020: Current European flood-rich period exceptional compared with past 500 years. – Nature **583**, 560–566, DOI: 10.1038/s41586-020-2478-3.

BÖER, W., H. SCHUBERT, O. WILSER, 1959: Das Sommerhochwasser der Elbe im Juli 1954. – Mitteilungen zum Deutschen Gewässerkundlichen Jahrbuch Nr. 19 Akademie-Verlag, Berlin.

BÖHM, O., K.F. WETZEL, 2006: Flood history of the Danube tributaries Lech and Isar in the Alpine foreland of Germany. – Hydrological Sciences Journal **51**, 784–798, DOI: 10.1623/hysj.51.5.784.

BRÁZDIL, R., O. KOTYZA, P. DOBROVOLNÝ, 2006: July 1432 and August 2002–two millennial floods in Bohemia?. – Hydrological Sciences Journal **51**, 848–863, DOI: 10.1623/hysj.51.5.848.

BRENDEL, C., E. BRISSON, F. HEYNER, E. WEIGL, B. AHRENS, 2014: Bestimmung des atmosphärischen Konvektionspotentials über Thüringen. – Berichte des Deutschen Wetterdienstes **244**, 72.

BRISSON, E., K. VAN WEVERBERG, M. DEMUZERE, A. DEVIS, S. SAEED, M. STENGEL, VAN N.P.M. LIPZIG, 2016a: How well can a convection-permitting climate model reproduce decadal statistics of precipitation, temperature and cloud characteristics?. – Climate Dynamics **47**, 3043–3061, DOI: 10.1007/s00382-016-3012-z.

BRISSON, E., M. DEMUZERE, VAN N.P. LIPZIG, 2016b: Modelling strategies for performing convection-permitting climate simulations. – Meteorologische Zeitschrift **25**, 149–163, DOI: 10.1127/metz/2015/0598.

BRISSON, E., N. LEPS, B. AHRENS, 2017: Konvektionserlaubende Klimamodellierung. – Promet - Meteorologische Fortbildung **Heft 99**, 41–48.

BRISSON, E., C. BRENDEL, S. HERZOG, B. AHRENS, 2018: Lagrangian evaluation of convective shower characteristics in a convection-permitting model. – Meteorologische Zeitschrift **27**, 59–66, DOI: 10.1127/metz/2017/0817.

BROCKHAUS, P., D. LÜTHI, C. SCHÄR, 2008: Aspects of the diurnal cycle in a regional climate model. – Meteorologische Zeitschrift **17**, 433–443, DOI: 10.1127/0941-2948/2008/0316.

BUEH, C., H. NAKAMURA, 2007: Scandinavian pattern and its climatic impact. – Quarterly Journal of the Royal Meteorological Society **133**, 2117–2131, DOI: 10.1002/qj.173.

BÜELER, D., S. PFAHL, 2017: Potential Vorticity Diagnostics to Quantify Effects of Latent Heating in Extratropical Cyclones. Part I: Methodology. – Journal of the Atmospheric Sciences **74**, 3567–3590, DOI: 10.1175/JAS-D-17-0041.1.

CASPARY, H.J., 1995: Recent winter floods in Germany caused by changes in the atmospheric circulation across Europe. – Physics and Chemistry of the Earth **20**, 459–462, DOI: 10.1016/S0079-1946(96)00006-7.

CHAN, S.C., E.J. KENDON, H.J. FOWLER, S. BLENKINSOP, C.A.T. FERRO, D.B. STEPHENSON, 2013: Does increasing the spatial resolution of a regional climate model improve the simulated daily precipitation?. – Climate Dynamics **41**, 1475–1495, DOI: 10.1007/s00382-012-1568-9.

CHIODO, G., L. HAIMBERGER, 2010: Interannual changes in mass consistent energy budgets from ERA-Interim and satellite data. – Journal of Geophysical Research **115**, DOI: 10.1029/2009JD012049.

CHUNG, C., S. NIGAM, 1999: Weighting of geophysical data in Principal Component Analysis. – Journal of Geophysical Research: Atmospheres **104**, 16925–16928, DOI: 10.1029/1999JD900234.

CIRIC, D., R. NIETO, L. LOSADA, A. DRUMOND, L. GIMENO, 2018: The Mediterranean Moisture Contribution to Climatological and Extreme Monthly Continental Precipitation. – Water **10**, 519, DOI: 10.3390/w10040519.

CLARK, M.P., M.C. SERREZE, D.A. ROBINSON, 1999: Atmospheric controls on Eurasian snow extent. – International Journal of Climatology **19**, 27–40, DOI: 10.1002/(SICI)1097-0088(199901)19:1<27::AID-JOC346>3.0.CO;2-N.

CLEVELAND, W.S., E. GROSSE, W.M. SHYU, 1992: Statistical Models in S, chapter Local regression models, 68 Wadsworth & Brooks/Cole, DOI: 10.1201/9780203738535.

COHEN, J., H. YE, J. JONES, 2015: Trends and variability in rain-on-snow events. – Geophysical Research Letters **42**, 7115–7122, DOI: 10.1002/2015GL065320.

COMAS-BRU, L., F. MCDERMOTT, 2014: Impacts of the EA and SCA patterns on the European twentieth century NAO-winter climate relationship. – Quarterly Journal of the Royal Meteorological Society **140**, 354–363, DOI: 10.1002/qj.2158.

COMPO, G.P., J.S. WHITAKER, P.D. SARDESHMUKH, N. MATSUI, R.J. ALLAN, X. YIN, B.E. GLEASON, R.S. VOSE, G. RUTLEDGE, P. BESSEMOULIN, S. BRÖNNIMANN, M. BRUNET, R.I. CROUTHAMEL, A.N. GRANT, P.Y. GROISMAN, P.D. JONES, M.C. KRUK, A.C. KRUGER, G.J. MARSHALL, M. MAUGERI, H.Y. MOK, Ø. NORDLI, T.F. ROSS, R.M. TRIGO, X.L. WANG, S.D. WOODRUFF, S.J. WORLEY, 2011: The Twentieth Century Reanalysis Project. – Quarterly Journal of the Royal Meteorological Society **137**, 1–28, DOI: 10.1002/qj.776.

CORNES, R.C., VAN DER G. SCHRIER, VAN DEN E.J.M. BESSELAAR, P.D. JONES, 2018: An Ensemble Version of the E-OBS Temperature and Precipitation Data Sets. – Journal of Geophysical Research: Atmospheres **123**, 9391–9409, DOI: 10.1029/2017JD028200.

DANCOFF, S.M., H. QUASTLER, 1953: The Information Content and Error Rate of Living Things niversity of Illinois Press.

DAS SHARMA, S., D.S. RAMESH, C. BAPANAYYA, P.A. RAJU, 2012: Sea surface temperatures in cooler climate stages bear more similarity with atmospheric CO2 forcing. – Journal of Geophysical Research: Atmospheres **117**, n/a–n/a, DOI: 10.1029/2012JD017725.

DAVIES, H.C., 1976: A lateral boundary formulation for multi-level prediction models. – Quarterly Journal of the Royal Meteorological Society **102**, 405–418, DOI: 10.1002/qj.49710243210.

DE ROOY, W.C., P. BECHTOLD, K. FRÖHLICH, C. HOHENEGGER, H. JONKER, D. MIRONOV, A. PIER SIEBESMA, J. TEIXEIRA, J.I. YANO, 2013: Entrainment and detrainment in cumulus convection: an overview. – Quarterly Journal of the Royal Meteorological Society **139**, 1–19, DOI: 10.1002/qj.1959.

DEE, D.P., S.M. UPPALA, A.J. SIMMONS, P. BERRISFORD, P. POLI, S. KOBAYASHI, U. ANDRAE, M.A. BALMASEDA, G. BALSAMO, P. BAUER, P. BECHTOLD, A.C.M. BELJAARS, VAN DE L. BERG, J. BIDLOT, N. BORMANN, C. DELSOL, R. DRAGANI, M. FUENTES, A.J. GEER, L. HAIMBERGER, S.B. HEALY, H. HERSBACH, E.V. HÓLM, L. ISAKSEN, P. KÅLLBERG, M. KÖHLER, M. MATRICARDI, A.P. MCNALLY, B.M. MONGE-SANZ, J.J. MORCRETTE, B.K. PARK, C. PEUBEY, DE P. ROSNAY, C. TAVOLATO, J.N. THÉPAUT, F. VITART, 2011: The ERA-Interim reanalysis: configuration and performance of the data assimilation system. – Quarterly Journal of the Royal Meteorological Society **137**, 553–597, DOI: 10.1002/qj.828.

DENIS, B., J. CÔTÉ, R. LAPRISE, 2002: Spectral Decomposition of Two-Dimensional Atmospheric Fields on Limited-Area Domains Using the Discrete Cosine Transform (DCT). – Monthly Weather Review **130**, 1812–1829, DOI: 10.1175/1520-0493(2002)130<1812:SDOTDA>2.0.CO;2.

DIETERICH, C., S. SCHIMANKE, S. WANG, G. VÄLI, Y. LIU, R. HORDOIR, L. AXELL, H. MEIER, 2013: Evaluation of the SMHI coupled atmosphere-ice-ocean model RCA4-NEMO. Tech. Rep. 47, Sveriges Meteorologiska och Hydrologiska Institut (SMHI), Sweden.

DIMITROV, A.G., A.A. LAZAR, J.D. VICTOR, 2011: Information theory in neuroscience. – Journal of Computational Neuroscience **30**, 1–5, DOI: 10.1007/s10827-011-0314-3.

DOMINGUEZ, F., P. KUMAR, X.Z. LIANG, M. TING, 2006: Impact of Atmospheric Moisture Storage on Precipitation Recycling. – Journal of Climate **19**, 1513–1530, DOI: 10.1175/JCLI3691.1.

DONAT, M.G., L.V. ALEXANDER, H. YANG, I. DURRE, R. VOSE, R.J.H. DUNN, K.M. WILLETT, E. AGUILAR, M. BRUNET, J. CAESAR, B. HEWITSON, C. JACK, A.M.G. KLEIN TANK, A.C. KRUGER, J. MARENGO, T.C. PETERSON, M. RENOM, C. ORIA ROJAS, M. RUSTICUCCI, J. SALINGER, A.S. ELRAYAH, S.S. SEKELE, A.K. SRIVASTAVA, B. TREWIN, C. VILLARROEL, L.A. VINCENT, P. ZHAI, X. ZHANG, S. KITCHING, 2013: Updated analyses of temperature and precipitation extreme indices since the beginning of the twentieth century: The HadEX2 dataset. – Journal of Geophysical Research: Atmospheres **118**, 2098–2118, DOI: 10.1002/jgrd.50150.

DONNER, L.J., B.L. WYMAN, R.S. HEMLER, L.W. HOROWITZ, Y. MING, M. ZHAO, J.C. GOLAZ, P. GINOUX, S.J. LIN, M.D. SCHWARZKOPF, J. AUSTIN, G. ALAKA, W.F. COOKE, T.L. DELWORTH, S.M. FREIDENREICH, C.T. GORDON, S.M. GRIFFIES, I.M. HELD, W.J. HURLIN, S.A. KLEIN, T.R. KNUTSON, A.R. LANGENHORST, H.C. LEE, Y. LIN, B.I. MAGI, S.L. MALYSHEV, P.C.D. MILLY, V. NAIK, M.J. NATH, R. PINCUS, J.J. PLOSHAY, V. RAMASWAMY, C.J. SEMAN, E. SHEVLIAKOVA, J.J. SIRUTIS, W.F. STERN, R.J. STOUFFER, R.J. WILSON, M. WINTON, A.T. WITTENBERG, F. ZENG, 2011: The Dynamical Core, Physical Parameterizations, and Basic Simulation Characteristics of the Atmospheric Component AM3 of the GFDL Global Coupled Model CM3. – Journal of Climate **24**, 3484–3519, DOI: 10.1175/2011JCLI3955.1.

DOTTORI, F., W. SZEWCZYK, J.C. CISCAR, F. ZHAO, L. ALFIERI, Y. HIRABAYASHI, A. BIANCHI, I. MONGELLI, K. FRIELER, R.A. BETTS, L. FEYEN, 2018: Increased human and economic losses from river flooding with anthropogenic warming. – Nature Climate Change **8**, 781–786, DOI: 10.1038/s41558-018-0257-z.

DREWS, I., C. HANGEN-BRODERSEN, B. ZUM KLEY-FIQUET, 2003: Hochwasservorsorge in Deutschland – Lernen aus der Katastrophe 2002 im Elbegebiet, volume 29 of *Schriftenreihe des DKKV* – Deutsches Komitee für Katastrophenvorsorge e. V. (DKKV), Bonn.

DROBINSKI, P., S. BASTIN, T. ARSOUZE, K. BÉRANGER, E. FLAOUNAS, M. STÉFANON, 2018: North-western Mediterranean sea-breeze circulation in a regional climate system model. – Climate Dynamics **51**, 1077–1093, DOI: 10.1007/s00382-017-3595-z.

ECMWF, 2015: Part III: Dynamics and Numerical Procedures, chapter 2.1 IFS Documentation. ECMWF Operational implementation 12 May 2015.

ELMER, F., J. HOYMANN, D. DÜTHMANN, S. VOROGUSHYN, H. KREIBICH, 2012: Drivers of flood risk change in residential areas. – Natural Hazards and Earth System Sciences **12**, 1641–1657, DOI: 10.5194/nhess-12-1641-2012.

EMANUEL, K.A., 1991: A Scheme for Representing Cumulus Convection in Large-Scale Models. – Journal of the Atmospheric Sciences **48**, 2313–2329, DOI: 10.1175/1520-0469(1991)048<2313:ASFRCC>2.0.CO;2.

EYRING, V., S. BONY, G.A. MEEHL, C.A. SENIOR, B. STEVENS, R.J. STOUFFER, K.E. TAYLOR, 2016: Overview of the Coupled Model Intercomparison Project Phase 6 (CMIP6) experimental design and organization. – Geoscientific Model Development **9**, 1937–1958, DOI: 10.5194/gmd-9-1937-2016.

FABIAN, W., G. BARTELS, 1928: Das Hochwasser der Oder im Sommer 1926, volume 5 27–42.

FELL, E., 2003: Hochwasser im Rheingebiet–Winter 2002/2003. LfW Rheinland-Pfalz. Report 206/03.

FICKERT, R., 1932: Die Hochwässer in der Sächsischen Lausitz im Juni 1926 und Oktober/November 1930. – Wasserkraft und Wasserwirtschaft **27**, 241–245, 258–262, 272–274 München and Berlin.

FISCHER, G., 1938: Centralblatt für Bakteriologie, Parasitenkunde und Infektionskrankheiten Number 141-142.

FISCHER, K., 1904: Entstehung und Verlauf des Oderhochwassers im Juli 1903. – Geographische Zeitschrift **10**, 316–332 Leipzig.

FISCHER, S., A. SCHUMANN, 2018: A distribution-free ordinal classification of floods based on moments. – Hydrological Sciences Journal **63**, 1605–1618, DOI: 10.1080/02626667.2018.1525614.

FONTRODONA BACH, A., VAN DER G. SCHRIER, L.A. MELSEN, A.M.G. KLEIN TANK, A.J. TEULING, 2018: Widespread and Accelerated Decrease of Observed Mean and Extreme Snow Depth Over Europe. – Geophysical Research Letters **45**, 12,312–12,319, DOI: 10.1029/2018GL079799.

FOSSER, G., S. KHODAYAR, P. BERG, 2015: Benefit of convection permitting climate model simulations in the representation of convective precipitation. – Climate Dynamics **44**, 45–60, DOI: 10.1007/s00382-014-2242-1.

FRAEDRICH, K., 2007: Forecasting: Predictability, Probability, and Persistence. – Mitteilungen der Mathematische Gesellschaft in Hamburg **26**, 5–28.

FREUDIGER, D., I. KOHN, K. STAHL, M. WEILER, 2014: Large-scale analysis of changing frequencies of rain-on-snow events with flood-generation potential. – Hydrology and Earth System Sciences **18**, 2695–2709, DOI: 10.5194/hess-18-2695-2014.

FRIEDRICH, W., 1930: Die Wasserstandsverhältnisse der norddeutschen Stromgebiete im Oktober und im Gesamtabflußjahr 1930. – Zentralblatt der Bauverwaltung **50**, 873 Berlin.

FROIDEVAUX, P., J. SCHWANBECK, R. WEINGARTNER, C. CHEVALIER, O. MARTIUS, 2015: Flood triggering in Switzerland: the role of daily to monthly preceding precipitation. – Hydrology and Earth System Sciences **19**, 3903–3924, DOI: 10.5194/hess-19-3903-2015.

GANGOITI, G., E. SÁEZ DE CÁMARA, L. ALONSO, M. NAVAZO, M.C. GÓMEZ, J. IZA, J.A. GARCÍA, J.L. ILARDIA, M.M. MILLÁN, 2011a: Origin of the water vapor responsible for the European extreme rainfalls of August 2002: 1. High-resolution simulations and tracking of air masses. – Journal of Geophysical Research: Atmospheres **116**, DOI: 10.1029/2010JD015530.

GANGOITI, G., I. GÓMEZ-DOMENECH, E. SÁEZ DE CMARA, L. ALONSO, M. NAVAZO, J. IZA, J.A. GARCÍA, J.L. ILARDIA, M.M. MILLÁN, 2011b: Origin of the water vapor responsible for the European extreme rainfalls of August 2002: 2. A new methodology to evaluate evaporative moisture sources, applied to the August 11-13 central European rainfall episode. – Journal of Geophysical Research: Atmospheres **116**, 1–16, DOI: 10.1029/2010JD015538.

GANGOITI, G., E. SÁEZ DE CÁMARA, I. GÓMEZ-DOMENECH, L. ALONSO, M. NAVAZO, J. IZA, J.A. GARCÍA, M.M. MILLÁN, 2015: Re-evaluation of moisture sources for the August 2002 extreme rainfall episode in central Europe: Evaporation from falling precipitation included in a mesoscale modeling system. – Journal of Hydrology **529**, 696–710, DOI: 10.1016/j.jhydrol.2015.08.055.

GERKEN, T., B.L. RUDDELL, R. YU, P.C. STOY, D.T. DREWRY, 2019: Robust observations of land-to-atmosphere feedbacks using the information flows of FLUXNET. – Climate and Atmospheric Science **2**, 37, DOI: 10.1038/s41612-019-0094-4.

GIORGI, F., 2006: Climate change hot-spots. – Geophysical Research Letters **33**, L08707, DOI: 10.1029/2006GL025734.

GIORGI, F., C. JONES, G. ASRAR, 2009: Addressing climate information needs at the regional level: the CORDEX framework. – WMO Bulletin **58**, 175–183.

GÖB, R., K. LURZ, 2015: The Use of Inequalities of Camp-Meidell Type in Nonparametric Statistical Process Monitoring. – In: Knoth S., Schmid W. (eds) Frontiers in Statistical Quality Control **11**, Springer, Cham, 163–182, DOI: 10.1007/978-3-319-12355-4_11.

GOCHIS, D.J., W.J. SHUTTLEWORTH, Z.L. YANG, 2002: Sensitivity of the Modeled North American Monsoon Regional Climate to Convective Parameterization. – Monthly Weather Review **130**, 1282–1298, DOI: 10.1175/1520-0493(2002)130<1282:SOTMNA>2.0.CO;2.

GRAMS, C.M., H. BINDER, S. PFAHL, N. PIAGET, H. WERNLI, 2014: Atmospheric processes triggering the central European floods in June 2013. – Natural Hazards and Earth System Sciences **14**, 1691–1702, DOI: 10.5194/nhess-14-1691-2014.

GRASSELT, R., 2009: Validation of the COSMO Land-Surface Parameterization TERRA-ML with discharge Ph.D. thesis, Rheinische Friedrich-Wilhelms-Universität Bonn 103 p.

GRASSELT, R., D. SCHÜTTEMEYER, K. WARRACH-SAGI, F. AMENT, C. SIMMER, 2008: Validation of TERRA-ML with discharge measurements. – Meteorologische Zeitschrift **17**, 763–773, DOI: 10.1127/0941-2948/2008/0334.

GUSE, B., B. MERZ, L. WIETZKE, S. ULLRICH, A. VIGLIONE, S. VOROGUSHYN, 2020: The role of flood wave superposition in the severity of large floods. – Hydrology and Earth System Sciences **24**, 1633–1648, DOI: 10.5194/hess-24-1633-2020.

GUTZLER, D.S., R.D. ROSEN, 1992: Interannual Variability of Wintertime Snow Cover across the Northern Hemisphere. – Journal of Climate **5**, 1441–1447, DOI: 10.1175/1520-0442(1992)005<1441:IVOWSC>2.0.CO;2.

GVOŽDÍKOVÁ, B., M. MÜLLER, 2017: Evaluation of extensive floods in western/central Europe. – Hydrology and Earth System Sciences **21**, 3715–3725, DOI: 10.5194/hess-21-3715-2017.

HALL, J., G. BLÖSCHL, 2018: Spatial patterns and characteristics of flood seasonality in Europe. – Hydrology and Earth System Sciences **22**, 3883–3901, DOI: 10.5194/hess-22-3883-2018.

HARDWICK JONES, R., S. WESTRA, A. SHARMA, 2010: Observed relationships between extreme sub-daily precipitation, surface temperature, and relative humidity. – Geophysical Research Letters **37**, n/a–n/a, DOI: 10.1029/2010GL045081.

HARRIS, I., T.J. OSBORN, P. JONES, D. LISTER, 2020: Version 4 of the CRU TS monthly high-resolution gridded multivariate climate dataset. – Scientific Data **7**, 109, DOI: 10.1038/s41597-020-0453-3.

HELLMANN, G., G. VON ELSNER, 1911: Meteorologische Untersuchungen über die Sommerhochwasser der Oder, volume 230 – Veröffentlichungen des Königlich Preußischen Meterologischen Instituts.

HENDERSON, G.R., D.J. LEATHERS, 2010: European snow cover extent variability and associations with atmospheric forcings. – International Journal of Climatology **30**, 1440–1451, DOI: 10.1002/joc.1990.

HERRMANN, M., S. SOMOT, S. CALMANTI, C. DUBOIS, F. SEVAULT, 2011: Representation of spatial and temporal variability of daily wind speed and of intense wind events over the Mediterranean Sea using dynamical downscaling: impact of the regional climate model configuration. – Natural Hazards and Earth System Sciences **11**, 1983–2001, DOI: 10.5194/nhess-11-1983-2011.

HERSBACH, H., B. BELL, P. BERRISFORD, S. HIRAHARA, A. HORÁNYI, J. MUÑOZ-SABATER, J. NICOLAS, C. PEUBEY, R. RADU, D. SCHEPERS, A. SIMMONS, C. SOCI, S. ABDALLA, X. ABELLAN, G. BALSAMO, P. BECHTOLD, G. BIAVATI, J. BIDLOT, M. BONAVITA, G. CHIARA, P. DAHLGREN, D. DEE, M. DIAMANTAKIS, R. DRAGANI, J. FLEMMING, R. FORBES, M. FUENTES, A. GEER, L. HAIMBERGER, S. HEALY, R.J. HOGAN, E. HÓLM, M. JANISKOVÁ, S. KEELEY, P. LALOYAUX, P. LOPEZ, C. LUPU, G. RADNOTI, P. ROSNAY, I. ROZUM, F. VAMBORG, S. VILLAUME, J. THÉPAUT, 2020: The ERA5 global reanalysis. – Quarterly Journal of the Royal Meteorological Society **146**, 1999–2049, DOI: 10.1002/qj.3803.

HIRSCHBOECK, K., 1988: Flood Hydroclimatology. – Flood Geomorphology 27–49.

HLAVÁČOVÁ-SCHINDLER, K., M. PALUŠ, MILANAND VEJMELKA, J. BHATTACHARYA, 2007: Causality detection based on information-theoretic approaches in time series analysis. – Physics Reports **441**, 1–46, DOI: 10.1016/j.physrep.2006.12.004.

HO-HAGEMANN, H.T.M., S. HAGEMANN, B. ROCKEL, 2015: On the role of soil moisture in the generation of heavy rainfall during the Oder flood event in July 1997. – Tellus, Series A: Dynamic Meteorology and Oceanography **6**, DOI: 10.3402/tellusa.v67.28661.

HOFSTÄTTER, M., G. BLÖSCHL, 2019: Vb Cyclones Synchronized With the Arctic-/North Atlantic Oscillation. – Journal of Geophysical Research: Atmospheres **124**, 3259–3278, DOI: 10.1029/2018JD029420.

HOFSTÄTTER, M., B. CHIMANI, 2012: Van Bebber's cyclone tracks at 700 hPa in the Eastern Alps for 1961-2002 and their comparison to Circulation Type Classifications. – Meteorologische Zeitschrift **21**, 459–473, DOI: 10.1127/0941-2948/2012/0473.

HOFSTÄTTER, M., B. CHIMANI, A. LEXER, G. BLÖSCHL, 2016: A new classification scheme of European cyclone tracks with relevance to precipitation. – Water Resources Research **52**, 7086–7104, DOI: 10.1002/2016WR019146.

HOFSTÄTTER, M., A. LEXER, M. HOMANN, G. BLÖSCHL, 2018: Large-scale heavy precipitation over central Europe and the role of atmospheric cyclone track types. – International Journal of Climatology **38**, e497–e517, DOI: 10.1002/joc.5386.

HOHENEGGER, C., P. BROCKHAUS, C.S. BRETHERTON, C. SCHÄR, 2009: The Soil Moisture-Precipitation Feedback in Simulations with Explicit and Parameterized Convection. – Journal of Climate **22**, 5003–5020, DOI: 10.1175/2009JCLI2604.1.

HONG, S.Y., M. KANAMITSU, 2014: Dynamical downscaling: Fundamental issues from an NWP point of view and recommendations. – Asia-Pacific Journal of Atmospheric Sciences **50**, 83–104, DOI: 10.1007/s13143-014-0029-2.

HORDOIR, R., C. DIETERICH, C. BASU, H. DIETZE, H. MEIER, 2013: Freshwater outflow of the Baltic Sea and transport in the Norwegian current: A statistical correlation analysis based on a numerical experiment. – Continental Shelf Research **64**, 1–9, DOI: 10.1016/j.csr.2013.05.006.

HURRELL, J.W., 1995: Decadal Trends in the North Atlantic Oscillation: Regional Temperatures and Precipitation. – Science **269**, 676–679, DOI: 10.1126/science.269.5224.676.

HWONG, Y.L., S. SONG, S.C. SHERWOOD, A.J. STIRLING, C. RIO, R. ROEHRIG, C.L. DALEU, R.S. PLANT, D. FUCHS, P. MAHER, L. TOUZÉ-PEIFFER, 2021: Characterizing Convection Schemes Using Their Responses to Imposed Tendency Perturbations. – Journal of Advances in Modeling Earth Systems **13**, DOI: 10.1029/2021MS002461.

ICPDR, 2020: Danube Basin: Facts & Figures – International Commission for Protection of the Danube River, 30 pp.

IKSE, 2005: Die Elbe und ihr Einzugsgebiet, Ein geographisch-hydrologischer und wasserwirtschaftlicher Überblick, 262 Internationale Kommission zum Schutz der Elbe.

IONITA, M., M. DIMA, G. LOHMANN, P. SCHOLZ, N. RIMBU, 2015: Predicting the June 2013 European Flooding Based on Precipitation, Soil Moisture, and Sea Level Pressure. – Journal of Hydrometeorology **16**, 598–614, DOI: 10.1175/JHM-D-14-0156.1.

JAEGER, E.B., I. ANDERS, D. LÜTHI, B. ROCKEL, C. SCHÄR, S.I. SENEVIRATNE, 2008: Analysis of ERA40-driven CLM simulations for Europe. – Meteorologische Zeitschrift **17**, 349–367, DOI: 10.1127/0941-2948/2008/0301.

JAMES, P., A. STOHL, N. SPICHTINGER, S. ECKHARDT, C. FORSTER, 2004: Climatological aspects of the extreme European rainfall of August 2002 and a trajectory method for estimating the associated evaporative source regions. – Natural Hazards and Earth System Science **4**, 733–746, DOI: 10.5194/nhess-4-733-2004.

JONES, T.R., D.A. RANDALL, 2011: Quantifying the limits of convective parameterizations. – Journal of Geophysical Research **116**, D08210, DOI: 10.1029/2010JD014913.

KASPAR, F., G. MÜLLER-WESTERMEIER, E. PENDA, H. MÄCHEL, K. ZIMMERMANN, A. KAISER-WEISS, T. DEUTSCHLÄNDER, 2013: Monitoring of climate change in Germany – data, products and services of Germany's National Climate Data Centre. – Advances in Science and Research **10**, 99–106, DOI: 10.5194/asr-10-99-2013.

KEEF, C., C. SVENSSON, J.A. TAWN, 2009: Spatial dependence in extreme river flows and precipitation for Great Britain. – Journal of Hydrology **378**, 240–252, DOI: 10.1016/j.jhydrol.2009.09.026.

KELEMEN, F.D., P. LUDWIG, M. REYERS, S. ULBRICH, J.G. PINTO, 2016: Evaluation of moisture sources for the Central European summer flood of May/June 2013 based on regional climate model simulations. – Tellus, Series A: Dynamic Meteorology and Oceanography **68**, DOI: 10.3402/tellusa.v68.29288.

KELEMEN, F.D., C. PRIMO, H. FELDMANN, B. AHRENS, 2019: Added Value of Atmosphere-Ocean Coupling in a Century-Long Regional Climate Simulation. – Atmosphere **10**, 537, DOI: 10.3390/atmos10090537.

KELLER, H., 1903: Die Hochflut in der Oder vom Juli 1903, ihre Ursachen und die Abwehr der Hochwasser-Gefahren. – Deutsche Bauzeitung **37**, 580–584, 586–592 Berlin.

KENDON, E.J., N.M. ROBERTS, C.A. SENIOR, M.J. ROBERTS, 2012: Realism of Rainfall in a Very High-Resolution Regional Climate Model. – Journal of Climate **25**, 5791–5806, DOI: 10.1175/JCLI-D-11-00562.1.

KIRSCHNER, M.J., A. KRUG, D. LUN, B. AHRENS, 2021: Zeitliche Häufung von Rain-on-Snow Hochwasser – Zufall oder Grundlage ihrer Vorhersagbarkeit?. – 12. Deutsche Klimatagung, online **DKT-12-40**.

KLEMEŠ, V., 1974: Some problems in pure and applied stochastic hydrology. – In Proceedings of the Symposium on Statistical Hydrology, Miscellaneaous Publications U.S. Dep. Agric. **1275**, 2–15.

KLEMEŠ, V., 1993: Probability of extreme hydrometeorological events - a different approach. – In: Z. W. K. ET AL. (Ed.), Extreme Hydrological Events: Precipitation, Floods and Droughts, volume 213 of *IAHS Publ*, 167–176.

KLING, H., M. FUCHS, M. PAULIN, 2012: Runoff conditions in the upper Danube basin under an ensemble of climate change scenarios. – Journal of Hydrology **424-425**, 264–277, DOI: 10.1016/j.jhydrol.2012.01.011.

KNIGHT, C.G., S.H.E. KNIGHT, N. MASSEY, T. AINA, C. CHRISTENSEN, D.J. FRAME, J.A. KETTLEBOROUGH, A. MARTIN, S. PASCOE, B. SANDERSON, D.A. STAINFORTH, M.R. ALLEN, 2007: Association of parameter, software, and hardware variation with large-scale behavior across 57,000 climate models.

– Proceedings of the National Academy of Sciences **104**, 12259–12264, DOI: 10.1073/pnas.0608144104.

KNIST, S., K. GOERGEN, C. SIMMER, 2020: Evaluation and projected changes of precipitation statistics in convection-permitting WRF climate simulations over Central Europe. – Climate Dynamics **55**, 325–341, DOI: 10.1007/s00382-018-4147-x.

KRAKAUER, N.Y., M.D. GROSSBERG, I. GLADKOVA, H. AIZENMAN, 2013: Information Content of Seasonal Forecasts in a Changing Climate. – Advances in Meteorology **2013**, 1–12, DOI: 10.1155/2013/480210.

KRESSER, W., 1957: Die Hochwässer der Donau, volume 32/33 of *Schriftenreihe des Österreichischen Wasserwirtschaftsverbandes* – Springer Verlag, Wien.

KREYLING, J., H. HENRY, 2011: Vanishing winters in Germany: soil frost dynamics and snow cover trends, and ecological implications. – Climate Research **46**, 269–276, DOI: 10.3354/cr00996.

KRUG, A., B. AHRENS, 2018: Analyse des Wasserdampftransports und intensiver Niederschlagsereignisse über dem Mittelmeerraum (WVTMed) – Water vapor transport and extreme precipitation events in theMediterranean region. – Abschlussbericht DWD-Auftrag 3043989/17-RAD

KRUG, A., B. AHRENS, 2020: Cyclone tracks from 1901 to 2010 in dynamically downscaled ERA-20C reanalysis (COSMO-CLM+NEMO) [Data set]. – Zenodo , DOI: 10.5281/zenodo.4333258.

KRUG, A., F. AEMISEGGER, M. SPRENGER, B. AHRENS, 2020a: Moisture sources of heavy precipitation in Central Europe during Vb-cyclones. – submitted to Climate Dynamics (published in 2022 with the revised title "Moisture sources of heavy precipitation in Central Europe in synoptic situations with Vb-cyclones", DOI: 10.1007/s00382-022-06256-7)

KRUG, A., C. PRIMO, S. FISCHER, A. SCHUMANN, B. AHRENS, 2020b: On the temporal variability of widespread rain-on-snow floods. – Meteorologische Zeitschrift **29**, 147–163, DOI: 10.1127/metz/2020/0989.

KRUG, A., P.K. POTHAPAKULA, C. PRIMO, B. AHRENS, 2021: Heavy Vb-cyclone precipitation: a transfer entropy application showcase. – Meteorologische Zeitschrift **30**, 279–284.

KRUG, A., F. AEMISEGGER, M. SPRENGER, B. AHRENS, 2022: Moisture sources of heavy precipitation in Central Europe in synoptic situations with Vb-cyclones. – Climate Dynamics , DOI: 10.1007/s00382-022-06256-7.

KUNDZEWICZ, Z.W., K. SZAMALEK, P. KOWALCZAK, 1999: The Great Flood of 1997 in Poland. – Hydrological Sciences Journal **44**, 855–870, DOI: 10.1080/02626669909492285.

KUNDZEWICZ, Z.W., U. ULBRICH, T. BRÜCHER, D. GRACZYK, A. KRÜGER, G.C. LECKEBUSCH, L. MENZEL, I. PIŃSKWAR, M. RADZIEJEWSKI, M. SZWED, 2005: Summer Floods in Central Europe – Climate Change Track?. – Natural Hazards **36**, 165–189, DOI: 10.1007/s11069-004-4547-6.

KUNDZEWICZ, Z.W., V. KRYSANOVA, R. DANKERS, Y. HIRABAYASHI, S. KANAE, F.F. HATTERMANN, S. HUANG, P.C.D. MILLY, M. STOFFEL, P.P.J. DRIESSEN, P. MATCZAK, P. QUEVAUVILLER, H.J. SCHELLNHUBER, 2016: Differences in flood hazard projections in Europe – their causes and consequences for decision making. – Hydrological Sciences Journal 02626667.2016.1241398, DOI: 10.1080/02626667.2016.1241398.

LÄDERACH, A., H. SODEMANN, 2016: A revised picture of the atmospheric moisture residence time. – Geophysical Research Letters **43**, 924–933, DOI: 10.1002/2015GL067449.

LANGHANS, W., J. SCHMIDLI, O. FUHRER, S. BIERI, C. SCHÄR, 2013: Long-Term Simulations of Thermally Driven Flows and Orographic Convection at Convection-arameterizing and Cloud-Resolving Resolutions. – Journal of Applied Meteorology and Climatology **52**, 1490–1510, DOI: 10.1175/JAMC-D-12-0167.1.

LATERNSER, M., M. SCHNEEBELI, 2003: Long-term snow climate trends of the Swiss Alps (1931-99). – International Journal of Climatology **23**, 733–750, DOI: 10.1002/joc.912.

LEBEAUPIN BROSSIER, C., K. BÉRANGER, C. DELTEL, P. DROBINSKI, 2011: The Mediterranean response to different space-time resolution atmospheric forcings using perpetual mode sensitivity simulations. – Ocean Modelling **36**, 1–25, DOI: 10.1016/j.ocemod.2010.10.008.

LEBEAUPIN BROSSIER, C., K. BÉRANGER, P. DROBINSKI, 2012: Sensitivity of the northwestern Mediterranean Sea coastal and thermohaline circulations simulated by the 1/12°-resolution ocean model NEMO-MED12 to the spatial and temporal resolution of atmospheric forcing. – Ocean Modelling **43-44**, 94–107, DOI: 10.1016/j.ocemod.2011.12.007.

LEHNER, B., P. DÖLL, J. ALCAMO, T. HENRICHS, F. KASPAR, 2006: Estimating the Impact of Global Change on Flood and Drought Risks in Europe: A Continental, Integrated Analysis. – Climatic Change **75**, 273–299, DOI: 10.1007/s10584-006-6338-4.

LEHR, C., P.J. WARD, M. KUMMU, 2012: Impact of Large-scale Climatic Oscillations on Snowfall-related Climate Parameters in the World's Major Downhill Ski Areas: A Review. – Mountain Research and Development **32**, 431–445, DOI: 10.1659/MRD-JOURNAL-D-12-00062.1.

LENDERINK, G., VAN E. MEIJGAARD, 2008: Increase in hourly precipitation extremes beyond expectations from temperature changes. – Nature Geoscience **1**, 511–514, DOI: 10.1038/ngeo262.

LENDERINK, G., VAN E. MEIJGAARD, 2010: Linking increases in hourly precipitation extremes to atmospheric temperature and moisture changes. – Environmental Research Letters **5**, 025208, DOI: 10.1088/1748-9326/5/2/025208.

LENDERINK, G., H.Y. MOK, T.C. LEE, VAN G.J. OLDENBORGH, 2011: Scaling and trends of hourly precipitation extremes in two different climate zones – Hong Kong and the Netherlands. – Hydrology and Earth System Sciences **15**, 3033–3041, DOI: 10.5194/hess-15-3033-2011.

LENDERINK, G., R. BARBERO, J.M. LORIAUX, H.J. FOWLER, 2017: Super-Clausius-Clapeyron Scaling of Extreme Hourly Convective Precipitation and Its Relation to Large-Scale Atmospheric Conditions. – Journal of Climate **30**, 6037–6052, DOI: 10.1175/JCLI-D-16-0808.1.

LENGFELD, K., T. WINTERRATH, T. JUNGHÄNEL, M. HAFER, A. BECKER, 2019: Characteristic spatial extent of hourly and daily precipitation events in Germany derived from 16 years of radar data. – Meteorologische Zeitschrift **28**, 363–378, DOI: 10.1127/metz/2019/0964.

LENGGENHAGER, S., M. CROCI-MASPOLI, S. BRÖNNIMANN, O. MARTIUS, 2019: On the dynamical coupling between atmospheric blocks and heavy precipitation events: A discussion of the southern Alpine flood in October 2000. – Quarterly Journal of the Royal Meteorological Society **145**, 530–545, DOI: 10.1002/qj.3449.

LEONARD, M., S. WESTRA, A. PHATAK, M. LAMBERT, VAN DEN B. HURK, K. MCINNES, J. RISBEY, S. SCHUSTER, D. JAKOB, M. STAFFORD-SMITH, 2014: A compound event framework for understanding extreme impacts. – WIREs Climate Change **5**, 113–128, DOI: 10.1002/wcc.252.

LEUTWYLER, D., A. IMAMOVIC, C. SCHÄR, 2021: The Continental-Scale Soil-Moisture Precipitation Feedback in Europe with Parameterized and Explicit Convection. – Journal of Climate 1–56, DOI: 10.1175/JCLI-D-20-0415.1.

LI, D., D.P. LETTENMAIER, S.A. MARGULIS, K. ANDREADIS, 2019: The Role of Rain-on-Snow in Flooding Over the Conterminous United States. – Water Resources Research **55**, 8492–8513, DOI: 10.1029/2019WR024950.

LIZIER, J.T., 2014: JIDT: An Information-Theoretic Toolkit for Studying the Dynamics of Complex Systems. – Frontiers in Robotics and AI **1**, DOI: 10.3389/frobt.2014.00011.

LUN, D., S. FISCHER, A. VIGLIONE, G. BLÖSCHL, 2020: Detecting Flood-Rich and Flood-Poor Periods in Annual Peak Discharges Across Europe. – Water Resources Research **56**, DOI: 10.1029/2019WR026575.

MAASOUMI, E., 1993: A compendium to information theory in economics and econometrics. – Econometric Reviews **12**, 137–181, DOI: 10.1080/07474939308800260.

MADEC, G., THE NEMO TEAM, 2016: NEMO Ocean Engine. Note du Pôle de modélisation de l'Institut Pierre-Simon Laplace No 27, Paris. ISSN No 1288-1619.

MARTIUS, O., H. SODEMANN, H. JOOS, S. PFAHL, A. WINSCHALL, M. CROCI-MASPOLI, M. GRAF, E. MADONNA, B. MUELLER, S. SCHEMM, J. SEDLÁČEK, M. SPRENGER, H. WERNLI, 2013: The role of upper-level dynamics and surface processes for the Pakistan flood of July 2010. – Quarterly Journal of the Royal Meteorological Society **139**, 1780–1797, DOI: 10.1002/qj.2082.

MCCABE, G.J., M.P. CLARK, L.E. HAY, 2007: Rain-on-Snow Events in the Western United States. – Bulletin of the American Meteorological Society **88**, 319–328, DOI: 10.1175/BAMS-88-3-319.

MCGREGOR, G.R., 2019: Climate and rivers. – River Research and Applications rra.3508, DOI: 10.1002/rra.3508.

MEREDITH, E.P., U. ULBRICH, H.W. RUST, 2019: The Diurnal Nature of Future Extreme Precipitation Intensification. – Geophysical Research Letters **46**, 7680–7689, DOI: 10.1029/2019GL082385.

MERZ, B., J. AERTS, K. ARNBJERG-NIELSEN, M. BALDI, A. BECKER, A. BICHET, G. BLÖSCHL, L.M. BOUWER, A. BRAUER, F. CIOFFI, J.M. DELGADO, M. GOCHT, F. GUZZETTI, S. HARRIGAN, K. HIRSCHBOECK, C. KILSBY, W. KRON, H.H. KWON, U. LALL, R. MERZ, K. NISSEN, P. SALVATTI, T. SWIERCZYNSKI, U. ULBRICH, A. VIGLIONE, P.J. WARD, M. WEILER, B. WILHELM, M. NIED, 2014: Floods and climate: emerging perspectives for flood risk assessment and management. – Natural Hazards and Earth System Sciences **14**, 1921–1942, DOI: 10.5194/nhess-14-1921-2014.

MERZ, B., V.D. NGUYEN, S. VOROGUSHYN, 2016: Temporal clustering of floods in Germany: Do flood-rich and flood-poor periods exist?. – Journal of Hydrology **541**, 824–838, DOI: 10.1016/j.jhydrol.2016.07.041.

MERZ, B., N.V. DUNG, H. APEL, L. GERLITZ, K. SCHRÖTER, E. STEIROU, S. VOROGUSHYN, 2018: Spatial coherence of flood-rich and flood-poor periods across Germany. – Journal of Hydrology **559**, 813–826, DOI: 10.1016/j.jhydrol.2018.02.082.

MERZ, R., G. BLÖSCHL, 2008a: Flood frequency hydrology: 1. Temporal, spatial, and causal expansion of information. – Water Resources Research **44**, DOI: 10.1029/2007WR006744.

MERZ, R., G. BLÖSCHL, 2008b: Flood frequency hydrology: 2. Combining data evidence. – Water Resources Research **44**, DOI: 10.1029/2007WR006745.

MERZ, R., L. TARASOVA, S. BASSO, 2020: The flood cooking book: ingredients and regional flavors of floods across Germany. – Environmental Research Letters **15**, 114024, DOI: 10.1088/1748-9326/abb9dd.

MESSMER, M., J.J. GÓMEZ-NAVARRO, C.C. RAIBLE, 2015: Climatology of Vb cyclones, physical mechanisms and their impact on extreme precipitation over Central Europe. – Earth System Dynamics **6**, 541–553, DOI: 10.5194/esd-6-541-2015.

MESSMER, M., J.J. GÓMEZ-NAVARRO, C.C. RAIBLE, 2017: Sensitivity experiments on the response of Vb cyclones to sea surface temperature and soil moisture changes. – Earth System Dynamics **8**, 477–493, DOI: 10.5194/esd-8-477-2017.

MESSMER, M., C.C. RAIBLE, J.J. GÓMEZ-NAVARRO, 2020: Impact of climate change on the climatology of Vb cyclones. – Tellus A: Dynamic Meteorology and Oceanography **72**, 1–18, DOI: 10.1080/16000870.2020.1724021.

MITTERMEIER, M., M. BRAUN, M. HOFSTÄTTER, Y. WANG, R. LUDWIG, 2019: Detecting Climate Change Effects on Vb Cyclones in a 50-Member Single-Model Ensemble Using Machine Learning. – Geophysical Research Letters **46**, 14653–14661, DOI: 10.1029/2019GL084969.

MOORE, G.W.K., I.A. RENFREW, R.S. PICKART, 2013: Multidecadal Mobility of the North Atlantic Oscillation. – Journal of Climate **26**, 2453–2466, DOI: 10.1175/JCLI-D-12-00023.1.

MUNICH RE, 2019: NatCatSERVICE Database. Munich Reinsurance Company Geo Risks Research.

MURRAY, R., I. SIMMONDS, 1991: A numerical scheme for tracking cyclone centres from digital data. Part I: Development and operationof the scheme. – Australian Meteorological Magazine **39**, 155–166.

NAUMANN, A., H. SUJATA, K. KRAUSE, U. SEEGER, 1978: Sommerhochwasserder Oder 1977. – Wasserwirtschaft – Wassertechnik **28**, 21–57.

NEU, U., M.G. AKPEROV, N. BELLENBAUM, R. BENESTAD, R. BLENDER, R. CABALLERO, A. COCOZZA, H.F. DACRE, Y. FENG, K. FRAEDRICH, J. GRIEGER, S. GULEV, J. HANLEY, T. HEWSON, M. INATSU, K. KEAY, S.F. KEW, I. KINDEM, G.C. LECKEBUSCH, M.L.R. LIBERATO, P. LIONELLO, I.I. MOKHOV, J.G. PINTO, C.C. RAIBLE, M. REALE, I. RUDEVA, M. SCHUSTER, I. SIMMONDS, M. SINCLAIR, M. SPRENGER, N.D. TILININA, I.F. TRIGO, S. ULBRICH, U. ULBRICH, X.L. WANG, H. WERNLI, 2013: IMILAST: A Community Effort to Intercompare Extratropical Cyclone Detection and Tracking Algorithms. – Bulletin of the American Meteorological Society **94**, 529–547, DOI: 10.1175/BAMS-D-11-00154.1.

NICHOLLS, M.E., 2015: An investigation of how radiation may cause accelerated rates of tropical cyclogenesis and diurnal cycles of convective activity. – Atmospheric Chemistry and Physics **15**, 9003–9029, DOI: 10.5194/acp-15-9003-2015.

NIED, M., Y. HUNDECHA, B. MERZ, 2013: Flood-initiating catchment conditions: a spatio-temporal analysis of large-scale soil moisture patterns in the Elbe River basin. – Hydrology and Earth System Sciences **17**, 1401–1414, DOI: 10.5194/hess-17-1401-2013.

NIED, M., T. PARDOWITZ, K. NISSEN, U. ULBRICH, Y. HUNDECHA, B. MERZ, 2014: On the relationship between hydro-meteorological patterns and flood types. – Journal of Hydrology **519**, 3249–3262, DOI: 10.1016/j.jhydrol.2014.09.089.

NISSEN, K.M., U. ULBRICH, G.C. LECKEBUSCH, 2013: Vb cyclones and associated rainfall extremes over Central Europe under present day and climate change conditions. – Meteorologische Zeitschrift **22**, 649–660, DOI: 10.1127/0941-2948/2013/0514.

NOBRE, G.G., B. JONGMAN, J. AERTS, P.J. WARD, 2017: The role of climate variability in extreme floods in Europe. – Environmental Research Letters **12**, 084012, DOI: 10.1088/1748-9326/aa7c22.

OBERMANN, A., S. BASTIN, S. BELAMARI, D. CONTE, M.A. GAERTNER, L. LI, B. AHRENS, 2018: Mistral and Tramontane wind speed and wind direction patterns in regional climate simulations. – Climate Dynamics **51**, 1059–1076, DOI: 10.1007/s00382-016-3053-3.

OKI, T., Y.C. SUD, 1998: Design of Total Runoff Integrating Pathways (TRIP)–A Global River Channel Network. – Earth Interactions **2**, 1–37, DOI: 10.1175/1087-3562(1998)002<0001:DOTRIP>2.3.CO;2.

PAL, J.S., F. GIORGI, X. BI, 2004: Consistency of recent European summer precipitation trends and extremes with future regional climate projections. – Geophysical Research Letters **31**, DOI: 10.1029/2004GL019836.

PALL, P., L.M. TALLAKSEN, F. STORDAL, 2019: A Climatology of Rain-on-Snow Events for Norway. – Journal of Climate **32**, 6995–7016, DOI: 10.1175/JCLI-D-18-0529.1.

PAPRITZ, L., S. PFAHL, H. SODEMANN, H. WERNLI, 2015: A Climatology of Cold Air Outbreaks and Their Impact on Air–Sea Heat Fluxes in the High-Latitude South Pacific. – Journal of Climate **28**, 342–364, DOI: 10.1175/JCLI-D-14-00482.1.

PENDERGRASS, A.G., K.A. REED, B. MEDEIROS, 2016: The link between extreme precipitation and convective organization in a warming climate: Global radiative-convective equilibrium simulations. – Geophysical Research Letters **43**, 11,445–11,452, DOI: 10.1002/2016GL071285.

PETROW, T., B. MERZ, K.E. LINDENSCHMIDT, A.H. THIEKEN, 2007: Aspects of seasonality and flood generating circulation patterns in a mountainous catchment in south-eastern Germany. – Hydrology and Earth System Sciences **11**, 1455–1468, DOI: 10.5194/hess-11-1455-2007.

PETROW, T., J. ZIMMER, B. MERZ, 2009: Changes in the flood hazard in Germany through changing frequency and persistence of circulation patterns. – Natural Hazards and Earth System Sciences **9**, 1409–1423, DOI: 10.5194/nhess-9-1409-2009.

PFAHL, S., H. WERNLI, 2012: Quantifying the relevance of atmospheric blocking for co-located temperature extremes in the Northern Hemisphere on (sub-)daily time scales. – Geophysical Research Letters **39**, n/a–n/a, DOI: 10.1029/2012GL052261.

PFAHL, S., C. SCHWIERZ, M. CROCI-MASPOLI, C.M. GRAMS, H. WERNLI, 2015: Importance of latent heat release in ascending air streams for atmospheric blocking. – Nature Geoscience **8**, 610–614, DOI: 10.1038/ngeo2487.

PHAM, T.V., J. BRAUCH, C. DIETERICH, B. FRUEH, B. AHRENS, 2014: New coupled atmosphere-ocean-ice system COSMO-CLM/NEMO: assessing air temperature sensitivity over the North and Baltic Seas. – Oceanologia **56**, 167–189, DOI: 10.5697/oc.56-2.167.

PHAM, T.V., J. BRAUCH, B. FRÜH, B. AHRENS, 2017: Simulation of snowbands in the Baltic Sea area with the coupled atmosphere-ocean-ice model COSMO-CLM/NEMO. – Meteorologische Zeitschrift **26**, 71–82, DOI: 10.1127/metz/2016/0775.

PIAGET, N., P. FROIDEVAUX, P. GIANNAKAKI, F. GIERTH, O. MARTIUS, M. RIEMER, G. WOLF, C.M. GRAMS, 2015: Dynamics of a local Alpine flooding event in October 2011: moisture source and large-scale circulation. – Quarterly Journal of the Royal Meteorological Society **141**, 1922–1937, DOI: 10.1002/qj.2496.

POLI, P., H. HERSBACH, D.P. DEE, P. BERRISFORD, A.J. SIMMONS, F. VITART, P. LALOYAUX, D.G.H. TAN, C. PEUBEY, J.N. THÉPAUT, Y. TRÉMOLET, E.V. HÓLM, M. BONAVITA, L. ISAKSEN, M. FISHER, 2016: ERA-20C: An Atmospheric Reanalysis of the Twentieth Century. – Journal of Climate **29**, 4083–4097, DOI: 10.1175/JCLI-D-15-0556.1.

POTHAPAKULA, P.K., C. PRIMO, B. AHRENS, 2019: Quantification of Information Exchange in Idealized and Climate System Applications. – Entropy **21**, 1094, DOI: 10.3390/e21111094.

POTHAPAKULA, P.K., C. PRIMO, S. SØRLAND, B. AHRENS, 2020: The synergistic impact of ENSO and IOD on Indian summer monsoon rainfall in observations and climate simulations – an information theory perspective. – Earth System Dynamics **11**, 903–923, DOI: 10.5194/esd-11-903-2020.

POTHAPAKULA, P.K., A. KRUG, C. PRIMO, B. AHRENS, 2021: Source code for a transfer entropy application showcase (Heavy Vb-cyclone precipitation) [source code]. – Zenodo , DOI: 10.5281/zenodo.4568218.

PREIN, A.F., G.J. HOLLAND, R.M. RASMUSSEN, J. DONE, K. IKEDA, M.P. CLARK, C.H. LIU, 2013: Importance of Regional Climate Model Grid Spacing for the Simulation of Heavy Precipitation in the Colorado Headwaters. – Journal of Climate **26**, 4848–4857, DOI: 10.1175/JCLI-D-12-00727.1.

PREIN, A.F., W. LANGHANS, G. FOSSER, A. FERRONE, N. BAN, K. GOERGEN, M. KELLER, M. TÖLLE, O. GUTJAHR, F. FESER, E. BRISSON, S. KOLLET, J. SCHMIDLI, N.P.M. LIPZIG, R. LEUNG, 2015: A review on regional convection-permitting climate modeling: Demonstrations, prospects, and challenges. – Reviews of Geophysics **53**, 323–361, DOI: 10.1002/2014RG000475.

PREIN, A.F., R. RASMUSSEN, G. STEPHENS, 2017: Challenges and Advances in Convection-Permitting Climate Modeling. – Bulletin of the American Meteorological Society **98**, 1027–1030, DOI: 10.1175/BAMS-D-16-0263.1.

PRIMO, C., F.D. KELEMEN, H. FELDMANN, N. AKHTAR, B. AHRENS, 2019: A regional atmosphere-ocean climate system model (CCLMv5.0clm7-NEMOv3.3-NEMOv3.6) over Europe including three marginal seas: on its stability and performance. – Geoscientific Model Development **12**, 5077–5095, DOI: 10.5194/gmd-12-5077-2019.

PURR, C., E. BRISSON, B. AHRENS, 2019: Convective Shower Characteristics Simulated with the Convection-Permitting Climate Model COSMO-CLM. – Atmosphere **10**, 810, DOI: 10.3390/atmos10120810.

PURR, C., E. BRISSON, B. AHRENS, 2021: Convective rain cell characteristics and scaling in climate projections for Germany. – International Journal of Climatology **41**, 3174–3185, DOI: 10.1002/joc.7012.

R CORE TEAM, 2013: R: A Language and Environment for Statistical Computing R Foundation for Statistical Computing, Vienna, Austria ISBN 3-900051-07-0.

RAFFA, M., A. REDER, M. ADINOLFI, P. MERCOGLIANO, 2021: A Comparison between One-Step and Two-Step Nesting Strategy in the Dynamical Downscaling of Regional Climate Model COSMO-CLM at 2.2 km Driven by ERA5 Reanalysis. – Atmosphere **12**, 260, DOI: 10.3390/atmos12020260.

RAIBLE, C.C., P.M. DELLA-MARTA, C. SCHWIERZ, H. WERNLI, R. BLENDER, 2008: Northern Hemisphere Extratropical Cyclones: A Comparison of Detection and Tracking Methods and Different Reanalyses. – Monthly Weather Review **136**, 880–897, DOI: 10.1175/2007MWR2143.1.

ROCKEL, B., 2015: The Regional Downscaling Approach: a Brief History and Recent Advances. – Current Climate Change Reports **1**, 22–29, DOI: 10.1007/s40641-014-0001-3.

ROCKEL, B., A. WILL, A. HENSE, 2008: The Regional Climate Model COSMO-CLM (CCLM). – Meteorologische Zeitschrift **17**, 347–348, DOI: 10.1127/0941-2948/2008/0309.

RODDA, H.J.E., 2005: The Development and Application of a Flood Risk Model for the Czech Republic. – Natural Hazards **36**, 207–220, DOI: 10.1007/s11069-004-4549-4.

RUDOLF, B., J. RAPP, 2003: Das Jahrhunderthochwasser der Elbe: Synoptische Wetterentwicklung und klimatologische Aspekte. – Abdruck aus Klimastatusbericht 2002, DWD Offenbach

RUNGE, J., V. PETOUKHOV, J. KURTHS, 2014: Quantifying the Strength and Delay of Climatic Interactions: The Ambiguities of Cross Correlation and a Novel Measure Based on Graphical Models. – Journal of Climate **27**, 720–739, DOI: 10.1175/JCLI-D-13-00159.1.

RUPPERT, J.H., C. HOHENEGGER, 2018: Diurnal Circulation Adjustment and Organized Deep Convection. – Journal of Climate **31**, 4899–4916, DOI: 10.1175/JCLI-D-17-0693.1.

RUST, H.W., A. RICHLING, P. BISSOLLI, U. ULBRICH, 2015: Linking teleconnection patterns to European temperature – a multiple linear regression model. – Meteorologische Zeitschrift **24**, 411–423, DOI: 10.1127/metz/2015/0642.

RUTI, P.M., S. SOMOT, F. GIORGI, C. DUBOIS, E. FLAOUNAS, A. OBERMANN, A. DELL'AQUILA, G. PISACANE, A. HARZALLAH, E. LOMBARDI, B. AHRENS, N. AKHTAR, A. ALIAS, T. ARSOUZE, R. AZNAR, S. BASTIN, J. BARTHOLY, K. BÉRANGER, J. BEUVIER, S. BOUFFIES-CLOCHÉ, J. BRAUCH, W. CABOS, S. CALMANTI, J.C. CALVET, A. CARILLO, D. CONTE, E. COPPOLA, V. DJURDJEVIC, P. DROBINSKI, A. ELIZALDE-ARELLANO, M. GAERTNER, P. GALÀN, C. GALLARDO, S. GUALDI, M. GONCALVES, O. JORBA, G. JORDÀ, B. L'HEVEDER, C. LEBEAUPIN-BROSSIER, L. LI, G. LIGUORI, P. LIONELLO, D. MACIÀS, P. NABAT, B. ÖNOL, B. RAIKOVIC, K. RAMAGE, F. SEVAULT, G. SANNINO, M.V. STRUGLIA, A. SANNA, C. TORMA, V. VERVATIS, 2016: Med-CORDEX Initiative for Mediterranean Climate Studies. – Bulletin of the American Meteorological Society **97**, 1187–1208, DOI: 10.1175/BAMS-D-14-00176.1.

SAEED, S., E. BRISSON, M. DEMUZERE, H. TABARI, P. WILLEMS, VAN N.P.M. LIPZIG, 2017: Multidecadal convection permitting climate simulations over Belgium: sensitivity of future precipitation extremes. – Atmospheric Science Letters **18**, 29–36, DOI: 10.1002/asl.720.

SCHÄR, C., D. LÜTHI, U. BEYERLE, E. HEISE, 1999: The Soil–Precipitation Feedback: A Process Study with a Regional Climate Model. – Journal of Climate **12**, 722–741, DOI: 10.1175/1520-0442(1999)012<0722:TSPFAP>2.0.CO;2.

SCHÄR, C., O. FUHRER, A. ARTEAGA, N. BAN, C. CHARPILLOZ, S. DI GIROLAMO, L. HENTGEN, T. HOEFLER, X. LAPILLONNE, D. LEUTWYLER, K. OSTERRIED, D. PANOSETTI, S. RÜDISÜHLI, L. SCHLEMMER, T.C. SCHULTHESS, M. SPRENGER, S. UBBIALI, H. WERNLI, 2020: Kilometer-Scale Climate Models: Prospects and Challenges. – Bulletin of the American Meteorological Society **101**, E567–E587, DOI: 10.1175/BAMS-D-18-0167.1.

SCHMOCKER-FACKEL, P., F. NAEF, 2010a: Changes in flood frequencies in Switzerland since 1500. – Hydrology and Earth System Sciences **14**, 1581–1594, DOI: 10.5194/hess-14-1581-2010.

SCHMOCKER-FACKEL, P., F. NAEF, 2010b: More frequent flooding? Changes in flood frequency in Switzerland since 1850. – Journal of Hydrology **381**, 1–8, DOI: 10.1016/j.jhydrol.2009.09.022.

SCHNEIDER, T., J. TEIXEIRA, C.S. BRETHERTON, F. BRIENT, K.G. PRESSEL, C. SCHÄR, A.P. SIEBESMA, 2017: Climate goals and computing the future of clouds. – Nature Climate Change **7**, 3–5, DOI: 10.1038/nclimate3190.

SCHNEIDER, U., P. OTTO, B. RUDOLF, 2003: Das Niederschlagsgeschehen in Deutschland über den Jahreswechsel 2002/2003. Weltzentrum für Niederschlagsklimatologie, Deutscher Wetterdienst, Offenbach a.M.

SCHOLDER-AEMISEGGER, F., 2013: Atmospheric stable water isotope measurements at the timescale of extratropical weather systems. – PhD Thesis, ETH Zurich **21165**, 254 pp.

SCHREIBER, T., 2000: Measuring Information Transfer. – Physical Review Letters **85**, 461–464, DOI: 10.1103/PhysRevLett.85.461.

SCHRÖDER, U., 1990: Die Hochwasser an Rhein und Mosel im April und Mai 1983. – Bericht Nr. II-3 unter Schirmherrschaft der KHR

SCHRODIN, E., E.H., 2002: A new multi-layer soil model. Tech. Rep. 2, COSMO Newsletter.

SCHRÖTER, K., M. KUNZ, F. ELMER, B. MÜHR, B. MERZ, 2015: What made the June 2013 flood in Germany an exceptional event? A hydro-meteorological evaluation. – Hydrology and Earth System Sciences **19**, 309–327, DOI: 10.5194/hess-19-309-2015.

SEAGER, R., N. HENDERSON, 2013: Diagnostic Computation of Moisture Budgets in the ERA-Interim Reanalysis with Reference to Analysis of CMIP-Archived Atmospheric Model Data. – Journal of Climate **26**, 7876–7901, DOI: 10.1175/JCLI-D-13-00018.1.

SEVAULT, F., S. SOMOT, A. ALIAS, C. DUBOIS, C. LEBEAUPIN-BROSSIER, P. NABAT, F. ADLOFF, M. DÉQUÉ, B. DECHARME, 2014: A fully coupled Mediterranean regional climate system model: design and evaluation of the ocean component for the 1980-2012 period. – Tellus A: Dynamic Meteorology and Oceanography **66**, 23967, DOI: 10.3402/tellusa.v66.23967.

SHANNON, C.E., 1948: A Mathematical Theory of Communication. – Bell System Technical Journal **27**, 379–423, DOI: 10.1002/j.1538-7305.1948.tb01338.x.

SHERWOOD, S.C., S. BONY, J.L. DUFRESNE, 2014: Spread in model climate sensitivity traced to atmospheric convective mixing. – Nature **505**, 37–42, DOI: 10.1038/nature12829.

SIMMONDS, I., R. MURRAY, R. LEIGHTON, 1999: A refinement cyclone tracking methods with data from FROST. – Australian Meteorological Magazine 35–49 Special edition as part of the Antarctic First Regional Observing Study of the Troposphere (FROST) project.

SODEMANN, H., E. ZUBLER, 2010: Seasonal and inter-annual variability of the moisture sources for Alpine precipitation during 1995-2002. – International Journal of Climatology **30**, 947–961, DOI: 10.1002/joc.1932.

SODEMANN, H., V. MASSON-DELMOTTE, C. SCHWIERZ, B.M. VINTHER, H. WERNLI, 2008a: Interannual variability of Greenland winter precipitation sources: 2. Effects of North Atlantic Oscillation variability on stable isotopes in precipitation. – Journal of Geophysical Research: Atmospheres **113**, DOI: 10.1029/2007JD009416.

SODEMANN, H., C. SCHWIERZ, H. WERNLI, 2008b: Interannual variability of Greenland winter precipitation sources: Lagrangian moisture diagnostic and North Atlantic Oscillation influence. – Journal of Geophysical Research **113**, D03107, DOI: 10.1029/2007JD008503.

SODEMANN, H., H. WERNLI, C. SCHWIERZ, 2009: Sources of water vapour contributing to the Elbe flood in August 2002 - A tagging study in a mesoscale model. – Quarterly Journal of the Royal Meteorological Society **135**, 205–223, DOI: 10.1002/qj.374.

SOHN, B.J., S.C. PARK, 2010: Strengthened tropical circulations in past three decades inferred from water vapor transport. – Journal of Geophysical Research **115**, D15112, DOI: 10.1029/2009JD013713.

SOHN, B.J., E.A. SMITH, F.R. ROBERTSON, S.C. PARK, 2004: Derived Over-Ocean Water Vapor Transports from Satellite-Retrieved E – P Datasets. – Journal of Climate **17**, 1352–1365, DOI: 10.1175/1520-0442(2004)017<1352:DOWVTF>2.0.CO;2.

SOMOT, S., P. RUTI, B. AHRENS, E. COPPOLA, G. JORDÀ, G. SANNINO, F. SOLMON, 2018: Editorial for the Med-CORDEX special issue. – Climate Dynamics **51**, 771–777, DOI: 10.1007/s00382-018-4325-x.

SORG, W., 1926: Ursachen und Verlauf des Oder-Hochwassers vom Juni 1926. – Geographischer Anzeiger **27**, 262–265 Gotha.

SPEARMAN, C., 1904: The Proof and Measurement of Association between Two Things. – The American Journal of Psychology **15**, 72, DOI: 10.2307/1412159.

SPENGLER, R., 2002: The new Quality Control- and Monitoring System of the Deutscher Wetterdienst. – Proceedings of the WMO TechnicalConference on Meteorological and Environmental Instruments and Methods of Observation Bratislava.

SPRENGER, M., H. WERNLI, 2015: The LAGRANTO Lagrangian analysis tool – version 2.0. – Geoscientific Model Development **8**, 2569–2586, DOI: 10.5194/gmd-8-2569-2015.

SPRENGER, M., G. FRAGKOULIDIS, H. BINDER, M. CROCI-MASPOLI, P. GRAF, C.M. GRAMS, P. KNIPPERTZ, E. MADONNA, S. SCHEMM, B. ŠKERLAK, H. WERNLI, 2017: Global climatologies of Eulerian and Lagrangian flow features based on ERA-Interim. – Bulletin of the American Meteorological Society , DOI: 10.1175/BAMS-D-15-00299.1.

STAHL, N., M. HOFSTÄTTER, 2018: Vb-Zugbahnen und deren Auftreten als Serie mit Bezug zu den resultierenden Hochwassern in Bayern und Auswirkungen auf Rückhalteräume im Isareinzugsgebiet. – Hydrologie & Wasserbewirtschaftung **62**, 77–97, DOI: 10.5675/HyWa_2018.

STEEN-LARSEN, H.C., A.E. SVEINBJÖRNSDOTTIR, T. JONSSON, F. RITTER, J.L. BONNE, V. MASSON-DELMOTTE, H. SODEMANN, T. BLUNIER, D. DAHL-JENSEN, B.M. VINTHER, 2015: Moisture sources and synoptic to seasonal variability of North Atlantic water vapor isotopic composition. – Journal of Geophysical Research: Atmospheres **120**, 5757–5774, DOI: 10.1002/2015JD023234.

STEIN, C., G. MALITZ, 2013: Das Hochwasser an Elbe und Donauim Juni 2013. – Berichte des Deutschen Wetterdienstes **242** Offenbach am Main: Selbstverlag des Deutschen Wetterdienstes.

STEINFELD, D., S. PFAHL, 2019: The role of latent heating in atmospheric blocking dynamics: a global climatology. – Climate Dynamics **53**, 6159–6180, DOI: 10.1007/s00382-019-04919-6.

STEINFELD, D., M. BOETTCHER, R. FORBES, S. PFAHL, 2020: The sensitivity of atmospheric blocking to upstream latent heating – numerical experiments. – Weather and Climate Dynamics **1**, 405–426, DOI: 10.5194/wcd-1-405-2020.

STEPHENSON, D.B., 2008: Definition, diagnosis, and origin of extreme weather and climate events, 11–23 Cambridge University Press, DOI: 10.1017/CBO9780511535840.004.

STOHL, A., P. JAMES, 2004: A Lagrangian Analysis of the Atmospheric Branch of the Global Water Cycle. Part I: Method Description, Validation, and Demonstration for the August 2002 Flooding in Central Europe. – Journal of Hydrometeorology **5**, 656–678, DOI: 10.1175/1525-7541(2004)005<0656:ALAOTA>2.0.CO;2.

STUCKI, P., R. RICKLI, S. BRÖNNIMANN, O. MARTIUS, H. WANNER, D. GREBNER, J. LUTERBACHER, 2012: Weather patterns and hydro-climatological precursors of extreme floods in Switzerland since 1868. – Meteorologische Zeitschrift **21**, 531–550, DOI: 10.1127/0941-2948/2012/368.

STUCKI, P., P. FROIDEVAUX, M. ZAMURIANO, F.A. ISOTTA, M. MESSMER, A. MARTYNOV, 2020: Simulations of the 2005, 1910, and 1876 Vb cyclones over the Alps – sensitivity to model physics and cyclonic moisture flux. – Natural Hazards and Earth System Sciences **20**, 35–57, DOI: 10.5194/nhess-20-35-2020.

SVENSSON, C., A. BROOKSHAW, A.A. SCAIFE, V.A. BELL, J.D. MACKAY, C.R. JACKSON, J. HANNAFORD, H.N. DAVIES, A. ARRIBAS, S. STANLEY, 2015: Long-range forecasts of UK winter hydrology. – Environmental Research Letters **10**, 064006, DOI: 10.1088/1748-9326/10/6/064006.

TARASOVA, L., S. BASSO, C. PONCELET, R. MERZ, 2018: Exploring Controls on Rainfall-Runoff Events: 2. Regional Patterns and Spatial Controls of Event Characteristics in Germany. – Water Resources Research **54**, 7688–7710, DOI: 10.1029/2018WR022588.

TARASOVA, L., R. MERZ, A. KISS, S. BASSO, G. BLÖSCHL, B. MERZ, A. VIGLIONE, S. PLÖTNER, B. GUSE, A. SCHUMANN, S. FISCHER, B. AHRENS, F. ANWAR, A. BÁRDOSSY, P. BÜHLER, U. HABERLANDT, H. KREIBICH, A. KRUG, D. LUN, H. MÜLLER-THOMY, R. PIDOTO, C. PRIMO, J. SEIDEL, S. VOROGUSHYN, L. WIETZKE, 2019: Causative classification of river flood events. – Wiley Interdisciplinary Reviews: Water **6**, e1353, DOI: 10.1002/wat2.1353.

THOBER, S., R. KUMAR, N. WANDERS, A. MARX, M. PAN, O. RAKOVEC, L. SAMANIEGO, J. SHEFFIELD, E.F. WOOD, M. ZINK, 2018: Multi-model ensemble projections of European river floods and high flows at 1.5, 2, and 3 degrees global warming. – Environmental Research Letters **13**, 014003, DOI: 10.1088/1748-9326/aa9e35.

THURNHERR, I., A. KOZACHEK, P. GRAF, Y. WENG, D. BOLSHIYANOV, S. LANDWEHR, S. PFAHL, J. SCHMALE, H. SODEMANN, H.C. STEEN-LARSEN, A. TOFFOLI, H. WERNLI, F. AEMISEGGER, 2020a: Meridional and vertical variations of the water vapour isotopic composition in the marine boundary layer over the Atlantic and Southern Ocean. – Atmospheric Chemistry and Physics **20**, 5811–5835, DOI: 10.5194/acp-20-5811-2020.

THURNHERR, I., K. HARTMUTH, L. JANSING, J. GEHRING, M. BOETTCHER, I. GORODETSKAYA, M. WERNER, H. WERNLI, F. AEMISEGGER, 2020b: The role of air–sea fluxes for the water vapour isotope signals in the cold and warm sectors of extratropical cyclones over the Southern Ocean. – Weather and Climate Dynamics Discussions **2020**, 1–42, DOI: 10.5194/wcd-2020-46.

TIEDTKE, M., 1989: A Comprehensive Mass Flux Scheme for Cumulus Parameterization in Large-Scale Models. – Monthly Weather Review **117**, 1779–1800, DOI: 10.1175/1520-0493(1989)117<1779:ACMFSF>2.0.CO;2.

TRENBERTH, K.E., A. DAI, R.M. RASMUSSEN, D.B. PARSONS, 2003: The Changing Character of Precipitation. – Bulletin of the American Meteorological Society **84**, 1205–1218, DOI: 10.1175/BAMS-84-9-1205.

TRENBERTH, K.E., J.T. FASULLO, J. MACKARO, 2011: Atmospheric Moisture Transports from Ocean to Land and Global Energy Flows in Reanalyses. – Journal of Climate **24**, 4907–4924, DOI: 10.1175/2011JCLI4171.1.

TRIGO, I.F., G.R. BIGG, T.D. DAVIES, 2002: Climatology of Cyclogenesis Mechanisms in the Mediterranean. – Monthly Weather Review **130**, 549–569, DOI: 10.1175/1520-0493(2002)130<0549:COCMIT>2.0.CO;2.

TRIGO, R.M., D. POZO-VÁZQUEZ, T.J. OSBORN, Y. CASTRO-DÍEZ, S. GÁMIZ-FORTIS, M.J. ESTEBAN-PARRA, 2004: North Atlantic oscillation influence on precipitation, river flow and water resources in the Iberian Peninsula. – International Journal of Climatology **24**, 925–944, DOI: 10.1002/joc.1048.

UHLEMANN, S., A. THIEKEN, B. MERZ, 2010: A consistent set of trans-basin floods in Germany between 1952–2002. – Hydrology and Earth System Sciences **14**, 1277–1295, DOI: 10.5194/hess-14-1277-2010.

ULBRICH, U., T. BRÜCHER, A.H. FINK, G.C. LECKEBUSCH, A. KRÜGER, J.G. PINTO, 2003a: The central European floods of August 2002: Part 1 – Rainfall periods and flood development. – Weather **58**, 371–377, DOI: 10.1256/wea.61.03A.

ULBRICH, U., T. BRÜCHER, A.H. FINK, G.C. LECKEBUSCH, A. KRÜGER, J.G. PINTO, 2003b: The central European floods of August 2002: Part 2 –Synoptic causes and considerations with respect to climatic change. – Weather **58**, 434–442, DOI: 10.1256/wea.61.03B.

VAN BEBBER, W.J., 1891: Die Zugstrassen der barometrischen Minima nach den Bahnenkarten der deutschen Seewarte für den Zeitraum 1875–1890. – Meteorologische Zeitschrift **8**, 361–366.

VANCOPPENOLLE, M., T. FICHEFET, H. GOOSSE, S. BOUILLON, G. MADEC, M.A.M. MAQUEDA, 2009: Simulating the mass balance and salinity of Arctic and Antarctic sea ice. 1. Model description and validation. – Ocean Modelling **27**, 33–53, DOI: 10.1016/j.ocemod.2008.10.005.

VICENTE, R., M. WIBRAL, M. LINDNER, G. PIPA, 2011: Transfer entropy—a model-free measure of effective connectivity for the neurosciences. – Journal of Computational Neuroscience **30**, 45–67, DOI: 10.1007/s10827-010-0262-3.

VOLOSCIUK, C., D. MARAUN, V.A. SEMENOV, N. TILININA, S.K. GULEV, M. LATIF, 2016: Rising Mediterranean Sea Surface Temperatures Amplify Extreme Summer Precipitation in Central Europe. – Scientific Reports **6**, 32450, DOI: 10.1038/srep32450.

VORMOOR, K., D. LAWRENCE, L. SCHLICHTING, D. WILSON, W.K. WONG, 2016: Evidence for changes in the magnitude and frequency of observed rainfall vs. snowmelt driven floods in Norway. – Journal of Hydrology **538**, 33–48, DOI: 10.1016/j.jhydrol.2016.03.066.

VOROGUSHYN, S., P.D. BATES, DE K. BRUIJN, A. CASTELLARIN, H. KREIBICH, S. PRIEST, K. SCHRÖTER, S. BAGLI, G. BLÖSCHL, A. DOMENEGHETTI, B. GOULDBY, F. KLIJN, R. LAMMERSEN, J.C. NEAL, N. RIDDER, W. TERINK, C. VIAVATTENE, A. VIGLIONE, S. ZANARDO, B. MERZ, 2018: Evolutionary leap in large-scale flood risk assessment needed. – WIREs Water **5**, e1266, DOI: 10.1002/wat2.1266.

WALTHER, A., J.H. JEONG, G. NIKULIN, C. JONES, D. CHEN, 2013: Evaluation of the warm season diurnal cycle of precipitation over Sweden simulated by the Rossby Centre regional climate model RCA3. – Atmospheric Research **119**, 131–139, DOI: 10.1016/j.atmosres.2011.10.012.

WANG, B., H. YANG, 2008: Hydrological issues in lateral boundary conditions for regional climate modeling: Simulation of east asian summer monsoon in 1998. – Climate Dynamics **31**, 477–490, DOI: 10.1007/s00382-008-0385-7.

WASKO, C., R. NATHAN, 2019: Influence of changes in rainfall and soil moisture on trends in flooding. – Journal of Hydrology **575**, 432–441, DOI: 10.1016/j.jhydrol.2019.05.054.

WEGMANN, M., Y. ORSOLINI, E. DUTRA, O. BULYGINA, A. STERIN, S. BRÖNNIMANN, 2017: Eurasian snow depth in long-term climate reanalyses. – The Cryosphere **11**, 923–935, DOI: 10.5194/tc-11-923-2017.

WEICHMANN, 1931: Der Hochwasserschutz in Schlesien und die Lehrendes Hochwassers vom Herbst 1930. – Der Kulturtechniker **34**, 258–272 Breslau.

WEIJS, S.V., G. SCHOUPS, VAN DE N. GIESEN, 2010: Why hydrological predictions should be evaluated using information theory. – Hydrology and Earth System Sciences **14**, 2545–2558, DOI: 10.5194/hess-14-2545-2010.

WEISMAN, M.L., W.C. SKAMAROCK, J.B. KLEMP, 1997: The Resolution Dependence of Explicitly Modeled Convective Systems. – Monthly Weather Review **125**, 527–548, DOI: 10.1175/1520-0493(1997)125<0527:TRDOEM>2.0.CO;2.

WERNLI, H., H.C. DAVIES, 1997: A Lagrangian-based analysis of extratropical cyclones. I: The method and some applications. – Quarterly Journal of the Royal Meteorological Society **123**, 467–489, DOI: 10.1256/smsqj.53810.

WERNLI, H., C. SCHWIERZ, 2006: Surface Cyclones in the ERA-40 Dataset (1958–2001). Part I: Novel Identification Method and Global Climatology. – Journal of the Atmospheric Sciences **63**, 2486–2507, DOI: 10.1175/JAS3766.1.

WICKER, L.J., W.C. SKAMAROCK, 2002: Time-Splitting Methods for Elastic Models Using Forward Time Schemes. – Monthly Weather Review **130**, 2088–2097, DOI: 10.1175/1520-0493(2002)130<2088:TSMFEM>2.0.CO;2.

WILL, A., N. AKHTAR, J. BRAUCH, M. BREIL, E. DAVIN, H.T.M. HO-HAGEMANN, E. MAISONNAVE, M. THÜRKOW, S. WEIHER, 2017: The COSMO-CLM 4.8 regional climate model coupled to regional ocean, land surface and global earth system models using OASIS3-MCT: description and performance. – Geoscientific Model Development **10**, 1549–1586, DOI: 10.5194/gmd-10-1549-2017.

WINSCHALL, A., 2013: Evaporative moisture sources for heavy precipitation events Ph.D. thesis, ETH Zurich, DOI: 10.3929/ethz-a-009755505.

WINSCHALL, A., S. PFAHL, H. SODEMANN, H. WERNLI, 2014: Comparison of Eulerian and Lagrangian moisture source diagnostics – the flood event in eastern Europe in May 2010. – Atmospheric Chemistry and Physics **14**, 6605–6619, DOI: 10.5194/acp-14-6605-2014.

WINSEMIUS, H.C., J.C.J.H. AERTS, VAN L.P.H. BEEK, M.F.P. BIERKENS, A. BOUWMAN, B. JONGMAN, J.C.J. KWADIJK, W. LIGTVOET, P.L. LUCAS, VAN D.P. VUUREN, P.J. WARD, 2016: Global drivers of future river flood risk. – Nature Climate Change **6**, 381–385, DOI: 10.1038/nclimate2893.

WINTERRATH, T., C. BRENDEL, M. HAFER, T. JUNGHÄNEL, A. KLAMETH, K. LENGFELD, E. WALAWENDER, E. WEIGL, A. BECKER, 2018: RADKLIM Version 2017.002: Reprocessed quasi gauge-adjusted radar data, 5-minute precipitation sums (YW).

YANG, S., E.A. SMITH, 2006: Mechanisms for Diurnal Variability of Global Tropical Rainfall Observed from TRMM. – Journal of Climate **19**, 5190–5226, DOI: 10.1175/JCLI3883.1.

YU, R., B.L. RUDDELL, M. KANG, J. KIM, D. CHILDERS, 2019: Anticipating global terrestrial ecosystem state change using FLUXNET. – Global Change Biology **25**, 2352–2367, DOI: 10.1111/gcb.14602.

ZAMPIERI, M., E. SCOCCIMARRO, S. GUALDI, 2013: Atlantic influence on spring snowfall over the Alps in the past 150 years. – Environmental Research Letters **8**, 034026, DOI: 10.1088/1748-9326/8/3/034026.

Acknowledgements

This thesis arose during my scientific activities at the Institute for Atmospheric and Environmental Sciences at the Goethe University Frankfurt. My work as a PhD student was funded by the German Research Foundation (Deutsche Forschungsgemeinschaft, DFG) in terms of the research group FOR 2416 Space-Time Dynamics of Extreme Floods (SPATE). The analysis presented in Appendix C was funded by Deutscher Wetterdienst (DWD), Germany's National Meteorological Service, under 3043989/17-RAD (WVTMed). This work used resources of the Deutsches Klimarechenzentrum (DKRZ) granted by its Scientific Steering Committee (WLA) under project ID bb1064 and resources of the Center for Scientific Computing (CSC).

During my PhD, I met numerous people I would like to thank for their contribution to my thesis. First and foremost, I am grateful to my PhD supervisor Prof. Dr. Bodo Ahrens. He supported me with his valuable and constructive suggestions during the planning and development of this research work and gave me always the necessary freedom to implement my ideas. I further thank Prof. Dr. Stephan Pfahl for thoroughly reviewing my thesis.

I also want to thank all members of the SPATE research group for the fruitful discussions and work done together. In particular, I would like to thank Dr. Cristina Primo for providing the centennial simulation data used in this thesis and giving me useful advice not only in statistics but also in academic life. I thank Prof. Dr. Andreas Schumann and Dr. Svenja Fischer for sharing their hydrological expertise with me and providing flood event classifications including the one presented in chapter 4 that substantially shaped the structure of this thesis.

Special thanks go to Dr. Franziska Aemisegger-Scholder and Dr. Michael Sprenger from the Atmospheric Dynamics working group at ETH Zurich. Even though my planned research visit in Zurich was not possible due to COVID-19, they shared their research experience and analyses tools with me, which was essential for chapter 6. I really enjoyed the fruitful discussions with them.

My time at the Goethe University Frankfurt would not have been the same without my colleagues at the IAU. I thank the entire department for active support whenever it was required. I appreciate our little chats in the „Teeküche"and that you made me feel welcome from the beginning. Further, I would like to thank the whole Mesoscale Meteorology and Climate group; Not only for the scientific discussions but also for sharing bad times and good times with laughter and jokes - no matter whether we met in person or remote.

Special thanks to Praveen Pothapakula Kumar, Nora Leps, Dr. Daniel Mewes, and all co-authors of my publications who spent their time reading a part of this thesis and provided helpful comments regarding writing style and content.

I am deeply attached and grateful to my husband, Dr. Michael Hoff, who was always there when I needed him, who gave me motivation, but also distraction when I needed distance from the work, and who was patient when I was sitting for hours at this manuscript. Last but not least, I thank my family for their constant support and encouragement.